The Pennsylvania State University

The Graduate School

RELEASED PIEZOELECTRIC THIN FILMS FOR PIEZOELECTRIC MICROMACHINED ULTRASOUND TRANSDUCERS (PMUT)

A Dissertation in

Materials Science and Engineering
by

Pannawit Tipsawat

Submitted in Partial Fulfillment
of the Requirements
for the Degree of

Doctor of Philosophy

August 2024

The dissertation of Pannawit Tipsawat was reviewed and approved by the following:

Susan Trolier-McKinstry
Evan Pugh University Professor and Flaschen Professor of Ceramic Science and Engineering and Electrical Engineering
Dissertation Advisor
Chair of Committee

Thomas N. Jackson
Robert E. Kirby Chair Professor of Electrical Engineering

Andrea P. Argüelles
Assistant Professor of Engineering Science and Mechanics

Sri-Rajasekhar Kothapalli
Associate Professor of Biomedical Engineering

John C. Mauro
Graduate Program Head, Professor of Materials Science and Engineering

ABSTRACT

This thesis focuses on the exploration of released PZT thin films, from the fundamentals that govern the magnitude of the piezoelectric response to applications. Quantitative measurement of the effective longitudinal piezoelectric coefficient of partially released PZT thin films was conducted to provide a better understanding of declamping from the substrate. Partially released structures were employed in the development and optimization of piezoelectric micromachined ultrasound transducers (PMUT) phased arrays tailored for neuromodulation applications. Further steps in developing piezoelectric devices for neuromodulation applications involved investigating the PZT PMUT with a fully released structure to offer feasibility in flexible and conformable applications such as implantable ultrasound stimulation.

The investigation of partially released PZT thin films was realized using the double beam laser interferometry technique to suppress the effect of substrate bending; such bending commonly inflates the values inferred from single beam laser interferometry. The partially released structures with 2 mol% Nb-doped $Pb(Zr_{0.52}Ti_{0.48})O_3$ thin film were fabricated using a two-step backside etching process with ZnO serving as both a sacrificial layer and the silicon deep reactive ion etch stop layer. This fabrication approach allowed the released boundary to be well-defined and provided a laser path for backside probing. Significant improvement in the effective longitudinal piezoelectric coefficient ($d^*_{33,f}$) was observed in the partially released structure, with the released structures exhibiting a 3-fold increase in $d^*_{33,f}$ compared to clamped samples, reaching values of 420 ± 8 pm/V in the 75% released structure. This enhancement is attributed to the change in stress level, the reduction in mechanical constraints, and improved domain wall mobility in the released structures. The results confirm that substrate declamping can substantially elevate the piezoelectric performance of thin films, bringing them closer to that of bulk ceramics.

Partially released PZT-based PMUT phased arrays on a silicon-on-insulator substrate were designed and fabricated. Utilizing a 1.5 μm thick 2 mol% Nb-doped $Pb(Zr_{0.52}Ti_{0.48})O$ thin film, a 32-element PMUT phased array was optimized for neuromodulation. The array was designed using k-Wave simulations to achieve a focal distance (F) of 20 mm and steering angles (θ_s) ranging from -60° to 60°. The rigid PMUT phased array was tested in a water tank and driven with 14.6 V unipolar pulses using appropriate time delays for beamforming and steering. The maximum peak-to-peak acoustic pressure from the phased array with beamforming was found to be 0.44 MPa at 1.4 MHz, with axial and lateral resolutions of 9.2 and 1 mm, respectively. The achievable acoustic intensity (I_{SPPA} = 1.29 W/cm^2) achieved at low driving voltages underscores the potential of rigid PMUT arrays for low-intensity focused ultrasound stimulation.

Fully flexible PMUT arrays were also explored to enable conformality to curved and complex surface structures such as the skull or brain membrane, aiming for potential implantable applications. The transition to flexible PMUTs involved fabricating these devices on polyimide substrates using a transfer and release method with a ZnO sacrificial layer. A critical aspect of this design was the incorporation of an electroplated Ni metal rigid support layer to optimize the operational resonance frequency, ensuring compatibility with the pitch required for effective beamforming. A rectangular prototype PMUT was demonstrated using a capacitor stack of Pt/PZT/Pt with a 1 μm thick 2 mol% Nb-doped $Pb(Zr_{0.52}Ti_{0.48})O_3$ thin film, deposited on a silicon substrate and patterned via plasma etching with an electroplated Ni hard mask. However, the design was prone to the high stress levels; the asymmetric structure led to stress concentrations and resulted in damaged devices after release. Challenges encountered included cracking and electrode delamination. To address the stress-related issues, the introduction of a compressive layer, such as SiO_2, is proposed to counterbalance the stress levels. Additionally, adjusting the electrode coverage

from 60% to 100% should reduce stress concentration at the edges of the electrodes, thereby mitigating the risk of cracking and peeling.

This thesis represents significant findings on the piezoelectric response of released PZT structures and advancements in the design, fabrication, and application of PMUTs. The findings provide insights into both rigid and flexible device configurations, highlighting the potential for these technologies in developing next-generation implantable ultrasound stimulation devices. The detailed exploration of material properties, device architectures, and fabrication techniques contributes to a deeper understanding of the critical factors influencing PMUT performance.

TABLE OF CONTENTS

LIST OF FIGURES

LIST OF TABLES

ACKNOWLEDGEMENTS

First and foremost, I would like to express my gratitude to my advisor, Dr. Susan Trolier-McKinstry, for the opportunity to join the STM group at Pennsylvania State University. Coming from Thailand with a bachelor's and master's degree in physics, I dreamt of conducting impactful research that would lead to real-world devices. This seemed unattainable until Dr. Trolier-McKinstry invited me to the Department of Materials Science and Engineering at Pennsylvania State University. Here, I built a solid foundation in Materials Science through coursework and hands-on experience in material deposition, characterization, and device fabrication. Throughout my PhD, despite numerous challenges and problems, she has consistently provided invaluable guidance and helped me expertise all my skills.

Transitioning from fundamental materials research to microfabrication of piezoelectric devices was challenging. Dr. Thomas Jackson was an important person of my research career; he offered crucial advice on materials processing, particularly wet and dry etching techniques, which broadened my understanding beyond the basics. I am also grateful for the opportunity to participate in his Thanksgiving dinner every year.

Microfabrication seems to be the strange wording to me when I first started working in STM group. I still remember Dr. McKinstry's assurance that I would have more than enough time and chance to work inside the nanofabrication lab. With her guidance and through several projects, I've learned and gained expertise in most of the techniques at Nanofabrication Lab – Materials Research Institute (MRI). I am immensely thankful for the Nanofabrication staff at MRI; their support from my initial training to process development has been crucial in achieving my research goals. I am particularly grateful to Guy Lavallee and Shane Miller for their insights on plasma etching, Michael Labella II and Kathleen Gehoski for their consistent support in lithography, Fan He, William Mahoney, and William Drawl for their assistance with sputtering and evaporation

techniques, Bangzhi Liu for his guidance on efficient SEM usage, and Andrew Fitzgerald for his patience during various wet chemical processes, especially nickel electroplating. Their encouragement was invaluable, particularly when I broke my first device wafer – William Drawl's and Guy Lavallee's humorous reassurance that "everyone breaks a wafer" helped me maintain perspective and resilience.

The STM group members have created a supportive environment that I deeply value. From one generation to the next, their collegiality has enriched my laboratory experience. Christopher Cheng, in particular, has been instrumental in honing my skills in piezoelectric micromachined ultrasound transducers and has been a dependable nanofabrication partner. Kathleen Coleman, Veronika Kovacova, Jung In Yang, Daisuke Hama, Betul Akkopru Akgun, Wanlin Zhu, Smitha Shetty, Leonard Jacques, Dixiong Wang, and Tianning Liu have significantly contributed to my understanding of piezoelectric and ferroelectric materials. Beth Jones provided invaluable advice from my first solution preparation session, enhancing my thought processes in $Pb(Zr,Ti)O_3$ processing. Michael Hann and Nathan Bishop were welcoming when I first arrived on campus, guiding me through the initial stages of my materials science education. Joining the group with Travis Peters, I can confidently say that navigating through MatSE 400 Crystal Chemistry and other graduate courses would have been insurmountable without his support. Song Won Ko, Shruti Gupta, Madeleine Petschnigg, Yeongwoo Son, Gavin Hennessey, Ryan Hawks, Haley Jones, Stanislav Udovenko, Yiwen Song, Kyuhwe Kang, Pedram Yousefin, Anthony Diaz-Huemme, Kae Nakamura, and Erdem Ozdemir have all contributed to a positive research culture in our group.

During my PhD, I also had the special opportunity to attend weekly group meetings of the JERG research group, where I further developed my engineering fundamentals, tool maintenance, and device processing skills under the guidance of Dr. Thomas Jackson and the JERG group

members: Sora Lee, Akanksha Gupta, Mohit Tendulkar, Sang Yoo, Quyen Tran, Akshay Agrawell, Xiaojun Zheng, Hanyaun Laing, Victoria Vasquez, Yuen Sun, and Lixian Yan.

I am thankful for the collaboration and contributions from all my colleagues throughout my projects: Junhyuk Park, Jeong Nyeon Kim, Sheikh Ilham, Zeinab Kashani, Roland Kessels, Sartanee Suebka, and all the co-PIs on the projects: Dr. Kyusun Choi, Dr. Mehdi Kiani, and Dr. Antoine Wojdyla.

My time at Pennsylvania State University ranks among the most memorable periods of my life, both academically and socially. I am grateful to have shared classes with exceptional colleagues in the Materials Science and Engineering department, particularly Benazir Yalcin, Cierra Chandle, Javier Mena, Stephanie Castro Baldivieso, Yosuke Endo, Cindy Chen, and Tatiana Kuznetsova. Additionally, my cooking partners, Kosuke Tsuji and Sun Hwi Bang, helped make my time during Covid far from dull. My PSU football watching friends also made Saturdays during the Fall semester the highlight of my year: Eriko Maeda, Koki Nakagawa, Vorrapard Kumthongdee, Phakphum Artkaew, Jeanpun Antarasen, Kittiphum Pawikhum, Nattaporn Plub-In, Korrawee Henprasert, Piyaphat Chaemchuen, and Thitiwat Tapha.

Last but not least, I owe a tremendous thank you to my family members: my father Pramote Tipsawad and my mother Piyanan An-gratoke, for their care and unwavering support, as well as Naiyana Tipsawad, who supported me throughout my PhD journey. One person who has been by my side every day during my PhD is my partner, Wisansaya Jaikeandee. I am profoundly grateful for her support and patience throughout our long-distance relationship, and for bearing with me through all the emotional highs and lows. Words cannot fully express my appreciation for her enduring presence during these challenging times.

To everyone I've met and spoken with, I wouldn't be the person I am today without you all.

Finally, I would like to acknowledge the financial support for this thesis provided by the National Aeronautics and Space Administration (NASA) with award numbers NNX17AF66G, 80NSSC19K0371, 80NSSC19K0234, and 80NSSC24K0326, the Flaschen Professorship supporting Chapter 3 - Quantitative Piezoelectric Measurements of Partially Released Pb(Zr, Ti)O_3 Structures, the National Institutes of Health (NIH) under Grants R21EY029424 and R21EY030700 for Chapter 4 - 32 Element Piezoelectric Micromachined Ultrasound Transducer Phased Array for Neuromodulation, and the National Science Foundation (NSF) with award number 2219811 for Chapter 5 - Process Development for Flexible Ultrasound Transducer Phased Arrays. Additionally, the Development and Promotion of Science and Technology Talents Project (DPST) through a Thai government scholarship partially funded my PhD studies.

Note: This dissertation presents the technical findings and conclusions that do not necessarily reflect the view of the funding agency.

Chapter 1

Introduction

This chapter provides a review of piezoelectric materials and their properties as well as the micromachining processes that are central to this thesis.

1.1 Piezoelectric Properties

Piezoelectric materials play a pivotal role in materials research, from the start of World War I to the modern era of semiconductors and 5G technology. This thesis discusses piezoelectricity: the ability to generate an electric charge in response to an applied mechanical stress—and conversely, to undergo mechanical deformation when subjected to an electric field, alongside an overview of dielectric and ferroelectric properties. The operational principles of piezoelectric microelectromechanical systems (piezoMEMS) are discussed. PiezoMEMS are creating new markets for miniaturized devices such as portable health monitors, microspeakers, and adjustable optics, among others.

1.1.1 The History of Piezoelectricity

The direct piezoelectric effect was first discovered by Jacques and Pierre Curie in 1880 in their work on single-crystal quartz. Upon the application of pressure, the crystal generated an electric charge/voltage. Gabriel Lippmann postulated the converse piezoelectric effect in 1881, using fundamentals of thermodynamics, which led to its experimental verification by the Curie

brothers. Early research in piezoelectricity, notably during World War I, led to Paul Langevin's development of underwater ultrasonic transmission in the so-called Langevin-type. This 40 kHz transducer, with a quartz crystal sandwiched between two metal plates, was hindered by quartz's low coupling factor, resulting in poor sensitivity and a narrow bandwidth [1]. Another early piezoelectric material, Rochelle salt ($NaKC_4H_4O_6 \cdot 4H_2O$), was developed in the United States by Nicholson, Anderson, and Cady [2]. While Rochelle salt exhibited an impressive electromechanical coupling factor, its water solubility and susceptibility to humidity degradation limited practical use.

Concurrently, during World War II, the perovskite ceramic barium titanate ($BaTiO_3$) was discovered by scientists in the United States, Japan, and Russia [3]-[5]. The piezoelectric effect in $BaTiO_3$ was serendipitously observed by R. B. Gary and S. Roberts in 1946 when randomly oriented polycrystalline $BaTiO_3$ crystals were electrically poled [6],[7]. However, $BaTiO_3$'s operational temperature range was constrained by its low Curie temperature.

The pursuit of stabilized $BaTiO_3$ led to A-site substitutions with elements such as Pb and Ca, culminating in the discovery of the $Pb(Zr, Ti)O_3$ solid solution system by E. Sawaguchi, G. Shirane, and Y. Takagi [8],[9]. Subsequent efforts to measure the electromechanical coupling factor around the morphotropic phase boundary by B. Jaffe, R. S. Roth, and S. Marzullo at the National Bureau of Standards revealed $Pb(Zr,Ti)O_3$'s substantial electromechanical response at the 52:48 composition [10]-[13]. This composition is highlighted in the phase diagram of PZT shown in Figure 1-1. A significant milestone for $Pb(Zr,Ti)O_3$ occurred at Clevite Corporation where H. Jaffe, B. Jaffe, W. R. Cook, and D. Berlincourt developed modified $Pb(Zr,Ti)O_3$ solid solutions [14][19]. Their groundbreaking works contributed to the famous book "Piezoelectric Ceramics" [20]. To date, bulk piezoelectric ceramics have proven vital for applications such as actuators, filters, medical transducers, speakers, and more. At present, piezoelectric thin films are receiving increasing focus for micromachined ultrasound transducers, microactuators, sensors, adjustable optics, and energy harvesters, etc.

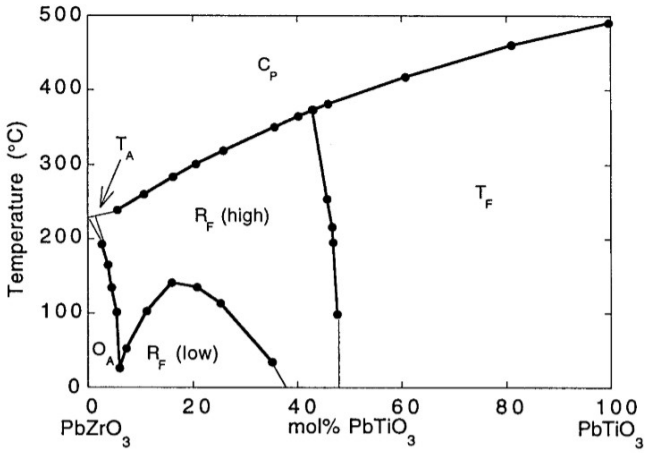

Figure 1-1: PZT phase diagram adapted from B. Jaffe *et al.* (1971) [20].

1.1.2 The Fundamental Piezoelectric Equations

Dielectric materials are electrical insulators in which charge can be displaced upon application of an electric field, creating net polarization from mechanisms such as electronic, ionic, dipolar, and space charge polarizability. For linear dielectric materials, the polarization, denoted by P_i, induced by the application of an electric field E_j, can be described as [21]:

$$P_i = \chi_{ij} E_j \tag{1.1}$$

where χ_{ij} is the material's dielectric susceptibility. Another crucial parameter to understand is the electric flux, or dielectric displacement (D_i), which can be represented as [21]:

$$D_i = \varepsilon_0 E_i + P_i \tag{1.2}$$

Here, ε_0 represents the permittivity of free space ($8.854 \times 10^{-12}\,\mathrm{Fm}^{-1}$). The dielectric displacement, D_i, signifies the total electric flux density, including the contribution from both the free charges and the polarization charges within the material.

Substituting Equations (1.1) and (1.2), the dielectric displacement can be reformulated to [21]:

$$D_i = \varepsilon_0 E_i + \chi_{ij} E_j = \left(\varepsilon_0 \delta_{ij} + \chi_{ij}\right) E_j = \varepsilon_{ij} E_j \tag{1.3}$$

Thus, the dielectric permittivity tensor ε_{ij} encompasses both the intrinsic permittivity of free space and the material's response to the electric field, measured by the dielectric susceptibility.

The relative permittivity or dielectric constant of a material, ε_r, is often used to represent the dielectric properties of materials. It is defined as the ratio of the material's permittivity tensor ε_{ij} to the permittivity of free space ε_0 [21]:

$$\varepsilon_r = \frac{\varepsilon_{ij}}{\varepsilon_0} \tag{1.4}$$

The dielectric loss tangent ($\tan\delta$), describes the energy loss due to the finite electrical resistivity in a capacitor. As the relative permittivity is a complex quantity ($\varepsilon_r = \varepsilon_r' - i\varepsilon_r''$), the loss tangent can be defined as [22]:

$$\tan\delta = \frac{\varepsilon_r''}{\varepsilon_r'} \tag{1.5}$$

where ε_r' and ε_r'' are the real and imaginary components of the dielectric constant, respectively. The loss tangent quantifies the phase lag between the external electric field and the polarization.

As mentioned previously, **piezoelectric materials** are a subclass of dielectric materials that exhibit both electrical and mechanical responses to external stimuli, enabling the conversion between electrical and mechanical energy. It is also important to understand the role of crystal symmetry on the materials' properties. Of the 32 crystal point groups, 21 are non-centrosymmetric, allowing them to possess odd-rank tensor properties [22][24]. Among these 21 non-centrosymmetric point groups, only one does not have the necessary symmetry to exhibit piezoelectricity. Thus, the remaining 20 non-centrosymmetric point groups enable potentially

piezoelectric materials. Of these point groups, 10 of them develop a unique polar axis where spontaneous polarization is observed [22][24]. These materials exhibit pyroelectric properties, where the polarization varies as a function of temperature. A subgroup of pyroelectric materials, in which polarization can be reoriented between crystallographically-defined states with the application of an external field, are then classified as possessing ferroelectric properties.

The **direct piezoelectric effect** describes the generation of an electric displacement (D_i) or field (E_i) in response to applied mechanical stress (σ_{jk}) or strain (S_{jk}), is given by [20], [22], [25]:

$$D_i = d_{ijk}\sigma_{jk} \tag{1.6}$$

$$D_i = e_{ijk}S_{jk} \tag{1.7}$$

where d_{ijk} and $-e_{ijk}$ represent the piezoelectric coefficient charge and strain tensors, respectively. Conversely, piezoelectric materials can generate mechanical stress or strain when subjected to an electric field or displacement, a phenomenon known as the **converse piezoelectric effect** [20], [22], [25]:

$$S_{ij} = d_{ijk}E_k \tag{1.8}$$

$$\sigma_{ij} = -e_{ijk}E_k \tag{1.9}$$

The **piezoelectric constitutive equations** provide a full expression of the piezoelectric relation between electric and elastic variables as [20], [23]:

$$S_{ij} = s^E_{ijkl}\sigma_{kl} + d_{ijl}E_l \tag{1.10}$$

$$D_i = d_{ikl}\sigma_{kl} + \varepsilon^S_{ij}E_j \tag{1.11}$$

$$\sigma_{ij} = c^D_{ijkl}S_{kl} - h^\sigma_{ijl}D_l \tag{1.12}$$

$$E_i = -h_{ikl}S_{kl} + \beta^S_{ij}D_j \tag{1.13}$$

$$S_{ij} = s^D_{ijkl}\sigma_{kl} + g^\sigma_{ijl}D_l \tag{1.14}$$

$$E_i = -g_{ikl}\sigma_{kl} + \beta_{ij}^{\sigma} D_j \tag{1.15}$$

$$\sigma_{ij} = c_{ijkl}^{E} S_{kl} - e_{ijl}^{\sigma} E_l \tag{1.16}$$

$$D_i = e_{ikl} S_{kl} + \varepsilon_{ij}^{S} E_j \tag{1.17}$$

Here, d, e, g, and h are the piezoelectric coefficient tensors, c_{ijkl} is the stiffness tensor, s_{ijkl} is the compliance tensor, ε_{ij} is the permittivity tensor, and β_{ij} is the inverse dielectric susceptibility. These **piezoelectric coefficients** are quantified as follows [20], [23]:

$$d_{ijk} = \frac{\partial D_i}{\partial \sigma_{jk}}_E = \frac{\partial S_{ij}}{\partial E_k}_\sigma \quad (\text{C N}^{-1} \text{ or m V}^{-1}) \tag{1.18}$$

$$e_{ijk} = -\frac{\partial \sigma_{ij}}{\partial E_k}_S = \frac{\partial D_i}{\partial S_{jk}}_E \quad (\text{C m}^{-2} \text{ or V m N}^{-1}) \tag{1.19}$$

$$g_{ijk} = -\frac{\partial E_i}{\partial \sigma_{jk}}_E = \frac{\partial D_i}{\partial S_{jk}}_\sigma \quad (\text{m}^2 \text{ C}^{-1} \text{ or N V}^{-1} \text{ m}^{-1}) \tag{1.20}$$

$$h_{ijk} = \frac{\partial \sigma_{ij}}{\partial D_k}_S = -\frac{\partial E_i}{\partial S_{JK}}_D \quad (\text{m V}^{-1} \text{ or N C}^{-1}) \tag{1.21}$$

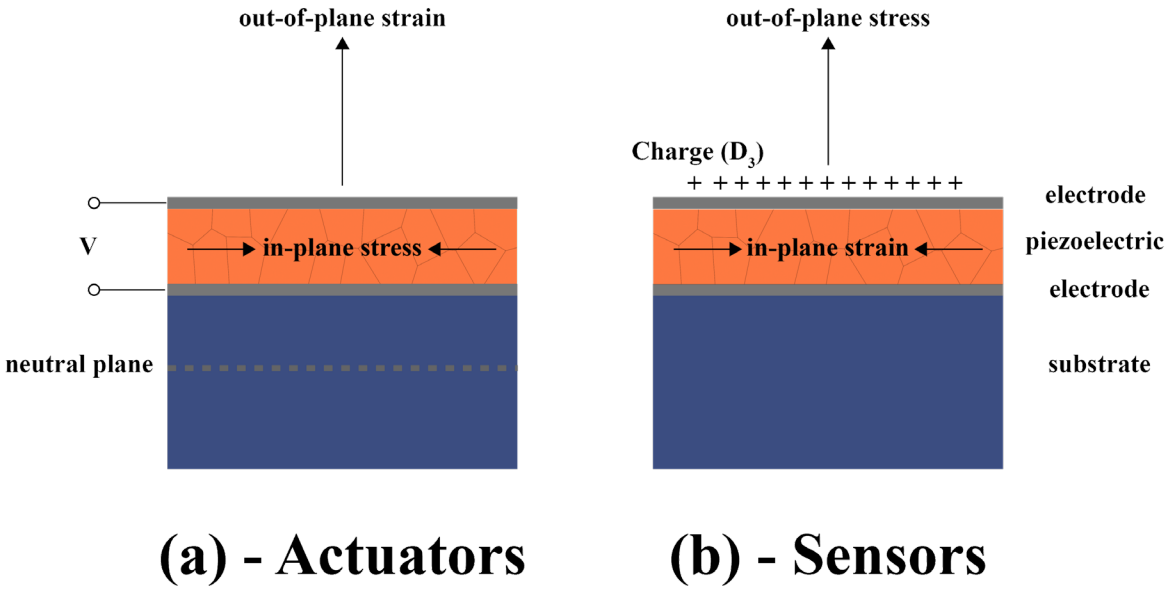

Figure 1-2: A schematic showing the response of piezoelectric films for (a) actuators and (b) sensors. Adapted from [23].

For piezoelectric thin films, the substrate plays a significant role; the substrate acts as a passive elastic layer that contributes to the overall strain of the structure. As illustrated in Figure 1-2(a), most piezoelectric MEMS actuators operate in a 31-mode based on the converse piezoelectric effect. The application of an electric field, E_3, initiates an in-plane stress, σ_1 and σ_2; together with the presence of the substrate, this results in bending motion in the out-of-plane direction (S_3). For sensor applications, the application of external stress (σ_3) generates an electric displacement, D_3, at the electrode; the generated charge is usually amplified by bending.

The longitudinal piezoelectric coefficient, d_{33}, and the transverse piezoelectric coefficient, e_{31}, are commonly used to characterize these scenarios. Studies by Lefki *et al.* [27] and Muralt *et al.* [23] demonstrate the effective piezoelectric coefficients for longitudinal, $d_{33,f}$, and transverse, $e_{31,f}$, applications, where the subscript *f* denotes the film under clamped conditions. These expressions are derived under two assumptions; the in-plane stresses are equal, $\sigma_1 = \sigma_2$, and the out-of-plane stress is zero, $\sigma_3 = 0$ [27].

$$d_{33} = \frac{\partial D_3}{\partial \sigma_3}_E = \frac{\partial S_3}{\partial E_3}_\sigma \tag{1.22}$$

And under clamped conditions:

$$S_1 = S_{11}^E \sigma_1 + S_{12}^E \sigma_2 + S_{13}^E \sigma_3 + d_{31} E_3 = 0 \tag{1.23}$$

$$S_2 = S_{11}^E \sigma_2 + S_{12}^E \sigma_1 + S_{13}^E \sigma_3 + d_{31} E_3 = 0 \tag{1.24}$$

$$S_3 = S_{13}^E (\sigma_1 + \sigma_2) + S_{33}^E \sigma_3 + d_{33} E_3 \tag{1.25}$$

where $S_1 = S_2 = 0$, $\sigma_1 = \sigma_2$ and $\sigma_3 = 0$. The effective longitudinal piezoelectric coefficient is then [27]:

$$d_{33,f} = \frac{S_3}{E_3} = \frac{e_{33}}{c_{33}^E} = d_{33} - \frac{2S_{13}^E}{S_{11}^E + S_{12}^E}, \quad d_{33} > d_{33,f} \tag{1.26}$$

A similar method was utilized for the effective transverse piezoelectric coefficient [23]:

$$e_{31} = -\frac{\partial \sigma_1}{\partial E_3}_S = \frac{\partial D_3}{\partial S_1}_E \tag{1.27}$$

where the average in-plane strain is:

$$\frac{\sigma_1 - \sigma_2}{2} = \frac{S_1 + S_2 - 2d_{31}E_3}{2(S_{11}^E + S_{12}^E)} \tag{1.28}$$

leading to the derived effective transverse piezoelectric coefficient [23]:

$$e_{31,f} = \frac{d_{31}}{S_{11}^E + S_{12}^E} = e_{31} - \frac{c_{13}^E}{c_{33}^E} e_{33}, \quad \left|e_{31,f}\right| > |e_{31}| \tag{1.29}$$

Piezoelectric materials are generally classified into lead-based and lead-free types. Lead-based perovskite materials, particularly lead zirconate titanate (PZT), have historically dominated in actuators, transducers, and sensors due to their superior dielectric and piezoelectric properties. Despite their performance, concerns about lead toxicity have driven research into alternatives such as potassium sodium niobate ($(K,Na)NbO_3$, KNN) and aluminum nitride (AlN) [28][29].

Lead-free materials like KNN thin films have advanced significantly, yet they often face stoichiometry issues due to the volatility of alkaline elements [30][32]. Bismuth ferrite ($BiFeO_3$) has been explored for its multiferroic properties but is hindered by high leakage currents at high fields due to defect concentrations [33][36]. Wurtzite materials like aluminum nitride (AlN) and zinc oxide (ZnO) are widely used in sensor and resonator applications. While ZnO and AlN boast excellent piezoelectric charge coefficients ($h_{31,f}$) and high piezoelectric coupling coefficients, their relatively low piezoelectric stress coefficients ($e_{31,f}$) limit their effectiveness in transducers and

actuators [25], [29], [37][39]. Nonetheless, scandium, Sc, doping in AlN has shown to improve $e_{31,f}$, enhancing its applicability in diverse fields [40][41].

Despite these innovations, PZT films remain unmatched in terms of piezoelectric stress coefficients, benefiting from polarization rotation and domain wall motion contributions. This work investigates the morphotropic phase boundary of $Pb(Zr_{0.52}Ti_{0.48})O_3$, leveraging its potential for piezoelectric microelectromechanical systems (piezoMEMS). Table 1-1 summarizes the piezoelectric properties of selected materials.

Table 1-1: Properties of select thin film piezoelectric materials [40][54].

Property	**PZT**	**ZnO**	**$Sc_xAl_{1-x}N$**	**AlN**	**$(K,Na)NbO_3$**	**$BiFeO_3$**
$-e_{31,f}$ **(Cm^{-2})**	12 - 16	1	3	1	2 - 5.6	2.9 - 3.5
$-h_{31,f}$ **(Cm^{-2})**	0.01	0.1	0.21	0.1	0.01	0.014 - 0.035
ε_r	1200	10	14	10	500 - 1000	100 -204
tanδ	< 0.05	0.01 - 0.1	< 0.1	0.003	< 0.07	< 0.1

1.2 Lead Zirconate Titanate Thin Films

$Pb(Zr,Ti)O_3$ is one of the most extensively researched materials in the realm of piezoelectric and ferroelectric systems. It has a perovskite-type unit cell that arises from the solid-solution of lead zirconate ($PbZrO_3$) and lead titanate ($PbTiO_3$). While its high temperature paraelectric phase is cubic and lacks spontaneous polarization, $Pb(Zr,Ti)O_3$ undergoes a phase transition upon cooling to lower symmetry phases—rhombohedral, tetragonal, orthorhombic, or monoclinic. This transition is accompanied by the emergence of spontaneous polarization in most cases due to the displacement of the B-site cations (zirconium or titanium) in the oxygen octahedra, as shown in Figure 1-3 [55][57]. This displacement leads to an imbalance of charge within the unit

cell, resulting in a non-zero net dipole moment. The collective orientation of these dipoles across the crystal allows for poling of the material's spontaneous polarization, which underlies the versatile piezoelectric and ferroelectric functionalities of $Pb(Zr,Ti)O_3$.

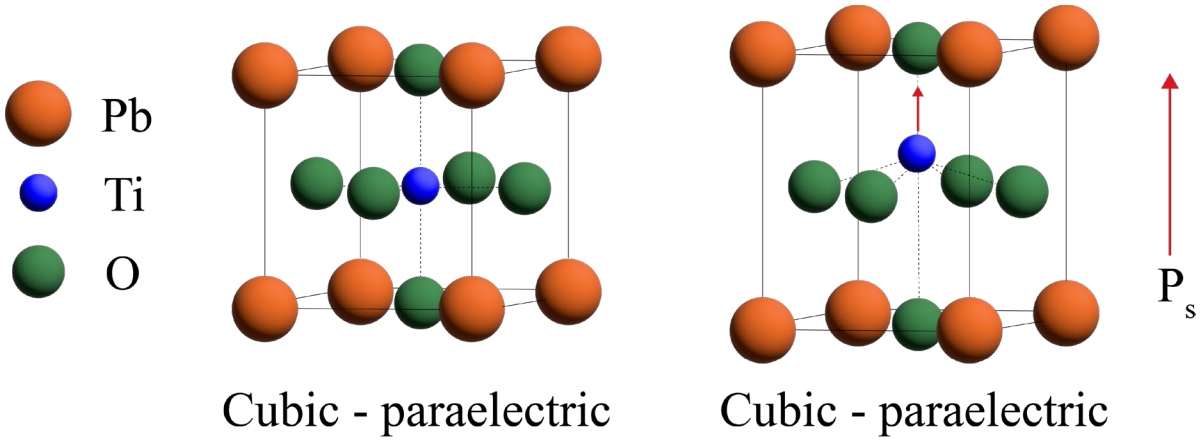

Figure 1-3: $Pb(Zr,Ti)O_3$ unit cell in paraelectric phase (cubic) and ferroelectric phase (tetragonal).

The polarizability reaches its maximum at the boundary of two phases, known as the morphotropic phase boundary (MPB) at a composition of $Pb(Zr_{0.52}Ti_{0.48})O_3$. At the morphotropic phase boundary, $Pb(Zr,Ti)O_3$ sits at the boundary between the tetragonal (6 directions for the spontaneous polarization) and rhombohedral (8 directions for the spontaneous polarization) phases, increasing the polarizability. Together with the low energy cost of making domain walls and improved domain wall movement at the MPB, this creates high electromechanical coupling at this composition. This phenomenon positions $Pb(Zr,Ti)O_3$ as currently unmatched for high-strain piezoMEMS actuators [58]60[60].

The contribution to the piezoelectric response in $Pb(Zr,Ti)O_3$ is not solely from the intrinsic contribution, (i.e., the field-induced displacement of atoms in the unit cell), but is also affected by the extrinsic contributions, such as domain wall motion and phase boundary motion. Domains in ferroelectric materials are regions with similar polarization directions. The plane separating two regions with different polarization directions is called a domain wall. Domain wall formation occurs in $Pb(Zr,Ti)O_3$ to minimize (i) the depolarizing field and (ii) the net mechanical strain

created from the ferroelectric phase transition as illustrated in Figure 1-4. For the first mechanism, as the material cools through the ferroelectric phase transition, the depolarizing field (E_d) arises from surface charges created by the spontaneous polarization, producing an internal electric field. This complicates the formation of an entirely single domain, as it is energetically expensive. The depolarizing field can be compensated by surrounding charges or minimized by splitting the domain into oppositely oriented states, frequently forming a 180° ferroelectric domain wall. An example of the second scenario can be given during the phase transition from a cubic to a tetragonal perovskite. During this phase transition, regions of the material develop polarization along the original *a*-axis, while other regions polarize along the original *c*-axis. The boundary between these domains constitutes a domain wall, which serves to minimize the elastic energy arising from the differences between the two states resulting in the nucleation of a ferroelastic 90° domain wall. This ferroelastic domain wall balances both the internal mechanical strain and depolarizing field.

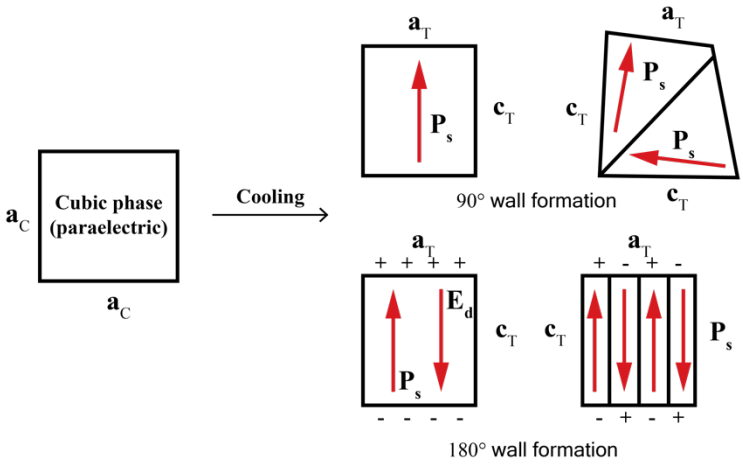

Figure 1-4: Schematic showing 180° and 90° domain wall formation in the tetragonal perovskite phase (adapted from [23]).

The allowed domain walls vary based on the difference in crystal structure of the ferroelectric from the paraelectric phase. For example, in the rhombohedral phase, where the polar axis is along the <111> direction of the cubic phase, this allows 71°, 109°, and 180° walls to form.

As the polarization can be reoriented, the domain wall can also be moved by the external electric field or stress. Note that both non-180° and 180° domain walls can be moved by an electric field; however, only non-180° domain walls can be moved by a uniform stress as the two domains differ in spontaneous strain.

Nucleation of domains and motion of domain walls is responsible for the characteristic polarization-electric field hysteresis of ferroelectric materials [23]. At smaller electric fields, domain wall motion is responsible for a significant portion of the extrinsic contribution to piezoelectric properties [61–64].

One important characterization technique employed to study $Pb(Zr,Ti)O_3$ in this work is the measurement of polarization as a function of the electric field. As shown in Figure 1-5(a), at point A, a small field is applied to the material, and the polarization begins to increase linearly, as described by equation 1.1; this behavior is typically observed in as-grown pristine films. As the field increases, domains start to align in the favorable direction, and polarization/charge rapidly increases up to point C. The increase from point C to D becomes linear again as the domains are fully aligned, a state commonly referred to as **saturation polarization,** P_{sat}.

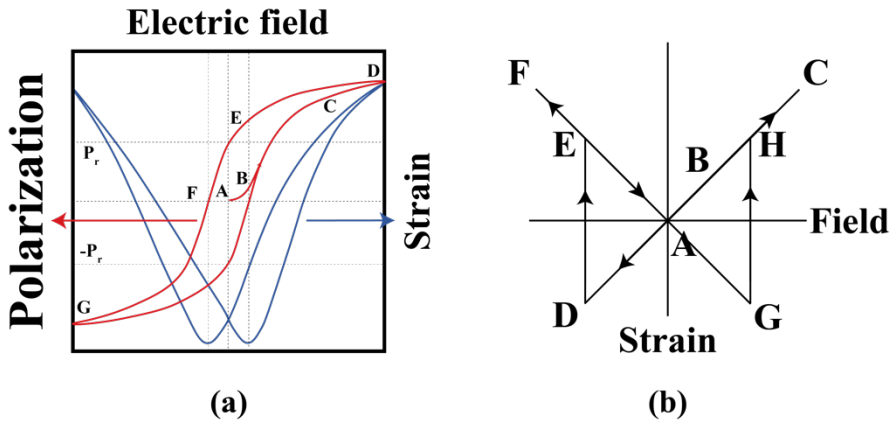

Figure 1-5: Schematic showing polarization – electric field and strain – electric field hysteresis loops and (b) the ideal strain hysteresis loop without ferroelastic domain motion (adapted from [23]).

As the electric field decreases, the polarization drops due to domain back-switching, and at zero field, the residual polarization is termed the **remanent polarization,** P_r. Subsequent application of an opposing field brings the net polarization to zero; this field is known as the **coercive field,** E_c. Continuing to apply the field past $-E_c$ causes dipole moments to align in the opposite direction, reaching the negative saturation polarization. As the electric field is reduced again, polarization also decreases and completes a full cycle back to the positive direction, as depicted in Figure 1-5(a).

The relation between strain and electric field is central to the piezoelectric effect. Three principal mechanisms contribute to the strain in piezoelectric substances: (i) the intrinsic piezoelectric effect, (ii) polarization switching, and (iii) domain wall motion. Figures 1-5(a) provides a representation of strain under an applied electric field, in conjunction with the polarization-electric field loop. A schematic for strain – electric field response is illustrated in Figure 1-5(b); at point A, where the external field is absent, the strain is null. With an increasing electric field, the strain first increases linearly, as prescribed by the converse piezoelectric effect, reaching a maximum strain through the path from A to B to C. On decreasing the electric field back to zero, the strain diminishes, and returns to point A Reversing the external field causes negative strain from A to D as the polarization direction is antiparallel to the applied field. When the field intensity is sufficient to reverse the polarization at point D, the strain increases towards the positive regime, reaching point E. Subsequently, the strain increases in the negative field direction, peaking at point F. As the field is removed, the strain decreases back to point A. The cycle is then completed by a reversal in polarization at point A, which leads to a negative strain shift towards point G and then ascends to point H and back to C.

It is important to acknowledge that strain measurements can be complex due to several factors. The contributions from domain wall movement and the switching of ferroelastic domains are as significant as the intrinsic piezoelectric contributions. The transition between polarization

states is typically not as abrupt as the schematic suggests in Figure 1-5(b). Additionally, remanent strain may lead to a non-zero strain at zero field, and domain wall motion contributes a nonlinear aspect to the overall strain-electric field response even at sub-switching fields.

Several methods are used to enhance the piezoelectric and ferroelectric properties in PZT. Doping $Pb(Zr,Ti)O_3$ with donor or acceptor elements is common; specifically, acceptor-doped $Pb(Zr,Ti)O_3$ known as hard PZT, results in more stable domain structure and a high coercive field. Conversely, some $Pb(Zr,Ti)O_3$ is doped with niobium (Nb), a donor-type dopant. Such doping leads to the creation of lead vacancies, thereby facilitating improved domain wall motion [65–68]. Despite $Pb(Zr,Ti)O_3$ thin films being considered mature materials in the piezoelectric-ferroelectric domain, opportunities for further improvement and research exploration remain substantial.

1.3 Thesis Organization

This thesis focuses on the fundamentals of piezoelectric properties and their applications in an ultrasound transducer for neuromodulation and neurostimulation. The first chapter provides a brief introduction to piezoelectricity in lead zirconate titanate (PZT); the later chapters include:

- **Chapter 2 - The Piezoelectric Micromachined Ultrasound Transducer:** This chapter provides the fundamental background on the principals of operation of a PMUT and the design criteria for $Pb(Zr,Ti)O_3$-based PMUT.
- **Chapter 3 - Quantitative Measurement of $d_{33,f}$ for Partially Released PZT Thin Films:** A methodology is presented to precisely measure the longitudinal piezoelectric coefficient in released piezoMEMS structures, including device design, fabrication, and experimental results.
- **Chapter 4 - 32 Elements PZT-Based Phased Array PMUT for Neuromodulation:** This chapter demonstrates the behavior of a PZT-based PMUT in a low-intensity focused ultrasound transducer. The phased arrays were fabricated on a silicon-on-insulator platform to operate in a beamforming/steering fashion, enhancing both the spatial resolution and the area coverage.

- **Chapter 5 - Flexible PMUT Phased Array for Neurostimulation:** This chapter illustrates further development of the PMUT phased array onto a flexible substrate and discussed the feasibility of applying an implantable ultrasound stimulation system.
- **Chapter 6 – Conclusions and Future Work:** This chapter emphasizes the findings from the thesis and provides possible avenues for future work.

Bibliography

[1] K. Honda, *Ultrasonic World*. Tokyo: NHK Books, 1994.

[2] A. Nicholson, "Piezophony," U.S. Patent 1,495,429, filed April 10, 1918, and patented May 10, 1924.

[3] E. Wainer, "High Titania Dielectrics," *Trans. Electrochem. Soc.*, vol. 89, no. 1, p. 331, 1946.

[4] B. Vul, "High and Ultrahigh Dielectric Constant Materials," *Electrichestvo*, vol. 3, p. 12, 1946.

[5] T. Ogawa and S. Waku, History of Barium Titanate Discovery in Japan, in Splendid Tita-Bari [in Japanese], Tokyo, Japan: Maruzen, 1990.

[6] H. Jaffe, "Piezoelectric Ceramics," *J. Am. Ceram. Soc.*, vol. 41, no. 11, pp. 494–498, 1958.

[7] S. Roberts, "Dielectric and Piezoelectric Properties of Barium Titanate," Phys. Rev., vol. 71, no. 12, p. 890, 1947.

[8] E. Sawaguchi, G. Shirane, and Y. Takagi, "Phase Transition in Lead Zirconate," *J. Phys. Soc. Jpn.*, vol. 6, no. 5, pp. 333–339, 1951.

[9] E. Sawaguchi, "Ferroelectricity versus Antiferroelectricity in the Solid Solutions of $PbZrO_3$ and $PbTiO_3$," *J. Phys. Soc. Jpn.*, vol. 8, no. 5, pp. 615–629, 1953.

[10] H. Jaffe, "Titanate Ceramics for Electro-mechanical Purposes," *Ind. Eng. Chem.*, vol. 2, pp. 264-268, 1950.

[11] B. Jeffe, R. S. Roth, and S. Marzullo, "Piezoelectric Properties of Lead Zirconate Titanate Solid Solution Ceramics," *J. Appl. Phys.*, vol. 25, no. 6, pp. 809-810, 1954.

[12] B. Jaffe, R. S. Roth, and S. Marzullo, "Properties of Piezoelectric Ceramics in the Solution Series Lead Titanate-Lead Zirconate-Lead Oxide-Tin Oxide and Lead Titanate-Lead Hafnate," *J. Res. Natl. Bur. Stand.*, vol. 55, pp. 239-243, 1955.

[13] B. Jaffe, "Piezoelectric Transducers using Lead Titanate and Lead Zirconate," U.S. Patent 2,708,244, May 10, 1955.

[14] D. Berlincourt, C. Cmolik, and H. Jaffe, "Piezoelectric Properties of Polycrystalline Lead Titanate-Zirconate Compositions," *Proc. IRE*, vol. 48, pp. 220-223, 1960.

[15] B. Jaffe, "Antiferroelectric ceramics with field-enforced transitions: a new nonlinear circuit element," *Proc. IRE*, vol. 49, no. 8, pp. 1264-1267, 1961.

[16] D. Berlincourt, H. Jaffe, H. H. A. Krueger, and B. Jaffe, "Release of electric energy in $PbNb(Zr,Ti,Sn)O_3$ by temperature- and by pressure-enforced phase transitions," *Appl. Phys. Lett.*, vol. 3, no. 5, pp. 90-92, 1963.

[17] R. Gerson and H. Jaffe, "Electrical Conductivity in Lead Titanate Zirconate Ceramics," J. *Phys. Chem. Solids*, vol. 24, no. 7, pp. 979-984, 1963.

[18] D. A. Berlincourt, D. R. Curran, H. Jaffe, "*Piezoelectric and piezomagnetic materials and their function in transducers*," in Physical Acoustics: Principles and Methods, vol. 1, Part A, New York: Academic Press, 1964, pp. 202-204.

[19] D. Berlincourt, H. H. A. Krueger, and B. Jaffe, "Stability of phases in modified lead zirconate with variation in pressure, electric field, temperature and composition," *J. Phys. Chem. Solids*, vol. 25, no. 7, pp. 659-674, 1964.

[20] B. Jaffe, W. R. Cook, and H. Jaffe, *Piezoelectric Ceramics*. London: Academic Press, 1971.

[21] D. J. Griffiths*, Introduction to Electrodynamics*, Cambridge: Cambridge University Press, 2023.

[22] S. Trolier-McKinstry and R. Newnham, *Materials Engineering: Bonding, Structure, and Structure-Property Relationships*. Cambridge: Cambridge University Press, 2017.

[23] D. Damjanovic, "Ferroelectric, Dielectric and Piezoelectric Properties of Ferroelectric Thin Films and Ceramics," *Rep. Prog. Phys.*, vol. 61, no. 9, p. 1267, 1998.

[24] R. E. Newnham, Properties of Materials: Anisotropy, Symmetry, Structure. Oxford, U.K.: Oxford University Press, 2005.

[25] S. Trolier-McKinstry and P. Muralt, "Thin Film Piezoelectrics for MEMS," *J. Electroceram.*, vol. 12, no. 7-17, 2004.

[26] P. Muralt, "Piezoelectric Thin Films for MEMS," *Integr. Ferroelectr.*, vol. 17, no. 1-4, pp. 297–307, 1997.

[27] K. Lefki and G. Dormans, "Measurement of Piezoelectric Coefficients of Ferroelectric Thin Films," *J. Appl. Phys.*, vol. 76, no. 3, pp. 1764–1767, 1994.

[28] M. D. Maeder, D. Damjanovic, and N. Setter, "Lead Free Piezoelectric Materials," *J. Electroceram.*, vol. 13, pp. 385-392, 2004.

[29] G. Piazza, V. Felmetsger, P. Muralt, R. H. Olsson III, and R. Ruby, "Piezoelectric aluminum nitride thin films for microelectromechanical systems," *MRS Bull.*, vol. 37, no. 11, pp. 1051-1061, 2012.

[30] M. Dolhen, A. Mahajan, R. Pinho, M. E. Costa, G. Trolliard, and P. M. Vilarinho, "Sodium Potassium Niobate ($K_{0.5}Na_{0.5}NbO_3$, KNN) Thick Films by Electrophoretic Deposition," *RSC Adv.*, vol. 5, pp. 4698–4706, 2014.

[31] H. J. Seog, A. Ullah, C. W. Ahn, I. W. Kim, S. Y. Lee, J. Park, H. J. Lee, S. S. Won, and S. Kim, "Recent Progress in Potassium Sodium Niobate Lead-Free Thin Films," *J. Korean Phys. Soc.*, vol. 72, pp. 1467–1483, 2018.

[32] J. Wu, "Perovskite Lead-Free Piezoelectric Ceramics," *J. Appl. Phys.*, vol. 127, p. 190901, 2020.

[33] M. Niu, H. Zhu, Y. Wang, J. Yan, N. Chen, P. Yan, and J. Ouyang, "Integration-Friendly, Chemically Stoichiometric $BiFeO_3$ Films with a Piezoelectric Performance Challenging that of PZT," *ACS Appl. Mater. Interfaces*, vol. 12, no. 30, pp. 33899–33907, 2020.

[34] X. Qi, J. Dho, R. Tomov, M. Blamire, and J. L. MacManus-Driscoll, "Greatly Reduced Leakage Current and Conduction Mechanism in Aliovalent Ion-Doped $BiFeO_3$," *Appl. Phys. Lett.*, vol. 86, no. 6, p. 062903, 2004.

[35] Y. Wang, L. Zhou, M. F. Zhang, X. Y. Chen, J. M. Liu, and Z. G. Liu, "Room-Temperature Saturated Ferroelectric Polarization in $BiFeO_3$ Ceramics Synthesized by Rapid Liquid Phase Sintering," *Appl. Phys. Lett.*, vol. 84, no. 10, p. 1731, 2004.

[36] N. Wang, X. Luo, L. Han, Z. Zhang, R. Zhang, H. Olin, and Y. Yang, "Structure, Performance, and Application of $BiFeO_3$ Nanomaterials," *Nano-Micro Lett.*, vol. 12, p. 81, 2020.

[37] M.-A. Dubois and P. Muralt, "Properties of Aluminum Nitride Thin Films for Piezoelectric Transducers and Microwave Filter Applications," *Appl. Phys. Lett.*, vol. 74, no. 20, pp. 3032–3034, 1999.

[38] B. Kumar and S.-W. Kim, "Energy Harvesting Based on Semiconducting Piezoelectric ZnO Nanostructures," *Nano Energy*, vol. 1, no. 3, pp. 342–355, 2012.

[39] N. Emanetoglu, C. Gorla, Y. Liu, S. Liang, and Y. Lu, "Epitaxial ZnO Piezoelectric Thin Films for SAW Filters," *Mater. Sci. Semicond. Process.*, vol. 2, no. 3, pp. 247–252, 1999.

[40] M. Akiyama, K. Umeda, A. Honda, and T. Nagase, "Influence of Scandium Concentration on Power Generation Figure of Merit of Scandium Aluminum Nitride Thin Films," *Appl. Phys. Lett.*, vol. 102, no. 2, 2013.

[41] O. Zywitzki, T. Modes, S. Barth, H. Bartzsch, and P. Frach, "Effect of Scandium Content on Structure and Piezoelectric Properties of AlScN Films Deposited by Reactive Pulse Magnetron Sputtering," *Surf. Coat. Technol.*, vol. 309, pp. 417–422, 2017.

[42] J. G. Gualtieri, J. A. Kosinski, and A. Ballato, "Piezoelectric Materials for Acoustic Wave Applications," *IEEE Trans. Ultrason. Ferroelectr. Freq. Control*, vol. 41, no. 1, pp. 53–59, 1994.

[43] G. Carlotti and G. Socino, "Acoustic Investigation of the Elastic Properties of ZnO Films," *Appl. Phys. Lett.*, vol. 51, no. 23, p. 1889.

[44] Q. Wang, Y. Lu, S. Mishin, Y. Oshmyansky, and D. A. Horsley, "Design, Fabrication and Characterization of Scandium Aluminum Nitride Based Piezoelectric Micromachined Ultrasonic Transducers," *J. Microelectromech. Syst.*, vol. 26, no. 5, pp. 1132–1139, 2017.

[45] S. Fichtner, T. Reimer, S. Chemnitz, F. Lofink, and B. Wagner, "Stress Controlled Pulsed Direct Current Co-Sputtered $Al_{1-x}Sc_xN$ as Piezoelectric Phase for Micromechanical Sensor Applications," *APL Mater.*, vol. 3, no. 11, p. 116102, 2015.

[46] M.-A. Dubois and P. Muralt, "Measurement of the Effective Transverse Piezoelectric Coefficient $e_{31,f}$ of AlN and Pb(Zr,Ti)O_3 Thin Films," *Sens. Actuators A Phys.*, vol. 77, pp. 106–112, 1999.

[47] S. W. Zhang, Z. Zhou, J. Luo, and J. F. Li, "Potassium-Sodium-Niobate Based Thin Films: Lead Free for Micro-Piezoelectrics," *Ann. Phys.*, vol. 531, no. 7, p. 1800525, 2019.

[48] S. Sharma, A. Kumar, V. Gupta, and M. Tomar, "Dielectric and Ferroelectric Studies of KNN Thin Film Grown by Pulsed Laser Deposition Technique," *Vacuum*, vol. 160, pp. 233–237, 2019.

[49] M. Nguyen, M. Dekkers, E. P. Houwman, H. T. Vu, H. N. Vu, and G. Rijnders, "Lead-Free $(K_{0.5}Na_{0.5})NbO_3$ Thin Films by Pulsed Laser Deposition Driving MEMS-Based Piezoelectric Cantilevers," *Mater. Lett.*, vol. 164, pp. 413–416, 2016.

[50] I. Kanno, T. Mino, S. Kuwajima, T. Suzuki, H. Kotera, and K. Wasa, "Piezoelectric Properties of (K,Na)NbO_3 Thin Films Deposited on (001) Sr-RuO_3/Pt/MgO Substrates," *IEEE Trans. Ultrason. Ferroelectr. Freq. Control*, vol. 54, no. 12, pp. 2562–2566, 2007.

[51] K. Kariya, T. Yoshimura, K. Ujimoto, and N. Fujimura, "Quantitative Analysis of the Direct Piezoelectric Response of Bismuth Ferrite Films by Scanning Probe Microscopy," *Sci. Rep.*, vol. 9, p. 19727, 2019.

[52] R. Maran, S. Yasui, E. Eliseev, A. Morozovska, H. Funakubo, I. Takeuchi, and N. Valanoor, "Enhancement of Dielectric Properties in Epitaxial Bismuth Ferrite-Bismuth Samarium Ferrite Superlattices," *Adv. Electron. Mater.*, vol. 2, no. 8, p. 1600170, 2016.

[53] K. Ujimoto, T. Yoshimura, K. Wakazono, A. Ashida, and N. Fujimura, "Crystal Structure and Local Piezoelectric Properties of Strain-Controlled (001) $BiFeO_3$ Epitaxial Thin Films," *Thin Solid Films*, vol. 550, pp. 738–741, 2014.

[54] N. Okamoto, K. Kariya, T. Yoshimura, and N. Fujimura, "The Effect of Crystal Distortion and Domain Structure on Piezoelectric Properties of $BiFeO_3$ Thin Films," *Jpn. J. Appl. Phys.*, vol. 57, no. 11S, p. 11UF07, 2018.

[55] N. Zhang, H. Yokota, A. M. Glazer, Z. Ren, D. A. Keen, D. S. Keeble, P. A. Thomas, and Z.-G. Ye, "The Missing Boundary in the Phase Diagram of $PbZr_{1-x}Ti_xO_3$," *Nat. Commun.*, vol. 5, p. 5231, 2014.

[56] V. R. Cooper, I. Grinberg, N. R. Martin, and A. M. Rappe, "Local Structure of PZT," in *AIP Conf. Proc.*, vol. 626, pp. 26–35, 2002.

[57] H. Fu and R. E. Cohen, "Polarization Rotation Mechanism for Ultrahigh Electromechanical Response in Single-Crystal Piezoelectrics," *Nature*, vol. 43, pp. 281–283, 2000.

[58] B. Noheda, D. E. Cox, G. Shirane, R. Guo, B. Jones, and L. E. Cross, "Stability of the Monoclinic Phase in the Ferroelectric Perovskite $PbZr_{1-x}Ti_xO_3$," *Phys. Rev. B Condens. Matter Mater. Phys.*, vol. 63, no. 1, 2001.

[59] B. Noheda and D. E. Cox, "Bridging Phases at the Morphotropic Boundaries of Lead Oxide Solid Solutions," *Phase Transit.*, vol. 79, no. 1-2, pp. 5–20, 2007.

[60] B. Noheda, J. Gonzalo, L. Cross, R. Guo, S. Park, D. E. Cox, and G. Shirane, "Tetragonal-To-Monoclinic Phase Transition in a Ferroelectric Perovskite: The Structure of $PbZr_{0.52}Ti_{0.48}O_3$," *Phys. Rev. B*, vol. 61, no. 13, 2000.

[61] F. Jona and G. Shirane, *Ferroelectric Crystals*, Oxford: Pergamon Press, 1962.

[62] L. E. Cross, "Ferroelectric Ceramics: Tailoring Properties for Specific Applications," in *Ferroelectric Ceramics: Tutorial Reviews, Theory, Processing, and Applications*, Springer, 1993, pp. 1–85.

[63] E. I. Bondarenko, V. Y. Topolov, and A. V. Turik, "The Role of 90° Domain Wall Displacements in Forming Physical Properties of Perovskite Ferroelectric Ceramics," *Ferroelectr. Lett. Sect.*, vol. 13, no. 1, p. 1, 1991.

[64] N. Bassiri-Gharb, "Dielectric and Piezoelectric Nonlinearities in Oriented $Pb(Yb_{1/2},Nb_{1/2})O_3$-$PbTiO_3$ Thin Films," PhD Thesis, Department of Materials Science and Engineering, Pennsylvania State University, University Park, USA, 2005.

[65] T. Haccart, D. Remiens, and E. Cattan, "Substitution of Nb Doping on the Structural, Microstructural and Electrical Properties in PZT Films," *Thin Solid Films*, vol. 423, no. 2, pp. 235–242, 2003.

[66] W. Zhu, I. Fujii, W. Ren, and S. Trolier-McKinstry, "Domain Wall Motion in A and B Site Donor-Doped $Pb(Zr_{0.52}Ti_{0.48})O_3$ Films," *J. Am. Ceram. Soc.*, vol. 95, no. 9, pp. 2906–2913, 2012.

[67] C. B. Yeager and S. Trolier-McKinstry, "Epitaxial $Pb(Zr,Ti)O_3$ ($0.30 \leq x \leq 0.63$) Films on (100)MgO Substrates for Energy Harvesting Applications," *J. Appl. Phys.*, vol. 112, no. 7, p. 074107, 2012.

[68] W. Zhu, I. Fujii, W. Ren, and S. Trolier-McKinstry, "Influence of Mn Doping on Domain Wall Motion in $Pb(Zr_{0.52}Ti_{0.48})O_3$ Films," *J. Appl. Phys.*, vol. 109, no. 6, p. 064105, 2010.

Chapter 2

Piezoelectric Micromachined Ultrasound Transducers

The advent of microfabrication methods has revolutionized the traditional bulk ceramic ultrasound transducers, paving the way for the development of miniaturized micromachined ultrasound transducers (MUT). These advances bring several advantages, including reduced operational voltages, flexibility in the resonant frequency of devices in a single wafer, and significant size reduction. This chapter provides an overview of piezoelectric micromachined ultrasound transducers, discussing their design, operational principles, and application in detail.

2.1 Conventional Ultrasound Transducers and Capacitive Micromachined Ultrasound Transducers (CMUT)

Building upon the foundational principles outlined in Chapter 1, the direct and converse piezoelectric effects serve both to generate and receive acoustic pressure waves in ultrasound transducers. Conventional ultrasound transducer technology, primarily leveraging the thickness mode of vibration, has found extensive application across various domains [1][4].

As the demand for small, portable, and high frequency ultrasound applications has grown, micromachined ultrasound transducers (MUT) offer an approach to scaling size, additional design flexibility, better impedance match with the media, and improved compatibility with complementary metal–oxide semiconductor (CMOS) circuitry [5][15]. The transition to MUT technology both leverages micromachining techniques for miniaturization and serves as also a means to mitigate the difficulties encountered with conventional piezoelectric ultrasound, such as complications in manufacturing thin matching layers and dicing small kerfs required for high-

frequency ultrasound [16-19]. This chapter aims to briefly introduce the operational principles underlying conventional bulk ultrasound transducers and CMUT. It will then explore the fundamentals and fabrication methods for PMUTs, highlighting the development of device structures and their integration into miniaturized devices.

2.1.1 Conventional Bulk Ceramic/Single Crystal Ultrasound Transducers

Ultrasound transducers are a well-established technology where piezoelectric ceramics or piezoelectric single crystals typically undergo vibrational motion in thickness mode. The common ceramic materials of choice are PZT ceramics, such as PZT-5H, due to their excellent electromechanical coupling properties (d_{33} ~ 593 pC/N, k_{33} ~ 0.75) [18], [21], [22]. Alternatively, single crystal relaxor-PT materials, such as $Pb(Mg_{1/3}Nb_{2/3})–PbTiO_3$ (PMN-PT) (d_{33} ~ 1500-2800 pC/N, k_{33} ~ 0.94) and $Pb(In_{1/2}Nb_{1/2})–Pb(Mg_{1/3}Nb_{2/3})–PbTiO_3$ (PIN-PMN-PT) (d_{33} ~ 1500-2700 pC/N, k_{33} ~ 0.95), are also employed in ultrasound transducers due to their large piezoelectric coefficients and high coupling coefficients [23][25]. However, it is notable that these relaxor-PT materials possess low Curie or rhombohedral to tetragonal phase transition temperatures (T_c ~ 130°C for PMN-PT, ~ 200°C for PIN-PMN-PT), which might limit their stability during operation when subjected to heat [23],[27][29].

As these transducers operate in thickness mode, the resonant frequency, f_r, is determined by the thickness [3]:

$$t = n\,{}^{c_{piezo}}/_{2f_r} \qquad \text{Eq. 1}$$

where t is the thickness of the piezoelectric material, n is the harmonic number of the resonant frequency, and c_{piezo} is the sound velocity in the piezoelectric. The piezoelectric material oscillates at specific frequencies upon excitation by electrical impulses, generating acoustic waves that

propagate through the media. The efficiency of this process heavily relies on the piezoelectric coefficients and electromechanical coefficient of the piezoceramics, as well as the matching and backing layer.

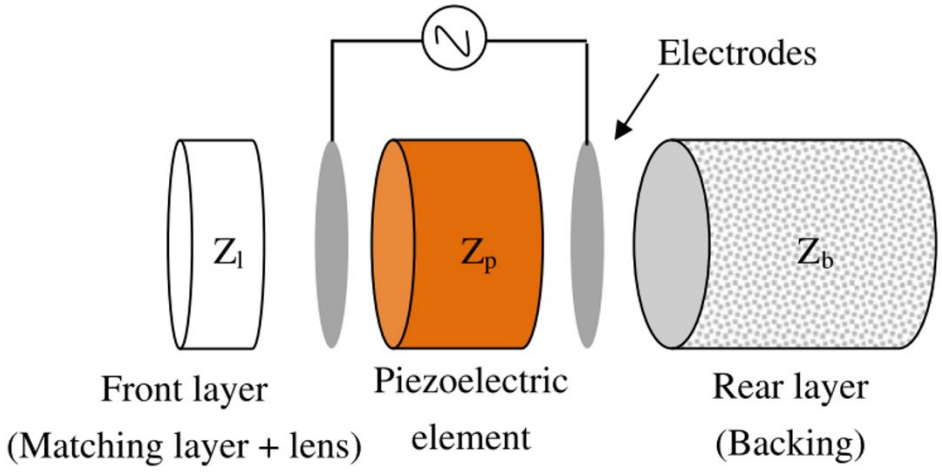

Figure 2-1: Schematic of a conventional piezoelectric ceramic ultrasound transducer consisting of matching layer, lens, piezoelectric element, electrode, and backing layer. The figure adapted from [19].

The matching layer is an important element of the transducer because of the large mismatch in acoustic impedance between most piezoelectric ceramics/single crystals ($Z_p \approx 33$ MRayl) and the medium ($Z_l \approx 1.5$ MRayl for water) [2]. The transmission coefficient (T) is defined by [19]:

$$T = {2Z_l}/{Z_p + Z_l} \qquad \text{Eq. 2}$$

Here, Z_l and Z_p are the acoustic impedances of the load (medium) and the piezoelectric material, respectively. For instance, the transmission coefficient for a piezoelectric ceramic transducer in water is only about 10%. To address this problem, one or more matching layers with an optimized acoustic impedance is added to the front-end of the transducer. For a single matching layer, the

thickness is a quarter wavelength, and the optimal acoustic impedance of the matching layer (Z_m) is [19][20]:

$$Z_m = \left(Z_p Z_l\right)^{1/2} \quad \text{Eq. 3}$$

Another important element is the backing layer attached to the back of the transducer. The backing layer is used to absorb acoustic waves at the backside of the transducer, damp unwanted vibration, and prevent ringing as the piezoelectric layer generates acoustic waves in both directions [1]-[4].

Generally, ultrasound transducers are used either as a single element, as shown in Figure 2-1, or as an array. An ultrasound transducer array consists of multiple elements arranged in 1D, 1.5D, or 2D configurations, allowing each element to be excited for electrical focusing and steering. The array can be prepared as a piezocomposite, where pieces of piezoelectric ceramics, single crystals, and polymers are fabricated into specific shapes [30]. For example, a 1-3 composite consists of pillars of piezoelectric material embedded in a polymer matrix, while a 2-2 composite consists of alternating planks of piezoelectric materials and polymer. Figure 2-2(a) demonstrates the focusing of a linear phased array by controlling the time delay of individual excitation pulses so that the acoustic pulses arrive at the focus point simultaneously [16]. Ideally, the linear phased array is arranged with the pitch between each element being λ/2 to minimize side/grating lobes [16]. The time delay profile can also be adjusted to steer the beam at a desired angle, as shown in the schematic in Figure 2-2(b). In Chapter 4, the concepts of focusing and steering will be discussed and applied to PMUT phased arrays.

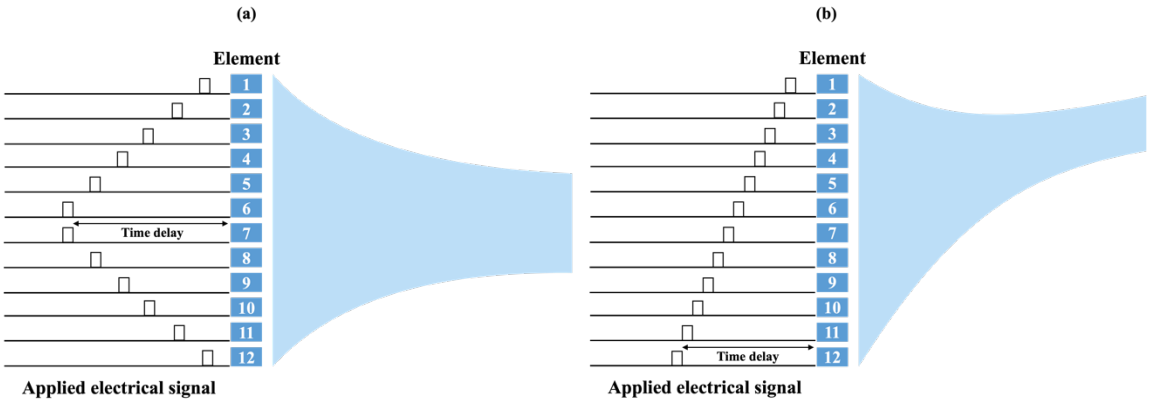

Figure 2-2: Schematic for (a) electrical focusing and (b) steering of linear phased array.

Conventional transducers are widespread and diverse, showcasing the adaptability and effectiveness of piezoelectric technology. Early applications, such as underwater sound systems and sonar (sound navigation and ranging), are indispensable for underwater navigation and detection [31]. In imaging applications, transducers enable detailed representations of internal body structures, blood flow, and fetal development [23]. Furthermore, the emergence of wearable devices allows for remote healthcare monitoring [32]. These advancements highlight the critical role of conventional piezoelectric transducers.

2.1.2 Capacitive Micromachined Ultrasound Transducers (CMUT)

There are two types of MUT based on their operational principles: capacitive micromachined ultrasound transducers (CMUT) and piezoelectric micromachined ultrasound transducers (PMUT). In this section, a brief introduction of CMUT will be given. The operational principle of a CMUT is based on the flexural vibration of membrane structure generated by field-induced electrostatic attraction. CMUT were first reported by K. Suzuki *et al.*, utilizing silicon IC processes to fabricate a so-called "electrostatic ultrasonic transducer" [33]]. The membrane

structure, depicted in Figure 2-3, features top and bottom electrodes separated by a vacuum gap and an insulating layer. The membrane motion, driven by DC and AC voltages, is determined by the oscillating electrostatic force. This simple membrane structure enables integration of CMUT directly on CMOS as demonstrated in the development of a single-chip ultrasound imaging array CMUT-on-CMOS [34][37]. Additionally, the literature reports a large bandwidth, up to 175%, and an electromechanical coupling coefficient (k^2) of up to 85% [38], [39].

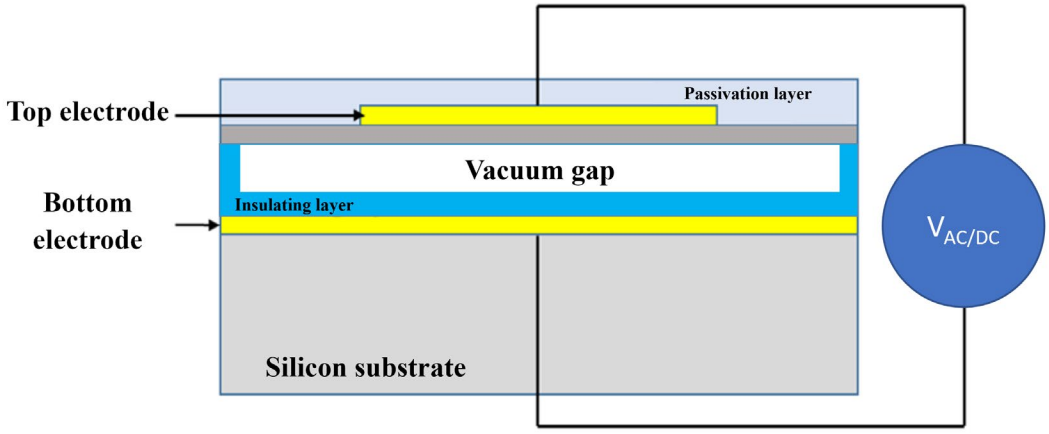

Figure 2-3: Schematic of capacitive micromachined ultrasound transduction (CMUT) [7].

The key parameter for CMUT operation is the collapse voltage or pull-in voltage, which refers to the critical voltage at which the movable membrane of the CMUT collapses onto the stationary electrode. CMUT operation can be divided into three modes: conventional mode [11], collapse mode [40], and collapse and snap mode [41].

In the conventional mode, electrostatic transduction occurs as the top electrode (free membrane) vibrates upon the application of external voltage without touching the underlying electrode (backplate), as depicted in Figure 2-4(a). In collapse mode, the free membrane is DC biased at the collapse voltage, causing the top electrode to remain in contact with the bottom electrode throughout operation. Acoustic pressure is then generated by the application of an AC field, as shown in Figure 2-4(b).

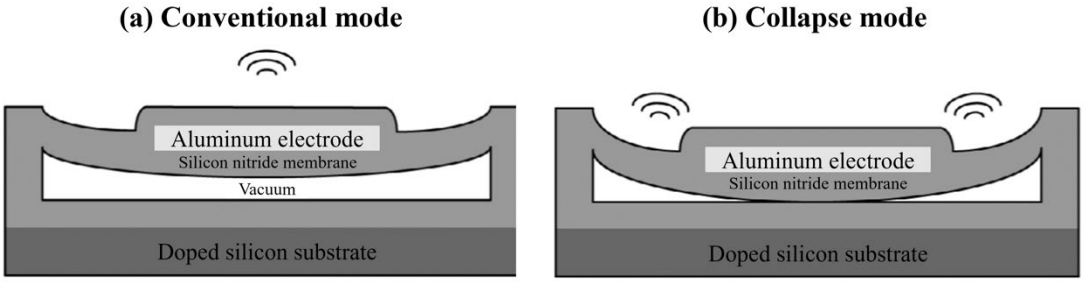

Figure 2-4: CMUT operating principle: (a) conventional and (b) collapse. Figure from reference [40].

The final operation mode is collapse and snap mode. In this mode, the membrane is initially driven by a DC voltage higher than the collapse voltage. The voltage is then reduced below the collapse voltage but higher than the snapback voltage so that the membrane remains in contact with the backplate, as illustrated in region 2 in Figure 2-5. Simultaneously, an AC voltage is applied to generate the vibration motion.

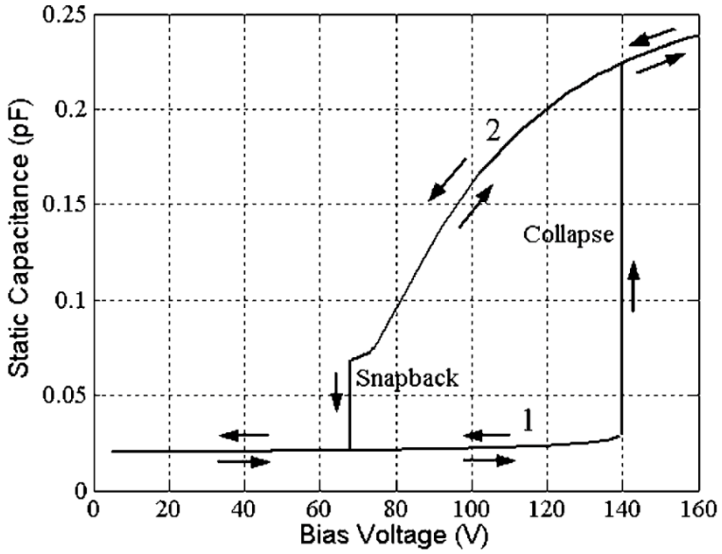

Figure 2-5: The simulation of the voltage-capacitance curve of CMUT operated in collapse and snap back mode [41].

As discussed above, CMUT operation involves us of high voltage to control the vibration mode, with typical operating voltages reaching up to 100 V [42]. This implies challenges in high-voltage CMOS and the integration in small-scale devices, particularly for wearable technology and implantable devices where operating voltage is a crucial safety factor. This issue highlights the potential of PMUTs, as their mechanism relies on electromechanical coupling through piezoelectric properties, allowing them to operate at lower voltages compared to both bulk ceramic transducers and CMUTs.

2.2 The Piezoelectric Micromachined Ultrasound Transducers

Piezoelectric micromachined ultrasound transducers or PMUTs are devices that integrate the basic principle of piezoelectricity with advanced microfabrication techniques enabling the miniaturization of ultrasound devices. Unlike their conventional counterparts, PMUTs operate based on a flexural vibration mode. This offers an advantage, as the resonant frequency can be tuned by adjusting device geometry such as device shape, lateral dimensions, diaphragm structure, and boundary conditions [6][8].

The initial development of PMUT technology can be traced back to the pioneering work on ZnO sensor devices fabricated using planar magnetron sputtering by Shiosaka *et al.* [43]. In 1983, building upon techniques from Shiosaki's publications, a released structure of a 5 μm ZnO on a Si diaphragm for acoustic sensors was successfully demonstrated, achieving a sensitivity of 25 μV/μbar [44]. Following this, significant efforts were made to develop and establish the fundamentals and application space of PMUT technology. Notable developments included the demonstration of ferroelectric/piezoelectric PZT thin films for micromotors by Udayakumar *et al.* in 1990 and the utilization of PZT-based PMUT arrays for in-water imaging by Bernstein *et al.* in 1997 [45], [46]. The exploration of materials continued with the introduction of AlN by Shelton *et*

al. in 2009 [47]. From the significant improvements in piezoelectric responses demonstrated in Al,ScN by Akiyama *et al.* [48], Wang *et al.* developed the first Al,ScN-based PMUT with an enhanced electromechanical coupling coefficient (k^2) of 36%, exceeding those available from AlN PMUT [49]. Additionally, the piezoelectric polymer P(VDF-TrFE) was explored for PMUT applications by Chao *et al.* [50].

2.2.1 Operational Principle and Resonant Frequency Design

PMUT structures consist of an active piezoelectric layer and a passive elastic layer, where the diaphragm's vibration behavior is the result of the interaction between these two layers. The diaphragm typically operates in the 31-mode, with the piezoelectric active layer sandwiched between top and bottom electrodes. The applied electric field along the thickness direction (E_3) induces an in-plane strain (S_1) causing the piezoelectric layer to alternately contract and expand in the lateral dimension, as shown in Figures 2-6(a) and (b), respectively. This lateral contraction occurs as the electric field direction is parallel to the polarization. In-plane expansion can also occur if the domain reorientation is exploited, though that is rarely done [51]. Alternatively, the diaphragm can also operate in 33-mode via the interdigitated (IDT) electrodes as demonstrated in [52][55]. It is important to note that the neutral plane of the diaphragm must be positioned in the passive layer for the piezoelectric effect to be optimized such that opposing voltages or strains are not developed within the active layer [56].

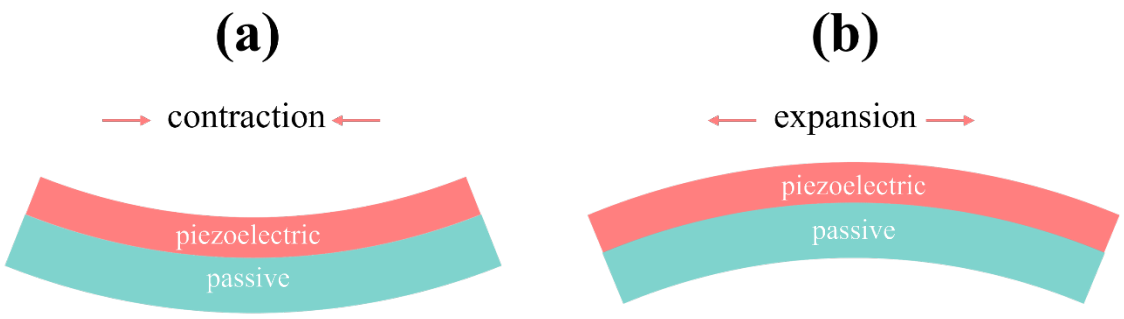

Figure 2-6: Illustration of bending induced from (a) contraction and (b) expansion of the piezoelectric layer in simplified PMUT structure.

This dynamic bending from the converse piezoelectric effect is utilized in actuator/transmit operations, as the oscillation from out-of-plane deflection generates acoustic pressure output. Conversely, incoming acoustic waves can be sensed by the diaphragm as they induce vibration in the structure; the direct piezoelectric effect generates electrical charges in the sensor/receive mode. This dual functionality highlights the PMUT's capability to both transmit and receive acoustic signals.

In their review papers, Qiu *et al.* [6], Jung *et al.* [7], and Roy *et al.* [8], provided comprehensive summaries of various PMUT fabrication methods. A common structure among these methods involves PMUTs micromachined on silicon-on-insulator (SOI) substrates, as illustrated in Figure 2-7(a). In this configuration, the passive layer is predominantly the thickness of the device silicon layer of the SOI substrate. The diaphragm can be fabricated using through-silicon vias to release the bulk silicon substrate, as shown in Figure 2-7(b). The SOI layer supports the sequential assembly of the active device stack, which includes a SiO_2 diffusion barrier, a Ti/Pt bottom electrode, the active PZT piezoelectric layer, and a Ti/Pt top electrode.

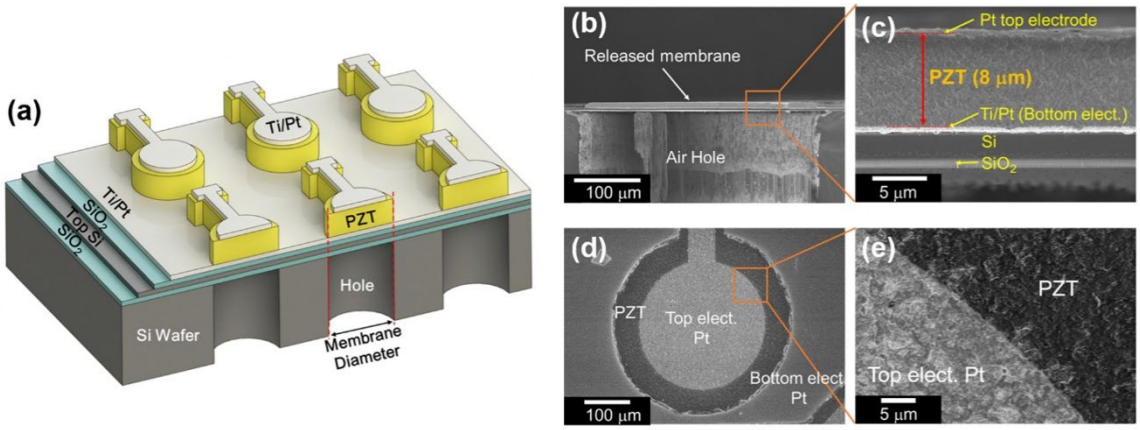

Figure 2-7: (a) PMUT schematic, (b) – (c) cross-section and (d) – (e) SEM images showing the active area of the PMUT: top/bottom electrode and PZT thin film [57].

The passive elastic layer plays an important role as a mechanical amplifier, enhancing the diaphragm's bending motion. This mode of vibration differs from the thickness mode employed in conventional bulk transducers; the sound pressure results from bending in the out-of-plane direction.

The diaphragm vibrational behavior for PMUTs can be characterized as: i) thin plate, ii) membrane, and iii) mixed behavior. This classification can be justified using a nondimensional kappa (κ^2) coefficient, which is determined by the residual stress and flexural rigidity of the diaphragm, as suggested by Dangi *et al.*: [58]

$$\kappa^2 = {T_e a^2}/{D_e} \qquad \text{Eq. 3}$$

where a is the radius of diaphragm and net structural pretension (T_e) and flexural rigidity (D_e) are defined as: [59]

$$T_e = \sum_i \sigma_i h_i \qquad \text{Eq. 4}$$

$$D_e = \sum_i \left(\frac{E_i}{1-v_i^2}\right)\left(\frac{h_i^3}{12} - z_i^2 h_i\right) \qquad \text{Eq. 5}$$

where E_i is the Young's modulus, v is Poisson's ratio, h_i is thickness and z_i is the distance of each layer from the neutral plane. This implies that for:

- **Membrane behavior**: When the diaphragm is large and thin, its response is primarily influenced by the pretension or residual stress of the structure.
- **Plate behavior**: When the diaphragm is thick and small, its vibration motion is governed by its flexural rigidity, where the Young's modulus and Poisson's ratio of each material dominate the bending motion.

For circular membrane's PMUT with clamped edge boundary conditions operating in the plate regime, the resonant frequency can be denoted as: [59] [60]

$$2\pi f_r = \frac{\alpha}{a^2} \cdot \sqrt{\frac{D_e(E, v)}{\rho_i t_i}} \qquad \text{Eq. 6}$$

where D_e is the flexural rigidity which is a function of Young's modulus (E) and Poisson's ratio (v), ρ_i and t_i is the density and the thickness of each layer of the structure.

When the diaphragm becomes thinner, the residual stress (σ) dominates the bending motion instead of the flexural rigidity. Hence, the diaphragm resonant frequency in the membrane regime is given as: [59]

$$2\pi f_r = \frac{\alpha}{a} \cdot \sqrt{\frac{\sigma}{\rho_i t_i}} \qquad \text{Eq. 6}$$

2.2.2 PMUT development

Residual stress is unavoidable in PMUTs, as stress can build up during thermal annealing, especially for PZT which requires high temperature crystallization temperature (typically ~ 600ºC – 700ºC). This residual stress initiates zero-bias membrane deflection and, in some cases, reduces electromechanical coupling [[61]-[63]]. Additionally, the resonant frequency is directly influenced

by residual stress, as reported by Muralt *et al.* [56], [64]. Sammoura *et al.* investigated the influence of residual stress on circular 31-mode PMUTs using a Green's function technique, finding that the center displacement of PMUTs decreases with tensile stress and suggesting that zero-bias deflection can be suppressed by adding an outer dummy electrode extending to the edge of the plate [61]. Wang *et al.* constructed zero-static-bending PMUT using AlN thin films and reported improved transmit sensitivity of 123 nm/V (an ~450% improvement over the reference PMUT) [65].

One method to enhance the electromechanical coupling coefficient is to limit the electrode coverage for the clamped boundary condition, to 60-70% of the diaphragm area [62], [66][68], . Analytical calculations by Lu *et al.* reported that the optimized electrode coverage area is where the sum of tangential and radial stress is zero for circular PMUT [69]. This ratio might not be true for other boundary conditions, as shown by Sammoura *et al.*, who demonstrated that the coupling coefficient for simply supported boundary conditions is maximized at 100% electrode coverage [70].

Muralt *et al.* fabricated partially clamped membranes by releasing the edges of the PMUT structure, and k^2 was 5.3% [68]. Wang *et al.* also showed a similar trend in the enhancement of the coupling coefficient for partially clamped structures, where PMUTs with isolation trenches were fabricated along with clamped membranes. In this work, it was reported that the average membrane displacement for partially clamped structures showed a 61% improvement over clamped devices [71]

To further improve the performance of PMUTs, three-dimensional structures were employed. In curved structure PMUTs, the piezoelectric strain has a non-zero vertical element, resulting in more vertical deformation of the structure. Hajati *et al.* demonstrated 3D dome shaped PMUTs, as shown in Figure 2-8(a), with a measured $|e_{31,f}|$ ~ 23 C/m^2 where the 64-element array showed acoustic output pressures of 85 and 115 kPa/V for the first and second resonant modes [72].

The curved AlN PMUT shown in Figure 2-8(b) was fabricated from 2 mm AlN thin film with a radius of curvature of 1065 mm by Akhbari *et al.* [73]. The deflection of the curved PMUT was characterized using a Laser Doppler Vibrometer, showing a DC vertical displacement of 1.1 nm/V away from resonance and 45 nm/V for the center displacement at resonance. Sammoura *et al.* theoretically studied curved PMUTs using Love's first approximation theory, showing that the resonant frequency is a function of the curvature, thickness, and radius of the diaphragm, and that the center displacement increases with the radius of curvature before reaching a maximum and gradually decreasing [74].

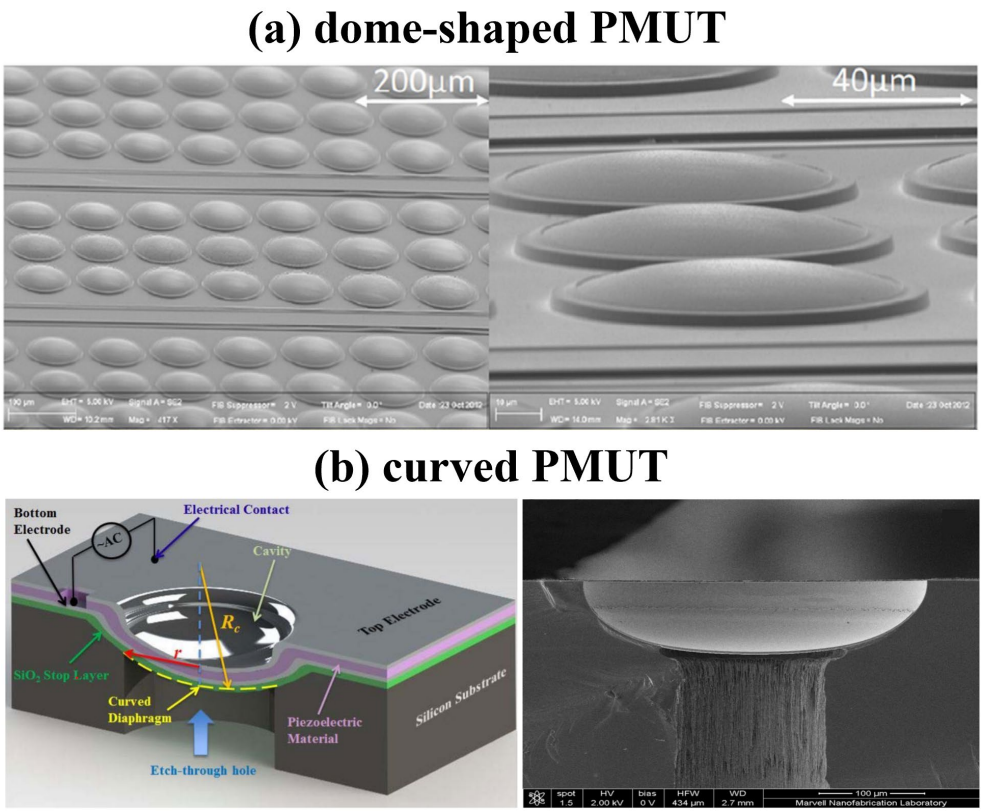

Figure 2-8: (a) Dome shaped PMUT show enhancement of the coupling coefficient (k^2) to 45% [72]. (b) curved PMUT demonstrated vertical displacement of 45 nm/V [73].

As discussed earlier, partially releasing the diaphragm structure and lowering the stress in the diaphragm leads to improvements in PMUT performance. An alternative approach was

demonstrated by Liu *et al.* [75] in the fabrication of fully released PMUTs on a polyimide substrate, supported by simulations for flexible PMUT arrays by Kim *et al.* [76]. In this work, PZT thin film was prepared on a platinized silicon substrate using the sol-gel method with a ZnO sacrificial layer. After the PZT bar was patterned and capped with Al_2O_3, polyimide was spin-coated onto the device substrate. This was followed by wet etching of ZnO to release the structure from the silicon substrate and transfer it to the deposited polyimide, resulting in a fully released device that operates predominantly in a width extension rather than a flexural mode. The single element PMUT showed an acoustic pressure output of 33 kPa at a resonant frequency (f_r) of ~9.5 MHz for a 5 V peak driving voltage. The apparent resonant frequency deviated from the analytical calculation, which was believed to be due to the mass loading effect from the electrode and polyimide substrate, potentially inducing a flexural mode in the system.

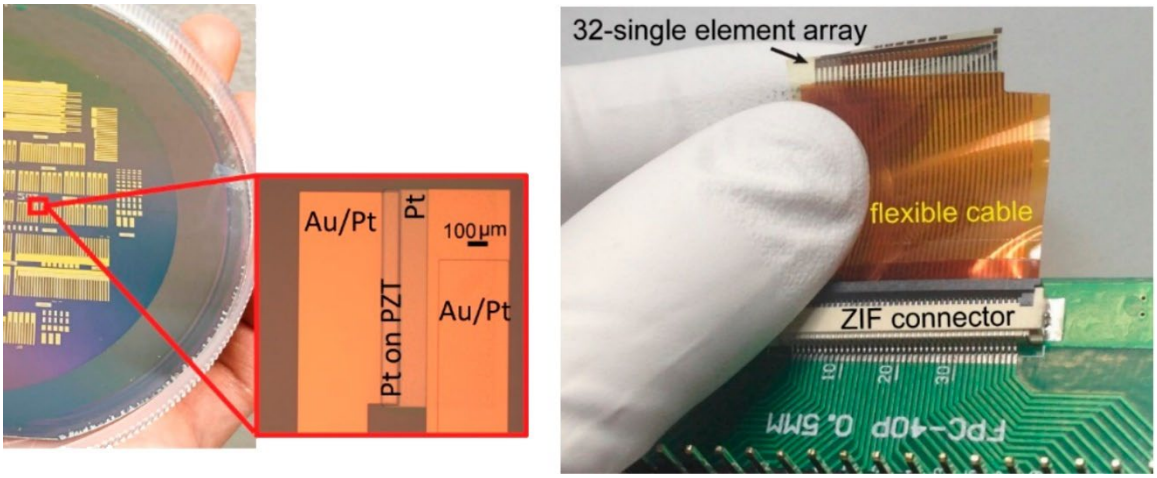

Figure 2-9: Fully released PZT single transducer fabricated on polyimide substrate from [75].

2.2.3 PMUT Fabrication Methods

The micromachining of PMUTs can be categorized into three cases: i) bulk micromachining, ii) surface micromachining, and iii) transfer and release. To provide an overview of the processes, three examples of fabrication are illustrated in Figures 2-10, 2-11, and 2-12.

- Bulk Micromachining:

Figure 2-10 shows the workflow for PMUTs fabricated through bulk silicon micromachining, as presented by Cheng *et al.* [77]. Here, a circular PZT-based PMUT structure was prepared on an SOI substrate and released by deep reactive ion etching (DRIE). The front-side process began with the deposition of a Nb-doped PZT thin film using the sol-gel method, followed by patterning with inductively coupled plasma-reactive ion etching (ICP-RIE) and capping with a Ti/Pt/Au top electrode. The device structure is shown in Figure 2-10(b). The bulk micromachining of the silicon backside was then accomplished using the Bosch process with SF_6 and C_4F_8 to achieve the release structure [78], [79]. Alternatively, anisotropic wet etching with common silicon etchants such as ethylenediamine pyrocatechol (EDP) and KOH can also be used for bulk micromachining of silicon for PMUT fabrication [80], [81].

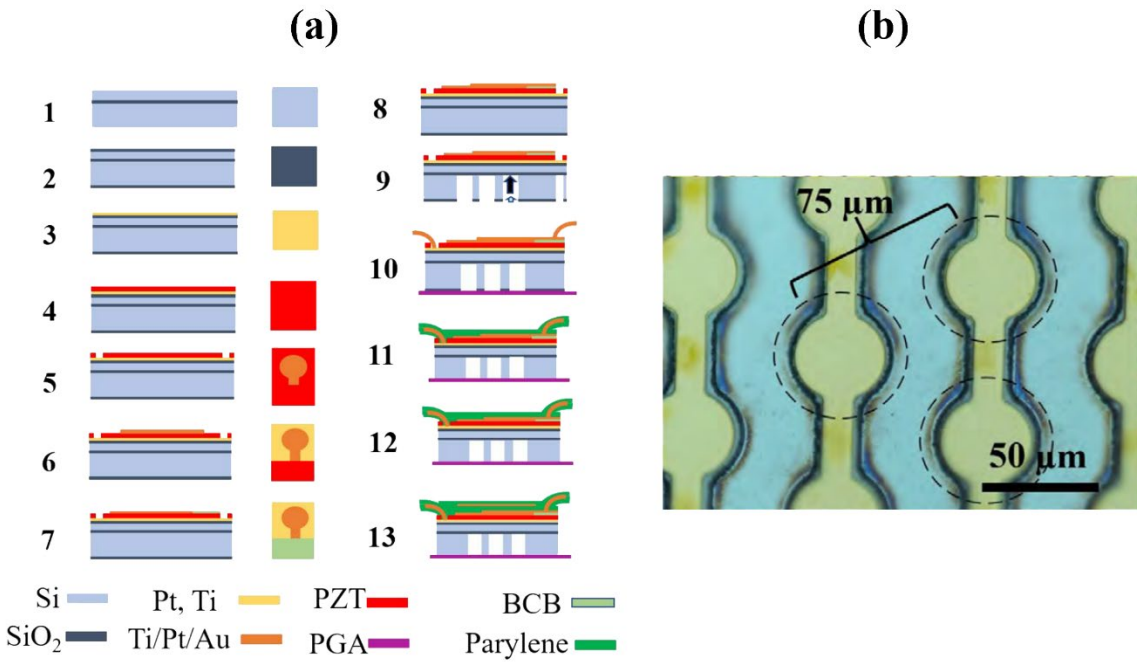

Figure 2-10: Example fabrication flow for bulk silicon micromachining of PMUT on an SOI wafer with a through-silicon trench fabricated by DRIE. PGA stands for Pin Grid Array, and BCB stands for Bis(benzocyclobutene). [77]

- Surface Micromachining:

The second approach is surface micromachining, as depicted in Figure 2-11. The AlN-based PMUT was fabricated on a silicon substrate with a pre-patterned polysilicon sacrificial layer, as demonstrated by Lu *et al.* [82] . The fabrication started with the deposition and patterning of polysilicon, which later defined the released area of the AlN diaphragm. This was followed by the deposition and chemomechanical polishing of a SiO_2 layer, then the deposition and etching of the electrode and AlN thin film layers. Surface micromachining was achieved by isotropic silicon etching using vapor phase XeF_2, forming the released structure. Finally, the etched hole and the active device were sealed with Parylene-C. Another notable example of surface micromachining with XeF_2 was demonstrated in the fabrication of a xylophone-bar type transducer using PZT thin films by H. Kim *et al.* [83]. This work involved releasing a linear T-shaped transducer structure from the silicon substrate. Alternatively, the Silicon-on-Nothing (SON) approach uses silicon migration trenches to pre-fabricate the cavity, as demonstrated by D. Choong *et al.* in the fabrication of high fill-factor AlScN PMUT arrays on an 8-inch silicon substrate [84]. The cavity was formed by i) plasma etching silicon substrate into trenches in the desired cavity area, ii) annealing in a hydrogen atmosphere at high temperature (~ 1000°C) and lower pressure (~ 10^{-5} Pa), and iii) silicon trenches forming a cavity structure via surface-migrating of silicon [85].

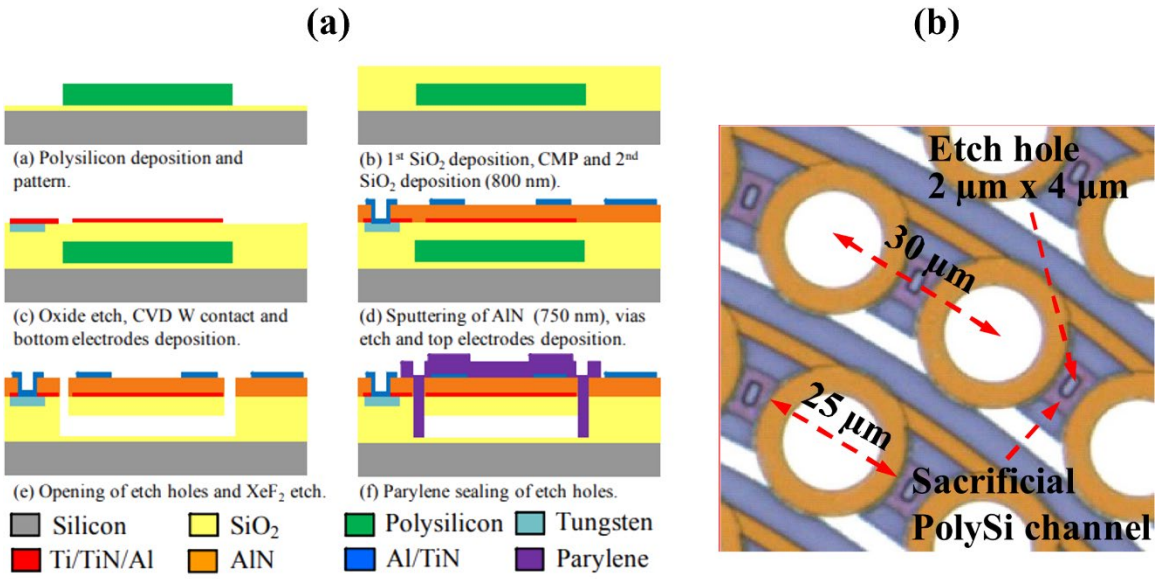

Figure 2-11: Example fabrication flow for surface micromachining of a PMUT with a polysilicon sacrificial layer [82].

- Transfer and Release Method:

The third approach is the transfer and release method, in which the piezoelectric layer is prepared on a sacrificial layer and transferred to the desired substrate later in the process. This method offers flexibility to overcome process limitations, such as the high crystallization temperature of lead zirconate titanate and enables the fabrication of fully released structures. Figure 2-12 shows the process flow and a rectangular PZT bar resonator reported by Liu *et al.* [75]. In this work, the PZT rectangular bar was deposited and patterned on a silicon substrate with ZnO and Al_2O_3 serving as sacrificial and insulator layers, respectively. Before polyimide deposition, a thick Al_2O_3 layer was deposited as a protective layer to prevent PZT degradation during imidization. Polyimide was then spin-coated and cured to form the desired substrate structure. Finally, ZnO was wet-etched using acetic acid to release the transducer from the parent substrate to the flexible polyimide substrate. Similar approaches have been adapted for other PMUT fabrication routes. For example, Sun *et al.* transferred AlN-based PMUTs from silicon substrates by wet etching of SiO_2

via a PDMS stamp to PMMA substrates [86]; Jeong *et al.* transferred P(VDF-TrFE)-based PMUTs initially prepared on glass carrier wafers to polyimide substrates [87]. It should be noted that it is critical when surface micromachining is employed that the undercut process not damage the piezoelectric layer or its electrodes.

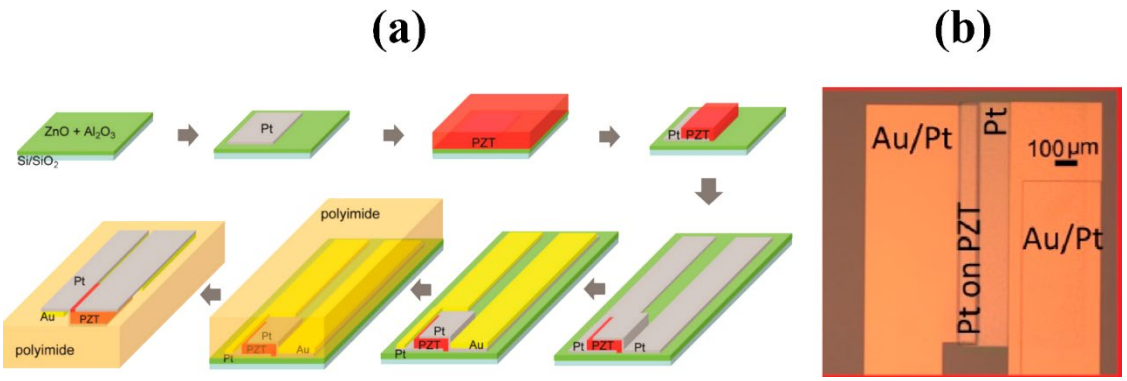

Figure 2-12: Example fabrication flow for transfer and release method. The PMUT was released by wet etching of the ZnO sacrificial layer and transferred to a polyimide substrate. [75].

In summary, various methods and materials have been explored for the fabrication of PMUTs, each with its unique advantages and challenges. Given this context, the piezoelectric material employed in this thesis for piezoelectric micromachined ultrasound transducers is a 2 mol% Nb doped $Pb(Zr_{0.52}Ti_{0.48})O_3$ thin film, due to its superior piezoelectric response, especially in the transverse piezoelectric coefficient $e_{31,f}$. To maximize the piezoelectric response in PMUTs, highly {001} oriented PZT thin films are preferred. In this work, a highly [111] oriented high-temperature deposited Pt bottom electrode was used in Chapter 4, following the process presented by Fox *et al.* (2015) [88]. Non-PZT seed layers such as $PbTiO_3$, PbO, and $LaNiO_3$ are commonly used to promote textured PZT films [89], [92]. However, these seed layers have their own drawbacks, which can affect the properties of PZT thin films. For instance, $LaNiO_3$ has a higher resistivity than metal electrodes, especially platinum [93], [94], and excessive PbO can lower the breakdown strength of PZT thin films [95]. Alternatively, the seed layer for {001} orientation,

employed in Chapter 4, can be prepared using commercial Mitsubishi E-1 solution with a composition of 52/48 and 10 – 16 at. % excess Pb [96][98].

2.2.4 Applications of PMUT

As discussed earlier, PMUTs can operate as transmitters, receivers, and transceivers. Brief examples of PMUT applications based on these operational modes are shown in Figure 2-13 and 2-14. **The transmit mode** relies on the strain coefficient $e_{31,f}$, as PMUT diaphragm deflection is induced by S_1. PZT thin films are the dominant candidate for this purpose, as they show a high $|e_{31,f}| \sim 12$ Cm^{-2} [103, 104]. Figure 2-13(a) demonstrates the acoustophoretic effect to manipulate 4 μm silica beads across the generated acoustic pressure gradient using PZT-based PMUTs on an SOI substrate [77]. It was shown that particles could be moved from one electrode to the neighboring electrode by controlling the acoustic potential gradient by controlling the drive voltage and/or tuning the resonant frequency. Ultimately, this approach should allow manipulation of micro-scale objects such as particles, cells, proteins, and enzymes in microfluidic systems. Another excellent example of a transmitting application is the piezoelectric MEMS speaker. Materials such as ZnO, PZT, and AlN thin films have been explored for use as vibration diaphragms coupled with acoustic cavities to create audible acoustic waves for applications such as hearing aids and earphone devices [105-107]. A notable step of a piezoelectric MEMS speaker is an available commercially from Usound, with a sound pressure level of 116 dB under a driving voltage of 15 V [108].

The receiver mode emphasizes the sensor characteristics of PMUTs, with the related piezoelectric coefficient being the voltage coefficient $h_{31,f}$. Figure 2-13(b) shows PZT PMUTs used as piezoelectric ultrasonic energy harvesters (PUEH), demonstrating potential for integration into self-powered implantable devices [105]. The concept was examined using bulk PZT transducers as transmitters and PZT based PMUT arrays as receivers. Performance was reported in

both in-water and in-vitro testing. In the in-vitro experiment, a bulk transducer transmitted acoustic waves through 6 mm thick pork tissue, with the transmitted output power density of 1 mW/cm^2, PMUT an output power of 85.2 nW at a 330 kHz driving frequency highlighting the potential of PMUT integration into implantable biomedical devices for long-term operation.

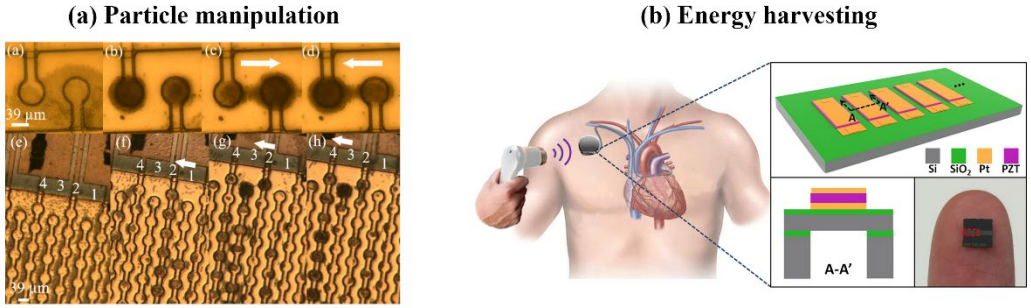

Figure 2-13: Examples of PMUT applications reported in the literature: (a) transmitter PMUT for particle manipulation [77], (b) PMUT energy harvester for self-powered implantable biomedical devices [105].

For **the transceiver application** PMUTs function as both actuators and sensors to transmit and receive acoustic waves. Figure 2-14(a) illustrates a 3D ultrasonic rangefinder on a chip using AlN MEMS transducers integrated with CMOS ASIC, with a 1-meter range in air [106]. The transducer's structure is a unimorph, with two AlN layers acting as both the active piezoelectric and passive elastic layers, separated by a Mo electrode. Beamforming and steering were used to track objects from 45 mm to 1 m with an angular range of ±45°. The time-of-flight was determined from the echo signal, with a maximum range of 1 m and an echo returning after 5.8 ms. This demonstrates the potential of AlN PMUTs for mobile device capabilities, providing efficient proximity sensing, wake-on-approach features, and 3D motion gestures.

Figure 2-14(b) shows the integration of PZT-based PMUT arrays with 256 and 512 active elements into intracardiac catheters for real-time 3D ultrasound imaging [107]. The connection between PMUT and catheter was achieved by through-silicon interconnects using PMUT backside connection and a separately prepared wire substrate. These two substrates were then wafer-bonded

using a flip-chip bonder to accommodate large array of connections. The PMUT array was tested in adult swine, and the prototype volume ultrasound scanner was advanced through the femoral vein and right atrium, marking the first in-vivo ultrasound imaging using a PMUT array.

Figure 2-14(c) presents a monolithic ultrasound fingerprint sensor using an AlN PMUT array connected to a CMOS wafer using wafer-bonded techniques [108]. Two types of PMUTs were fabricated: circular and rectangular elements. The rectangular shape showed superior performance due to the higher fill-factor, with 70.8 kPa output pressure compared to 41.9 kPa from the circular-shaped PMUT. The fabricated array demonstrated an axial resolution of 127 μm, with the ultrasound image from the epidermis and sub-epidermis layers, shown in Figure 2-14(c) insets, matching the optical microscope picture of the fingerprint. Since the initial attempt at a fingerprint sensor using PMUT by Lu *et al.* [109], many efforts in the literature [110][112], have led to the commercialization of fingerprint sensors by Qualcomm as the in-display PMUT 3D sonic sensor [113]. This marks the advent of PMUT from research to the worldwide market.

Figure 2-14(d) illustrates the B-mode imaging results for both in-vitro and in-vivo applications using a 1D PMUT array. Savoia *et al.* demonstrated the fabrication and integration of a PZT PMUT array for biomedical ultrasound imaging. The array featured a 64-element array where each element comprised 184 circular PMUT cells. The transmitting and receiving sensitivities were measured to be 31 kPa/V and 3.2 mV/kPa, respectively, with 5 V excitation. This yields 85% bandwidth and a center frequency of 2.5 MHz. The PMUT array was integrated into an ultrasound probe equipped with low-noise amplifiers (LNAs), the MAX14822 from Maxim Integrated Products, and the ULA-OP 256 scanner for the ultrasound imaging tests.

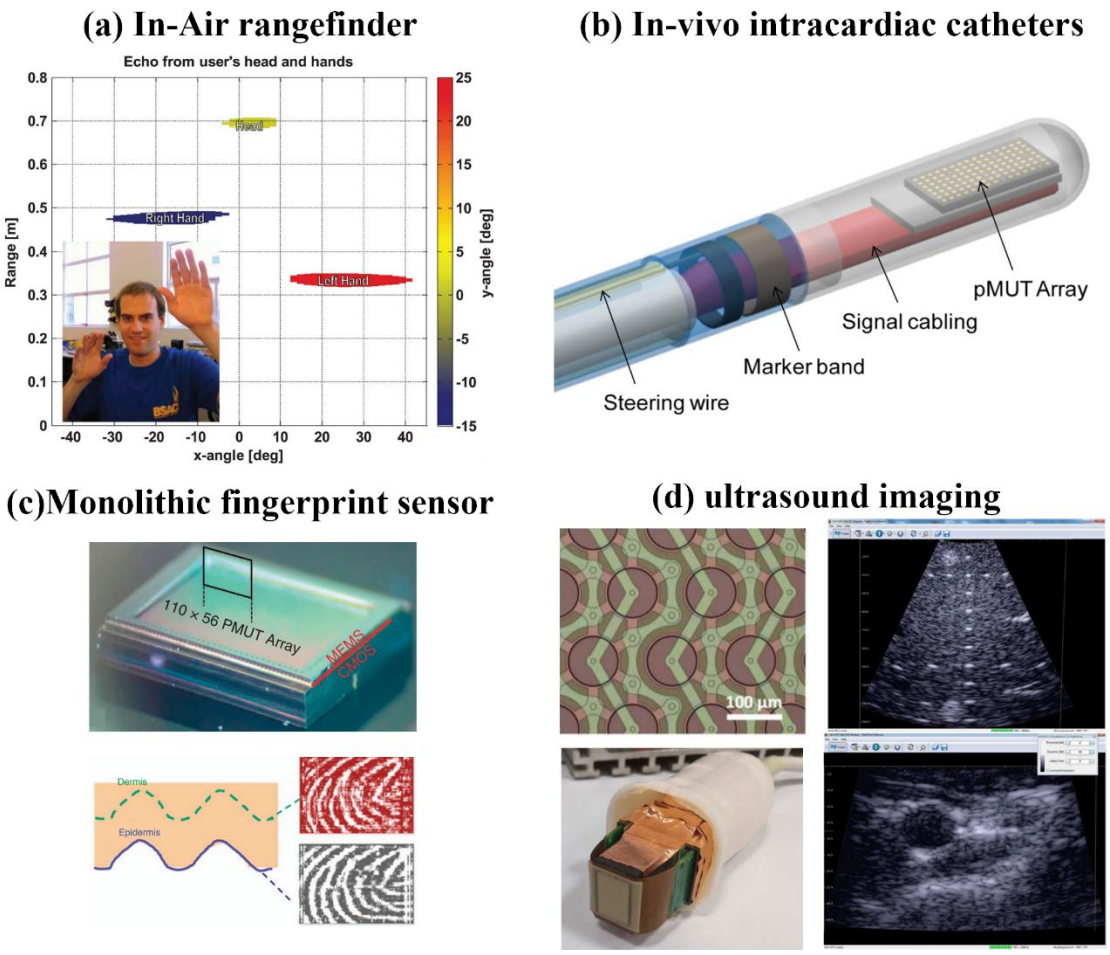

Figure 2-14: Examples of PMUT applications in transceiver: (a) in-air rangefinder [106]: (b) intracardiac catheters [107]: (c) monolithic fingerprint sensor [108]: (d) biomedical ultrasound imaging [114].

Bibliography

[1] A. Arnau, *Piezoelectric Transducers and Applications*, 2nd ed. Berlin, Heidelberg: Springer, 2008.

[2] A. Safari and E. K. Akdogan, *Piezoelectric and Acoustic Materials for Transducer Applications* , New York, NY: Springer-Verlag, 2008.

[3] K. Nakamura, *Ultrasonic Transducers: Materials and Design for Sensors, Actuators and Medical Applications*, Cambridge, UK: Woodhead Publishing Limited, 2010.

[4] K. Uchino, *Ferroelectric Devices*, 2nd ed. Boca Raton FL: CRC Press, 2018.

[5] J. W. Judy, "Microelectromechanical systems (MEMS): fabrication, design and applications," *Smart Mater. Struct.*, vol. 10, no. 6, pp. 1115, 2001.

[6] Y. Qiu, J. V. Gigliotti, M. Wallace, F. Griggio, C. E. M. Demore, S. Cochran, and S. Trolier-McKinstry, "Piezoelectric Micromachined Ultrasound Transducer (PMUT) Arrays for Integrated Sensing, Actuation and Imaging," *Sensors*, vol. 15, no. 4, pp. 8020-8041, 2015.

[7] J. Jung, W. Lee, W. Kang, E. Shin, J. Ryu, and H. Choi, "Review of Piezoelectric Micromachined Ultrasonic Transducers and Their Applications," *J. Micromech. Microeng.*, vol. 27, no. 11, p. 113001, 2017.

[8] K. Roy, J. E.-Y. Lee, and C. Lee, "Thin-Film PMUTs: A Review of Over 40 Years of Research," *Microsys. Nanoeng.*, vol. 9, no. 1, p. 95, 2023.

[9] A. S. Savoia, M. Casavola, E. Boni, M. Ferrera, C. Prelini, P. Tortoli, D. Giusti, and F. Quaglia "Design, Fabrication, Characterization, and System Integration of a 1-D PMUT Array for Medical Ultrasound Imaging," *2021 IEEE International Ultrasonics Symposium (IUS)*, Xi'an, China, 2021, pp. 1-3.

[10] A. Savoia, G. Caliano, B. Mauti, and M. Pappalardo, "Performance Optimization of a High Frequency CMUT Probe for Medical Imaging," *2011 IEEE International Ultrasonics Symposium (IUS)*, Orlando, FL, USA, 2011.

[11] A. Caronti, M. Hochman, T. Xu, S. Satir, G. Gurun, M. Karaman, F. L. Degertekin, "Capacitive Micromachined Ultrasonic Transducer (CMUT) Arrays for Medical Imaging," *Microelectronics J.*, vol. 37, no. 8, pp. 770–777, 2006.

[12] A. Caronti, G. Caliano, R. Carotenuto, A. Savoia, M. Pappalardo, E. Cianci, and V. Foglietti, "Capacitive Micromachined Ultrasonic Transducer (CMUT) Arrays for Medical Imaging," *Microelectron. J.*, vol. 37, no. 8, pp. 770-777, 2006.

[13] Y. Yang, H. Tian, Y.-F. Wang, Y. Shu, C.-J. Zhou, H. Sun, C.-H. Zhang, H. Chen, and T.-L. Ren, "An Ultra-High Element Density pMUT Array with Low Crosstalk for 3-D Medical Imaging," *Sensors*, vol. 13, no. 8, pp. 9624-9634, 2013.

[14] D. E. Dausch, J. B. Castellucci, D. R. Chou, and O. T. Von Ramm, "Theory and Operation of 2-D Array Piezoelectric Micromachined Ultrasound Transducers," *IEEE Trans. Ultrason. Ferroelectr. Freq. Control*, vol. 55, no. 11, pp. 2484-2492, 2008.

[15] Y. Lu, H. Tang, S. Fung, Q. Wang, J. M. Tsai, M. Daneman, B. E. Boser, and D. A. Horsley, "Ultrasonic Fingerprint Sensor using a Piezoelectric Micromachined Ultrasonic Transducer Array Integrated with Complementary Metal Oxide Semiconductor Electronics," *Appl. Phys. Lett.*, vol. 106, no. 26, 2015.

[16] K. K. Shung and M. Zippuro, "Ultrasonic transducers and arrays," in *IEEE Engineering in Medicine and Biology Magazine*, vol. 15, no. 6, pp. 20-30, 1996.

[17] J. A. Brown, S. Sharma, J. Leadbetter, S. Cochran and R. Adamson, "Mass-spring matching layers for high-frequency ultrasound transducers: a new technique using vacuum

deposition," in IEEE Transactions on Ultrasonics, Ferroelectrics, and Frequency Control, vol. 61, no. 11, pp. 1911-1921, November 2014

[18] K. K. Shung, J. M. Cannata, and Q. F. Zhou, "Piezoelectric materials for high frequency medical imaging applications: A review," *J. Electroceram.*, vol. 19, pp. 141-147, 2007.

[19] Q. Zhou, S. Lau, D. Wu, and K. Kirk Shung, "Piezoelectric Films for High Frequency Ultrasonic Transducers in Biomedical Applications," *Prog. Mater. Sci.*, vol. 56, no. 2, pp. 139–174, 2011.

[20] L. E. Kinsler, A. R. Frey, A. B. Coppens, and J. V. Sanders, Ed. Fundamentals of Acoustics, 3rd ed. New York: John Wiley & Sons, 1982.

[21] G.S. Kino, *Acoustic Waves: Devices, Imaging, and Analog Signal Processing*, New Jersey : Prentice-Hall , 1987

[22] M. J. Zipparo, K. K. Shung and T. R. Shrout, "Piezoceramics for High-Frequency (20 to 100 MHz) Single-Element Imaging Transducers," *IEEE Trans. Ultrason. Ferroelectr. Freq. Control*, vol. 44, no. 5, pp. 1038-1048, Sept. 1997

[23] Q. Zhou, K. H. Lam, H. Zheng, W. Qiu, and K. K. Shung, "Piezoelectric Single Crystal Ultrasonic Transducers for Biomedical Applications," *Prog. Mater. Sci.*, vol. 66, pp. 87-111, 2014.

[24] R. Zhang, B. Jiang, and W. Cao, "Elastic, Piezoelectric, and Dielectric Properties of Multidomain $0.67Pb(Mg_{1/3}Nb_{2/3})O_3$-$0.33PbTiO_3$ Single Crystals," *J. Appl. Phys.*, vol. 90, no. 7, pp. 3471-3475, 2001.

[25] S. Zhang, F. Li, N. P. Sherlock, J. Luo, H. J. Lee, R. Xia, R. J. Meyer Jr., W. Hackenberger, and T. R. Shrout, "Recent Development on High Curie Temperature PIN–PMN–PT Ferroelectric Crystals," *J. Cryst. Growth*, vol. 318, pp. 846–850, 2011.

[26] X. Liu, S. Zhang, J. Luo, T. R. Shrout, and W. Cao, "Complete Set of Material Constants of $Pb(In_{1/2}Nb_{1/2})O_3$–$Pb(Mg_{1/3}Nb_{2/3})O_3$–$PbTiO_3$ Single Crystal with Morphotropic Phase Boundary Composition," *J. Appl. Phys.*, vol. 106, no. 074112, 2009.

[27] H. Luo, G. Xu, P. Wang, and Z. Yin, "Growth and Characterization of Relaxor Ferroelectric PMNT Single Crystal," Ferroelectrics, vol. 231, pp. 97-102, 1999.

[28] Y. Guo, H. Luo, T. He, and Z. Yin, "Peculiar Properties of a High Curie Temperature $Pb(In_{1/2}Nb_{1/2})O_3$–$PbTiO_3$ Single Crystal Grown by the Modified Bridgeman Technique," *Solid State Commun.*, vol. 123, no. 9, pp. 417-420, 2002.

[29] G. Xu, K. Chen, D. Yang, and J. Li, "Growth and Electrical Properties of Large Size $Pb(In_{1/2}Nb_{1/2})O_3$–$Pb(Mn_{1/3}Nb_{2/3})O_3$–$PbTiO_3$ Crystals Prepared by the Vertical Bridgeman Technique," *Appl. Phys. Lett.*, vol. 90, p. 032901, 2007.

[30] S. Cochran, "Piezoelectricity and Basic Configurations for Piezoelectric Ultrasonic Transducers," in *Ultrasonic Transducers*, K. Nakamura, Ed., Cambridge, UK: Woodhead Publishing Limited, 2012, pp. 3–35.

[31] J. L. Butler and C. H. Sherman, *Transducers and Arrays for Underwater Sound*, Cham, Switzerland: Springer International Publishing, 2016.

[32] C. Wang, X. Li, H. Hu, L. Zhang, Z. Huang, M. Lin, Z. Zhang, Z. Yin, B. Huang, H. Gong, S. Bhaskaran, Y. Gu, M. Makihata, Y. Guo, Y. Lei, Y. Chen, C. Wang, Y. Li, T. Zhang, Z. Chen, A. P. Pisano, L. Zhang, Q. Zhou, and S. Xu, "Monitoring of the Central Blood Pressure Waveform Via a Conformal Ultrasonic Device," *Nat. Biomed. Eng.*, vol. 2, pp. 687-695, 2018.

[33] K. Suzuki, K. Higuchi, and H. Tanigawa, “A Silicon Electrostatic Ultrasonic Transducer,” *IEEE Trans. Ultrason. Ferroelectr. Freq. Control*, vol. 36, no. 6, pp. 620–627, 1989.

[34] I. O. Wygant, X. Zhuang, D. T. Yeh, O. Oralkan, A. S. Ergun, M. Karaman, and B. T. Khuri-yakub, "Integration of 2D CMUT Arrays with Front-end Electronics for Volumetric Ultrasound Imaging," *IEEE Trans. Ultrason. Ferroelectr. Freq. Control*, vol. 55, no. 2, pp. 327-342, 2008

[35] G. Gurun, P. Hasler, and F. L. Degertekin, "Front-End Receiver Electronics for High-Frequency Monolithic CMUT-on-CMOS Imaging Arrays," *IEEE Trans. Ultrason. Ferroelectr. Freq. Control*, vol. 58, no. 8, pp. 1658–1668, 2011.

[36] G. Gurun, C. Tekes, J. Zahorian, T. Xu, M. Karaman, J. Hasler, and F. L. Degertekin, "Single-Chip CMUT-on-CMOS Front-End System for Real-Time Volumetric IVUS and ICE Imaging," *IEEE Trans. Ultrason. Ferroelectr. Freq. Control*, vol. 61, no. 2, pp. 239-250, 2014.

[37] J. Zahorian, M. Hochman, T. Xu, S. Satir, G. Gurun, M. Karaman, and F. L. Degertekin, "Monolithic CMUT-on-CMOS Integration for Intravascular Ultrasound Applications," *IEEE Trans. Ultrason. Ferroelectr. Freq. Control*, vol. 58, no. 12, pp. 2659–2667, 2011.

[38] A. S. Ergun, Y. Huang, C.-H. Cheng, O. Oralkan, J. Johnson, H. Jagannathan, U. Demirci, G. G. Yaralioglu, M. Karaman, and B. T. Khuri-Yakub, "Broadband Capacitive Micromachined Ultrasonic Transducers Tanging from 10 kHz to 60 MHz for Imaging Arrays and More," *2002 IEEE Ultrasonics Symposium*, 2002. Proceedings., Munich, Germany, 2002, pp. 1039-1043 vol.2

[39] G. G. Yaralioglu, A. S. Ergun, B. Bayram, E. Haeggstrom, and B. T. Khuri-Yakub, "Calculation and Measurement of Electromechanical Coupling Coefficient of Capacitive Micromachined Ultrasonic Transducers," *IEEE Trans. Ultrason. Ferroelectr. Freq. Control*, vol. 50, no. 4, pp. 449–456, 2003.

[40] Ö. Oralkan, B. Bayram, G. G. Yaralioglu, A. S. Ergun, M. Kupnik, D. T. Yeh, I. O. Wygant, and B. T. Khuri-Yakub, "Experimental Characterization of Collapse-Mode CMUT

Operation,” *IEEE Trans. Ultrason. Ferroelectr. Freq. Control*, vol. 53, no. 8, pp. 1513–1523, 2006.

[41] B. Bayram, E. Hæggström, G. G. Yaralioglu, and B. T. Khuri-Yakub, “A New Regime for Operating Capacitive Micromachined Ultrasonic Transducers,” *IEEE Trans. Ultrason. Ferroelectr. Freq Control*, vol. 50, no. 9, pp. 1184–1190, 2003.

[42] E. Moisello, L. Novaresi, E. Sarkar, P. Malcovati, T. L. Costa, and E. Bonizzoni, “PMUT and CMUT Devices for Biomedical Applications: A Review,” *IEEE Access*, vol. 12, pp. 18640–18657, 2024.

[43] T. Shiosaki, T. Yamamoto, A. Kawabata, R. S. Muller and R. M. White, "Fabrication and Characterization of ZnO Piezoelectric Films for Sensor Devices," *1979 International Electron Devices Meeting*, Washington, DC, USA, 1979, pp. 151-154

[44] M. Royer, J. O. Holmen, M. A. Wurm, O. S. Aadland, and M. Glenn, “ZnO on Si Integrated Acoustic Sensor,” *Sensors and Actuators*, vol. 4, pp. 357–362, 1983.

[45] K. R. Udayakumar, S. F. Bart, A. M. Flynn, J. Chen, L. S. Tavrow, L. E. Cross, R. A. Brooks, and D. J. Ehrlich, "Ferroelectric Thin Film Ultrasonic Micromotors," *[1991] Proceedings. IEEE Micro Electro Mechanical Systems*, Nara, Japan, 1991, pp. 109-113.

[46] J. J. Bernstein, S. F. Bart, A. M. Flynn, J. Chen, L. S. Tavrow, L. E. Cross, R. A. Brooks, and D. J. Ehrlich, “Micromachined High Frequency Ferroelectric Sonar Transducers,” *IEEE Trans. Ultrason. Ferroelectr. Freq. Control*, vol. 44, no. 5, pp. 960–969, 1997.

[47] S. Shelton, M.-L. Chan, H. Park, D. Horsley, B. Boser, I. Izyumin, R. Przybyla, T. Frey, M. Judy, K. Nunan, F. Sammoura, and K. Yang, "CMOS-Compatible AlN Piezoelectric Micromachined Ultrasonic Transducers," *2009 IEEE International Ultrasonics Symposium*, Rome, Italy, 2009, pp. 402-405.

[48] M. Akiyama, T. Kamohara, K. Kano, A. Teshigahara, Y. Takeuchi, and N. Kawahara, “Enhancement of Piezoelectric Response in Scandium Aluminum Nitride Alloy Thin Films Prepared by Dual Reactive Cosputtering,” *Adv. Mater.*, vol. 21, no. 5, pp. 593–596, 2009.

[49] Q. Wang, Y. Lu, S. Mishin, Y. Oshmyansky, and D. A. Horsley, “Design, Fabrication, and Characterization of Scandium Aluminum Nitride-Based Piezoelectric Micromachined Ultrasonic Transducers,” *J. Microelectromech. Syst.*, vol. 26, no. 5, pp. 1132–1139, 2017.

[50] C. Chao, T. -Y. Lam, K. -W. Kwok and H. L. W. Chan, "Piezoelectric Micromachined Ultrasonic Transducers Based on P(VDF-TrFE) Copolymer Thin Films," 2006 15th IEEE International Symposium on the Applications of Ferroelectrics, Sunset Beach, NC, USA, 2006, pp. 120-123.

[51] D. E. Dausch, “Asymmetric 90° Domain Switching in Rainbow Actuators,” *Ferroelectrics*, vol. 210, no. 1–4, pp. 31–45, 1998.

[52] J.J. Bernstein, J. Bottari, K. Houston, G. Kirkos, R. Miller, B. Xu, Y. Ye, L.E. Cross, "Advanced MEMS Ferroelectric Ultrasound 2D Arrays," *1999 IEEE Ultrasonics Symposium. Proceedings. International Symposium (Cat. No.99CH37027)*, Tahoe, NV, USA, 1999, pp. 1145-1153 vol.2.

[53] Eunki Hong, S. Trolier-McKinstry, R. L. Smith, S. V. Krishnaswamy and C. B. Freidhoff, "Design of MEMS PZT Circular Diaphragm Actuators to Generate Large Deflections," *J. Microelectromech. Syst.*, vol. 15, no. 4, pp. 832-839, Aug. 2006

[54] M. Klee, H. Boots, B. Kumar, C. van Heesch, R. Mauczok, W. Keur, M. de Wild, H. van Esch, A. L. Roest, K. Reimann, L. van Leuken, O. Wunnicke, J. Zhao, G. Schmitz, M. Mienkina, M. Mleczko, M. Tiggelman, "Ferroelectric and Piezoelectric Thin Films and Their Applications for Integrated Capacitors, Piezoelectric Ultrasound Transducers and Piezoelectric Switches," *IOP Conf. Ser.: Mater. Sci. Eng.*, vol. 8, no. 1, p. 012008, 2010.

[55] M. Klee, R. Mauczok, Ch. van Heesch, H. Boots, M. de Wild, B. op het Veld, W. Soer, G. Schmitz, and M. Mleczko "Piezoelectric Thin Film Platform for Ultrasound Transducer Arrays," *2011 IEEE International Ultrasonics Symposium (IUS),* Orlando, FL, USA, 2011, pp. 196-199.

[56] P. Muralt and J. Baborowski, “Micromachined Ultrasonic Transducers and Acoustic Sensors Based on Piezoelectric Thin Films,” *J. Electroceram.*, vol. 12, no. 1–2, pp. 101–108, 2004.

[57] J. Jung, V. Annapureddy, G.-T. Hwang, Y. Song, W. Lee, W. Kang, J. Ryu, and H. Choi, "31-Mode Piezoelectric Micromachined Ultrasonic Transducer with PZT Thick Film by Granule Spraying in Vacuum Process," *Appl. Phys. Lett.*, vol. 110, no. 21, 212903, 2017.

[58] A. Dangi and R. Pratap, “System Level Modeling and Design Maps of PMUTs with Residual Stresses,” *Sens. Actuators A Phys.*, vol. 262, pp. 18–28, 2017.

[59] S. Timoshenko, S. Woinowsky-Krieger, *Theory of Plates and Shells*, vol. 2, McGraw-Hill New York, 1959.

[60] A. W. Leissa, *Vibration of Plates*, vol. 160. Scientific and Technical Information Division, National Aeronautics and Space Administration, 1969.

[61] F. Sammoura, K. Smyth, S. Bathurst and S. -G. Kim, "An Analytical Analysis of the Sensitivity of Circular Piezoelectric Micromachined Ultrasonic Transducers to Residual Stress," *2012 IEEE International Ultrasonics Symposium*, Dresden, Germany, 2012, pp. 580-583.

[62] F. Akasheh, J. D. Fraser, S. Bose, and A. Bandyopadhyay, “Piezoelectric Micromachined Ultrasonic Transducers: Modeling the Influence of Structural Parameters on Device Performance,” *IEEE Trans. Ultrason. Ferroelectr. Freq. Control*, vol. 52, no. 3, pp. 455–468, 2005.

[63] J. H. Mo, A. L. Robinson, D. W. Fitting, F. L. Terry, and P. L. Carson, “Micromachining for Improvement of Integrated Ultrasonic Transducer Sensitivity,” *IEEE Trans. Electron. Devices.*, vol. 37, no. 1, pp. 134–140, 1990.

[64] P. Muralt, “PZT Thin Films for Microsensors and Actuators: Where Do We Stand?,” *IEEE Trans. Ultrason. Ferroelectr. Freq. Control*, vol. 47, no. 4, pp. 903–915, 2000.

[65] T. Wang and C. Lee, “Zero-Bending Piezoelectric Micromachined Ultrasonic Transducer (PMUT) with Enhanced Transmitting Performance,” *J. Microelectromech. Syst.*, vol. 24, no. 6, pp. 2083–2091, 2015.

[66] K. Smyth and S.-G. Kim, “Experiment and Simulation Validated Analytical Equivalent Circuit Model for Piezoelectric Micromachined Ultrasonic Transducers,” *IEEE Trans. Ultrason. Ferroelectr. Freq. Control*, vol. 62, no. 4, pp. 744–765, 2015.

[67] K. Smyth, S. Bathurst, F. Sammoura, and S. G. Kim, “Analytic Solution for N-Electrode Actuated Piezoelectric Disk with Application to Piezoelectric Micromachined Ultrasonic Transducers,” *IEEE Trans. Ultrason. Ferroelectr. Freq. Control*, vol. 60, no. 8, pp. 1756–1767, 2013.

[68] P. Muralt, N. Ledermann, J. Paborowski, A. Barzegar, S. Gentil, B. Belgacem, S. Petitgrand, A. Bosseboeuf, and N. Setter, “Piezoelectric Micromachined Ultrasonic Transducers Based on PZT Thin Films,” *IEEE Trans. Ultrason. Ferroelectr. Freq. Control*, vol. 52, no. 12, pp. 2276–2288, 2005.

[69] Y. Lu and D. A. Horsley, “Modeling, Fabrication, and Characterization of Piezoelectric Micromachined Ultrasonic Transducer Arrays Based on Cavity SOI Wafers,” *J. Microelectromech. Syst.*, vol. 24, no. 4, pp. 1142–1149, 2015.

[70] F. Sammoura, K. Smyth, and S. G. Kim, “Optimizing the Electrode Size of Circular Bimorph Plates with Different Boundary Conditions for Maximum Deflection of

Piezoelectric Micromachined Ultrasonic Transducers," *Ultrasonics*, vol. 53, no. 2, pp. 328–334, 2013.

[71] M. Wang, Y. Zhou, and A. Randles, "Enhancement of the Transmission of Piezoelectric Micromachined Ultrasonic Transducer with an Isolation Trench," *J. Microelectromech. Syst.*, vol. 25, no. 4, pp. 691–700, 2016.

[72] A. Hajati, D. Latev, D. Gardner, A. Hajati, D. Imai, M. Torrey, and M. Schoeppler, "Three-Dimensional Micro Electromechanical System Piezoelectric Ultrasound Transducer," *Appl Phys Lett*, vol. 101, no. 25, p. 253101, 2012

[73] S. Akhbari, F. Sammoura, S. Shelton, C. Yang, D. Horsley, and L. Lin, "Highly Responsive Curved Aluminum Nitride pMUT," *2014 IEEE 27th International Conference on Micro Electro Mechanical Systems (MEMS)*, San Francisco, CA, USA, 2014, pp. 124-127.

[74] F. Sammoura, S. Akhbari, and L. Lin, "An Analytical Solution for Curved Piezoelectric Micromachined Ultrasonic Transducers with Spherically Shaped Diaphragms," *IEEE Trans. Ultrason. Ferroelectr. Freq. Control*, vol. 61, no. 9, pp. 1533–1544, 2014.

[75] T. Liu, A. Dangi, J. N. Kim, S.-R. Kothapalli, K. Choi, S. Trolier-McKinstry, and T. Jackson, "Flexible Thin-Film PZT Ultrasonic Transducers on Polyimide Substrates," *Sensors*, vol. 21, no. 3, p. 1014, 2021.

[76] J. N. Kim, T. Liu, T. N. Jackson, K. Choi, S. Trolier-McKinstry, R. L. Tutwiler, and J. A. Todd, "10 MHz Thin-Film PZT-Based Flexible PMUT Array: Finite Element Design and Characterization," *Sensors,* vol. 20, no. 15, p. 4335, 2020.

[77] C. Y. Cheng, A. Dangi, L. Ren, S. Tiwari, R. R. Benoit, Y. Qiu, H. S. Lay, S. Agrawal, R. Pratap, S.-R. Kothapalli, T. E. Mallouk, S. Cochran, and S. Trolier-McKinstry, "Thin Film PZT-Based PMUT Arrays for Deterministic Particle Manipulation," *IEEE Trans. Ultrason. Ferroelectr. Freq. Control*, vol. 66, no. 10, pp. 1605–1615, 2019.

[78] F. Larmer and P. Schilp "Method of Anisotropically Etching Silicon," German Patent DE4241045, 1994.

[79] S. A. Campbell, "*Fabrication Engineering at the Micro and Nanoscale*," 3rd ed., New York: Oxford University Press, 2008.

[80] F. Akasheh, T. Myers, J. D. Fraser, S. Bose, and A. Bandyopadhyay, “Development of Piezoelectric Micromachined Ultrasonic Transducers,” *Sens. Actuators A Phys.*, vol. 111, no. 2–3, pp. 275–287, 2004.

[81] Z. Wang, W. Zhu, H. Zhu, J. Miao, C. Chao, C. Zhao, and O. K. Tan, “Fabrication and Characterization of Piezoelectric Micromachined Ultrasonic Transducers with Thick Composite PZT Films,” *IEEE Trans. Ultrason. Ferroelectr. Freq. Control*, vol. 52, no. 12, pp. 2289–2297, 2005.

[82] Y. Lu, A. Heidari, S. Shelton, A. Guedes, and D. A. Horsley, “High Frequency Piezoelectric Micromachined Ultrasonic Transducer Array for Intravascular Ultrasound Imaging,” *2014 IEEE 27th International Conference on Micro Electro Mechanical Systems (MEMS)*, San Francisco, CA, USA, 2014, pp. 745-748.

[83] H. Kim, F. Griggio, I. S. Kim, K. Choi, R. L. Tutwiler, T. N. Jackson, and S. Trolier-McKinstry, "Piezoelectric Thin Films for a High Frequency Ultrasound Transducer with Integrated Electronics," Sensors, 2010 IEEE, Waikoloa, HI, USA, 2010, pp. 2186-2188.

[84] D. S. W. Choong, D. S. H. Chen, D. J. Goh, J. Liu, S. Ghosh, Y. Koh, J. Sharma, S. Merugu, F. Quaglia, M. Ferrera, A. S. Savoia, and E. J. Ng, "Silicon-On-Nothing ScAlN pMUTs," *2021 IEEE International Ultrasonics Symposium (IUS)*, Xi'an, China, 2021, pp. 1-4.

[85] J. Su, X. Zhang, G. Zhou, C. Xia, W. Zhou, and Q. Huang, "A Review: Crystalline Silicon Membranes Over Sealed Cavities for Pressure Sensors by Using Silicon Migration Technology," *J. Semiconductors*, vol. 39, no. 7, 071005, 2018.

[86] S. Sun, M. Zhang, C. Gao, B. Liu, and W. Pang, “Flexible Piezoelectric Micromachined Ultrasonic Transducers Towards New Applications,” *2018 IEEE International Ultrasonics Symposium (IUS)*, Kobe, Japan, 2018, pp. 1-4.

[87] Y. Jeong, J. Genoe, P. Gijsenbergh, J. Segers, P. L. Heremans, and D. Cheyns, “Fully Flexible PMUT Based on Polymer Materials and Stress Compensation by Adaptive Frequency Driving,” *J. Microelectromech. Syst.*, vol. 30, no. 1, pp. 137–143, 2021.

[88] A. J. Fox, B. Drawl, G. R. Fox, B. J. Gibbons, and S. Trolier-Mckinstry, “Control of Crystallographic Texture and Surface Morphology of Pt/TiO_2 Templates for Enhanced PZT Thin Film Texture,” *IEEE Trans. Ultrason. Ferroelectr. Freq. Control*, vol. 62, no. 1, pp. 56–61, 2015.

[89] S. L. Swartz, S. J. Bright, P. J. Melling, and T. R. Shrout, “Sol-Gel Processing of Composite $PbTiO_3$/PLZT Thin Films,” *Ferroelectrics*, vol. 108, no. 1, pp. 71–76, 1990.

[90] Y. Bastani and N. Bassiri-Gharb, “Processing Optimization of Lead Magnesium Niobate-Lead Titanate Thin Films for Piezoelectric MEMS Application,” *J. Am. Ceram. Soc.*, vol. 95, no. 4, pp. 1269–1275, 2012.

[91] P. Muralt, “Recent Progress in Materials Issues for Piezoelectric MEMS,” *J. Am. Ceram. Soc.*, vol. 91, no. 5, pp. 1385–1396, 2008.

[92] H. G. Yeo, X. Ma, C. Rahn, and S. Trolier-McKinstry, “Efficient Piezoelectric Energy Harvesters Utilizing (001) Textured Bimorph PZT Films on Flexible Metal Foils,” *Adv. Funct. Mater.*, vol. 26, no. 32, pp. 5940–5946, 2016.

[93] B. Ea Kim, F. Varniere, B. Agius, and R. Bisaro, "Pt Electrode Investigation and Electrical Properties of RF Magnetron Sputtered Pb $(Zr,Ti)O_3$," *Microelectron. Eng.*, vol. 29, no. 1-4, pp. 231-234, 1995.

[94] C.-C. Yang, M.-S. Chen, T.-J. Hong, C.-M. Wu, J.-M. Wu, and T.-B. Wu, "Preparation of (100)-Oriented Metallic $LaNiO_3$ Thin Films on Si Substrates by Radio Frequency Magnetron Sputtering for the Growth of Textured Pb $(Zr_{0.53}Ti_{0.47})O_3$," *Appl. Phys. Lett.*, vol. 66, no. 20, pp. 2643-2645, 1995.

[95] W. Zhu, T. Borman, K. DeCesaris, B. Truong, M. M. Lieu, S. W. Ko, P. Mardilovich, and S. Trolier-McKinstry, "Influence of PbO Content on the Dielectric Failure of Nb-Doped {100}-Oriented Lead Zirconate Titanate Films," *J. Am. Ceram. Soc.*, vol. 102, no. 4, pp. 1734–1740, 2019.

[96] T. M. Borman, S. W. Ko, P. Mardilovich, and S. E. Trolier-McKinstry, "Development of Crystallographic Texture in Chemical Solution Deposited Lead Zirconate Titanate Seed Layers," *J. Am. Ceram. Soc.*, vol. 100, no. 10, pp. 4476–4482, 2017.

[97] T. Doi, H. Sakurai, and N. Soyama, "Method of Forming PNbZT Ferroelectric Thin Film," U.S. Patent 10,005,101, 26, 2014.

[98] T. Doi, T. Noguchi, J. Fuji, N. Soyama, and H. Sakurai, "The Orientation and Grain Texture Effect on Life Time Reliability of Sol–Gel Derived $PbZr_{0.52}Ti_{0.48}O_3$ Films," *Jpn. J. Appl. Phys.*, vol. 51, no. 9S1, p. 09LA15, 2012.

[99] N. Ledermann, P. Muralt, J. Baborowski, S. Gentil, K. Mukati, M. Cantoni, A. Seifert, and N. Setter, "{100}-Textured, Piezoelectric $Pb(Zr_x, Ti_{1-x})O_3$ Thin Films for MEMS: Integration, Deposition and Properties," *Sens. Actuators A Phys.*, vol. 105, no. 2, pp. 162–170, 2003.

[100] S. Trolier-McKinstry and P. Muralt, "Thin Film Piezoelectrics for MEMS," *J. Electroceram.*, vol. 12, no. 1, pp. 7–17, 2004.

[101] S. H. Yi and E. S. Kim, "Micromachined Piezoelectric Microspeaker," *Jpn. J. Appl. Phys.*, vol. 44, no. 6R, p. 3836, 2005.

[102] K. Seo, J. Park, H. Kim, D. Kim, S. Ur, and S. Yi, “Micromachined Piezoelectric Microspeakers Fabricated with High Quality AlN Thin Film,” Integr. Ferroelectr., vol. 95, pp. 74-82, 2007.

[103] I. J. Cho, S. Jang, and H. J. Nam, “A Piezoelectrically Actuated MEMS Speaker with Polyimide Membrane and Thin Film Pb(Zr,Ti)O_3 (PZT) Actuator,” *Integr. Ferroelectr.*, vol. 105, no. 1, pp. 27-36, 2009.

[104] H. Wang, Y. Ma, Q. Zheng, K. Cao, Y. Lu, and H. Xie, "Review of Recent Development of MEMS Speakers," *Micromachines*, vol. 12, no. 10, p. 1257, 2021.

[105] Q. Shi, T. Wang, and C. Lee, “MEMS Based Broadband Piezoelectric Ultrasonic Energy Harvester (PUEH) for Enabling Self-Powered Implantable Biomedical Devices,” *Sci. Rep.*, vol. 6, no. 1, pp. 1–10, 2016.

[106] R. J. Przybyla, H. Y. Tang, A. Guedes, S. E. Shelton, D. A. Horsley, and B. E. Boser, “3D Ultrasonic Rangefinder on a Chip,” *IEEE J. Solid-State Circuits*, vol. 50, no. 1, pp. 320–334, 2015.

[107] D. E. Dausch, K. H. Gilchrist, J. B. Carlson, S. D. Hall, J. B. Castellucci, and O. T. Von Ramm, “In Vivo Real-Time 3-D Intracardiac Echo using PMUT Arrays,” *IEEE Trans. Ultrason. Ferroelectr. Freq. Control*, vol. 61, no. 10, pp. 1754–1764, 2014.

[108] X. Jiang, Y. Lu, H.-Y. Tang, J. M. Tsai, E. J. Ng, M. J. Daneman, B. E. Boser, and D. A. Horsley, “Monolithic Ultrasound Fingerprint Sensor,” *Microsyst. Nanoeng.*, vol. 3, no. 1, pp. 1–8, 2017.

[109] Y. Lu, H. Tang, S. Fung, Q. Wang, J. M. Tsai, M. Daneman, B. E. Boser, and D. A. Horsley, “Ultrasonic Fingerprint Sensor using a Piezoelectric Micromachined Ultrasonic Transducer Array Integrated with Complementary Metal Oxide Semiconductor Electronics,” *Appl. Phys. Lett.*, vol. 106, no. 26, p. 263503, 2015.

[110] H. Tang, Y. Lu, S. Fung, J. M. Tsai, M. Daneman, D. A. Horsley, and B. E. Boser, “Pulse-Echo Ultrasonic Fingerprint Sensor on a Chip,” *2015 Transducers - 2015 18th International Conference on Solid-State Sensors, Actuators and Microsystems (TRANSDUCERS)*, Anchorage, AK, USA, 2015, pp. 674-677.

[111] X. Jiang, H.-Y. Tang, Y. Lu, X. Li, J. M. Tsai, E. J. Ng, M. J. Daneman, M. Lim, F. Assaderaghi, B. E. Boser, and D. A. Horsley, “Monolithic 591×438 DPI Ultrasonic Fingerprint Sensor,” *2016 IEEE 29th International Conference on Micro Electro Mechanical Systems (MEMS*), Shanghai, China, 2016, pp. 107-110.

[112] D. A. Horsley, Y. Lu, H.-Y. Tang, X. Jiang, B. E. Boser, J. M. Tsai, E. J. Ng, and M. J. Daneman, “Ultrasonic Fingerprint Sensor based on a PMUT Array Bonded to CMOS Circuitry,” *2016 IEEE International Ultrasonics Symposium (IUS)*, Tours, France, 2016, pp. 1-4.

[113] H. V. Panchawagh, S. Ganti, K. D. Djordjev, D. W. Burns, T. A. Dickinson, D. W. Kidwell, R. V. Shenoy, J. B. Lasiter, H.-Y. Tang, and Y. Lu, “Integrated Piezoelectric Micromechanical Ultrasonic Transducer Pixel and Array,” U.S. Patent 10,497,748, Dec. 03, 2019.

[114] A. S. Savoia, M. Casavola, E. Boni, M. Ferrera, C. Prelini, P. Tortoli, D. Giusti, and F. Quaglia, "Design, Fabrication, Characterization, and System Integration of a 1-D PMUT Array for Medical Ultrasound Imaging," *2021 IEEE International Ultrasonics Symposium (IUS)*, Xi'an, China, 2021, pp. 1-3

Chapter 3

Quantitative Piezoelectric Measurements of Partially Released Pb(Zr, Ti)O_3 Structures

This chapter is dedicated to the quantitative measurement of the longitudinal piezoelectric coefficient in released structures of piezoelectric thin films. Leveraging the precision of micromachining, the released structures were prepared with well-defined boundary conditions, thereby overcoming the limitations previously reported in the literature. Utilizing a double beam laser interferometer, the large signal longitudinal piezoelectric coefficient ($d^*_{33,f}$) of a piezoelectric membrane has been measured quantitatively for the first time.

3.1 Introduction

Piezoelectric materials are widely utilized in a variety of micro-electromechanical systems (MEMS), including sensors, actuators, and transducers. Over time, piezoelectric thin films have gained considerable interest due to their small size, low power consumption, and significant displacement [1], [2]. Lead zirconate titanate (PZT) thin films are an excellent choice for piezoelectric MEMS (piezoMEMS) applications, due to their superior piezoelectric response and well-established processing techniques.

PZT exhibits a distorted perovskite structure, with its morphotropic phase boundary showing the highest piezoelectric response due to the structural instability between tetragonal, rhombohedral, and monoclinic symmetries. In general, there are two key factors that influence the piezoelectric response: i) intrinsic contributions and ii) extrinsic contributions [3]. Extrinsic contributions such as domain wall motion substantially impact the macroscopic piezoelectric

response, contributing more than 50% of the piezoelectric coefficient in bulk PZT ceramics at room temperature [4 - 5]. However, in thin films, the submicron grain size, higher defect concentration, film orientation, and substrate clamping significantly reduce the piezoelectric coefficient [6 - 19].

To address the constraints inherent in clamped piezoelectric thin films on stiff substrates, K. Lefki defined an effective longitudinal piezoelectric coefficient for clamped thin films, denoted as $d_{33,f}$, as demonstrated in reference [20]:

$$d_{33} = \left(\frac{\partial S_3}{\partial E_3}\right)_T \quad \text{Eq. 1}$$

where d_{33} is the longitudinal piezoelectric coefficient, S_3 is the strain in the 3-direction, E_3 is an electric field in the 3-direction, and the subscript T denotes the constant stress condition. For a clamped film, the strain in the 3-direction can be written as:

$$S_3 = s_{13}^E(T_1 + T_2) + s_{33}^E T_3 + d_{33}E_3 \quad \text{Eq. 2}$$

where s^E is the elastic compliance under a constant electric field, T_1 and T_2 are in-plane stress, and T_3 is out-of-plane stress. In this scenario, the out-of-plane stress is assumed to be zero since the surface of the sample is free ($T_3 = 0$). Additionally, the in-plane strain is assumed to be zero, i.e. ($S_1 = S_2 = 0$), which is a reasonable starting point, although it is not completely correct due to the ability to bend thick substrates [21 - 23]. According to the assumptions, equation 2 is modified to yield:

$$S_3 = -2d_{31}s_{13}^E/(s_{11}^E + s_{12}^E) + d_{33}E_3 \quad \text{Eq. 3}$$

By substituting equation 3 back to equation 1, the effective longitudinal piezoelectric coefficient ($d_{33,f}$) can be written as:

$$d_{33,f} = d_{33} - 2d_{31}\left(\frac{s_{13}^E}{s_{11}^E + s_{12}^E}\right) \quad \text{Eq. 4}$$

where d_{33} and d_{31} are the free longitudinal and transverse piezoelectric coefficients. Since d_{33} and s_{13}^E are positive, and $(s_{13}^E/s_{11}^E + s_{12}^E) < 1$, $d_{33,f}$ for a clamped film is smaller than d_{33} of the unconstrained piezoelectric.

3.1.1 Longitudinal piezoelectric coefficient measurement by optical interferometry

A single-beam Michelson interferometer employs the principles of homodyne laser interferometry, dividing a monochromatic light source into two beams: a reference beam and a measurement beam. The measurement beam reflects off the surface of the top electrode; the change in phase of the measurement beam generates an interference pattern that can be used to monitor the displacement of the upper surface [24], [25]. That is, the intensity of the light changes due to a phase difference $\Delta\emptyset$ of the two light beams as [26]:

$$I = \frac{1}{2}(I_{max} + I_{min}) + \frac{1}{2}(I_{max} - I_{min})\cos\,(2\pi\frac{2\Delta\emptyset}{\lambda}) \qquad \text{Eq. 4}$$

The intensity change due to the thickness change is described as [26]:

$$I = \frac{1}{2}(I_{max} + I_{min}) + \frac{1}{2}(I_{max} - I_{min})\cos\,(2\pi\frac{2\Delta L}{\lambda} + \frac{\pi}{2}) \qquad \text{Eq. 5}$$

where I is the intensity of the light, I_{max} and I_{min} are the maximum and minimum light intensity, ΔL is the change in height of the sample surface, and λ is the wavelength of the laser. As the operation point is normally selected at the most sensitive position ($\pi/2$), equation 5 can be reduced to

$$I = (I_{max} - I_{min})2\pi\frac{\Delta d}{\lambda} \qquad \text{Eq. 6}$$

where the thickness change is

$$\Delta d = \frac{I \cdot \lambda}{2\pi(I_{max} - I_{min})} \qquad \text{Eq. 7}$$

The voltage signal at the photodetector ($V_{out}(t)$) is:

$$V_{out}(t) = V_{DC} + (\frac{2\pi}{\lambda})V_{PP}\Delta L(t) \quad \text{Eq. 8}$$

where V_{DC} is the dc offset, and V_{PP} is the full-fringe displacement peak-to-peak voltage.

An inevitable drawback of utilizing a single-beam laser interferometer is that the measurement beam only probes the top electrode. Consequently, substrate bending often significantly inflates the apparent value of $d_{33,f}$.

To counteract the bending contribution, double-beam laser interferometry was proposed by Pan and Cross and later modified by Kholkin [29][27]. Unlike its single-beam counterpart, the double-beam laser interferometer uses the modified Mach-Zehnder interferometer configuration. In a double beam laser interferometer, the laser beam is divided into reference and measurement beams. The measurement beam travels to the upper and lower surfaces of the sample. Thus, the change in optical path length reflects the change in the sample thickness generated from an AC voltage excitation, and the effect of substrate bending is suppressed. The measurement beam and the reference beam combine and create the interference pattern monitored by the photodetector. Again, the displacement can be calculated from equations 5 and 6. In this scenario, the bending contribution is canceled by the optical path differences of the top and bottom measured beams.

3.1.2 Released piezoelectric thin films

As discussed earlier, substrate-induced clamping in thin films can substantially reduce the piezoelectric coefficient. Consequently, release methods have been explored to study clamping-free conditions in piezoelectric thin films. Buhlmann *et al.* reported enhanced domain wall mobility and piezoelectric response through submicron-scale lateral patterning in a $Pb(Zr_{0.40}Ti_{0.60})O_3$ thin film [30]. As the 200 nm epitaxial PZT film was patterned to 100 - 200 nm in lateral size,

piezoelectric scanning force microscopy detected a notable increase in the piezoelectric coefficient. Griggio *et al.* demonstrated that substrate clamping affects the extrinsic contributions to dielectric and piezoelectric behavior; films released from their substrates exhibit greater domain wall motion than clamped ones [31] This reduction in extrinsic contribution due to substrate clamping is directly tied to the pinning of non-180° ferroelectric/ferroelastic domain walls.

Wallace *et al.* investigated the relationship between mechanical boundary constraints and ferroelectric/ferroelastic domain wall motion in tetragonal $PbZr_{0.3}Ti_{0.7}O_3$ with 1% Mn on the B site, using synchrotron x-ray diffraction and varying the percentage of release between the piezoelectric thin film and the Si substrate [32]. The 002/200 Bragg reflection peaks were investigated as a function of the applied electric field to study domain reorientation. The results indicated that the higher the degree of release, the greater the domain reorientation under DC fields. Thin films released over 75% of the area demonstrated a level of 90° domain reorientation comparable to bulk ceramics. These findings confirmed the significant role substrate clamping plays in controlling extrinsic contributions to piezoelectricity and underscored the utility of released piezoelectric thin films for piezoMEMS applications.

Liu *et al.* demonstrated an ~ 45 % improvement in the remanent polarization of fully released PZT thin film on a 5 μm thick polyimide substrate via the transfer method compared to that of a similar composition PZT thin film prepared on a rigid substrate [33]. These findings suggest that the piezoelectric coefficient could be significantly enhanced if films are properly released. However, quantitative measurement of fully released piezoelectric thin film on a polymer proved challenging due to the extreme flexibility of the sample, as demonstrated by Liu *et al.* [34]. In that report, a 1 mm thick PZT thin film with random orientation was prepared on a 10 mm thick polyimide substrate. As shown in Figure 3-1, a double-beam laser interferometer was used to study the longitudinal piezoelectric coefficient. While the effect of substrate bending was expected to be suppressed, the large displacement amplitude produced by the asymmetrical test structure exceeded

the fundamental limit of the interferometer. This resulted in an erroneous $d_{33,f}$ of over 9600 pm/V. The main sources of error were identified as i) the asymmetrical structure of the test device, ii) residual polyimide in the bottom electrode vias, and iii) the continuous PZT thin films. In addition, finite element analysis was undertaken to examine the displacement profile of a sample with varied hole diameters on the rigid supporter (polycarbonate). It was observed that the bending profile was directly influenced by the diameters of the holes. The finite compliance of the rigid support is speculated to induce the bending, as depicted in Figure 3-1(b). It is also suggested that the complex bending profile could potentially be reduced if the film adhered properly to the carrier.

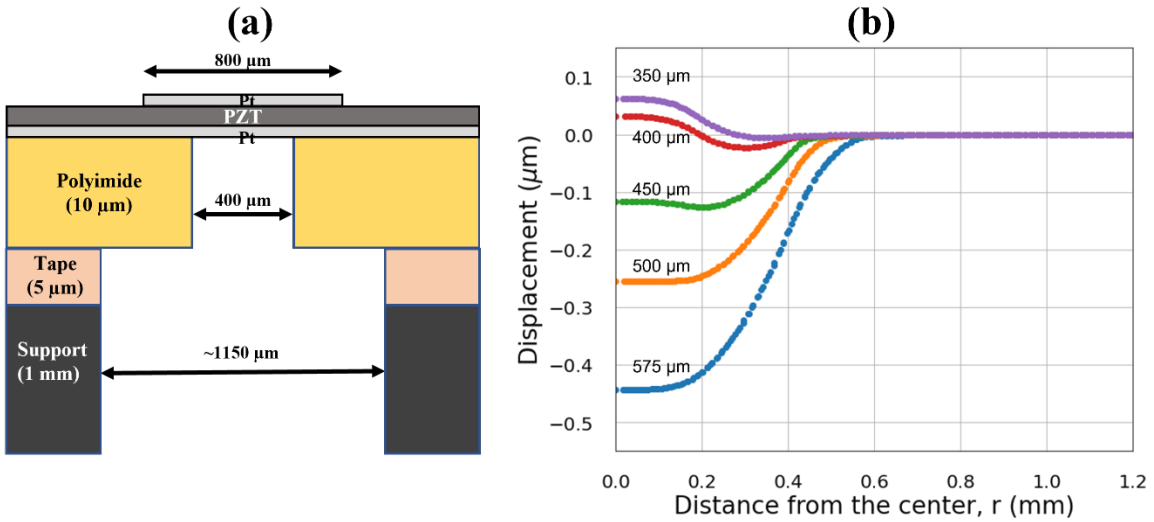

Figure 3-1: Challenges in measurement of the piezoelectric coefficient of fully released PZT on a polyimide substrate (a) device schematic and (b) finite element analysis of the displacement profile as a function of the punched hole diameter, adapted from [34].

In this chapter, a test device was specifically designed to quantify the longitudinal piezoelectric coefficient of a released PZT thin film. It was constructed with a released PZT film on a rigid Si substrate, with the release achieved through backside deep reactive ion etching (DRIE) and patterned ZnO wet etching. The device stack consisted of ZnO/Al_2O_3/Pt/PZT/Pt layers, where the ZnO functions as an etch stop layer during the backside etching process. Subsequently, the ZnO

exposed during backside etching was removed through wet etching, and the degree of release was regulated by controlling the area of the patterned ZnO. Additionally, the backside etched vias provide a pathway for rear laser probing for double-beam measurements. To characterize the displacement profile and piezoelectric response, both double-beam and single-beam laser interferometry were utilized.

3.2 Experimental Method

3.2.1 The Device Design

Liu *et al.* showed that significant errors arose when a sample exhibited asymmetry, the probing surface quality was uneven, and the PZT thin film vibrated globally [34]. To address device asymmetry, the sample was designed to release the PZT thin film on a rigid substrate, creating an accessible, precisely aligned bottom electrode via micromachining processes. The ZnO thin film served as both the DRIE stop layer and the sacrificial layer as it was resistant to the fluorine plasma [34]-[38]. Additionally, it was easily etched in weak acid solutions, such as acetic acid, nitric acid or dilute hydrochloric acid. Importantly, Lee demonstrated that ZnO could be selectively etched using an acetic buffer solution (composed of acetic acid and sodium acetate) without damaging the Al_2O_3 thin film [38]. To avoid global motion caused by a blanket layer of PZT, the PZT thin film was patterned into a circular shape via inductive-coupled plasma–reactive ion etching (ICP-RIE). Consequently, this test structure allowed the released area to be varied with well-defined mechanical boundary conditions.

The test sample was designed to explore three different regimes while maintaining constant values for the diameter of the top electrode (800 μm), the patterned PZT (1400 μm), and the DRIE vias (400 μm). These regimes where: i) the diameter of the release area (patterned ZnO) is smaller

than that of the top electrode, ii) the diameter is equal to that of the top electrode, and iii) the diameter is larger than that of the top electrode. By devising the test devices with well-defined mechanical boundary conditions, it is expected that the displacement bending profiles across these three different release states should be comparable [34]. However, due to the fragility of the released structures, only those with ZnO diameters of either 400 μm or 600 μm survived the process. These two types of devices are designated as 50% and 75% released samples, correlating to the proportion of the electrode area covered (800 μm).

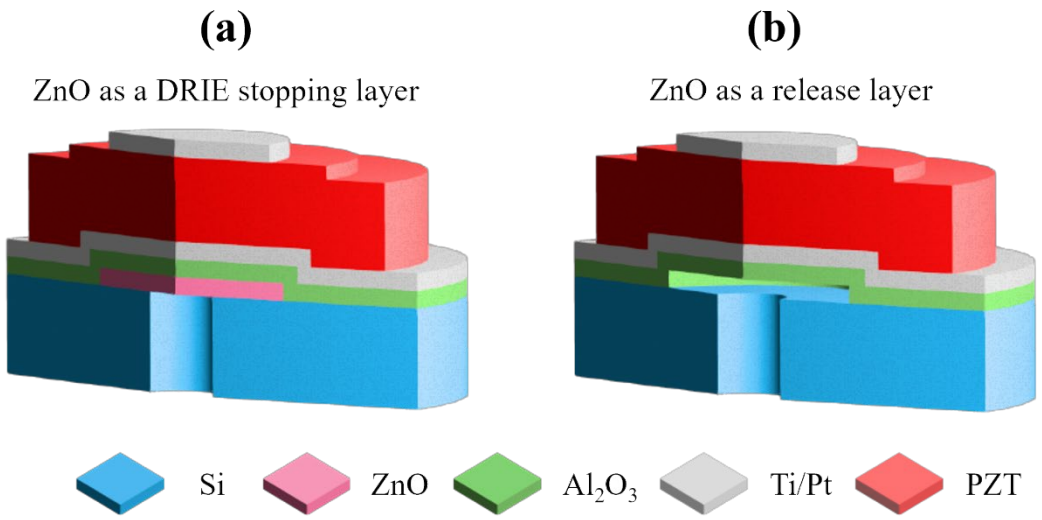

Figure 3-2: Schematic representation of the device for longitudinal piezoelectric coefficient measurement via laser interferometry. (Left) The diagram depicts a patterned ZnO as the etch-stop layer during backside etching. (Right) The ZnO is etched and acts as a defining parameter for the release.

3.2.2 Device Fabrication

As shown in Figure 3-3(a), the fabrication process began with the preparation of a Si substrate using a standard RCA cleaning process. A 4-inch Si substrate (Nova) was immersed in an SC1 solution bath (5:1:1 ratio of H_2O: NH_3: H_2O_2) to remove organic contamination, followed by a 30 second dip in a 1:50 ratio of 2 vol.% HF: DI water solution to eliminate the SiO_2 layer. The

substrate was then rinsed with deionized water. Subsequently, the wafer was immersed in an SC2 solution bath (6:1:1 ratio of H_2O: HCl: H_2O_2), followed by another rinse with DI water [39].

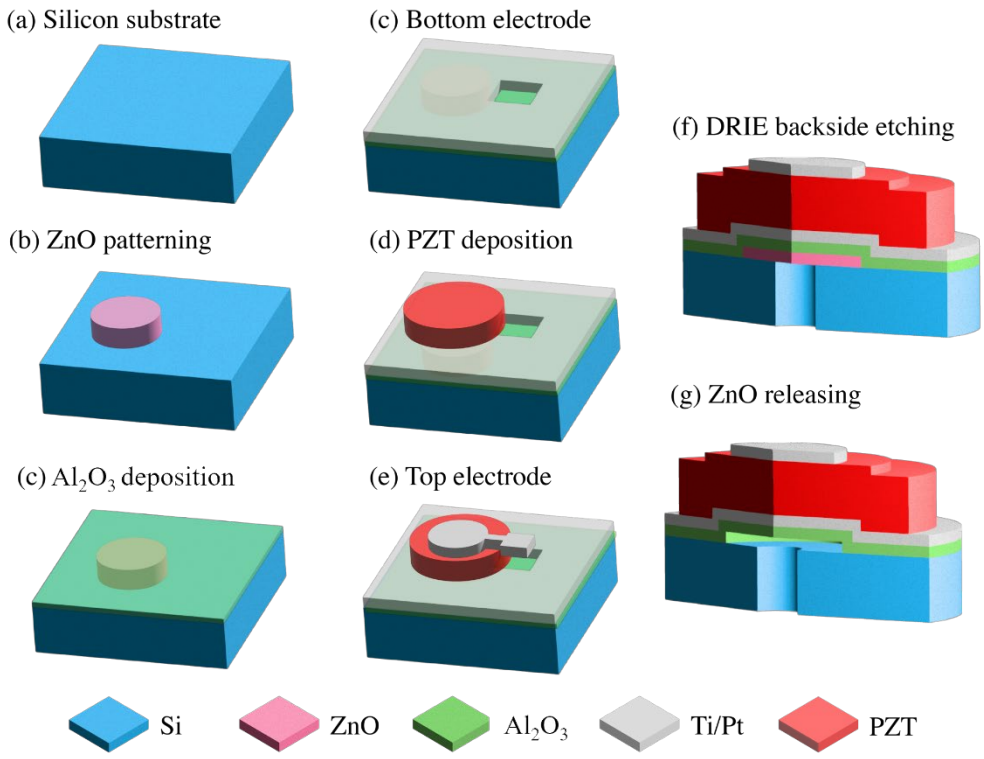

Figure 3-3: Process flow of the device fabrication starting from (a) a clean silicon substrate, (b) the patterning of sacrificial layer ZnO, (c) the blanket deposition of Al_2O_3 insulator layer, (c) – (e) the bottom electrode, PZT, and top electrode deposition and patterning, (f) backside DRIE via etching, and (g) ZnO sacrificial layer release.

A 10 nm thin Al_2O_3 layer was then deposited on the Si substrate by atomic layer deposition (Kurt J. Lesker ALD-150LE system) at 200°C using tetramethylammonium hydroxide (TMAH) and H_2O as precursors. This layer serves as the etch stop layer from silicon deep reactive ion etching [40], [41].

Next, a 150 nm ZnO thin film was deposited by a custom-made plasma-enhanced atomic layer deposition (PEALD) system at 200°C using diethylzinc (DEZ) as a precursor and N_2O as the

oxidant. More details on this deposition are given elsewhere [42], [43]. The ZnO film was subsequently patterned through a wet etching process using an acetic buffer etchant (0.11 M acetic acid and 0.78 M sodium acetate) at room temperature with an etch rate of 111 nm/minute. Here, LOR5A and SPR3012 photoresist served as soft masks. Initially, LOR5A was spun onto the blanket ZnO thin film at 4000 rpm for 45 seconds and baked at 190 °C for 5 minutes. Then, SPR3012 was spun at 4000 rpm for 45 seconds and baked at 90 °C for 1 minute. The photoresist was exposed using a commercial maskless aligner (Heidelberg MLA150) at 200 mJ/cm^2 and developed in a TMAH-based developer, Microposit CD26, for 1 minute. Prior to etching, oxygen plasma was used to descum the residual photoresist with 200 sccm of O_2, 50 sccm of He, at a pressure of 550 mTorr, and an RF power at 200 W for 3 minutes using a TePla M4L plasma asher. The prepared ZnO thin film was etched into a circular shape in an acetic acid buffer bath for 1.5 minutes and rinsed with deionized water as shown in Figure 3-3(b). The photoresist mask was removed by soaking the sample in acetone, isopropanol and deionized water, followed by an oxygen plasma process with the same recipe for 5 minutes. Finally, the patterned film was coated with a 200 nm layer of Al_2O_3 using thermal atomic layer deposition (ALD) similar to the previous deposition. Al_2O_3 acted as a diffusion barrier and an insulator layer for the PZT device.

The bottom electrode consisted of a 30 nm Ti adhesion layer and a 150 nm Pt layer; the bottom electrodes were patterned by the lift-off process. A reentrant profile was achieved using a LOR5A and SPR3012 photoresist mask. The photoresist was patterned using a maskless aligner at 200 mJ/cm^2 and developed in CD26 for 75 seconds. Prior to the deposition of the bottom electrode, the developed photoresist was subjected to an oxygen plasma cleaning process in a Tepla M4L asher to remove organic residues. The sample was then transferred into the vacuum chamber of a DC magnetron sputter deposition system (Kurt J. Lesker CM18). The deposition process began with a 30 nm layer of Ti at room temperature, with the pressure regulated at 2 mTorr and the DC power set at 200 W. Without breaking the vacuum, a layer of Pt was deposited at room temperature;

the pressure was maintained at 2.5 mTorr and the DC power set to 200 W. To strip off the photoresist soft mask, the sample was immersed in a PRS3000 bath at 80°C for 1 hour, followed by an oxygen plasma cleaning process to remove organic residues with 300 sccm of O_2, 50 sccm of He, pressure at 500 mTorr, and 300 W for 5 minutes. The bottom electrode is depicted in Figure 3-3(d). After that, the prepared sample was annealed in air at 500°C for 1 hour, followed by rapid thermal annealing at 700 °C for 1 minute in O_2 to release any trapped hydrogen from the Al_2O_3 and ZnO films as shown in Figure 3-4.

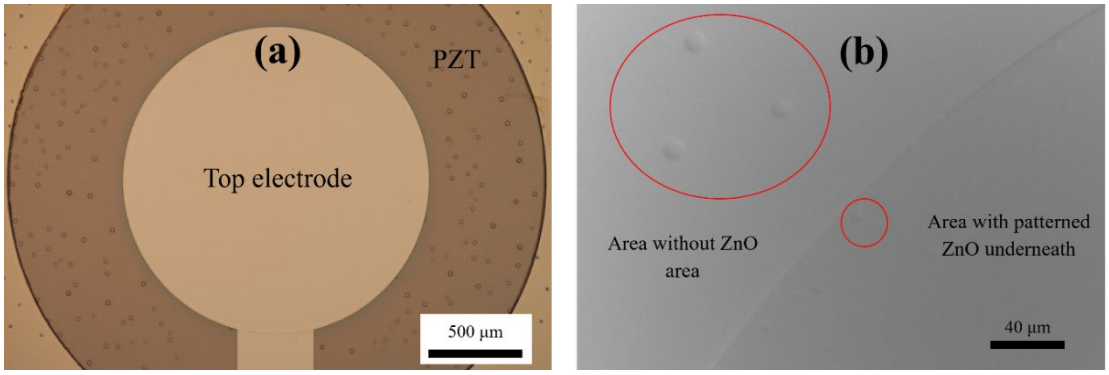

Figure 3-4: Optical microscope image and (b) SEM image showing evidence for blisters originating from the buried Al_2O_3 layer. Note that for this particular sample, blistering is observed across the wafer, even over the ZnO region, as the sample had a blanket layer of 10 nm Al_2O_3 below the patterned ZnO.

A 1 µm thick PZT thin film was deposited on the patterned bottom electrode using the sol-gel technique. A 15 wt% PZT sol gel E1 solution, 2 mol% Nb doped PZT (52/48) with 14% excess Pb, supplied by Mitsubishi Materials, was spin-coated onto the substrate at 2750 rpm for 45 seconds. The film was dried on a hotplate, initially set at 100°C for 1 minute, then the temperature was increased to 300°C for an additional 4 minutes to pyrolyze the layer. Following this, the film underwent crystallization at a temperature of 700°C for 1 minute in a rapid thermal annealer with 2 slpm O_2 flow [33], [44]. This process was repeated until the desired thickness was achieved. To compensate for the Pb loss incurred during the process, a 2-methoxyethanol (2-MOE)-based PbO

solution was spun onto the film at 6000 rpm for 45 seconds as a capping layer. It was then baked at 100°C for 1 minute and 300°C for 2 minutes before undergoing a crystallization process by rapid thermal annealing at 700°C for 1 minute in O_2 [45]. Comparable films prepared on Pt-coated silicon wafers had a relative permittivity of 1330 ± 9.6, a dielectric loss tangent of 1.78 ± 0.012 %, a remanent polarization of (15.39, -16.55) μC/cm^2, and a coercive field of (49.14, -36.24) kV/cm.

As can be observed in Figure 3-4, during PZT crystallization, some micron-sized domes developed; these were attributed to an Al_2O_3 blister effect [46][48]. This is commonly reported when ALD Al_2O_3 (with a thickness greater than 10 nm) is directly deposited onto a clean silicon wafer and subsequently subjected to high-temperature heat treatment. It is notable that on another sample, blisters were not observed after high temperature annealing in locations where ZnO is in contact with silicon layer instead of Al_2O_3; this confirms that the blister originates from the Al_2O_3/SiO_2 interface. These blisters did not significantly degrade the structural integrity of the PZT layer.

Before the deposition of the top electrode, the PZT thin film was evaluated using X-ray diffraction (XRD, Malvern Panalytical Empyrean) and field-emission scanning electron microscopy (Merlin, Zeiss FESEM). Figure 3-5(a) shows the XRD spectra of the prepared 1 mm thick polycrystalline PZT thin films with additional peaks associated with the substrate. Figure 3-5(b) reveals a surface that is pyrochlore-free, with a dense grain structure with an average lateral grain size of 160 ± 36 nm following the Heyn intercept method [49].

Subsequently, the PZT was patterned using a thick AZ4620 photoresist. The AZ4620 was spun at 1500 rpm to achieve a target thickness of 12 μm and then baked at 90°C for 1 minute, followed by 105°C for 3 minutes. Thereafter, the spun photoresist was left in the atmosphere for 1 hour before exposure to allow for re-hydration [49]. The photoresist was exposed at 800 mJ/cm^2 using a maskless aligner and developed in a KOH-based, 1:4 AZ400k developer, for 4 minutes. Prior to PZT etching, the sample underwent a descum process using a Tepla M4L oxygen asher.

The PZT was then etched using inductively-coupled plasma reactive ion etching (ICP-RIE), in an Ulvac NE550, with 20 sccm of Ar, 28 sccm of CF_4, and 7 sccm of Cl_2 at 150 W bias power and 700 W ICP power, maintaining an etching pressure of 3.8 mTorr [44]. The etching process was performed in alternating cycles of 30 seconds etching followed by 60 seconds rest to prevent overheating of the photoresist mask. This produced an average etch rate of 70 nm per minute. Once the PZT was patterned, the remaining photoresist was stripped by immersing the sample in PRS3000 at 80 °C. This was followed by a subsequent cleaning using the oxygen plasma asher. The process employed an O_2 flow of 300 sccm and 50 sccm of He at 300 W, with the pressure regulated at 550 mTorr for 5 minutes.

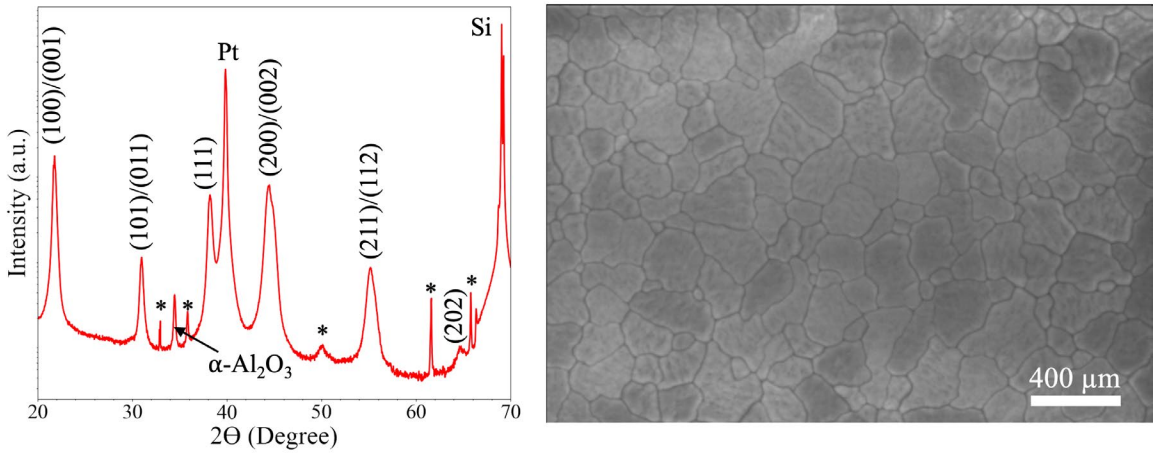

Figure 3-5: The XRD pattern with substrate peaks labeled with an asterisk and corresponding FESEM image from the 1 µm thick polycrystalline PZT thin film prepared by the chemical solution deposition method.

Before deposition of the top electrode, a 50 nm insulating layer of Al_2O_3 was deposited and patterned using wet etching in Microposit CD26. The blanket deposition of Al_2O_3 was carried out using ALD at 200ºC. The photoresist used in this step was SPR1813, spun at 4000 rpm for 45 seconds and baked at 105ºC for 1 minute. The pattern was created by exposing the photoresist via a maskless aligner at 200 mJ/cm^2 and developing in Microposit CD26, followed by a descumming clean in the Tepla M4L asher. Prior to the wet etching, the photoresist underwent a soft bake at

110ºC for 5 minutes to enhance adhesion. The Al_2O_3 was then etched by soaking in Microposit CD26 for 20 minutes with constant hand stirring. After patterning the Al_2O_3, the photoresist was removed by immersing the sample in a PRS3000 positive photoresist stripper and cleaned with an oxygen plasma in the Tepla M4L.

To complete the PZT stack, the top electrode, comprising 3 nm of Ti and 100 nm of Pt, was deposited using DC magnetron sputtering and patterned via the lift-off method. This was followed by photolithography and lift-off using LOR5A and SPR3012, employing a similar recipe as for the bottom electrode deposition. The front-side process concluded with the spin coating of Protek B3, a protective coating, to protect the front side from any further damage during the subsequent micromachining of backside vias. Protek was spun at 2000 rpm for 60 seconds and baked at 140ºC for 3 minutes and 205ºC for 2 minutes. Following this, thick photoresist AZ4620 was spun onto the back side of the wafer and patterned using a method similar to the one employed during the PZT etching process. The wafer was then transferred to a silicon deep reactive ion etching tool (DRIE) for backside via etching.

DRIE was performed using the Bosch process, with a high aspect ratio recipe using SF_6 and C_4F_8 with the substrate temperature set to 3ºC to create vias with a depth of 500 μm. The etching process stopped upon reaching the Al_2O_3/ZnO layer on the front side as neither film creates volatile products in SF_6 plasma etching [36], [37], [40], [41] Finally, the sample was cleaved into test samples using the LatticeAX420 cleaving system.

The process to etch the sacrificial ZnO layer beneath the PZT began with soaking the cleaved sample, with the photoresist and Protek B3 left intact, in a NaOH bath at 56ºC for 4 minutes. This step ensured the removal of any residual Al_2O_3. Subsequently, the buffered acetic acid solution was employed to remove the sacrificial ZnO layer as depicted in Figure 3-6. The temperature of the bath was maintained at 40ºC to expedite the etching.

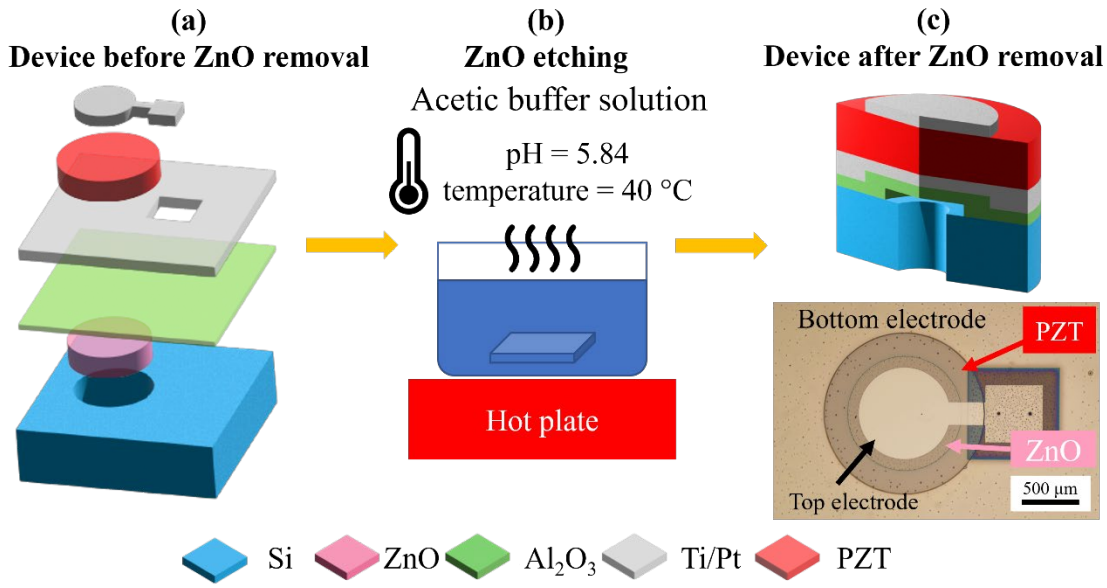

Figure 3-6: Method to release the underlying ZnO: (a) backside vias were achieved by DRIE, (b) the sample was soaked in the selective etchant: 0.11 M CH_3COOH and 0.78 M CH_3COONa, at 40ºC, and (c) the device schematic (upper) and optical microscope image of the device (lower).

It is noteworthy that etching ZnO through backside vias presents its own set of challenges. The small size of the backside holes significantly hampers the mass transport between the etching surface and the solution bath. Additionally, it was observed that the diaphragm of the majority of devices sustained damage during the wet etching process as shown in Figure 3-7. The devices that survived the process were then cleaned using acetone, isopropanol, and deionized water. This was followed by an oxygen plasma clean on the front side to completely remove any residual material from the Protek B3, preparing the devices for measurement.

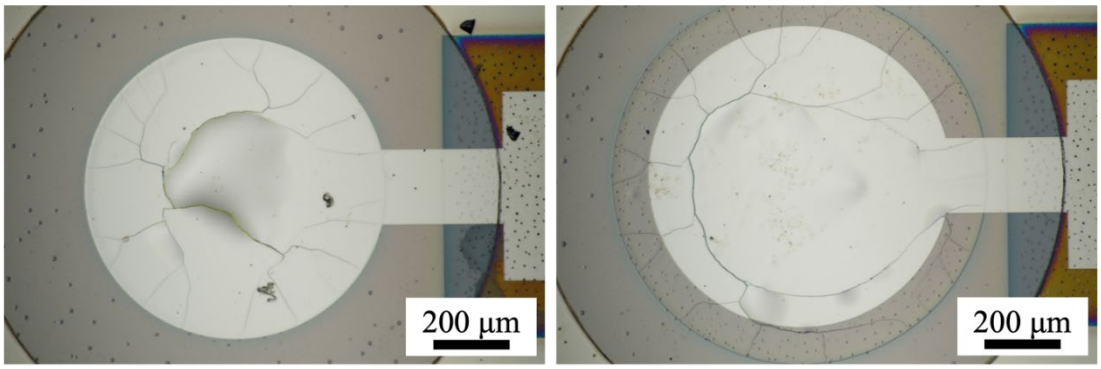

Figure 3-7: Optical microscope images showing broken diaphragms after the wet-etching release of ZnO in a buffered acetic acid etchant.

To verify the gap created by the ZnO wet etching process, the sample was first cross-sectioned using a focused-ion-beam (FIB) in the Thermo Scientific Scios™ 2 Dual Beam FIB-SEM system. Subsequently, it was imaged with the Zeiss Gemini 500 field emission scanning electron microscope to obtain high-resolution images of the etched regions. Following this, the surface topography of the released diaphragm was examined. For this purpose, optical profilometry using the Zygo NexView 3D system was employed, where white light interferometry characterized the height profile of the diaphragm before and after wet etching. In parallel, to establish a baseline for the electrical properties of the fabricated devices, measurements of capacitance and loss tangent across a frequency range from 100 Hz to 1 MHz were conducted. A Hewlett Packard 4284A LCR meter was used with 30 mV_{AC} excitation. To study the domain behavior, Rayleigh dielectric measurements were also carried out at 1 kHz using the LCR meter. Finally, the electric-field induced displacements were measured using an aixACCT double beam laser interferometer system with a complementary single beam laser interferometer mode. This allowed separate characterization of any field-induced bending of the diaphragm.

3.2.3 Double Beam Laser Interferometer – AixACCT aixDBLI System

A commercial double-beam laser interferometer from AixACCT was employed in this chapter to quantitatively measure the $d_{33,f}$ of partially released PZT structures. Multiple optical elements are included in the system's schematics, as shown in Figure 3-8. The stabilized 632.8 nm He-Ne laser is installed on the rear panel, highlighted in green. The coherent laser beam passes through an optical Faraday isolator, ensuring that no reflected beam reenters the laser source. Then the beam travels from the rear to the front panel by reflecting off mirrors M0 and M1. In the front panel, the coherent laser beam passes through the λ/2 plate and mirror M2. At the λ/2 plate, the beam's rotation determines the intensity that will be divided by the polarized beam splitter (PBS) since the polarization in the *y*-direction is delayed by λ/2. PBS1 splits the incoming laser beam into reference (polarization out of plane) and measurement (polarization in plane) beams based on their polarization components. The measurement beam path continues towards the sample's upper surface, passing through a λ/4 plate (which delays the polarization by λ/4), an electric shutter, mirror M3, and is focused by lens L1 onto the sample surface. The beam then travels back along a similar path where it is again rotated at the λ/4 plate, resulting in out-of-plane polarization. Consequently, the measurement beam is reflected by PBS1 and travels to the lower part, where it is directed by PBS2 to probe the sample's lower surface. After passing through another λ/4 plate, mirror M4, and lens L2, the beam is focused onto the sample surface before traveling back on the same path with in-plane polarization, which is transmitted through PBS2 to beam splitter BS3. Here, the beam is reflected into half of its original intensity, independent of polarization. On the reference beam path, after being reflected by PBS1, the beam goes through a λ/4 plate, is reflected back by the piezoelectric mirror M7, and reenters the λ/4 plate, yielding an in-plane polarized beam. This beam is then transmitted through PBS1 to PBS2, reflected by mirrors M5 and M6, and finally encounters BS3, where it interferes with the measurement beam. The interference observed at the

photodetector results from the optical path difference (OPD) due to the displacement of the sample. The change in interference fringes is defined by the equation:

$$\Delta\emptyset = \frac{2\pi}{\lambda} \cdot OPD \quad \text{Eq. 9}$$

where $\Delta\emptyset$ is the phase difference induced from optical path difference.

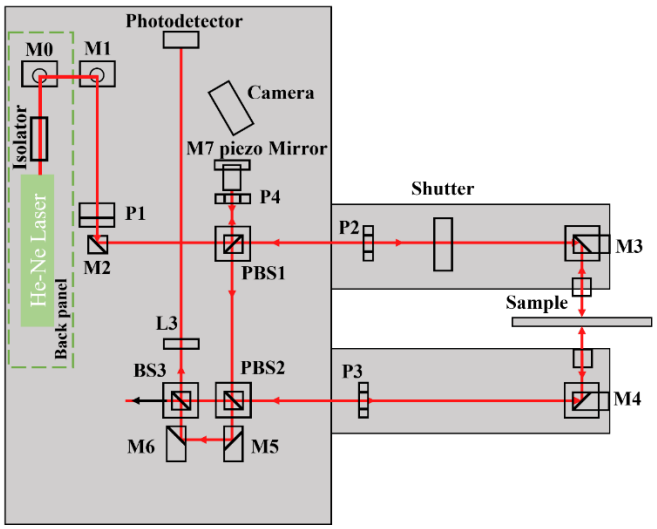

Figure 3-8: Schematic of the optical beam path of the aixDBLI system, aixACCT system GmbH. Reproduced from [26].

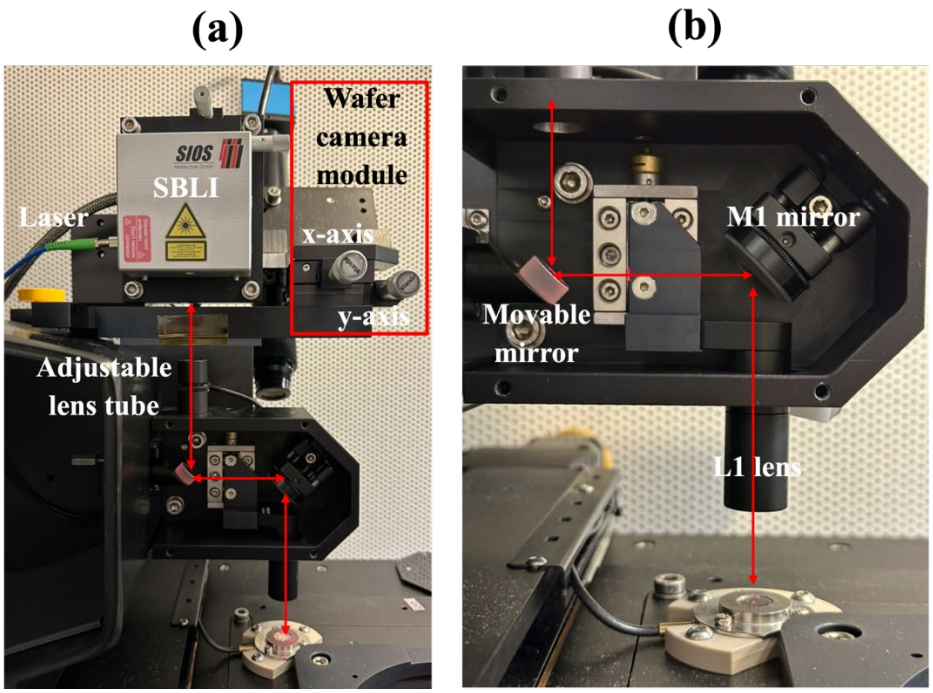

Figure 3-9: Optical beam path of the aixDBLI system, aixACCT system GmbH in the single beam configuration.

Additionally, the aixDBLI system is equipped with a single-beam laser interferometry module, as shown in Figure 3-9. The system comprises a stabilized He-Ne laser source connected to the SIOS SP120/2000 miniature plane-mirror interferometer. This configuration shares the front optical components with the double beam set-up, as shown in Figure 3-9(a). The miniature interferometer, featuring modified Michelson optics and a photodetector, sits on a movable base fitted with a micrometer screw for alignment in the x and y directions. To operate in single-beam mode, the movable mirror is lowered to block the laser beam from the double beam path, thereby creating an optical path for the single beam mode, as illustrated by the solid red line in Figure 3-9. In this configuration, the measurement beam from the miniature interferometer passes through the adjustable lens tube and is reflected by the movable mirror, as displayed in Figure 3-9(b). The beam then follows a path similar to that of the DBLI system, traveling to the M1 mirror and through the

L1 lens to focus on the top surface of the sample. The reflected beam retraces this path, is refocused by the adjustable lens tube, and returns to the auxiliary diaphragm on the sensor head.

3.3 Result and Discussion

The cross-section, prepared by focused ion milling, was employed to assess the wet etching of ZnO through the DRIE vias. Notably, the diaphragm incurred damage during the milling operation; the observed cracks initiated at the milling sites located at the boundary of the released diaphragm and propagated towards the center, suggesting the presence of considerable residual stress. Figures 3-10(a) and (b) display the PZT stack without the underlying ZnO (the clamped region) and the etched ZnO region (the released area). As indicated in Figure 3-10(b), a distinct modified region was observed between Al_2O_3 and ZnO, resulting in a residual layer of ZnO. This observation is consistent with reports of inter-diffusion of Al_2O_3 and ZnO at temperatures consistent with those used during crystallization of $Pb(Zr,Ti)O_3$ [51][53].

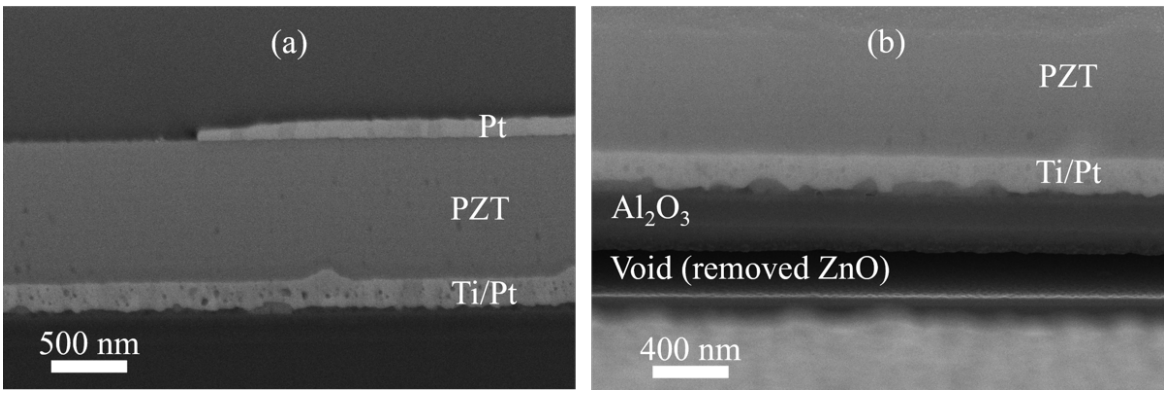

Figure 3-10: The cross-section SEM represents (a) the PZT region without ZnO underneath and (b) with a void created by wet etching the ZnO from the vias created by the backside DRIE.

Optical profilometry was utilized to analyze the diaphragm profile and confirm the absence of micro-cracks. The results revealed that i) the surviving diaphragms are crack-free, and ii) the height in the released ZnO area was lower compared to the sample before ZnO release. This

reduction is clearly illustrated in Figure 3-11(a), where the ZnO diameter matched the DRIE via diameter; the height was approximately 150 nm before ZnO wet etching and was reduced to 110 nm. This implies that upon the release of ZnO, the flexural rigidity of the structure is reduced, along with the partial release of in-plane stress, leading to zero-field bending. Figures 3-11(b) and (c) depict the post-release diaphragms with larger ZnO diameters, where the change is more pronounced, manifested as downward bending in the profile. It is important to note that ZnO etching in this scenario is challenging due to three factors: i) mass transfer limitations resulting from the small DRIE vias, ii) poor etchant accessibility through the etched voids as shown in Figure 3-10(b), and iii) downward bending of the diaphragm which might close the diaphragm gap. These etching challenges result in the diaphragm profile shown in Figures 3-11(b) and (c) where, in Figure 3-11(b), the leftover ZnO forms a noticeably higher region at the perimeter of the ZnO, and in Figure 3-11(c), where the ZnO diameter is significantly larger than the DRIE vias, the etchant cannot reach further, leaving an under-etched diaphragm. Several diaphragms were also observed to break at this step, limiting this study to released diaphragms with released regions of 50% (Figure 3-11(a)) or 75% (Figure 3-11(b)) of the top electrode area. Devices comparable to those depicted in Figure 3-11(c) were excluded, due to the undefined etching area along the edge of diaphragm.

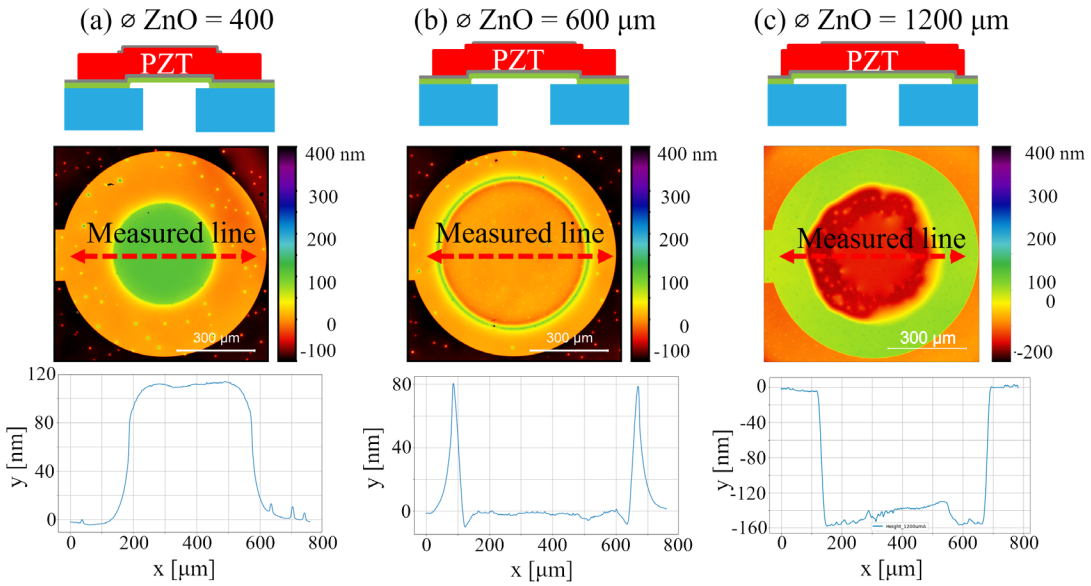

Figure 3-11: Optical profilometry results illustrating the effect of ZnO etching on the PZT thin film diaphragm for (a) 400 mm, (b) 600 mm, and 1200 mm diameter ZnO, with the height profile measured across the center of the diaphragm labeled as the measured line.

Low-field measurements of dielectric permittivity were conducted to examine the characteristics associated with the irreversible Rayleigh coefficient (α_ε) and the reversible coefficient (ε_{init}). α_ε arises from the contribution of irreversible domain wall motion, whereas ε_{init} contains contributions from the intrinsic properties of the lattice and reversible motion of domain walls. The dielectric Rayleigh measurement is governed by:

$$\varepsilon_r = \alpha_\varepsilon E_0 + \varepsilon_{init} \qquad \text{Eq. 7}$$

where ε_r is the relative dielectric coefficient and the E_0 is the applied electric field. The dielectric permittivity as a function of frequency and AC field amplitude were measured at each fabrication step. The ratio between the irreversible and the reversible Rayleigh coefficients ($\alpha_\varepsilon/\varepsilon_{init}$) before and after annealing, and after removal of the ZnO are compared in Figure 3-12. It was found that the release process itself produced no significant difference in the $\alpha_\varepsilon/\varepsilon_{init}$ ratio, presumably because the domain state was unchanged, as the films were unpoled.

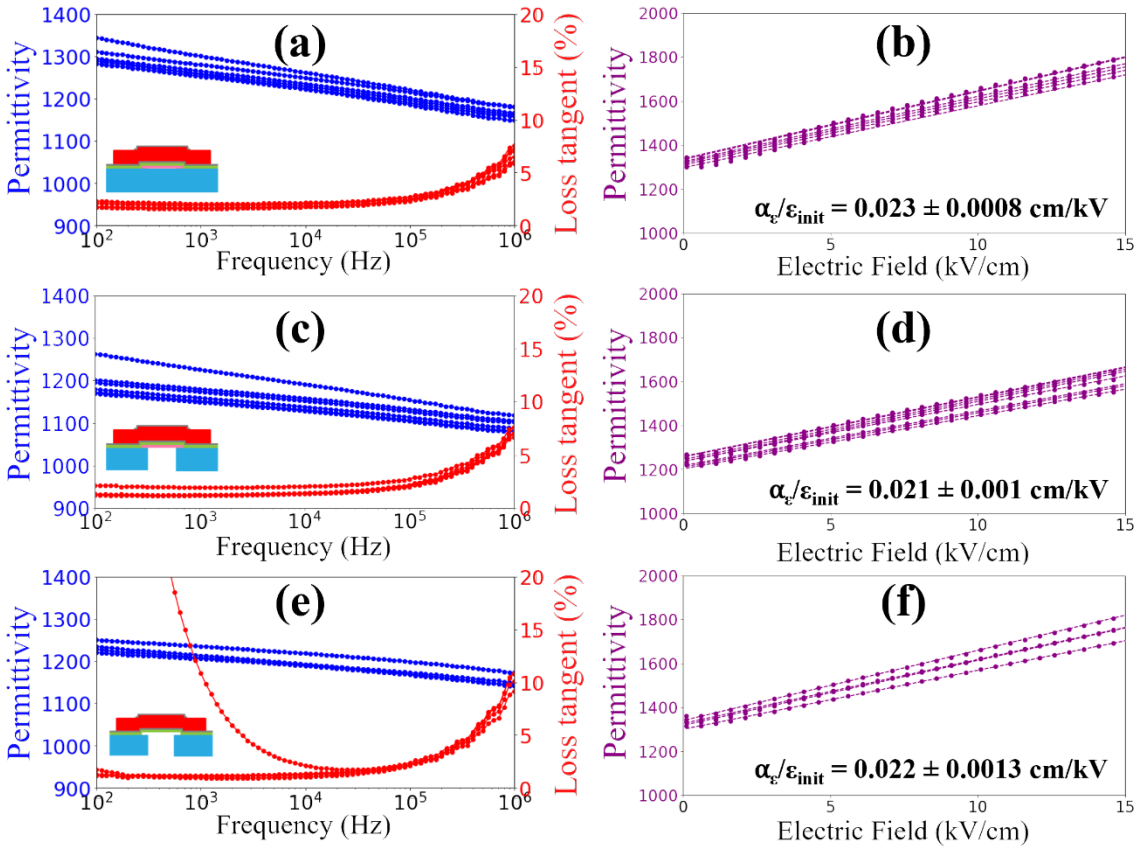

Figure 3-12: Dielectric measurements of unpoled PZT films as the function of frequency and AC field at 1 kHz for (a) – (b) before the DRIE process, (c) – (d) after the DRIE, and (e) – (f) after the ZnO etching.

The large signal unipolar $d^*_{33,f}$ was measured from the average slope of the displacement as a function of unipolar field via interferometry. "Large signal" in this context refers to the fact that the applied field exceeds the coercive field, which in this case the approximately two times the coercive voltage (~ 10 V) unipolar triangular wave at 50 Hz with an average of 200 cycles was applied to the sample [54]. Prior to measurement, the samples underwent poling at 10 V for 20 minutes in two different steps at room temperature, as illustrated in Figure 3-13; the solid lines and dashed lines denote polarization and displacement, respectively. An increasing in maximum displacement before pole and each poling cycle was observed, as shown in Figure 3-13.

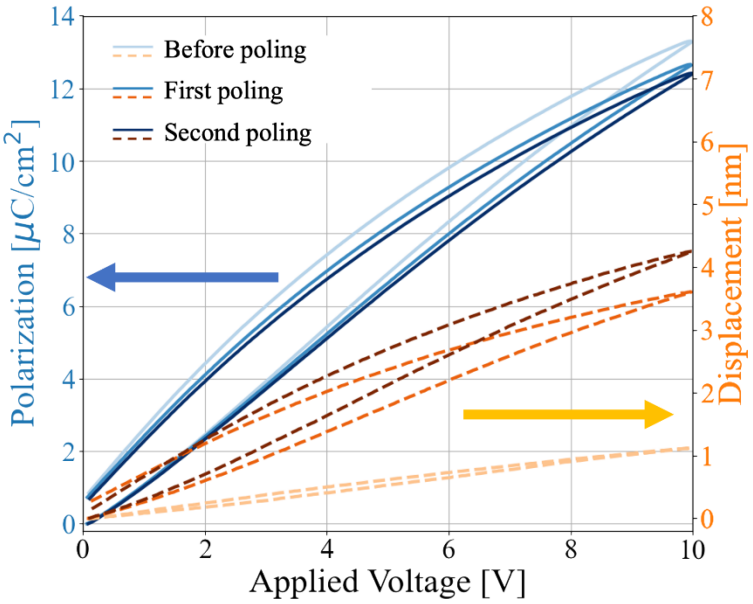

Figure 3-13: DBLI measurement shows progressive increases in field-induced displacement on room temperature poling. The solid lines correspond to the polarization and dashed lines represent displacement.

To elucidate the effect of the release process on the piezoelectric response, samples with 400 µm (50% release) and 600 µm (75% release) ZnO diameters were selected for comparison with the clamped PZT sample with reported $d^*_{33,f}$ being the average of 10 measurements on each sample. The clamped PZT was prepared alongside the other sample but did not undergo backside etching. Note that the sample with partially etched ZnO, as depicted in Figure 3-11(c), was excluded due to the poorly-defined released edge, potentially complicating diaphragm motion. Figure 3-14 presents the measurement results for induced polarization and displacement measured by double-beam interferometry. The $d^*_{33,f}$value for clamped, 50% released sample, and 75% released sample, are 126 ± 12.8 pm/V, 410 ± 5.9 pm/V, and 420 ± 8.1 pm/V, respectively, following poling. Note that to ensure the repeatability of the observed results, the $d^*_{33,f}$ represent an average of 10 different measurements. These data for the clamped sample agree with reported data for clamped PZT thin films [54]. The released PZT samples exhibited significant improvements over the clamped sample, with a greater than 3-fold increase in longitudinal piezoelectric coefficients.

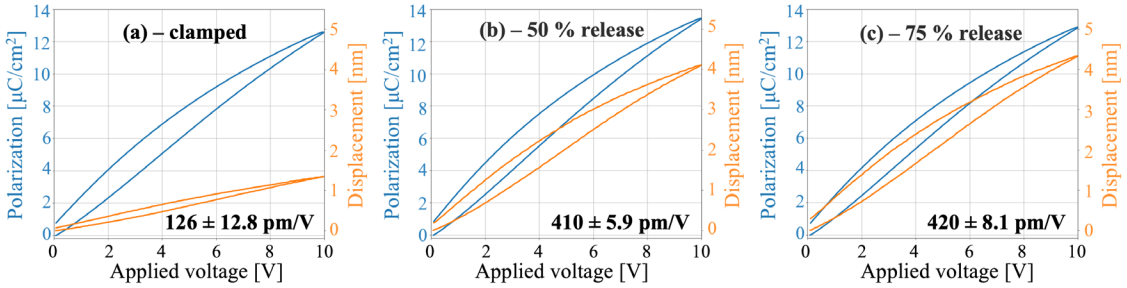

Figure 3-14: The DBLI measurement of the (a) clamped PZT, (b) 50% released PZT, (c) 75% released PZT where the blue and orange lines represent the polarization and displacement, respectively.

There are several factors which could, in principle, contribute to this increase, including **i.** artifacts associated with bending of the thin diaphragms (which can be exacerbated by beam misalignment in a double beam interferometer, and **ii.** an increase in $d_{33,f}^{*}$ due to release from the substrate (including the reduction in residual stress which controls the domain state). The flexural rigidity (D) of the diaphragm is directly proportional to the cube of the material's thickness, as defined by [55]:

$$D = \frac{Eh^3}{12(1-v^2)} \qquad \text{Eq. 8}$$

where E, h, v are Young's modulus, thickness, and Poisson's ratio, respectively. Releasing the underlying layer decreases the PZT diaphragm's rigidity. Additionally, the removal of ZnO may partially alleviate some of the tensile in-plane stress by increasing bending. Some zero-field bending was observed through optical profilometry; this may account for the small increase in $d_{33,f}^{*}$ for the 75% released relative to the 50% released sample. Moreover, removal of the mechanical constraints from the substrate facilitates ferroelastic domain reorientation, as suggested by Wallace *et al.*, [32]. This, in turn, increases both the degree of poling and the extrinsic contributions to the piezoelectric effect. In principle, this could allow $d_{33,f}^{*}$ values for Nb-doped PZT thin films to rival

those of their bulk ceramic counterparts (typical large signal values for d_{33}^* of soft PZT ceramics range from approximately 565 to 880 pC/N, depending on the composition) [56][61].

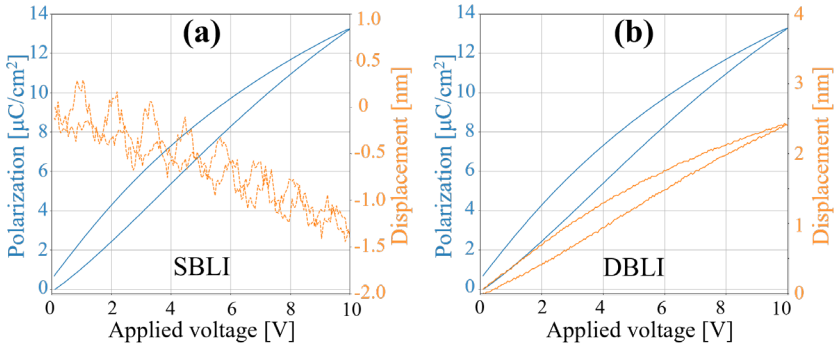

Figure 3-15: Measurements in the (a) single beam and (b) double beam modes on the released PZT thin films.

To assess the possibility of artifacts from field-induced bending as well as to compare to the single surface measurement techniques, the single beam laser interferometry (SBLI) mode on the DBLI system was utilized to capture the magnitude of diaphragm deflection during the excitation. As previously reported by Liu *et al.* [34], the large deflection generated in the fully released membrane on polymeric substrate coupled with finite laser beam misalignment in the DBLI measurement, leading to an incorrect $d_{33,f}^*$ value. With the laser beam probing the center of the top electrode, a 10 V unipolar triangular wave at 200 Hz was applied to the PZT, and the deflection was measured; the result is shown in Figure 3-15(a), along with the double beam mode shown in Figure 3-15(b). The displacement recorded in single beam mode indicated a maximum displacement of 1.4 nm in the negative direction, suggesting a small downward bending of the diaphragm. Conversely, the double beam mode recorded a positive displacement of approximately 2.5 nm. Both deflections are well inside the within the correctable range for the double beam laser interferometer, where the bending effect is neutralized, and the actual thickness expansion is correctly measured. Thus, these measurements of the large signal $d_{33,f}^*$ value using double beam laser interferometry are *quantitative*, for the first time.

Accurate values for thin film piezoelectric coefficients are important to finite element analysis of piezoelectric MEMS devices. In many cases, as the full set of coefficients is not known, values for bulk piezoelectric ceramics are used as approximations. This study presents a means of quantitatively measuring the large signal $d^*_{33,f}$ of thin films which are not fully clamped, and hence which are more germane to those used in bending devices.

3.4 Conclusions

A PZT device structure for effective longitudinal piezoelectric coefficient measurement was proposed, involving a two-step backside releasing process using a ZnO sacrificial layer and DRIE vias. With the designed geometry, the fabricated devices enabled quantitative $d^*_{33,f}$ measurements of 1 μm thick released PZT thin film by using double beam laser interferometry. The clamped $d^*_{33,f}$, established as the baseline for the investigation, was 126 ± 13 pm/V. In comparison, the $d^*_{33,f}$ of the released sample with 50% and 75% of the area released relative to the top electrode were 410 ± 6 pm/V and 420 ± 8 pm/V, respectively. Validation from the single beam interferometry showed that the measured displacement was within the correctable range for the double beam system, revealing the true $d^*_{33,f}$ of the partially released PZT thin film. The observed improvement in the apparent $d^*_{33,f}$ is attributed to the change in diaphragm stress level, the removal of mechanical constraints from the substrate, and enhanced domain wall motion. The finding regarding the $d^*_{33,f}$ is beneficial for accurately simulating piezoMEMS devices, fulfilling the need for precise piezoelectric coefficients. These results are the first quantitative measurement of $d^*_{33,f}$ for unclamped thin films.

Bibliography

[1] S. Trolier-McKinstry and P. Muralt, “Thin Film Piezoelectrics for MEMS,” *J. Electroceram.*, vol. 12, no. 1, pp. 7–17, 2004.

[2] P. Muralt, “PZT Thin Films for Microsensors and Actuators: Where Do We Stand?,” *IEEE Trans. Ultrason. Ferroelectr. Freq. Control*, vol. 47, no. 4, pp. 903–915, 2000.

[3] D. Damjanovic, “Ferroelectric, Dielectric and Piezoelectric Properties of Ferroelectric Thin Films and Ceramics,” *Rep. Prog. Phys.*, vol. 61, no. 9, pp. 1267–1324, 1998.

[4] D. A. Hall, “Review Nonlinearity in Piezoelectric Ceramics,” *J. Mater. Sci.*, vol. 36, no. 19, pp. 4575–4601, 2001.

[5] C. Zhao, D. Hou, C.-C. Chung, H. Zhou, A. Kynast, E. Hennig, W. Liu, S. Li, and J. L. Jones, “Deconvolved Intrinsic and Extrinsic Contributions to Electrostrain in High Performance, Nb-doped $Pb(Zr_xTi_{1-x})O_3$ Piezoceramics ($0.50 \leq x \leq 0.56$),” *Acta. Mater.*, vol. 158, pp. 369–380, 2018.

[6] E. L. Colla, S. Hong, D. V Taylor, A. K. Tagantsev, N. Setter, and K. No, “Direct Observation of Region by Region Suppression of The Switchable Polarization (Fatigue) In $Pb(Zr,Ti)O_3$ Thin Film Capacitors with Pt Electrodes,” *Appl. Phys. Lett.*, vol. 72, no. 21, pp. 2763–2765, 1998.

[7] T. M. Shaw, S. Trolier-McKinstry, and P. C. McIntyre, “The Properties of Ferroelectric Films at Small Dimensions,” *Annu. Rev. Mater. Sci.*, vol. 30, no. 1, pp. 263–298, 2000.

[8] M. M. Saad, D. J. Baxter, J. McAneney, A. Lookman, L. J. Sinnamon, P. Evans, A. Schilling, T. Adams, X. Zhu, R. J. Pollard, R. M. Bowman, J. M. Gregg, D. J. Jung, F. D. Morrison, and J. F. Scott, “Investigating the Effects of Reduced Size on the Properties of Ferroelectrics,” *IEEE Trans. Ultrason. Ferroelectr. Freq. Control*, vol. 53, no. 12, pp. 2208–2225, 2006.

[9] F. Griggio and S. Trolier-McKinstry, “Grain Size Dependence of Properties in Lead Nickel Niobate-Lead Zirconate Titanate Films,” *J. Appl. Phys.*, vol. 107, no. 2, p. 024105, 2010.

[10] G. E. Menk, S. B. Desu, W. Pan, and D. P. Vijay, “Dry Etching Issues in the Integration of Ferroelectric Thin Film Capacitors,” *MRS Online Proc. Libr.*, vol. 433, no. 1, pp. 189–200, 1996.

[11] U. Egger, K. Tomioka, G. Stojakovic, Y. Taniguchi, R. Bruchhaus, H. Zhuang, H. Kanaya, G. Beitel, and S. Sugimoto, “High Temperature Plasma Etching of PZT Capacitor Stacks for High Density FERAMs,” *MRS Online Proc. Libr.*, vol. 748, no. 1, p. 17, 2003.

[12] K. T. Kim, M. G. Kang, and C. Il Kim, "Study on the Etching Damage Characteristics of PZT Thin Films after Etching in Cl-based Plasma," *Microelectron. Eng.*, vol. 71, no. 3-4, pp. 294–300, May 2004.

[13] W. Pan, C. L. Thio, and S. B. Desu, "Reactive Ion Etching Damage to the Electrical Properties of Ferroelectric Thin Films," *J. Mater. Res.*, vol. 13, no. 2, pp. 362–367, Jan. 1998.

[14] S. Trolier-McKinstry, J. F. Shepard, J. L. Lacey, T. Su, G. Zavala, and J. Fendler, "Piezoelectricity in Ferroelectric Thin Films: Domain and Stress Issues," *Ferroelectrics*, vol. 206-207, no. 1-4, pp. 381–392, 1998.

[15] M. D. Nguyen, M. Dekkers, E. Houwman, R. Steenwelle, X. Wan, A. Roelofs, T. Schmitz-Kempen, and G. Rijnders, “Misfit Strain Dependence of Ferroelectric and Piezoelectric Properties of Clamped (001) Epitaxial $Pb(Zr_{0.52},Ti_{0.48})O_3$ Thin Films,” *Appl. Phys. Lett.*, vol. 99, no. 25, p. 252904, 2011.

[16] V. Nagarajan, S. P. Alpay, C. S. Ganpule, B. K. Nagaraj, S. Aggarwal, E. D. Williams, A. L. Roytburd, and R. Ramesh, “Role of Substrate on the Dielectric and Piezoelectric

Behavior of Epitaxial Lead Magnesium Niobate-Lead Titanate Relaxor Thin Films," *Appl. Phys. Lett.*, vol. 77, no. 3, pp. 438–440, 2000.

[17] N. Bassiri-Gharb, I. Fujii, E. Hong, S. Trolier-McKinstry, D. V Taylor, and D. Damjanovic, "Domain Wall Contributions to the Properties of Piezoelectric Thin Films," *J. Electroceram.*, vol. 19, no. 1, pp. 49–67, 2007.

[18] X. H. Du, U. Belegundu, and K. Uchino, "Crystal Orientation Dependence of Piezoelectric Properties in Lead Zirconate Titanate: Theoretical Expectation for Thin Films," *Jpn. J. Appl. Phys.*, vol. 36, no. 9A, pp. 5580–5587, 1997.

[19] X. H. Du, J. Zheng, U. Belegundu, and K. Uchino, "Crystal Orientation Dependence of Piezoelectric Properties of Lead Zirconate Titanate Near the Morphotropic Phase Boundary," *Appl. Phys. Lett.*, vol. 72, no. 19, pp. 2421–2423, 1998.

[20] K. Lefki and G. J. M. Dormans, "Measurement of Piezoelectric Coefficients of Ferroelectric Thin Films," *J. Appl. Phys.*, vol. 76, no. 3, pp. 1764–1767, 1994.

[21] K. Prume, P. Gerber, C. Kugeler, A. Roelofs, U. Bottger, R. Waser, T. Schmitz-Kempen, and S. Tiedke, "Simulation and Measurements of the Piezoelectric Properties Response (d_{33}) of Piezoelectric Layered Thin Film Structures Influenced by the Top-Electrode Size," *14th IEEE International Symposium on Applications of Ferroelectrics*, 2004. ISAF-04. 2004, Montreal, Que., Canada, 2004, pp. 7-10.

[22] S. Sivaramakrishnan, P. Mardilovich, A. Mason, A. Roelofs, T. Schmitz-Kempen, and S. Tiedke, "Electrode Size Dependence of Piezoelectric Response of Lead Zirconate Titanate Thin Films Measured by Double Beam Laser Interferometry," *Appl. Phys. Lett.*, vol. 103, no. 13, p. 132904, 2013.

[23] R. Wilke, R. L. Johnson-Wilke, V. Cotroneo, S. McMuldroch, P. B. Reid, D. A. Schwartz, and S. Trolier-McKinstry, "Fabrication of Adjustable Cylindrical Mirror Segments for the

SMART-X Telescope," *IEEE Trans. Ultrason. Ferroelectr. Freq. Control*, vol. 61, no. 8, pp. 1386–1392, 2014.

[24] S. Shetty, J. I. Yang, J. Stitt, and S. Trolier-McKinstry, "Quantitative and High Spatial Resolution d_{33} Measurement of Piezoelectric Bulk and Thin Films," *J. Appl. Phys.*, vol. 118, no. 17, p. 174104, 2015.

[25] Q. M. Zhang, W. Y. Pan, and L. E. Cross, "Laser Interferometer for the Study of Piezoelectric and Electrostrictive Strains," *J. Appl. Phys.*, vol. 63, no. 8, pp. 2492–2496, 1988.

[26] aixACCT Systems GmbH, *aixDBLI: Semi-Automatic Double Beam Laser Interferometer, Research Line, Version 3.5*, Aachen, Germany: aixACCT Systems GmbH, 2014.

[27] W. Y. Pan and L. E. Cross, "A Sensitive Double Beam Laser Interferometer for Studying High-Frequency Piezoelectric and Electrostrictive Strains," *Rev. Sci. Instrum.*, vol. 60, no. 8, pp. 2701–2705, 1989.

[28] W. Y. Pan, H. Wang, L. E. Cross, and B. R. Li, "Double Beam Laser Interferometer Measurements of Surface Displacements at The Resonance Frequencies of PZT Piezoelectric Ceramic Resonators," *Ferroelectrics*, vol. 120, no. 1, pp. 231–239, 1991.

[29] A. L. Kholkin, C. Wütchrich, D. V. Taylor, and N. Setter, "Interferometric Measurements of Electric Field-Induced Displacements in Piezoelectric Thin Films," *Rev. Sci. Instrum.*, vol. 67, no. 5, pp. 1935–1941, 1996.

[30] S. Bühlmann, B. Dwir, J. Baborowski, and P. Muralt, "Size-Effect in Mesoscopic Epitaxial Ferroelectric Structures: Increase of Piezoelectric Response with Decreasing Feature-Size," *Integr. Ferroelectr.*, vol. 50, no. 1, pp. 261–267, 2010.

[31] F. Griggio, S. Jesse, A. Kumar, O. Ovchinnikov, H. Kim, T. N. Jackson, D. Damjanovic, S. V. Kalinin, and S. Trolier-McKinstry, "Substrate Clamping Effects on Irreversible Domain

Wall Dynamics in Lead Zirconate Titanate Thin Films," *Phys. Rev. Lett.*, vol. 108, no. 15, p. 157604, 2012.

[32] M. Wallace, R. L. Johnson-Wilke, G. Esteves, C. M. Fancher, R. H. T. Wilke, J. L. Jones, and S. Trolier-McKinstry, "In Situ Measurement of Increased Ferroelectric/Ferroelastic Domain Wall Motion in Declamped Tetragonal Lead Zirconate Titanate Thin Films," *J. Appl. Phys.*, vol. 117, no. 5, p. 54103, 2015.

[33] T. Liu, M. Wallace, S. Trolier-McKinstry, and T. N. Jackson, "High-Temperature Crystallized Thin-Film PZT on Thin Polyimide Substrates," *J. Appl. Phys.*, vol. 122, no. 16, p. 164103, 2017.

[34] T. Liu, P. Tipsawat, W. Zhu, T. N. Jackson, M. Sivaramakrishnan, P. Mardilovich, T. Schmitz-Kempen, and S. Trolier-McKinstry, "Challenges in Double-Beam Laser Interferometry Measurements of Fully Released Piezoelectric Films," *J. Appl. Phys.*, vol. 131, no. 21, p. 214102, 2022.

[35] T. Liu, J. Nyeon Kim, S.-R. Kothapalli, K. Choi, S. Trolier-McKinstry, and T. Jackson, "Flexible Thin-Film PZT Ultrasonic Transducers on Polyimide Substrates," *Sensors*, vol. 21, no. 3, p. 1014, 2021.

[36] J. C. Woo, G. H. Kim, J. G. Kim, and C. I. Kim, "Etching Characteristic of ZnO Thin Films in an Inductively Coupled Plasma," *Surf. Coat. Technol.*, vol. 202, no. 22–23, pp. 5705–5708, 2008.

[37] A. Gwiazda, A. Rumyantseva, A. Gokarna, K. Nomenyo, C. Chevalier-César, and G. Lérondel, "Simple and Versatile High Aspect Ratio Nanostructuring via Zinc Oxide Masking," *Adv. Mater. Technol.*, vol. 2, no. 9, p. 1700107, 2017.

[38] S. Lee, T. N. Walter, S. E. Mohney, and T. N. Jackson, "High-Temperature-Capable ALD-based Inorganic Lift-Off Process," *Mater Sci Semicond Process*, vol. 130, p. 105809, 2021.

[39] W. Kern, "The Evolution of Silicon Wafer Cleaning Technology," *J. Electrochem. Soc.*, vol. 137, no. 6, p. 1887, 1990.

[40] M. Drost, S. Marschmeyer, M. Fraschke, O. Fursenko, F. Bärwolf, I. Costina, M. K. Mahadevaiah, and M. Lisker, "Etch Mechanism of an Al_2O_3 Hard Mask in the Bosch Process," *Micro Nano Eng.*, vol. 14, p. 100102, 2022.

[41] M. D. Henry, S. Walavalkar, A. Homyk, and A. Scherer, "Alumina Etch Masks for Fabrication of High-Aspect-Ratio Silicon Micropillars and Nanopillars," *Nanotechnology*, vol. 20, no. 25, p. 255305, 2009.

[42] S. H. K. Park, C. S. Hwang, H. S. Kwack, J. H. Lee, and H. Y. Chu, "Characteristics of ZnO Thin Films by Means of Plasma-Enhanced Atomic Layer Deposition," *Electrochem. Solid-State Lett.*, vol. 9, no. 10, p. G299, 2006.

[43] D. A. Mourey, D. A. Zhao, J. Sun, and T. N. Jackson, "Fast PEALD ZnO Thin-Film Transistor Circuits," *IEEE Trans. Electron Devices*, vol. 57, no. 2, pp. 530–534, 2010.

[44] C. Y. Cheng, A. Dangi, L. Ren, S. Tiwari, R. R. Benoit, Y. Qiu, H. S. Lay, S. Agrawal, R. Pratap, S.-R. Kothapalli, T. E. Mallouk, S. Cochran, and S. Trolier-McKinstry, "Thin Film PZT-based PMUT Arrays for Deterministic Particle Manipulation," *IEEE Trans. Ultrason. Ferroelectr. Freq. Control*, vol. 66, no. 10, pp. 1605–1615, 2019.

[45] Toshihiko Tani, Charles D. E. Lakeman, Jie-Fang Li, Zhengkui Xu, and David A. Payne, "Crystallization Behavior and Improved Properties for Sol-Gel Derived PZT and PLZT Thin Layers Processed with a Lead Oxide Cover Coating," *Ferroic Materials*, vol. 43, p. 89, 1994.

[46] O. Beldarrain, M. Duch, M. Zabala, J. M. Rafí, M. B. González, and F. Campabadal, "Blistering of Atomic Layer Deposition Al_2O_3 Layers Grown on Silicon and its Effect on Metal–Insulator–Semiconductor Structures," *J. Vac. Sci. Technol. A*, vol. 31, no. 1, 2013.

[47] M. Broas, H. Jiang, A. Graff, T. Sajavaara, V. Vuorinen, and M. Paulasto-Kröckel, “Blistering Mechanisms of Atomic-Layer-Deposited AlN and Al_2O_3 Films,” *Appl. Phys. Lett.*, vol. 111, no. 14, p. 141606, 2017.

[48] M. Broas, O. Kanninen, V. Vuorinen, M. Tilli, and M. Paulasto-Kröckel, “Chemically Stable Atomic-Layer-Deposited Al_2O_3 Films for Processability,” *ACS Omega*, vol. 2, no. 7, pp. 3390–3398, 2017.

[49] O. Lehar, M. A. Spak, S. Meyer, R. R. Dammel, C. J. Brodsky, and C. G. Willson, “Resist Rehydration During Thick Film Processing,” *Adv. Resist Technol. Process. XVIII*, vol. 4345, no. 24, pp. 463–474, 2001.

[50] **ASTM E112-13**: "Standard Test Methods for Determining Average Grain Size," ASTM International, West Conshohocken, PA, 2013

[51] Y. W. Jang, S. Bang, H. Jeon, and J. Y. Lee, “Role of Post Annealing Temperature on the Microstructure of Al_2O_3/ZnO Thin Films Grown by Atomic Layer Deposition for TFT Applications,” *Phys. Status Solidi A*, vol. 207, no. 9, pp. 2185–2189, 2010.

[52] C. H. Ahn, S. H. Kim, Y. K. Kim, H. S. Lee, and H. K. Cho, “Effect of Post-Annealing Temperatures on Thin-Film Transistors with ZnO/Al_2O_3 Superlattice Channels,” *Thin Solid Films*, vol. 584, pp. 336–340, 2015.

[53] A. Zolotaryov, S. Goetze, R. Zierold, D. Novikov, B. Birajdar, D. Hesse, and K. Nielsch, “Temperature-Dependent Solid-State Reactions with and without Kirkendall Effect in Al_2O_3/ZnO, Fe_2O_3/ZnO, and Co_XO_Y/ZnO Oxide Thin Film Systems,” *Adv Eng Mater*, vol. 12, no. 6, pp. 509–516, 2010.

[54] T. Schmitz-Kempen, S. Tiedke, P. Mardilovich, S. Sivaramakrishnan, T. Lisec, F. Stoppel, S. Trolier-McKinstry, and P. Muralt, "Comparable Measurements and Modeling of Piezoelectric Thin Films for MEMS Application," *2013 Joint IEEE International*

Symposium on Applications of Ferroelectric and Workshop on Piezoresponse Force Microscopy (ISAF/PFM), Prague, Czech Republic, 2013, pp. 211-213.

[55] F. Bitsie, W. P. Eaton, D. W. Plummer, and J. H. Smith, "A New Analytical Solution for Diaphragm Deflection and its Application to a Surface-Micromachined Pressure Sensor," *Proc. Int. Conf. Modeling Simulation Microsyst.*, pp. 1-4, 1999.

[56] D. Zhou, M. Kamlah, and D. Munz, "Uniaxial Compressive Stress Dependence of the High-Field Dielectric and Piezoelectric Performance of Soft PZT Piezoceramics," *J. Mater. Res.*, vol. 19, no. 3, pp. 834–842, 2004.

[57] A. J. Masys, W. Ren, G. Yang, and B. K. Mukherjee, "Piezoelectric Strain in Lead Zirconate Titanate Ceramics as a Function of Electric Field, Frequency, and DC Bias," *J. Appl. Phys.*, vol. 94, no. 2, pp. 1155–1162, 2003.

[58] D. Zhou, M. Kamlah, and D. Munz, "Effects of Uniaxial Prestress on the Ferroelectric Hysteretic Response of Soft PZT," *J. Eur. Ceram. Soc.*, vol. 25, no. 4, pp. 425–432, 2004.

[59] S. Kong, C. Hong, W. Zhang, Y. Liu, Z. Wang, X. Yang, R. Su, X. Long, and C. He, "Performance Enhancement of Soft-PZT5 Piezoelectric Ceramics using poling Technique," *J. Am. Ceram. Soc.*, vol. 105, no. 7, pp. 4744–4750, 2022.

[60] L. Burianova, P. Hana, M. Pustka, M. Prokopova, and J. Nosek, "Nonlinear Properties of PZT Ceramics in the Wide Temperature Range," *Elecroceramics IX*, vol. 25, no. 12, pp. 2405–2409, 2005.

[61] M. Algueró, B. L. Cheng, F. Guiu, M. J. Reece, M. Poole, and N. Alford, "Degradation of the d_{33} Piezoelectric Coefficient for PZT Ceramics under Static and Cyclic Compressive Loading," *J. Eur. Ceram. Soc.*, vol. 21, no. 10, pp. 1437–1440, 2001.

Chapter 4

32 Element Piezoelectric Micromachined Ultrasound Transducer Phased Array for Neuromodulation

This chapter discusses using partially released PZT thin films in a PMUT phased array for a neuromodulation application. The film was fabricated into individual rectangular elements with an electrode design with three parallel fingers. The phased array was composed of a 32 element PMUT, driven to achieve maximum output and produce low-intensity focused ultrasound stimulation (LIFUS).

4.1 Introduction

Low intensity transcranial focused ultrasound stimulation (tFUS) is a promising approach in noninvasive neuromodulation treatment; its millimeter spatial resolution is smaller than modalities such as transcranial magnetic, direct current, or alternating current stimulation [1] – [3]. Multifarious therapeutic applications of tFUS in animal models such as mice, rats, sheep, and nonhuman primates have been reported over the past decade, most of which target fundamental neuroscience studies [4] – [14]. This was followed by a recent surge in application of tFUS neuromodulation in human subjects, largely for clinical neuroscience studies [15] – [24]. Moreover, tFUS has already been associated with other extant imaging technologies, such as magnetic resonance imaging (MRI) or brightness mode (B-mode) ultrasound imaging which promise further improvement in the accuracy of neuromodulation in both basic and clinical neuroscience applications [1], [7].

Conventionally, tFUS experiments utilize single element ultrasound (US) transducers with a relatively large diameter (tens of millimeters) and a fixed focal spot. A precise manipulator is required to mechanically alter the focal spot to stimulate different brain regions, which is a major shortcoming of conventional tFUS systems. However, this limitation can be overcome by leveraging the electronic beam focusing and steering capabilities of optimally designed US phased arrays. In particular, a US phased array enables electronically controllable stimulation over a large tissue volume, i.e., large-scale stimulation.

As depicted in Figure 4-1, the acoustic beam profile of a single element US can be distinguished into near field (Fresnel) and far field (Fraunhofer) zones [25]. In the region near the transducer, the Fresnel zone, the acoustic profile may be complicated, and intensity can vary significantly since the waves have not yet converged. The length of the near field zone can be defined by:

$$F = {D^2}/{4\lambda} \qquad \text{Eq. 1}$$

where D is the transducer aperture and λ is the wavelength of the sound wave. The focal point, depicted in Figure 4-1 as the maximum acoustic intensity point, is the distance where the sound waves converge, and the cross-section of the ultrasound beam becomes smallest. Farther away from the focal point, the waves begin to diverge and spread out. In this area, the intensity generally decreases with distance in a more predictable manner than in the near field.

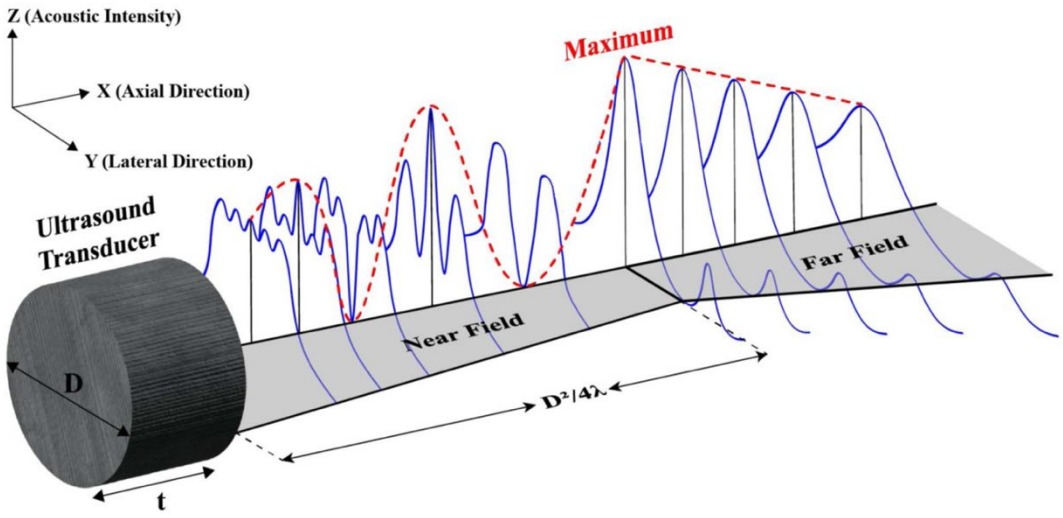

Figure 4-1: The acoustic beam profile generated from a flat unfocused transducer, reproduced from [26].

As mentioned above, to overcome the limitations of a single element US transducer, an array of US transducers can be operated as a phased array by controlling the timing (phase) used to drive each element to form constructive interference at the focal point. A linear phased array consists of a number of transducers (*N*) with identical geometry and interelement spacing (d). To achieve beam formation and acoustic wave steering from a multi-element phased array, the time delay for each element (Δt_n) for the n^{th} element can be calculated as: [27]

$$\Delta t_n = \left({}^{F}/_{c}\right)\left(1 - \sqrt{1 + \left({}^{nd}/_{F}\right)^2 - {}^{2ndsin(\theta_s)}/_{F}}\right) + t_0 \qquad \text{Eq. 2}$$

where F is the focal distance, c is the speed of sound, n is the element number in the phased array, θ_s is the steering angle, and t_0 is the time delay offset. It is important to note that the acoustic wave formed by the phased array gives rise to side/grating lobes. This is crucial to neuromodulation applications, as these lobes could damage off-target areas.

To analyze the beam directivity profile, the directivity function $H(\theta)$, as proposed by Von Ramm [28], quantifies the peak pressure produced by the N element phased array at an angle θ relative to the steering angle θ_s:

$$H(\theta) = \left| \frac{\sin\left[{}^{\pi\,\mathrm{asin}(\theta)}/_{\lambda}\right] \cdot \sin\left[\left(\pi d \left({}^{\sin(\theta_s) - \sin(\theta)}/_{\lambda}\right) N\right]\right.}{{}^{\pi\,\mathrm{asin}(\theta)}/_{\lambda} \cdot N sin[(\pi d({}^{\sin(\theta_s) - \sin(\theta)}/_{\lambda}))]} \right| \quad \text{Eq. 3}$$

This implies that directivity is dependent on the array geometry, where the side/grating lobes are minimized by reducing the $H(\theta)$. Increasing the interelement spacing (a larger d) can amplify the side/grating lobes. The optimal d_{max} for an N element phased array at steering angle θ_s is defined by: [28]

$$d_{max} = \lambda/(1 + sin\theta_s) \cdot (N - 1)/N \quad \text{Eq. 4}$$

This suggests that in a large array ($< N$) with a steering angle = 90°, the d_{max} should be ${}^{\lambda}/_{2}$ to minimize side/grating lobes which are undesirable for neuromodulation applications.

In recent years, several US phased array transducers designed for tFUS have been reported in the literature, especially diced ceramic transducers and capacitive micromachined ultrasound transducers (CMUTs). For example, a ring-shaped 32-element US phased array (CMUT) operating at 80 V_{DC} with a 100 V_{DC} offset at 183 kHz yielded a maximum 52 kPa pressure and generated a spatial-peak temporal-average acoustic intensity (I_{spta}) of ~55.4 mW/cm^2. The CMUT successfully stimulated motor cortical areas in freely moving mice [29]. A wearable 2D array device (CMUT) integrated with a complementary metal-oxide semiconductor (CMOS) chip was developed [30] which generated an acoustic pressure output of ~575 kPa while operating at 2 MHz with 60 V_{DC}. A 26×26 2D phased array using 267 μm thick PZT-5A piezoelectric ceramics as transducers was fabricated on a CMOS chip; it delivered an acoustic pressure of 40 kPa at 5 V excitation at 8.4 MHz [31]. Moreover, a relatively thin bulk PZT transducer was presented in [32] where the 16-

element array, with a 40 μm thick PZT layer on a silicon insulator (SOI) wafer, achieved a peak intensity up to 1.1 W/cm^2 with an input of 66 V.

Piezoelectric micromachined ultrasound transducers (PMUT) offer advantages in device miniaturization, high bandwidth and sensitivity, and compatibility with the front-end electronic integration [33]. However, the use of thin film PMUTs for tFUS applications has not yet been reported. A design methodology for geometry optimization for large-scale US neuromodulation has been proposed in [34]. The design method maximizes a figure of merit (FoM) that simultaneously considers the total input power required to embed the array, the peak pressure engendered at the focal spot, and the overall focal volume defined by the half power beam width. In brief, the figure of merit (FoM) is defined as:

$$FoM = P/(\sqrt{N \cdot a \cdot L} \cdot \sqrt[3]{V}) \quad \text{Eq. 4}$$

where P is the spatial peak US pressure output (for the same voltage amplitude across each element), a is the element width, L is the element length, and V is the half-power-beam-width focal volume at the focal spot. It is worth mentioning that N, a, and L have been included in the FoM to account for a constant total input power to the array as they are swept during the optimization. The described design methodology balances among the input power, the generated pressure, and the spatial resolution, thereby leading to an optimally performing phased array design. A 16-element linear phased array transducer at 833.3 kHz was fabricated using bulk PZT, outputting 1.15 MPa peak pressure within a beam having a lateral resolution of 1.6 mm at 12 mm focal distance with a 150 V_{pp} excitation voltage [34].

In this chapter, a comparable design methodology for phased array transducers was applied to PMUT with a 1.5 μm thick PZT thin film. It was specifically intended to be driven by relatively lower voltages < 20 V, while generating an acoustic pressure comparable to that of bulk $Pb(Zr,Ti)O_3$ arrays with a comparable input power consumption. An US PMUT array operating in the bending mode was designed, fabricated, and characterized for the neuromodulation application.

4.2 PMUT Array Design

Based on the design procedure presented in [34], the geometries including element length (L) element pitch (d), element width (a), and the number of elements (N) of an US phased array were optimized using k-Wave, an open-source MATLAB toolbox. Since the element thickness is not considered in k-Wave, the optimization process for a bulk array in [34] is applicable for the 2D geometry optimization of the PMUT array. The array was designed for a tFUS of a rat's brain with high FoM while having the least off target stimulation effects. For this design, the following assumptions were made: 1) the array aperture (D) and element length (L) were limited by the nominal dimensions of a rat's head (D_{max} = L_{max} = 25 mm); 2) the focal distance (F) was set to coincide with the depth between the standard depth of a rat's brain (F_{max} = 25 mm) [35]; 3) the excitation frequency (f) was set to ~ 1 MHz frequency US penetrating the scalp, skull, and brain tissue [36]; 4) the maximum steering angle $\theta_{s,max}$ was ± 60°; 5) the minimum kerf of 96.5 μm (λ/16, where λ is the wavelength) was set as the grid resolution of the k-Wave simulations; 6) $H(y)$ < 0.7, where $H(y)$ is an equivalent to the directivity function defined as the ratio of the peak output pressure and occurred on a line parallel to the *x*-axis (which corresponds to different y values when z = 0 in Figure 4-1) to the peak output pressure at the focal spot (which corresponds to a single point in the whole *xy* plane) [34]. Since the US beam area is defined by half of the maximum power, which corresponds to -0.7 of peak pressure, a threshold of 0.7 is reasonable for $H(y)$.

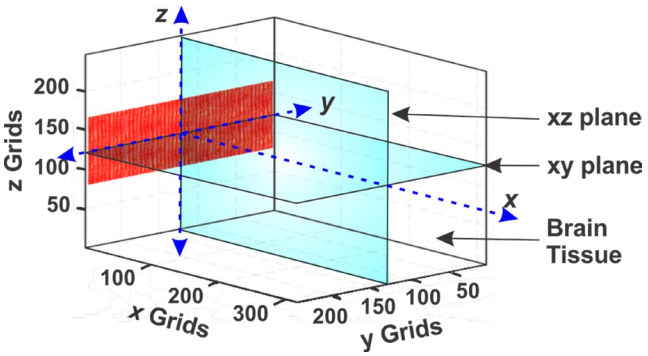

Figure 4-2: A linear transducer positioned in a 3D grid space defined in k-Wave. The *xy* and *xz* planes are defined as sensors. The medium has properties like brain tissue.

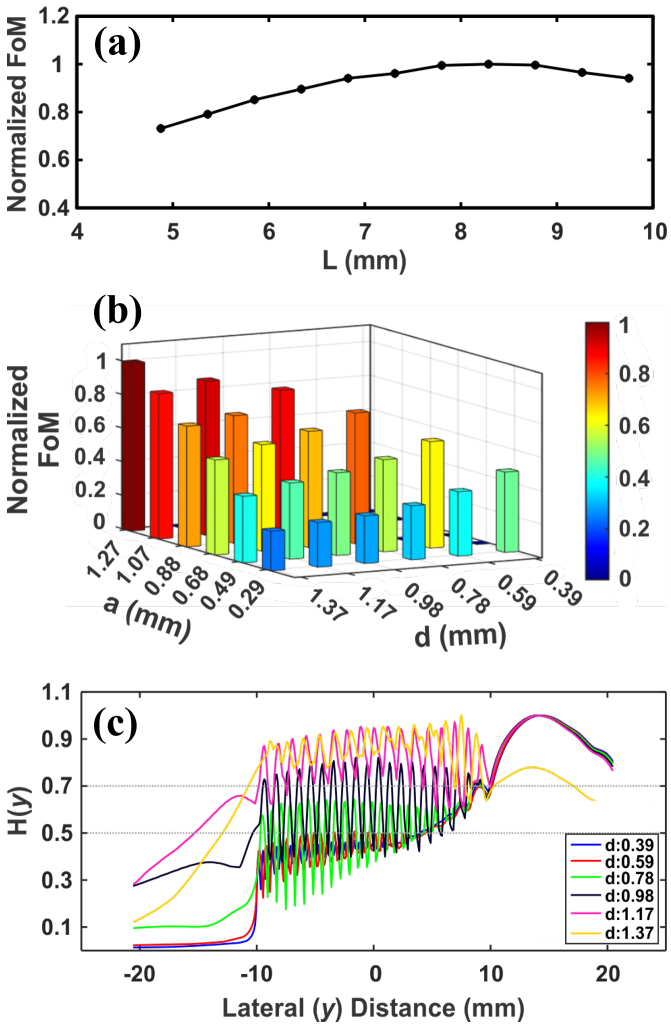

Figure 4-3: Optimization results for the phased array targeting F = 20 mm and $H(y) < 0.7$ at θ_s = 60°. (a) First iteration showing the normalized Figure of Merit (FoM) vs. L. (b) First iteration showing the normalized FoM vs d and a. (c) $H(y)$ at different d (with the optimum a).

Figure 4-2 shows the 3D k-Wave simulation setup with a 314 × 314 × 64 grid space having the properties of brain tissue. The spatial and temporal grid resolutions were set to 96.5 μm (1/16 and 18.75 ns (determined by the time needed to travel the diagonal of the grid space). To eliminate artifacts due to reflections from the grid boundaries, a perfect matching layer (PML) of 0.48 mm thickness was added to the boundaries. The sound speed, mass density, and the attenuation coefficients were set based on [37]. Each simulation took ~ 92 minutes on a regular desktop.

Figure 4-3 demonstrates the results acquired by implementing the optimization method described in [34]. Setting the initial values of the interelement spacing, $d = \lambda/2 = 0.78$ mm, and the element width, $a = d/2 = 0.385$ mm, the element length was optimized for the maximum FoM. The optimum value of L was found to be 8.3 mm, as shown in Figure 4-3(a). Next, d and a were simultaneously swept to maximize the FoM with the optimum L. Figure 4-3(b) depicts a 3D plot of normalized FoM as a function of d and a. The highest FoM was found at $d = 1.37$ mm with $a = 1.27$ mm. However, there was a trade-off between having a larger d and steering the beam with smaller grating/side lobes (i.e., the focused beam at $F = 20$ mm could yield $\theta_{s,max} = 60°$). Figure 4-3(b) shows that a larger d (having a larger a) tends to maximize the FoM while Figure 4-3(c) demonstrates that d should be limited by a threshold based on $H(y)$. One should note that $H(y)$ is equivalent to the directivity function (which should be considered to either avoid off-target stimulation or keep it under a particular threshold). It is worth mentioning that L, a, and d are the independent sweeping parameters, whereas N and D are dependent on d with the relation of $D = N \times d$ – kerf. The optimization of N and D as dependent parameters has been discussed in detail in [34]. By applying the iterative optimization procedure, the optimum array geometries were found to be $L = 8.3$ mm, $d = 0.78$ mm, $a = 0.68$ mm, and $N = 32$.

Table 4-1 summarizes the optimum design parameters achieved by the iterative method as well as the geometry of the fabricated array side by side. With the optimum array geometry, the

beam steering capability (at F = 20 mm with θ_s of -60° to 60°) of the array has been checked in simulations as depicted in Figure 4-4.

Table 4-1: Optimized design parameters.

Parameters	Optimized US Array	Fabricated US Array
Sonication Frequency, f (MHz)	1	1.4
Target Focal Distance, F (mm)	20	20
Number of US Elements, N	32	32
US Array Aperture, D (mm)	24.9	~25.3
US Element Length, L (mm)	8.3	~8.3
US Element Width, a (μm)	680	~521
US Interelement Spacing, d (mm)	0.78	~0.795
Steering Angle, θ_s (deg)	±60	±60
Kerf, *kerf* (μm)	96.5	~272

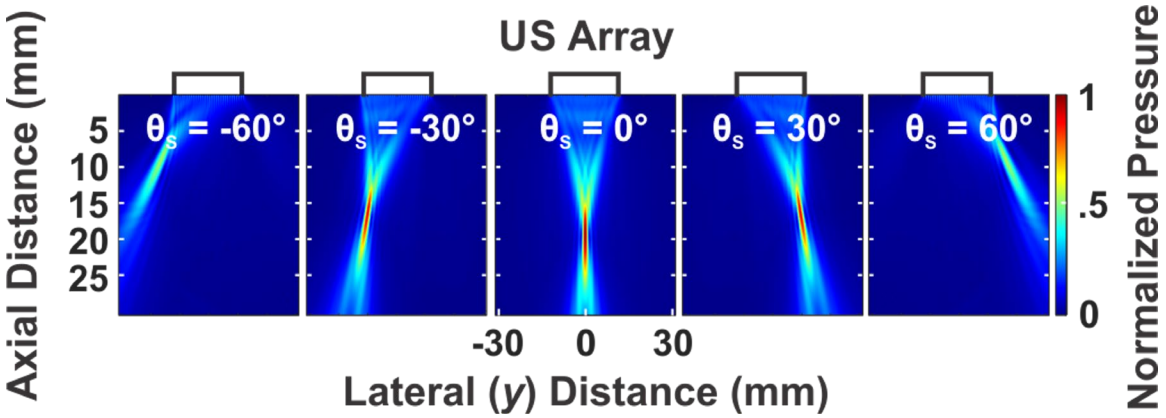

Figure 4-4: Simulated beam steering capability of the optimum array in Table 4-1.

Furthermore, an analytical method was used to design the active PMUT resonator area defined by the silicon etch trench through the Si handle wafer. The fundamental frequency of a clamped rectangular plate is given by: [38]

$$2\pi f_r = \left(\frac{1}{L^2} + \frac{1}{a^2}\right) \cdot \sqrt{\frac{D_r(E,\nu)}{\rho_i t_i}} \qquad \text{Eq. 2}$$

where L and a are the length and width of the rectangular plate, D_r is the flexural rigidity, ρ_i is the density of the i^{th} layer of a thin film stack, and t_i is the thickness of the i^{th} layer. The thin film stack consisted of the buried oxide (SiO_2) layer, Si layer, thermally deposited SiO_2, and the piezoelectric stack: TiO_2/Pt as a bottom electrode, PZT, and Ti/Pt as a top electrode. To achieve 1 MHz resonant frequency in water, a rectangular plate of 8000 µm in length and 130 µm in width with a 2 µm thick silicon layer were selected.

Then, the individual PMUT element was designed by combining two approaches. The PZT bar dimension was based on the 8.3 × 0.78 mm dimension found from the design methodology above, while the active piezoelectric area was defined by the trench dimension calculated analytically to be ~ 8000 × 130 µm. Since the trench area is relatively smaller than the PZT bar, three parallel trenches were fitted into the single element to maximize the output power. The fabricated PMUT phased array and device schematic are depicted in Figure 4-5.

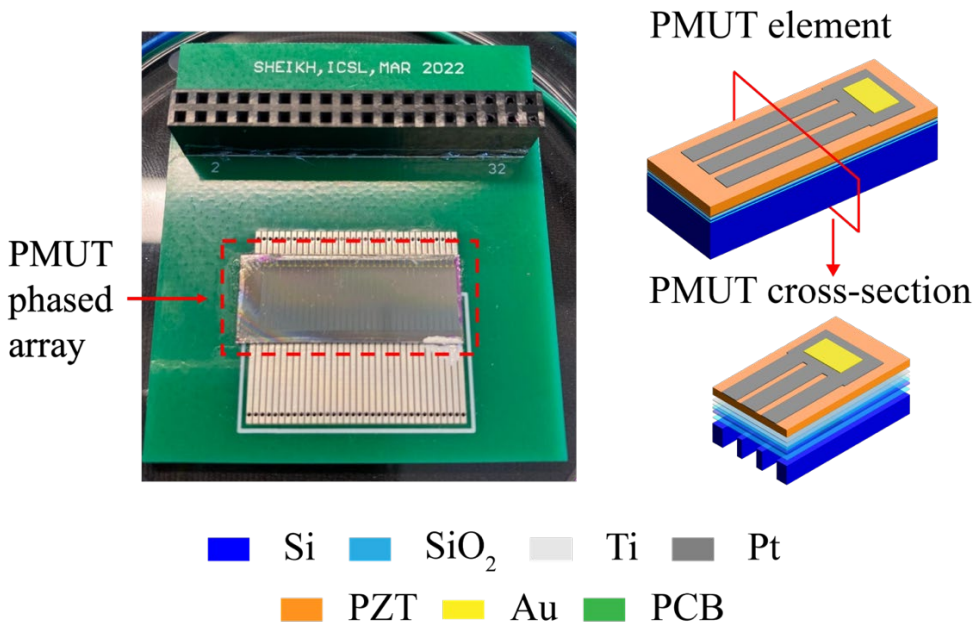

Figure 4-5: The schematic (Left) shows the overview of the phased array and (Right) illustrates a single element of the PMUT with three parallel electrodes and backside trenches.

4.3 PMUT Fabrication and Characterization

4.3.1 Fabrication

The microfabrication process flow used to fabricate the PMUT is illustrated in Figure 4-6; it is similar to that previously reported [39]. Each individual element was patterned into a 8570 × 682 µm PZT resonator bar with three parallel released trenches of 130 µm width with 60% top electrode coverage [40] – [42]. The element pitch was $\lambda/2$ (780 µm). The fabrication was based on a silicon on insulator (SOI) wafer with a 2 µm Si device thickness, 3 µm buried oxide layer and 400 µm handle thickness (Ultrasil Corp., CA, USA). The SOI wafer was coated with 560 nm SiO_2 by wet thermal oxidation on both sides.

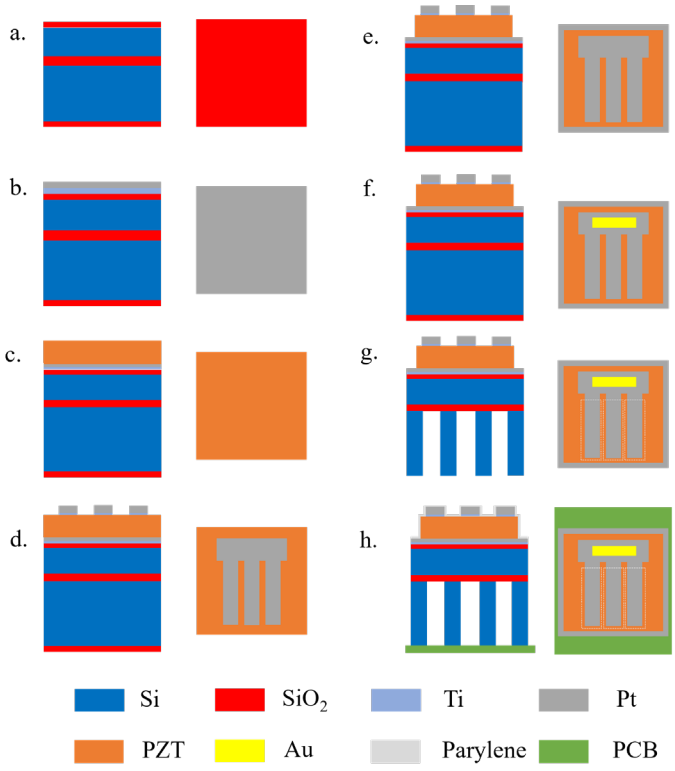

Figure 4-6: Schematic process flow for PMUT fabrication, a) SOI substrate with 2 µm of silicon on the device side, b) bottom electrode deposition, c) PZT spin coating, d) top electrode deposition and patterning, e) PZT patterning, f) contact pad deposition and patterning, g) back side silicon trench etching, and h) PCB mounting, wire bonding, and waterproofing with a polymer coating.

Highly {111} oriented Pt bottom electrodes were prepared as described by [43]. Prior to the bottom electrode deposition, the sputter system (Kurt J. Lesker CMS18 system) was pre-conditioned by depositing Ti for 20 minutes to reduce adventitious O_2 from the deposition chamber. The process began with the deposition of 30 nm of Ti by DC sputtered at room temperature with 200 W DC power at 2 mTorr. After that, the samples were annealed by rapid thermal annealing (RTA) with 10 slpm O_2 atmosphere at 700 °C for 15 minutes to form TiO_2. The high temperature Pt was DC sputter deposited in the same system at a substrate temperature set at 600°C stabilized for 1 hour before deposition. Then, the deposition was performed with 200 W DC power at 2.5 mTorr.

Chemical solution deposition (CSD) with the sol-gel method was utilized to prepare Nb-doped PZT thin films. The 2-methoxy ethanol (2-MOE) solution was first proposed by Budd *et al.* in 1986 for $PbTiO_3$ thin films and later modified by Dey *et al.* in 1985. It was later adopted by Wolf *et al.* at Pennsylvania State University [44-46].

Figure 4-7 outlines the process flow for 2MOE sol-gel solution for a 60 mL of a 0.4 M 2 mol.% Nb doped $Pb(Zr_{0.52}Ti_{0.48})TiO_3$ solution with 10% Pb excess for sol-gel deposition. The preparation begins with adding 9.923 g of lead acetate trihydrate to 60 mL 2-MOE, mixing the mixture in a rotary evaporator flask at 115ºC under the constant flow of Ar, and refluxing for 1 hour, followed by distillation. The other precursors, 5.723 g of zirconium (IV) n-propoxide, 3.308 g of titanium (IV) isopropoxide and 0.153 g of Niobium (V) ethoxide, are mixed with 30 mL of 2-MOE in an Erlenmeyer flask inside a glovebox, sealed, and mixed for 30 minutes. The mixture is then combined with the dried lead precursor after the distillation, then refluxed under constant Ar flow for 2 hours at 115ºC. After that, the mixture was distilled to 47 mL and cooled to room temperature. The final step is to add 13 mL of acetylacetone, a chelating agent, to the prepared solution, followed by a reflux at room temperature for 30 minutes.

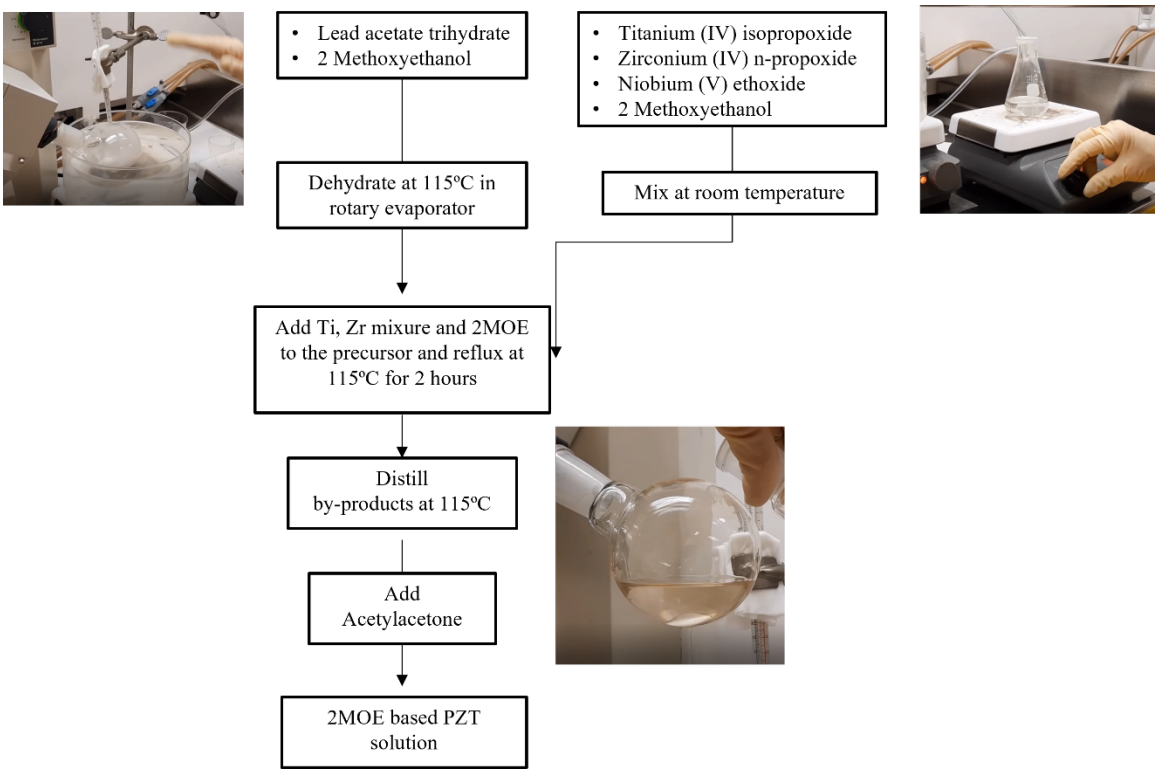

Figure 4-7: The process flow of 2-MOE sol-gel solution for PZT spin coating.

Due to the volatilization of PbO during crystallization, an additional layer is applied intermittently to compensate for the Pb-deficient pyrochlore/fluorite phase [47]. To prepare a 0.08 M PbO solution, a similar process to that shown in Figure 4-7 was used, but without the addition of Zr and Ti precursors. The process starts by mixing 1.81 g of the Pb precursor, lead acetate trihydrate, with 60 mL of 2-MOE in a rotary evaporator flask. The mixture is then stirred in the rotary evaporator for 1 hour at 110°C with a constant Ar flow. Afterward, the distillation process removes water from the lead precursor. The mixture is distilled until it transforms into a powder. Next, 47 ml. of 2-MOE is added to the powder, and the mixture is stirred in the rotary evaporator at 110°C for 1 hour to ensure thorough mixing. The final step is to cool the sol-gel solution to room temperature, add 13 mL of acetylacetone as a chelating agent, and mix it at room temperature for half an hour. Although it is common to use PbO to compensate for Pb deficiency in sol-gel PZT

films, it is important to note that excess PbO content can lower breakdown strength associated the lower electrical resistivity in the film with higher PbO content as studied by Zhu *et al.* [48].

The spin coating process began with the deposition of the seed layer. To maximize the piezoelectric response, it is important to obtain a highly {001} oriented PZT thin film [49],[50]. Hence, 2 mol% Nb-doped $PbZr_{0.44}Ti_{0.56}O_3$ sol gel solution (Mitsubishi Materials Corp., Hyogo, Japan) was employed as a seed layer. The seed layer solution was spun at 3500 rpm, pyrolyzed at 200°C for 2.5 minutes and crystallized in RTA at 700°C for 1 min in 2 slpm O_2 atmosphere, following the work in [51], [52]. Then, a 2 mol% Nb doped $PbTi_{0.52}Zr_{0.48}O_3$ was deposited using 0.4 Molar 2-MOE based solution by spin coating at 1500 rpm for 45 second, followed by pyrolysis at 225°C and 400°C for 2 and 3 minutes, respectively [53]. The crystallization was done in a rapid thermal annealer at 700°C for 1 min with 2 slpm of O_2. The process was repeated until the desired thickness of 1.5 μm was achieved.

After that, the PZT thin film was characterized with a field-emission microscope (FESEM; Carl Zeiss Microscopy LLC., White Plains, NY, USA) and x-ray diffraction (XRD; Malvern Panalytical Ltd., Malvern, UK) as shown in Figure 4-8. The {001} and {002} peaks occur at 21.9° and 44.6° of 2θ. These results confirmed that the PZT thin film was predominantly {001} oriented perovskite with a slight amount of surface pyrochlore along the grain boundaries. Finally, a 2 nm Ti adhesion layer and 100 nm of Pt were DC sputtered at room temperature using similar parameters without breaking vacuum as the top electrode.

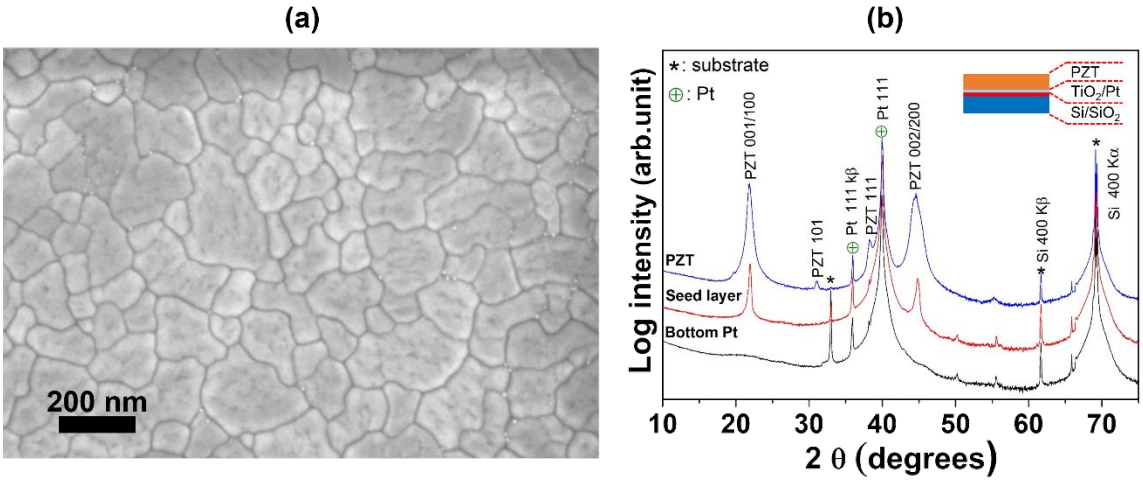

Figure 4-8: (a) The FESEM image and (b) the XRD patterns of a 1.5 µm thick {001} PZT thin film showing that well oriented PZT was achieved. The very fine white particles observed predominantly near triple points in (a) are the pyrochlore/fluorite second phase.

The Pt top electrode and PZT blanket films were then patterned into individual elements using an inductively coupled plasma – reactive ion etching (ICP-RIE) Ulvac NE-500 system (Ulvac, Inc., Kanagawa, Japan). The top electrode was patterned using a 2 µm thick SPR 955 photoresist, spin coated at 2000 rpm for 45 seconds, exposed in contact aligner Karl Suss MABA6 Contact Printer at 90 mJ/cm^2, and developed in CD26 for 2 minutes. The etching process was adapted from [54] and conducted in an ICP-RIE system in 30 sccm of Cl_2 and 40 sccm of Ar at 700 W ICP and 100 W RIE power. After etching, the photoresist was then removed by immersing the sample into Baker PRS3000 photoresist remover at 80°C for 30 minutes, followed by 3 minutes in an oxygen plasma. A Tepla M4L asher, with 200 sccm of O_2, 50 sccm of He at 300 W RF power with pressure regulated at 550 mTorr. For PZT etching, 13 µm thick AZ4620 was spun at 4500 rpm for 45 second and soft baked at 90 °C and 105 °C for 1 and 3 minutes, respectively. Before exposing the photoresist, the spun photoresist was rehydrated in air for an hour and exposed at 100 mJ/cm^2 for 8 cycles with 30 second delay times between each step. Then, the exposed photoresist was developed in a 1:4 AZ400K developer for 4 minutes. The ICP-RIE was performed in an ICP-

RIE system with 3.5 sccm of Cl_2, 7 sccm of CF_4, and 10 sccm of Ar with 600 W ICP and 150 W RIE power. The finished sample was cleaned using a similar process in a photoresist remover and an oxygen plasma, as mentioned earlier.

Figure 4-9(c) and (d) shows microscope images of individual elements after the top electrode and PZT patterning, respectively. 500 nm of Au was deposited by DC sputtering at room temperature with 200 W DC power at 5 mTorr. To pattern the Au pad, SPR3012 was spin coated at a mask for wet etching, the photoresist was spin coated at 4000 rpm for 45 seconds and baked at 95 °C for 1 minute. Then, it was exposed at 70 mJ/cm^2 in a contact aligner and developed in CD 26 for 1 minute. The sample was soaked in an Au etchant (TFA type), with an estimated etch rate ~ 2.8 nm/minute at room temperature, (Transene Company, Inc., MA, USA) to pattern the blanket Au into a contact pad for electrical connection. This is shown in Figure 4-9(e).

During fabrication, 400 μm deep backside release trenches were produced by silicon deep reactive ion etching (DRIE; SPTS Technologies Ltd., Ringland Way, Newport, UK). Before silicon etching, the SiO_2 on the wafer backside was cleaned by wet etching in BOE 6:1 at room temperature with the front side protected by SPR 1827 photoresist spin coated at 4000 rpm for 45 seconds and baked at 110°C for 5 minutes. The sample was then rinsed in acetone, isopropanol, and deionized water followed by oxygen plasma to remove residues from the photoresist. To protect the front side during DRIE, PMGI SF9 was spin coated at 2000 rpm for 45 seconds followed by a bake at 180°C for 1 minute. Afterward, an Al_2O_3 hard mask was deposited by atomic layer deposition at 150°C using a Kurt J. Lesker ALD-150LE system. The hard mark patterning was done using SPR 955 photoresist spin coated at 2000 rpm for 45 seconds, baked at 110 C for 1 minute, exposed in a contact aligner at 90 mJ/cm^2, and developed in CD-26 for 2 minutes. The sample was then patterned using an ICP-RIE system, Ulvac NE550, with 30 sccm BCl_3 and 10 sccm of Cl_2 gas at 1000 W ICP and 75 W RIE power, as shown in Figure 4-10(a).

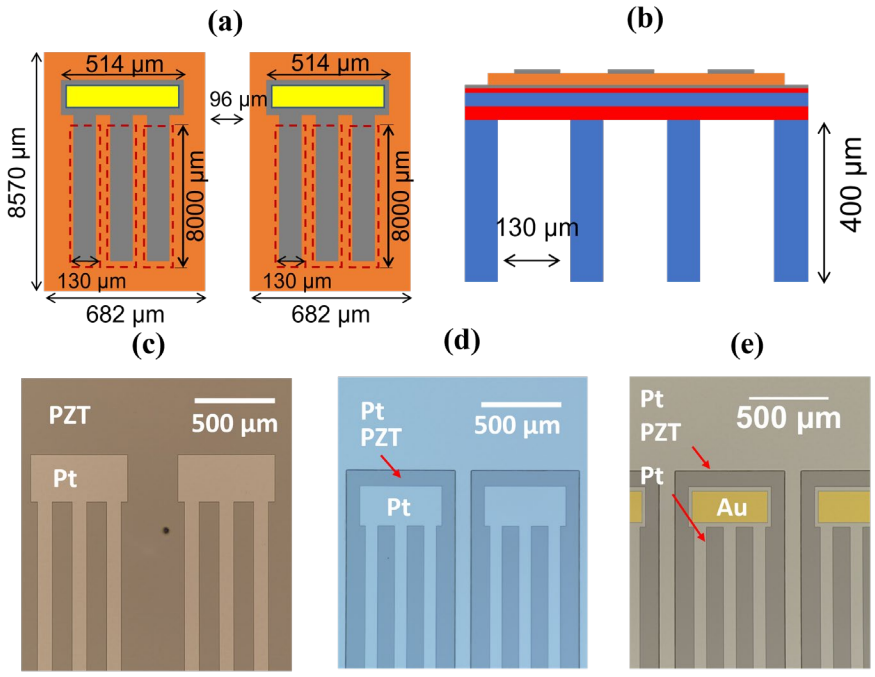

Figure 4-9: Schematics of the device with the dimensions shown in (a) cross section and (b) top view. The element width is 514 µm. Optical microscope images of device side pattern showed (c) top electrode pattern and (d) PZT pattern after ICP-RIE, and (e) Au pad after wet etching.

The deep reactive ion etching (DRIE), SPTS LPX Deep Silicon Etch, was performed immediately after the mask patterning using the Bosch process at 3°C. The BOX layer was used as the stopping layer and the trench depth was confirmed by optical profilometry (NexviewTM NX2, Zygo Corp., CT, USA) as shown Figure 4-10(c). Then, the sample was diced into an individual array with 32 active elements. The arrays were glued to a printed circuited board (PCB) and electrically connected via Au wire bonding. Following that, the PMUT was waterproofed using a 6 µm thick parylene coating, with parylene C as a precursor, deposited by a PDS 2010 LABCOTER system, for underwater measurement.

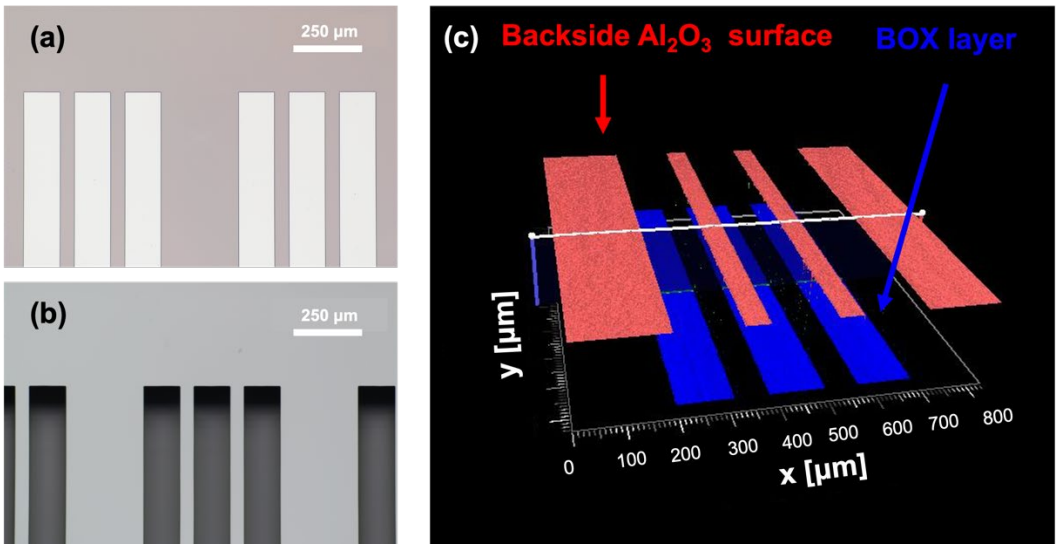

Figure 4-10: The backside etching: (a) a microscope of Al_2O_3 hard mask after patterned using ICP-RIE, (b) the microscope image of backside etching by Si DRIE, (c) the optical profilometry results show the three parallel etch trenches with a trench depth of 404.3 µm.

4.3.2 PMUT Characterization

A custom printed circuit board (PCB) was designed with an on board dual-row 36 position header connector. The ground plane of the thin film array was connected to the ground pads of the PCB with conductive silver paint. Each of the 32 elements was wire-bonded to the excitation pad. Notably, one additional element was shorted to the ground using silver paint and served as a ground connection to the PCB board, as shown previously in Figure 4-4.

In Figure 4-11(a), the relative permittivity and dielectric loss as a function of frequency from 100 Hz to 1 MHz was measured with a 30 mV_{AC} excitation using a Hewlett Packard 4284A LCR meter. The relative dielectric permittivity and loss tangent of PZT in the 32-element array was 1210 ± 12 and 1.9% ± 0.09%; all elements were operational. A Radiant Multiferroic test analyzer was used to analyze the polarization-electric field hysteresis loop (P–E), which is shown in Figure 4-11(b). The P–E loop shows a remanent polarization (P_r) and coercive fields (E_c) of 14.7 and 46.8 kV/cm before the DRIE and 16.2 µC/cm^2 and -54.9 and 39.2 kV/cm after the DRIE.

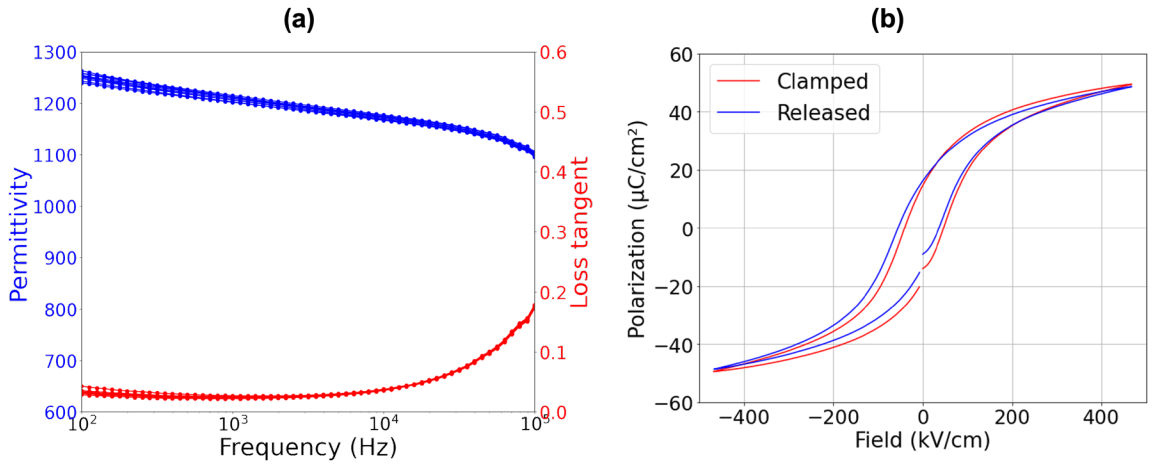

Figure 4-11: (a) The dielectric permittivity as a function of frequency showed a relative permittivity of 1210 ± 12 and dielectric loss of 1.9% ± 0.09%, and (b) polarization-electric field hysteresis of before DRIE (clamped) and after DRIE (released) showed P_r and E_c of 14.7 and 16.2 μC/cm^2, and 46.8 and (−54.9, 39.2) kV/cm for clamped and released states, respectively.

A 32 channel beamformer circuit (TX7332EVM, Texas Instruments, Dallas, TX, USA) was used to drive the array, as described in [34]. The beamformer provided a maximum of 6 W power, 200 V_{PP} pulses, and a delay range of 0-40 μs with 5 ns resolution. Figure 4-12 shows the beam measurement setup in a water tank, including the beamformer circuit (with an interface), 3-axis motorized translation stage with a resolution of 0.8 μm and maximum range of 5 cm (MTS50/M-Z8, Thorlabs, Newton, NJ) calibrated by an Onda HGL0085 hydrophone, (85 μm aperture, 0.25 – 40 MHz bandwidth, and pressure sensitivity of 48.2 nV/Pa at 1.4 MHz), with an Onda AG-2010 preamplifier, and digital oscilloscope (for data digitization and acquisition). A custom MATLAB code was used to coordinate all the equipment and automate the US beam scanning process. It should be noted that for each measurement, a delay time of 1.5 seconds was observed as a pause before and after data acquisition to ensure data reliability.

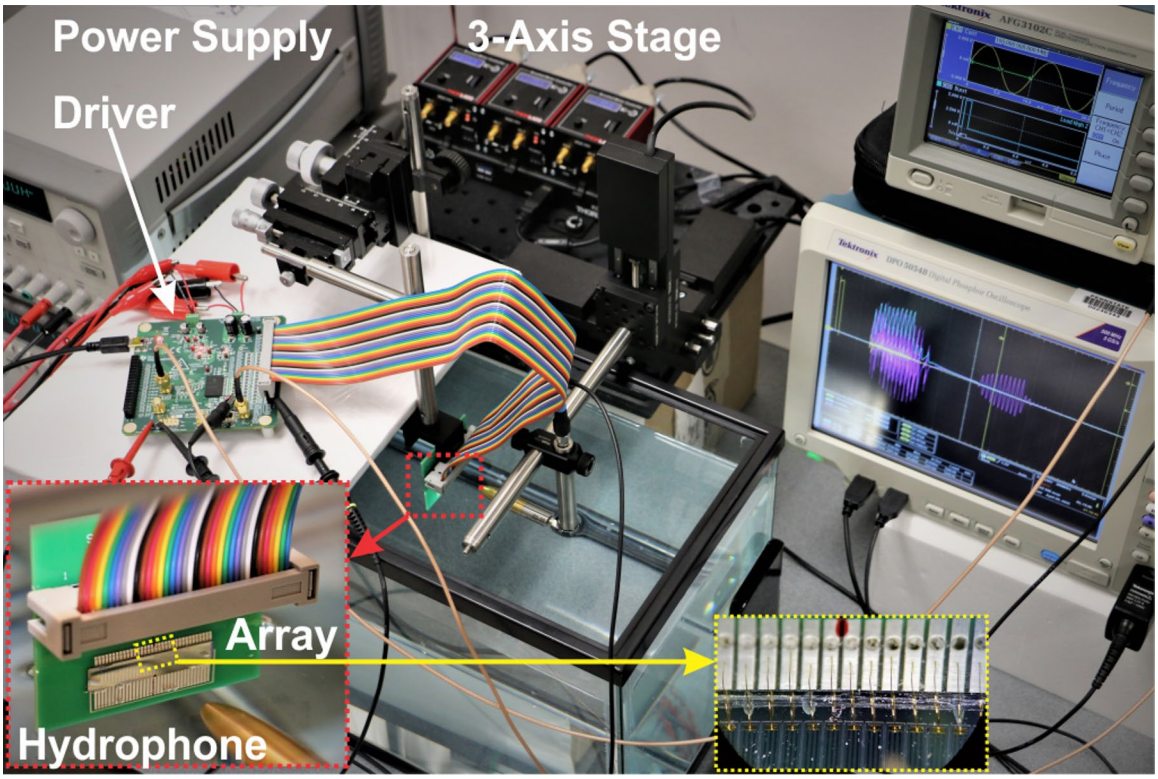

Figure 4-12: Beam profile measurement setup. Array assembly on a custom PCB with dual-row 36 position header connected to the driver.

4.3.3 Phased Array Ultrasonic Measurements

The electrical impedance of the individual elements was first measured at various frequencies ranging from 0.2 to 3.2 MHz, as shown in Figure 4-13(a). To find the optimum driving frequency, the ratio of the output pressure and the input voltage was measured as a function of frequency. Figure 4-13(b) shows the normalized output pressure over input voltage vs. frequency for 5 different elements. The optimum driving frequency was 1.4 MHz; the discrepancy in acoustic pressure output as a function of frequency for each element may originate from errors in positioning the PMUT array on a custom PCB and the measurement holder. The deviation of resonant frequency relative to the calculated value may result from the differences in dimension between the calculation and fabricated device due to errors in micromachining such as lithography

misalignment and/or over etching. Thus, 1.4 MHz was selected as the driving frequency for all subsequent measurements.

Figure 4-14 shows the waveform generated from the beamformer circuit showing i) the synchronized pulse, the voltage across a PMUT element, and the voltage received from the hydrophone. The voltage waveform received by the hydrophone equates to a spatial peak pressure output of ~ 0.367 MPa (45.9 kPa/V). The corresponding beam (F = 20 mm and θ_s = 0°) was generated by the 32 elements of the phased array being driven with 10 cycles of unipolar 1.4 MHz square pulses (8 V pulse amplitude) with the time delay for each element calculated from Equation 2. A smaller number of cycles was intentionally used for decoupling electrical interference.

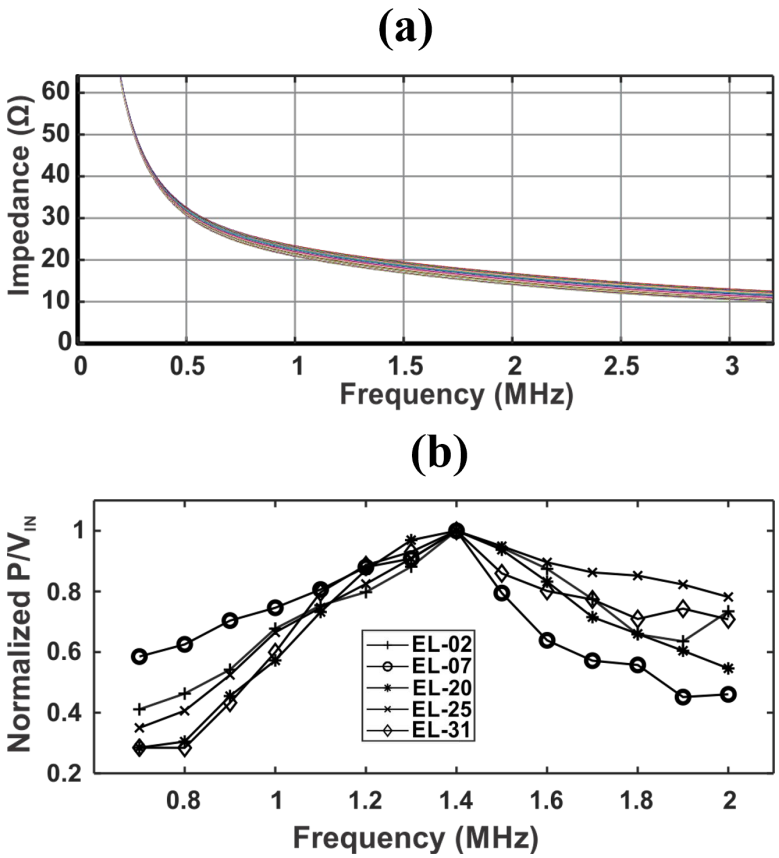

Figure 4-13: (a) Measured impedance of multiple elements. (b) Normalized output pressure over input voltage vs. frequency showing 1.4 MHz as the optimum driving frequency for multiple elements.

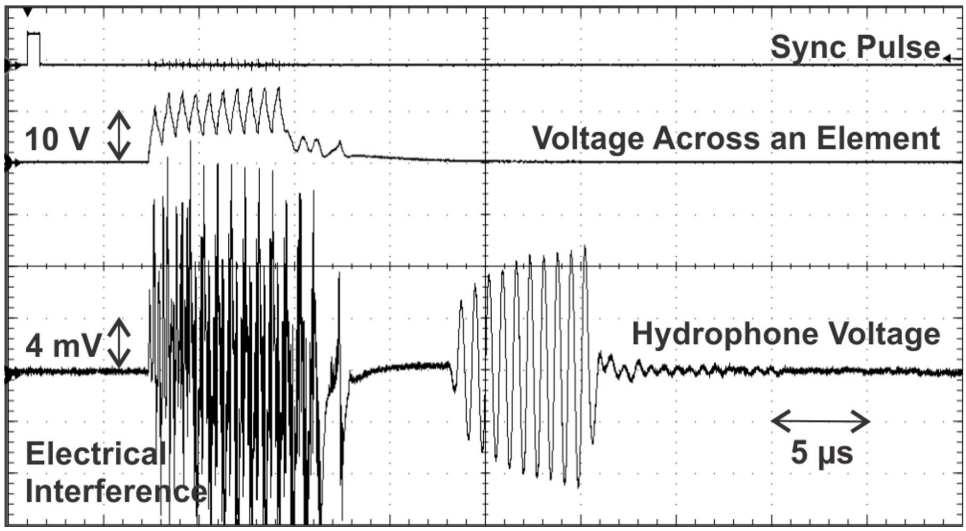

Figure 4-14: A hydrophone voltage waveform received from a beam formed at F = 20 mm (θ_s = 0˚) representing 45.9 kPa/V pressure output.

To examine the acoustic beam profile generated by the PMUT phased array, the array was actuated with a 14.6 V unipolar voltage and phased delays calculated for beamforming and steering across different focal distances. In the first scenario, the focal distance for beamforming and steering was set to the designed target of 20 mm. Figure 4-15(a), (c), and (e) present the 2D beam profiles from the simulation and measurement results with θ_s = 0°, 45°, and -45°, respectively. The simulated and measured axial resolutions at θ_s = 0°, 45°, -45° were 7.9, 9.9, 9.9 mm and 9.2, 10.3, 11.1 mm, respectively. For the lateral ($\boldsymbol{y}$) resolution, the simulated results were 1.2, 1.3, 1.3 mm while the measurement results were 1, 1.3, 1.4 mm at θ_s = 0°, 45°, and -45°, respectively. The measured beam profiles closely matched the simulated ones. With 14.6 V driving voltage, the spatial peak pressure measured at θ_s = 0°, 45°, and -45° were 0.44 MPa, 0.33 MPa, and 0.29 MPa, respectively. Additionally, as expected, there was no significant off target high pressure spot.

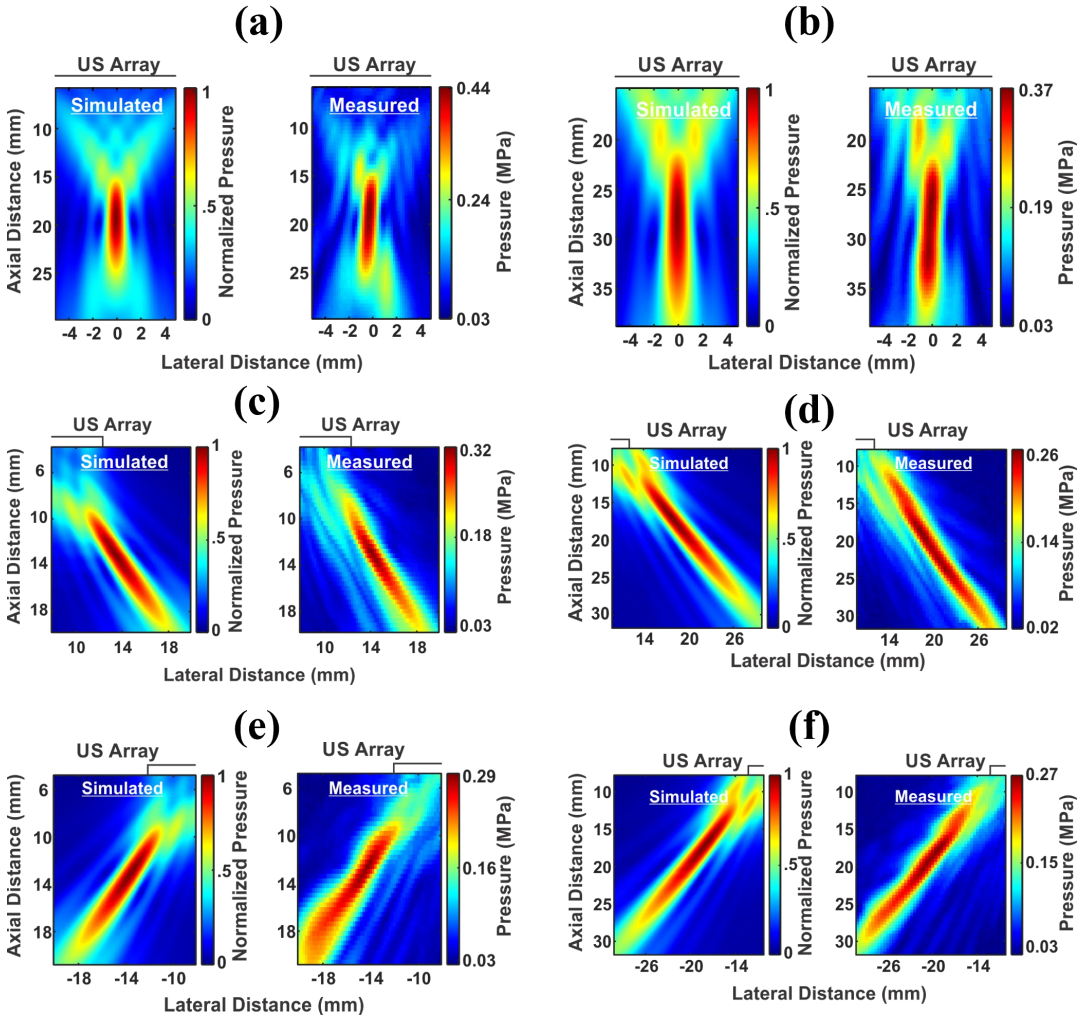

Figure 4-15: The 2D beam profiles of the phased array from simulations (left) and measurements (right) focused and steered at $\theta_s = 0^{\circ}, 40^{\circ}, -45^{\circ}$ where (a), (c), and (e) represent F = 20 mm and (b), (d), and (f) represent F = 30 mm.

To further investigate the PMUT performance at a distance from the designed F, the focal distance was set to F = 30 mm. Figure. 4-15(b), (d), and (f) show the 2D beam profiles comparing the simulated and measured results with the beam focused. The simulated and measured axial (lateral) resolutions at $\theta_s = 0°$, 45°, -45° were 14.1, 17.4, 17.4 mm (1.3, 1.9, 1.9 mm) and 13.6, 24.3, 22 mm (1.6, 2.2, 2 mm), respectively. As the targeted focal distance increased, the maximum acoustic pressure dropped to 0.37 MPa, 0.27 MPa, and 0.27 MPa at θ_s = 0°, 45°, and -45°, respectively.

Figure 4-16 (a) shows measured axial pressure profiles ($y = z = 0$) of the beams focused at different focal distances (F). Figure 4-16(b) shows measured lateral (y) pressure profiles of the beams as a function of the axial distance, where the peaks shown correspond to the maximum pressure output at different F from Figure 4-16(a). It is obvious that at $F = 30$ mm, which exceeds the F_{max} of 20 mm, the beam becomes comparatively wider (indicative of poor lateral resolution). In this circumstance, a higher N (or larger array aperture, D) could be used to compensate for the poor resolution. Figure 4-16(c) shows the measured pressure profiles parallel to the x axis (as defined in Figure 4-2) of the beams focused at $F = 20$ mm and steered at 0° to 60°. Figure 4-16(d) shows the measured lateral ($\boldsymbol{y}$) pressure profiles of the beams focused at $F = 20$ mm and steered at 0° to 60°. The fabricated array was optimally driven at 1.4 MHz, whereas it was designed for 1 MHz; however, the phase performance was still good and showed no unwanted grating lobes for the maximum steering angle of 60°.

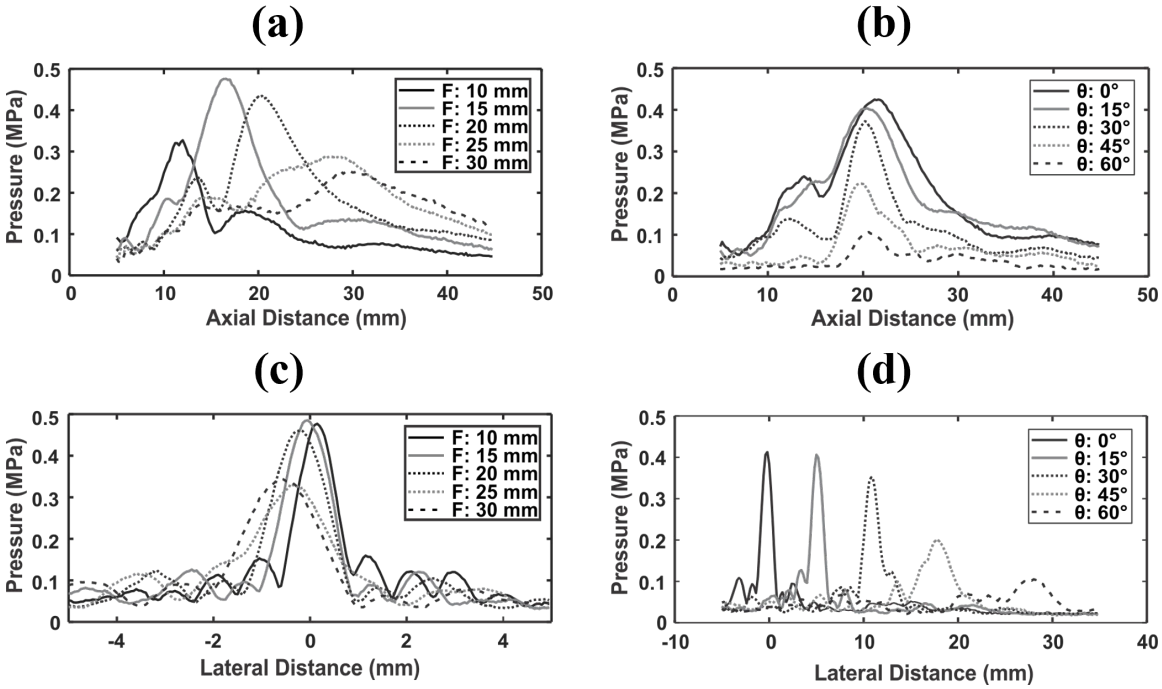

Figure 4-16: Measured 1D beam profiles focused and steered at different F and θ_s. (a) Axial pressure profiles at different F, (b) lateral (y) pressure profiles at different F, (c) pressure profiles parallel to the x-axis at different θ_s, and (d) lateral (y) pressure profiles at different θ_s.

Table 4-2 summarizes the simulated and measured 2D beam characteristics including the axial and lateral resolution, maximum peak-to-peak pressure, and the corresponding Intensity Spatial Peak Pulse Average (I_{SPPA}) for the beams focused at F = 20 and 30 mm and steered at θ_s = 0°, 45°, -45°. I_{SPPA} was calculated using the pulse intensity integral of the spatial peak pressure waveform as described in [9]. It should be noted that these results were obtained without the effect of a skull. The effect of a rat's skull on the US beam shape and pressure of a bulk array has already been discussed in previous work [34]. Given that the output pressures from the PMUT demonstrated in this work are high, it is anticipated that the PMUT array can also provide useful neurostimulation through a rat skull.

Table 4-2: Summary of simulated and measured 2d beam profiles of the thin film array.

Sim./ Meas.	Medium	F (mm)	θ_s (deg)	Axial Resolution (mm)	Lateral Resolution (mm)	Peak-to-Peak US Pressure (MPa)	*I*SPPA (W/cm^2)
Sim	Brain	20	0	7.9	1.2	1	-
Meas.	Water	20	0	9.2	1	0.44	1.29
Sim	Brain	20	45	9.9	1.3	0.74	-
Meas.	Water	20	45	10.3	1.3	0.33	0.76
Sim	Brain	20	-45	9.9	1.3	0.74	-
Meas.	Water	20	-45	11.1	1.4	0.29	0.55
Sim	Brain	30	0	14.1	1.3	0.75	-
Meas.	Water	30	0	13.6	1.6	0.37	0.91
Sim	Brain	30	45	17.4	1.9	0.54	-
Meas.	Water	30	45	24.3	2.2	0.27	0.45
Sim	Brain	30	-45	17.4	1.9	0.54	-
Meas.	Water	30	-45	22	2	0.27	0.46

*Simulated peak-to-peak US pressure values are normalized to that of F = 20 mm and θ_s = 0°.

Table 4-3 summarizes the fabricated PMUT phased array in comparison with other ultrasonic systems, including CMUT and bulk ceramics, as reported in the literature. With a focal length of 20 mm and low excitation voltage, the PMUT array achieved a comparable acoustic

output pressure of up to 0.44 MPa. This result underscores the feasibility of PMUT technology for neuromodulation applications.

Table 4-3: Comparison of selected recent ultrasonic transducer studies and this work.

Reported parameters	H. Kim *et al.* (2019) [29]	T. Costa *et al.* (2021) [31]	C. Seok *et al.* (2021) [30]	S. Ilham *et al.* (2021) [31]	This work
Type	Ring CMUT	Bulk PZT	CMUT	Bulk PZT	PMUT
Element	32	26 × 26	32 × 32	16	32
***f* (MHz)**	0.183	8.4	3.4	0.833	1.4
Focal Length (mm)	2.3	5	5	12	**20**
V_{in} (V_{pp})	90	5	60	150	**14.6**
Pressure (MPa)	0.052	0.1	1.89	1.15	**0.44**

4.4 Conclusions

In this chapter, the design methodology of a US transducer array for neuromodulation was applied to PMUT transducers, with a design goal of exceeding hundreds of kPa acoustic pressure at operating voltages below 20 V. The linear 32-element phased array PMUT thin film with a 1.4 MHz bending-mode resonant frequency was designed and fabricated on SOI wafer with 1.5 μm thick {100} oriented PZT as the piezoelectric layer and 2 μm of silicon as the passive elastic layer. With a commercial driver board, the 32-element array was driven using calculated time delays for beam focusing and steering at F = 20 – 30 mm and θ_s = 0° – 60°. The phased array demonstrated a maximum peak-to-peak acoustic pressure output of 0.44 MPa, corresponding to an acoustic intensity (I_{SPPA}) of 1.29 W/cm^2, achieved at 20 mm focal depth with 14.6 V unipolar square pulses in an immersion test. This work presents a new route to achieve low voltage US transducers for neuromodulation. Such PMUT US phased arrays can be integrated with a CMOS integrated circuit to drive the transducers.

Bibliography

[1] G. Darmani, T. Bergmann, K. B. Pauly, C. Caskey, L. De Lecea, A. Fomenko, E. Fouragnan, W. Legon, K. Murphy, T. Nandi, M.A. Phipps, G. Pinton, H. Ramezanpour, J. Sallet, S.N. Yaakub, S.S. Yoo, R. Chen, "Non-Invasive Transcranial Ultrasound Stimulation for Neuromodulation," *Clin. Neurophysiol.*, vol. 135, pp. 51–73, 2022

[2] W. Tyler, Y. Tufail, M. Finsterwald, M. Tauchmann, E. Olson, and C. Majestic, "Remote Excitation of Neuronal Circuits Using Low-Intensity, Low-Frequency Ultrasound," *PLoS ONE*, vol. 3, pp. 1–11, 2008.

[3] T. Wagner, A. Valero-Cabre, and A. Pascual-Leone, "Noninvasive Human Brain Stimulation," *Annu. Rev. Biomed. Eng.*, vol. 9, pp. 527–565, 2007.

[4] X. Niu, K. Yu, and B. He, "Transcranial Focused Ultrasound Induces Sustained Synaptic Plasticity in Rat Hippocampus," *Brain Stimul.*, vol. 15, no. 2, pp. 352–359, 2022.

[5] F. Munoz, A. Meaney, A. Gross, K. Liu, A. Pouliopoulos, D. Liu, E. Konofagou, and V. Ferrera, "Long Term Study of Motivational and Cognitive Effects of Low-Intensity Focused Ultrasound Neuromodulation in the Dorsal Striatum of Nonhuman Primates," *Brain Stimul.*, vol. 15, no. 2, pp. 360–372, 2022.

[6] Y. Liu, G. Wang, C. Cao, G. Zhang, E. B. Tanzi, Y. Zhang, W. Zhou, and Y. Li, "Neuromodulation Effect of Very Low Intensity Transcranial Ultrasound Stimulation on Multiple Nuclei in Rat Brain," *Front. Aging Neurosci.*, vol. 13, p. 656430, 2021.

[7] K. Abe and T. Taira, "Focused Ultrasound Treatment, Present and Future," *Neurologia medico-chirurgica*, vol. 57, no. 8, pp. 386-391, 2017.

[8] H. Zhou, L. Niu, X. Xia, Z. Lin, X. Liu, M. Su, R. Guo, L. Meng, and H. Zheng, "Wearable Ultrasound Improves Motor Function in an MPTP Mouse Model of Parkinson's Disease," *IEEE Trans. Biomed. Eng.*, vol. 66, no. 11, pp. 3006–3013, 2019.

[9] Y. Tufail, A. Yoshihiro, S. Pati, M. Li, and W. Tyler, "Ultrasonic Neuromodulation by Brain Stimulation with Transcranial Ultrasound," *Nat. Protoc.*, vol. 6, no. 9, pp. 1453–1470, 2011.

[10] G. Li, W. Qiu, Z. Zhang, Q. Jiang, M. Su, R. Cai, Y. Li, F. Cai, Z. Deng, D. X. Xu, and H. Zhang, "Noninvasive Ultrasonic Neuromodulation of Freely Moving Mice," *IEEE Trans. Biomed. Eng.*, vol. 66, no. 1, pp. 217–224, 2019.

[11] W. Lee, P. Croce, R. Margolin, A. Cammalleri, K. Yoon, and S. Yoo, "Transcranial Focused Ultrasound Stimulation of Motor Cortical Areas in Freely-Moving Awake Rats," *BMC Neurosci.*, vol. 19, p. 57, 2018.

[12] E. Mehic, J. Xu, C. Caler, N. Coulson, C. Moritz, and P. Mourad, "Increased Anatomical Specificity of Neuromodulation via Modulated Focused Ultrasound," *PLOS ONE*, vol. 9, pp. 1–13, 2014.

[13] W. Lee, S. Lee, M. Park, L. Foley, E. Purcell, H. Kim, K. Fischer, L. Maeng, and S. Yoo, "Image-Guided Focused Ultrasound–Mediated Regional Brain Stimulation in Sheep," *Ultrasound. Med. Biol.*, vol. 42, pp. 459–470, 2016.

[14] T. Deffieux, Y. Younan, N. Wattiez, M. Tanter, P. Pouget, and J. Aubry, "Low-Intensity Focused Ultrasound Modulates Monkey Visuomotor Behavior," *Curr. Biol.*, vol. 23, pp. 2430–2433, 2013.

[15] S. Zhu, B. Meng, J. Jiang, X. Wang, N. Luo, N. Liu, H. Shen, L. Wang, and Q. Li, "The Updated Role of Transcranial Ultrasound Neuromodulation in Ischemic Stroke: From Clinical and Basic Research," *Front. Cell. Neurosci.*, vol. 16, p. 839023, 2022.

[16] K. Yu, C. Liu, X. Niu, and B. He, "Transcranial Focused Ultrasound Neuromodulation of Voluntary Movement-Related Cortical Activity in Humans," *IEEE Trans. Biomed. Eng.*, vol. 68, no. 6, pp. 1923–1931, 2021.

[17] A. Guerra, E. Vicenzini, E. Cioffi, D. Colella, A. Cannavacciuolo, S. Pozzi, B. Caccia, G. Paparella, G. Di Stefano, A. Berardelli, and L. Bologna, "Effects of Transcranial Ultrasound Stimulation on Trigeminal Blink Reflex Excitability," *Brain Sci.*, vol. 11, no. 5, p. 645, 2021.

[18] K. Zeng, G. Darmani, A. Fomenko, X. Xia, S. Tran, J.-F. Nankoo, Y. Shamli Oghli, Y. Wang, A. M. Lozano, and R. Chen, "Induction of Human Motor Cortex Plasticity by Theta Burst Transcranial Ultrasound Stimulation," *Ann. Neurol.*, vol. 91, no. 2, pp. 238–252, 2022.

[19] W. Legon, A. Rowlands, A. Opitz, T. Sato, and W. Tyler, "Pulsed Ultrasound Differentially Stimulates Somatosensory Circuits in Humans as Indicated by EEG and fMRI," *PLoS ONE*, vol. 7, pp. 1–14, 2012.

[20] W. Legon, T. Sato, A. Opitz, J. Mueller, A. Barbour, and W. Tyler, "Transcranial Focused Ultrasound Modulates the Activity of Primary Somatosensory Cortex in Humans," *Nat. Neurosci.*, vol. 17, pp. 322–333, 2014.

[21] W. Lee, H. Kim, Y. Jung, Y. Chung, I. Song, J. Lee, and S. Yoo, "Transcranial Focused Ultrasound Stimulation of Human Primary Visual Cortex," *Sci. Rep.*, vol. 6, pp. 1–12, 2016.

[22] X. Niu, K. Yu, and B. He, "On the Neuromodulatory Pathways of the In Vivo Brain by Means of Transcranial Focused Ultrasound," *Curr. Opin. Biomed. Eng.*, vol. 8, pp. 61–69, 2018.

[23] A. Bystritsky and A. Korb, "A Review of Low-Intensity Transcranial Focused Ultrasound for Clinical Applications," *Curr. Behav. Neurosci. Rep.*, vol. 2, pp. 60–66, 2015.

[24] D. S. Hersh and H. M. Eisenberg, "Current and Future Uses of Transcranial Focused Ultrasound in Neurosurgery," *J. Neurosurg. Sci.*, vol. 61, no. 2, pp. 213–233, 2017.

[25] S. K. Edelman, *Understanding Ultrasound Physics.* The Woodlands, TX: ESP Ultrasound, 2012.

[26] A. Javid, S. Ilham, and M. Kiani, “A Review of Ultrasound Neuromodulation Technologies,” *IEEE Trans. Biomed. Circuits Syst.*, vol. 17, no. 5, pp. 1084–1096, 2023.

[27] O. T. Von Ramm and S. W. Smith, "Beam steering with linear arrays," *IEEE Trans. Biomed. Eng.*, no. 8, pp. 438-452, 1983.

[28] S. C. Wooh and Y. Shi, "Optimum beam steering of linear phased arrays," *Wave Motion*, vol. 29, no. 3, pp. 245-265, 1999.

[29] H. Kim, S. Kim, N. Sim, C. Pasquinelli, A. Thielscher, J. Lee, and H. Lee, "Miniature Ultrasound Ring Array Transducers for Transcranial Ultrasound Neuromodulation of Freely-Moving Small Animals," *Brain Stimul.*, vol. 12, no. 2, pp. 251–255, 2019.

[30] C. Seok, O. A. A. Bilgolu, F. Yamaner, and Ö. Oralkan, "A Wearable Ultrasonic Neurostimulator—Part II: A 2D CMUT Phased Array System with a Flip-Chip Bonded ASIC," *IEEE Trans. Biomed. Circuits Syst.*, vol. 15, pp. 705–718, 2021.

[31] T. Costa, C. Shi, K. Tien, J. Elliot, F. Cardoso, and K. Shepard, "An Integrated 2D Ultrasound Phased Array Transmitter in CMOS with Pixel Pitch-Matched Beamforming," *IEEE Trans. Biomed. Circuits Syst.*, vol. 15, pp. 731–742, 2021.

[32] J. Lee, K. Ko, H. Shin, S.-J. Oh, C. J. Lee, N. Chou, N. Choi, M. T. Oh, B. C. Lee, S. C. Jun, and I. J. Cho, "A MEMS Ultrasound Stimulation System for Modulation of Neural Circuits with High Spatial Resolution In Vitro," *Microsyst. Nanoeng.*, vol. 5, no. 1, p. 28, 2019.

[33] Y. Qiu, J. V. Gigliotti, M. Wallace, F. Griggio, C. E. M. Demore, S. Cochran, and S. Trolier-McKinstry, "Piezoelectric Micromachined Ultrasound Transducer (PMUT) Arrays for Integrated Sensing, Actuation and Imaging," *Sensors*, vol. 15, no. 4, pp. 8020–8041, 2015.

[34] S. J. Ilham, Z. Kashani, and M. Kiani, "Design and Optimization of Ultrasound Phased Arrays for Large-Scale Ultrasound Neuromodulation," *IEEE Trans. Biomed. Circuits Syst.*, vol. 15, no. 6, pp. 1454–1466, 2021.

[35] G. Paxinos and C. Watson, *The Rat Brain in Stereotaxic Coordinates: Hard Cover Edition*, Elsevier, 2006.

[36] P.-C. Tsai, H. S. Gougheri, and M. Kiani, "Skull Impact on the Ultrasound Beam Profile of Transcranial Focused Ultrasound Stimulation," *2019 41st Annual International Conference of the IEEE Engineering in Medicine and Biology Society (EMBC)*, Berlin, Germany, 2019, pp. 5188-5191.

[37] T. D. Mast, "Empirical Relationships Between Acoustic Parameters in Human Soft Tissues," *Acoust. Res. Lett. Online*, vol. 1, no. 2, pp. 37–42, 2000.

[38] S. Timoshenko, S. Woinowsky-Krieger, *Theory of Plates and Shells*, vol. 2, McGraw-Hill New York, 1959.

[39] C. Y. Cheng, A. Dangi, L. Ren, S. Tiwari, R. R. Benoit, Y. Qiu, H. S. Lay, S. Agrawal, R. Pratap, S.-R. Kothapalli, T. E. Mallouk, S. Cochran, and S. Trolier-McKinstry, "Thin Film PZT-Based PMUT Arrays for Deterministic Particle Manipulation," *IEEE Trans. Ultrason. Ferroelectr. Freq. Control*, vol. 66, no. 10, pp. 1606–1615, 2019.

[40] P. Muralt and J. Baborowski, "Micromachined Ultrasonic Transducers and Acoustic Sensors Based on Piezoelectric Thin Films," *J. Electroceram.*, vol. 12, pp. 101–108, 2004.

[41] R. J. Przybyla, *Ultrasonic 3D Rangefinder on a Chip*, Ph.D. thesis, University of California, Berkeley, Berkeley, CA, USA, 2013.

[42] Y. Lu and D. A. Horsley, "Modeling, Fabrication, and Characterization of Piezoelectric Micromachined Ultrasonic Transducer Arrays Based on Cavity SOI Wafers," *J. Microelectromech. Syst.*, vol. 24, no. 4, pp. 1142–1149, 2015.

[43] A. J. Fox, B. Drawl, G. R. Fox, B. J. Gibbons, and S. Trolier-McKinstry, "Control of Crystallographic Texture and Surface Morphology of Pt/TiO_2 Templates for Enhanced PZT Thin Film Texture," *IEEE Trans. Ultrason. Ferroelectr. Freq. Control*, vol. 62, no. 1, pp. 56–61, 2015.

[44] K. D. Budd, S. K. Dey, and D. A. Payne, "The Effect of Hydrolysis Conditions on the Characteristics of $PbTiO_3$ Gels and Thin Films," *MRS Proceedings*, vol. 72, p. 317, 1986.

[45] S. K. Dey, K. D. Budd, and D. A. Payne, "Thin-Film Ferroelectrics of PZT of Sol-Gel Processing," *IEEE Trans. Ultrason. Ferroelectr. Freq. Control*, vol. 35, no. 1, pp. 80–81, 1988.

[46] R. A. Wolf and S. Trolier-McKinstry, "Temperature Dependence of the Piezoelectric Response in Lead Zirconate Titanate Films," *J. Appl. Phys.*, vol. 95, no. 3, pp. 1397–1406, 2004.

[47] Toshihiko Tani, Charles D. E. Lakeman, Jie-Fang Li, Zhengkui Xu, and David A. Payne, "Crystallization Behavior and Improved Properties for Sol-Gel Derived PZT and PLZT Thin Layers Processed with a Lead Oxide Cover Coating," *Ceramic Transactions*, vol. 43, p. 89, 1994.

[48] W. Zhu, T. Borman, K. DeCesaris, B. Truong, M. M. Lieu, S. W. Ko, P. Mardilovich, and S. Trolier-McKinstry "Influence of PbO Content on the Dielectric Failure of Nb-Doped {100}-Oriented Lead Zirconate Titanate Films," *J. Am. Ceram. Soc.*, vol. 102, no. 4, pp. 1734–1740, 2019.

[49] T. Doi, H. Sakurai, and N. Soyama, "Method of forming PbNbZT ferroelectric thin film," U.S. Patent 10,005,101, Jun. 26, 2014.

[50] T. Doi, T. Noguchi, J. Fuji, N. Soyama, and H. Sakurai, "The Orientation and Grain Texture Effect on Life Time Reliability of Sol–Gel Derived $PbZr_{0.52}Ti_{0.48}O_3$ Films," *Jpn. J. Appl. Phys.*, vol. 51, no. 9S1, p. 09LA15, 2012.

[51] T. M. Borman, S. W. Ko, P. Mardilovich, and S. E. Trolier-McKinstry, "Development of Crystallographic Texture in Chemical Solution Deposited Lead Zirconate Titanate Seed Layers," *J. Am. Ceram. Soc.*, vol. 100, no. 10, pp. 4476–4482, 2017.

[52] T. M. Borman, W. Zhu, K. Wang, S. W. Ko, P. Mardilovich, and S. E. Trolier-McKinstry, "Effect of Lead Content on the Performance of Niobium Doped 100 Textured Lead Zirconate Titanate Films," *J. Am. Ceram. Soc.*, vol. 100, no. 8, pp. 3558–3567, 2017.

[53] H. G. Yeo and S. Trolier-McKinstry, "001 Oriented Piezoelectric Films Prepared by Chemical Solution Deposition on Ni Foils," *J. Appl. Phys.*, vol. 116, no. 1, p. 014105, 2014.

[54] L.-H. Chang, E. Apel, M. Kottke, and C. Tracy, "A Study of Platinum Electrode Patterning in a Reactive Ion Etcher," *J. Vac. Sci. Technol. A*, vol. 16, no. 3, pp. 1489–1496, 1998.

Chapter 5

Process Development for Flexible Ultrasound Transducer Phased Arrays

The previous chapter demonstrated the potential of PZT thin film PMUT phased arrays for neuromodulation applications. To further explore the possibility of neurostimulation via implantable ultrasound stimulation, the design and fabrication of a flexible PMUT phased array on polyimide was explored in this chapter. However, the nature of PZT on a polymeric substrate presents challenges, as the width extension mode limits the achievement of the λ/2 pitch, which is crucial for phased array operation. This chapter explores strategies to design and fabricate a flexible PMUT, optimizing the resonance frequency and achieving an ideal pitch for 0.5 – 2.5 MHz phased arrays suitable for neurostimulation applications.

5.1 Introduction

Conformal and flexible piezoelectric microelectromechanical systems (piezoMEMS) hold promise for numerous applications, especially where placement of the device directly on the test structure is required. In infrastructure health monitoring, conforming flexible ultrasound transducers onto curved or complex inspection sites enhances the performance of non-destructive evaluation (NDE) [1], [2]. Furthermore, flexible ultrasound transducers should be suitable for wearable ultrasound devices for continuous, non-invasive healthcare monitors for blood pressure, heart function, etc. [3-5].

Flexible piezoMEMS devices can be fabricated using various methods. One established approach involves the deposition of piezoelectric materials onto thin, flexible metal substrates, such as stainless steel, copper, or nickel foils [6-9]. For instance, K. Makiko *et al.* demonstrated pulse-echo measurements of a piezoelectric film prepared on stainless steel for infrastructure monitoring [1]. Similarly, H. G. Yeo *et al.* demonstrated a piezoelectric energy harvester bimorph structure based on PZT thin films on Ni foils designed to extract power from low-frequency movement [9]. The inherent durability of metal foils makes them suitable for energy harvesting.

S. Sadeghpour *et al.* demonstrated an alternative approach with bendable piezoelectric micromachined ultrasound transducers (PMUT) on silicon-on-insulator wafers [10]. The silicon substrate was patterned into springs and wrapped around a 3D-printed cube to demonstrate flexibility; they demonstrated 90° bends with a radius of 1 mm. Additionally, fully flexible piezoelectric ultrasound transducers can be achieved by fabricating devices on polymeric substrates using a transfer-release method. For example, Y. H. Do *et al.* used a laser lift-off process to transfer a PZT device from a sapphire substrate to an indium-tin-oxide (ITO) coated polyethylene terephthalate (PET) substrate [11]. Y. Jeong *et al.* reported a fully flexible PMUT with the piezoelectric polymer PV(DF-TrFE) prepared on a polyimide foil with a glass carrier substrate, where the PV(DF-TrFE) and polyimide layers were released by delamination from the glass later in the process [12].

Another interesting method is the transfer and release using an oxide sacrificial layer to transfer piezoelectric layers to flexible substrates. Sun *et al.* demonstrated the fabrication of AlN on polymer substrates using wet etching of a SiO_2 sacrificial layer. Then the structure was picked up using a polydimethylsiloxane (PDMS) stamp and transferred to a polyimide substrate on a carrier wafer; the polyimide was released in the final step of the process [13]. Liu *et al.* demonstrated a transfer-release method for 1 μm thick PZT films on polyimide substrates [14-16]. Initially, PZT films were deposited on silicon substrates with a ZnO sacrificial layer. After the PZT

layer and electrode layers were patterned, polyimide was spin-coated onto the PZT, followed by ZnO wet etching in acetic acid to transfer and release the PZT films to the polyimide. Liu reported that the fully released PZT showed significant improvement in the remanent polarization after release. This implied that there should also be an improvement in piezoelectric response from substrate declamping and enhanced domain wall motion [14], [17], [18]. Notably, a single element of a PZT transducer on 5 μm thick polyimide demonstrated ultrasonic output at 9.5 MHz, with a pressure output of 33 kPa at 6 mm distance with 5 V peak unipolar excitation [15]. This highlights the potential of flexible PMUT in transmit applications.

Fully released PMUT could advance catheter-based ultrasound imaging, intravascular ultrasound (IVUS) and neuromodulation, etc. [19-23]. Especially, high acoustic output would be beneficial for transmit-based applications such as neural therapy. There are efforts in the literature to demonstrate the feasibility of flexible ultrasound platforms for neuromodulation. For example, J. H. Lee *et al.* demonstrated the fabrication of a flexible piezoelectric transducer array using 55 μm thick bulk PZT fabricated on SOI and integrated on polydimethylsiloxane (PDMS) showing I_{sppa} of 44 mW/cm^2 at 80 V for low-intensity focused ultrasound stimulation [24]. Additionally, V. Pashaei reported the design and fabrication of a conformal ultrasound device for image-guided neural therapy using 0.4 and 1.5 mm thick diced PZT integrated on a flexible PCB with a pressure output of 20 – 80 kPa/V [25].

The challenge in neuromodulation techniques for non-invasive methods is the poor spatial resolution as well as the penetration depth [26]. Developing a flexible implantable transducer phased array offers minimal invasiveness as the device can be positioned on the brain surface without penetrating the brain parenchyma. This method would mitigate the penetration depth as well as offer good spatial resolution using beamforming and steering. To optimize any phased array for beamforming/steering with nominal side/grating lobes, a small pitch (interelement distance of each transducer) is required [27]. It is important to note that the fundamental frequency of a PZT

thin film in width extension mode as shown in [15] is not compatible with the desired pitch ($\lambda/2$) as the resonant frequency for width extension is defined by:

$$f_r = {}^{V_{PZT}}/_{2w} \quad \text{Eq. 1}$$

where V_{PZT} is the sound velocity in PZT and w is the width dimension. To counter this limitation, a local stiffening layer can be introduced as a passive elastic layer to introduce mass loading as suggested in [15], as well as alter the vibration mode to a flexural mode (which tends to vibrate at the lower resonant frequency) [27], [28].

This chapter uses design and fabrication methods to address this problem. A fully released PMUT on polyimide was designed to focus on tuning the transducer's resonant frequency using a stiff support layer. This converts the PZT transducers from a width extension to a plate-like bending behavior compatible with $\lambda/2$ pitch for focusing/steering. These current design, challenges, and limitations are explored, providing some insight into the critical factors influencing the fabrication of flexible ultrasound transducer phased arrays.

5.2 Device Design and Fabrication Method

5.2.1 Array design

Conventional PMUT designs on silicon, as shown earlier in Chapter 4, operate in a bending mode, where classical thin plate theory describes the resonant frequency and deflection motion provided appropriate boundary conditions are utilized [27-29]. In this case, the resonant frequency of the PMUT is governed by the device geometry and the flexural rigidity ($D(E, v)$). For example, the resonant frequency of a rectangular PMUT prepared on a silicon-on-insulator substrate (SOI)

with a backside released trench can be described as a rectangular plate with clamped edge boundary conditions:

$$2\pi f_r = 12\sqrt{\frac{7}{2}\left(\frac{1}{l^4}+\frac{4}{7l^2w^2}+\frac{1}{w^4}\right)}\cdot\sqrt{\frac{D(E,v)}{\rho t}} \qquad \text{Eq. 2}$$

where f_r is the fundamental mode resonant frequency, l and w are the length and width, ρ and t are the density and thickness of each layer, v is Poisson's ratio, and E is Young's modulus.

In contrast, as shown by Liu *et al*. [15] and Kim *et al.* [16], a fully released PZT transducer on polyimide is expected to operate in the width extension mode as governed by Equation 1. It is interesting to note that the resonant frequency of the fabricated transducer on polyimide deviated from the prediction for the width extension mode, and it is anticipated that the mass loading effect contributed to lowering the resonant frequency from 21.5 MHz from Equation 1 to the observed resonant frequency of 9.5 MHz [15].

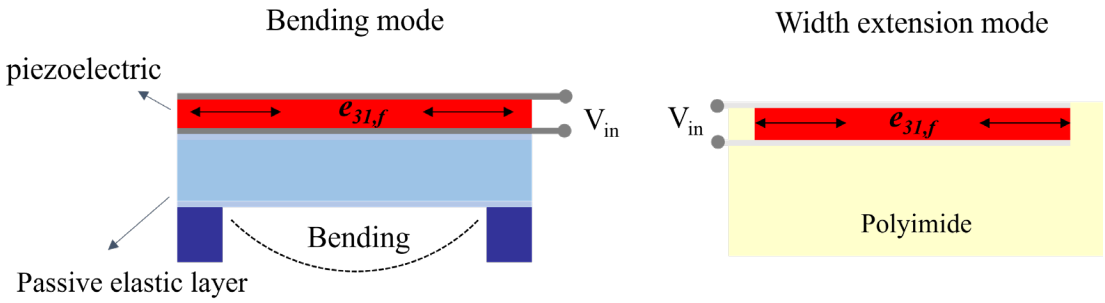

Figure 5-1: Mode of vibration for PZT thin film on a rigid and polymeric flexible substrate.

In ultrasound for neurostimulation, a resonance frequency of 0.5 – 1 MHz is preferred to reduce the attenuation of the sound wave, as it needs to travel through multiple layers of membrane, sometimes including the skull, which has a high acoustic impedance [30]. Another essential criterion for the thin film ultrasound transducer for neuromodulation is that it should be possible to operate it as a phased array to allow for focusing. In the width extension mode shown in Fig. 5-1,

the pitch between elements is larger than λ/2, which could impede beamforming/steering performance by emphasizing the side/grating lobe [31-33].

To mitigate this problem, the introduction of a stiff elastic layer is proposed in this study, as shown in Figure 5-2. An elastic layer with high Young's modulus increases both the mass and the flexural rigidity (D). Because it also moves the neutral axis of the structure out of the PZT, the structure operates in a bending mode governed by Equation 1. To implement the stiff supporting layer into the device stack, Ni was chosen; it also served a dual purpose as a metal mask for patterning of the PZT and local stiff elastic layer. It is proposed that the rectangular PZT PMUT, with a device schematic shown in Figure 5-2, be prepared via the release and transfer method using ZnO as a sacrificial layer following the methodology reported in [15]. In the initial attempts, electroplating was used to deposit the nickel layer on top of the PZT capacitor stack.

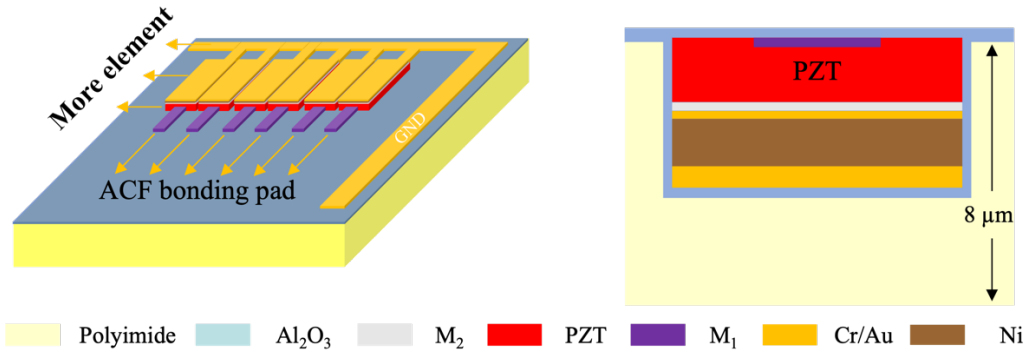

Figure 5-2: The proposed device schematic shows (left) the linear array arrangement and (right) the schematic for the cross section for PMUT on polyimide with a Ni rigid supporting layer. The device stack consists of a polyimide substrate, Al_2O_3 as a protective layer, Au as metal lines, Ni as a stiff supporting layer, Ti/Pt as a first metal electrode (M_1), PZT as a piezoelectric active layer, and Ti/Pt as a second metal electrode (M_2). ACF denotes anisotropic conductive film.

Plate theory was used to estimate the fundamental mode of vibration; however, there is not an available analytical solution for the resonant frequency in the case of a device with free boundary conditions for all edges. To navigate the device design, the equation for a device clamped on all edges, Equation 2, was used as the lower bound. The upper bound was derived from Equation 1,

modified by a factor of 1/2. This adjustment references the observed reduction in the resonant frequency of a PZT bar transducer reported in [14]. The mass loading from the electrodes and polyimide was identified as a contributing factor to the discrepancy. A model of simple harmonic vibration was employed to calculate the reduced frequency factor, estimated to be approximately 1/1.4 when polyimide and Pt account for half of the total mass [14]. In this study, as a 2 μm Ni stiff supporting layer is added to the structure previously reported in [14], the frequency factor is adjusted to 1/2.

Table 5-1: Materials properties for resonant frequency calculation [16], [34-45].

Materials	E **[GPa]**	ν	ρ **[kg/m^3]**
Al_2O_3	182	0.24	3100
Ti	90	0.32	4480
Pt	179	0.38	21400
PZT	101	0.39	7750
Au	62	0.78	19300
Ni	205	0.27	8900
Polyimide	5.32	0.34	1082

To accommodate the target frequency for neurostimulation, the length (l) was kept constant at 1000 μm, and the width (w) was varied from 400, 200, to 100 μm, as shown in Figure 5-3. Calculations were based on Equation 1 and 2 and the materials properties from Table 5-1. Because neither of the boundary conditions is correct, the actual resonance frequency of each device would range between the given numbers. Each type of array was labeled using its upper estimated resonant frequency as 2.5 MHz (Figure 5-3(a)), 5 MHz (Figure 5-3(b)), and 10 MHz (Figure 5-3(c)).

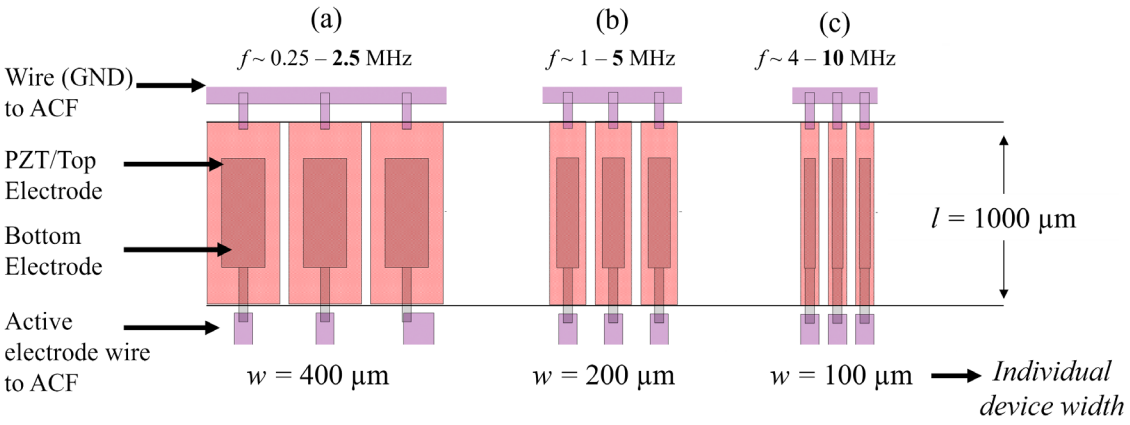

Figure 5-3: The device geometry for each case: (1) width = 400 µm, (2) 200 µm, and (3) 100 µm aiming for 2.5, 5, and 10 MHz when considering $f_{width}/2$ as the upper bound resonant frequency.

5.2.2 Hard Mask Development

A key feature of this flexible transducer is the Ni supporting layer, which serves both as a hard metal mask for PZT etching and as a structural support. Electroplated nickel has been developed as a hard mask for PMN-PT, as reported by Jiang *et al.* [46], and was adapted for PZT patterning by Welsh [47]. The process parameters in this work were adapted from Aaron Welsh's PhD thesis, which reported the optimal compressive residual stress for the electroplated Ni [47].

To verify the process for electroplating of nickel hard mask and find the optimized etch selectivity with PZT thin films, a 1 µm PZT film was prepared by the sol-gel method as described in Chapter 4, on a platinized silicon substrate. Before electroplating, a blanket conductive layer of 3 nm Cr and 100 nm Au was deposited on top of PZT thin films using DC magnetron sputtering at room temperature with the DC power set to 200 W at 5 mTorr without breaking vacuum. To create a photoresist mold for the Ni electroplating, a 7 µm AZ4620 photoresist was spun on at 4000 rpm and baked at 90°C for 1 minute and 105°C for 3 minutes. The photoresist was left at room temperature for an hour to rehydrate. It was then exposed using a maskless aligner MLA150 at 800

mJ/cm^2, soaked in a 1:4 AZ400K developer for 3 minutes, and cleaned with oxygen plasma in a Tepla M4L asher using O_2 (200 sccm), He (50 sccm), 550 mTorr pressure, and 200 W RF power.

Figure 5-4 shows a schematic of the pulse electroplating process. The nickel (II) sulfamate electroplating bath had a pH of 4.2. The bath temperature was set to 50°C, and the solution was stirred at 500 rpm. The prepared PZT sample with photoresist mold was electrically connected to the anode using alligator clips and immersed in the nickel sulfamate solution bath. The pulse electroplating process had a current density of 4 mA/cm^2 (profile shown in Figure 5-4 upper right). After deposition, the sample was rinsed with deionized water, and the photoresist was removed using a positive photoresist stripper (PRS3000), followed by acetone and isopropanol. A 1.2 µm layer of Ni was deposited at an estimated rate of approximately 80 nm per minute, as measured by profilometry.

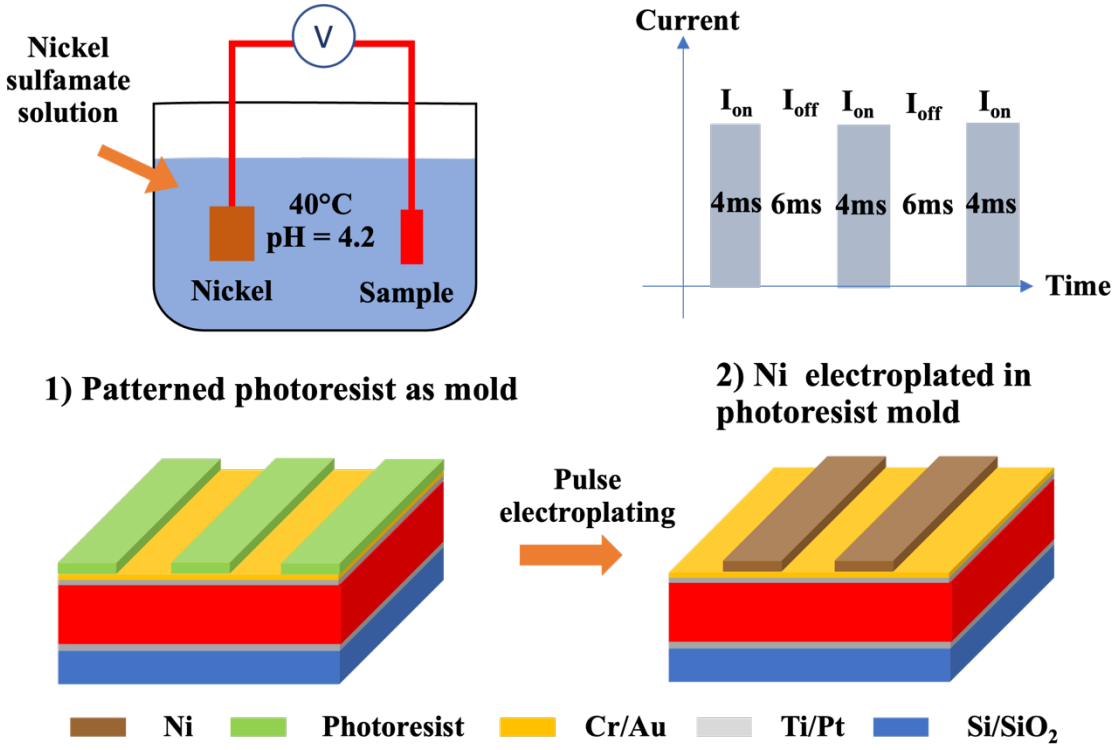

Figure 5-4: Ni electroplating schematic with the pulse profile shown a the upper left. Cr/Au was used as the electrical seed layer.

The sample with electroplated Ni was transferred to the ICP-RIE etching system (Ulvac NE550) to perform Au and PZT dry etching; the tool's chiller was set to 0°C. The Au conductive layer was patterned with a process pressure of 5 mTorr, Cl_2 at 40 sccm, the RF power at 1000 W, and the bias power at 75 W, providing an etch rate of 1500 Å per minute, optimized from [48]. After that, the 1 μm PZT was etched with the following process: pressure at 3.8 mTorr, Ar (20 sccm), CF_4 (28 sccm), Cl_2 (7 sccm), and RF/bias power set to 700 W/150 W with an etch rate of 80 Å per minute, adapted from [47], [49].

After etching, cross-sectional images were acquired using a field-emission scanning electron microscope (Zeiss Merlin FESEM) to inspect the side wall profile and to estimate the etch selectivity. The sidewall angle of the etched features in the sol-gel PZT shown in Figure 5-5 is approximately 70°. The etch ratio between Ni and PZT was 1:5, indicating that a 200 nm thick Ni hard mask is required for etching 1 μm of PZT.

In an attempt to remove the Ni hard mask, the etched sample was first soaked in Transene Ni TFB etchant (nitric acid-based etchant) at 40°C. However, as noted by Aaron Welsh, Ni often leaves residues on the etched features [47]. Thus, Cr and the Au layer, the electroplated seed layer, also served as a sacrificial layer to ensure the film surface was residue-free. The Cr and Au were removed by wet etching using Transene Au (iodine and potassium iodide-based etchant) etchant TFA type at room temperature, followed by soaking in Ni TFB etchant, as Cr can be removed in the Ni TFB etchant. Figure 5-5(c) shows the cross-section after the Cr/Au/Ni layers were removed using this method.

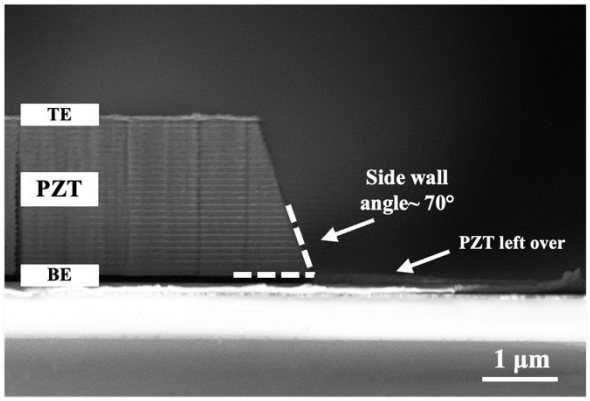

Figure 5-5: SEM cross-section image depicting the PZT sidewall profile after removal of the Cr, Au, and Ni layers. The plasma etching, performed using an electroplated Ni hard mask, results in a sidewall profile of approximately 70º.

Electron beam (E-beam) evaporation was investigated as an alternative method to deposit the Ni hard mask. A similar PZT test sample consisting of a 1.1 µm PZT layer capped with 3 nm Ti/100 nm Pt was employed to study dry etching using an E-beam Ni hard mask. The lift-off method with LOR10B and SPR3012 resists was used to pattern the E-beam evaporated Ni thin films. First, a 1 µm LOR10B was spin-coated at 4000 rpm for 45 seconds, then baked at 180°C for 3 minutes. Then SPR3012 was spun on at 4000 rpm for 45 seconds and baked at 95°C. The photoresist stack was exposed at 200 mJ/cm^2 in the Heidelberg MLA150 Maskless Aligner. The develop step for LOR10B/SPR3012 was done using a 1:1 ratio of DI water and concentrated Microposit developer. The sample was first soaked for 80 seconds, rinsed with DI water, baked at 140°C for 1 minute, and then further developed for 2 minutes to undercut the LOR10B, creating the reentrant profile. This LOR10B and SPR3012 bilayer process yields a 1 µm lift-off reentrant profile. The metal stack for the hard mask was composed of 3 nm Cr, 100 nm Au, and 250 nm Ni, with deposition rates set to 2 Å per second for Cr and Au and 1 Å per second for the Ni, respectively. The metal lift off process was done by immersing the prepared sample in a PRS3000 bath at 80°C for 1 hour, followed by an oxygen plasma cleaning with 200 sccm of O_2, 50 sccm of He, with the pressure regulated at 550 mTorr, and 300 W for 5 minutes.

To demonstrate etch selectivity, the sample was etched in an ICP-RIE (Ulvac NE550), with process conditions identical to those described in the previous section. Figures 5-6(a) and (b) show the cross-section of the etched PZT capacitor, revealing an etch ratio of 1:6.8 between PZT and the Ni mask and a sidewall angle of approximately 68°. Note that both evaporated and electroplated Ni provide comparable etch selectivity and sidewall profiles.

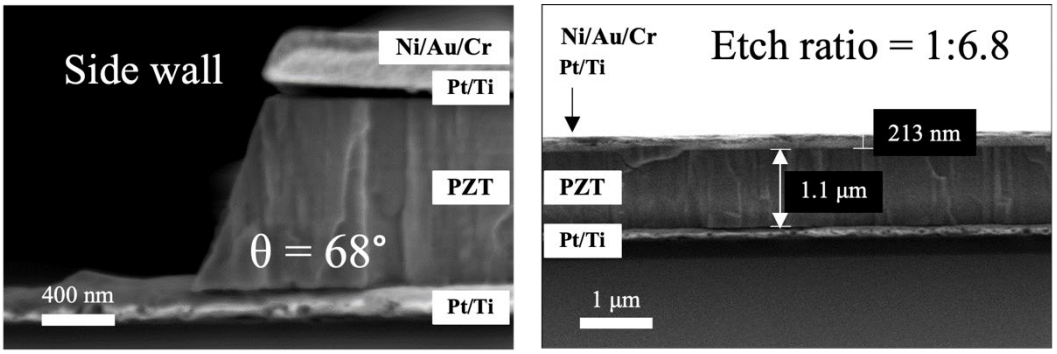

Figure 5-6: The SEM cross-section images showing the etched PZT profile using an evaporated Ni hard mask; the sidewall angle is 68º, and the etch ratio of Ni to PZT is 1:6.8.

5.2.3 Device Fabrication

The device geometries for each array are illustrated in Figure 5-7. L-Edit, a layout editor software, was used to design the photolithography masks. Three types of phased arrays were designed as shown in Figure 5-3, where the length (a) is fixed at 1000 μm and the width (b) varies from 400, 200, to 100 μm. The arrays are labeled according to their upper calculated resonant frequencies, based on width extension calculations, as 2.5, 5, and 10 MHz, respectively. The devices are designed to connect to the phased array driving circuit via an anisotropic-conductive-film (ACF) cable at an ACF pad. The pad is calculated to have a pitch of three lines per millimeter, as depicted in the bottom-right of Figure 5-7.

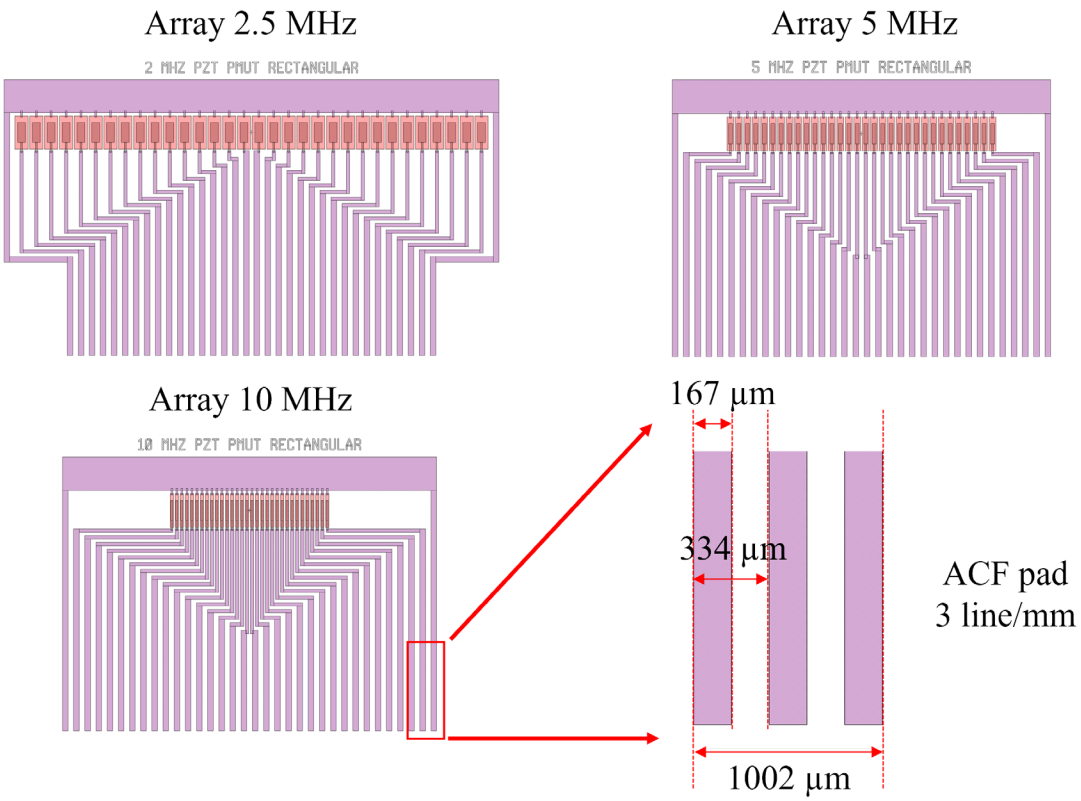

Figure 5-7: Images of array design for each type of device captured from Layout edit (*L-edit*) consisting of the transducer array, the dimensions of the contact pads, and the ACF pad area for electrical connection.

The fabrication process flow is outlined in Figure 5-8. The process began with a clean 1 µm SiO_2 / 550 µm Si substrate, followed by the deposition of 150 nm ZnO and 50 nm Al_2O_3 using a custom-built plasma-enhanced atomic layer deposition system with diethylzinc (DEZ) and trimethylaluminum (TMA) as metal-organic precursors, with N_2O and CO_2 as oxidants at 200°C for ZnO and Al_2O_3, respectively [50, 51]. The ZnO layer serves as the sacrificial layer, while Al_2O_3 is a diffusion barrier. Then, Al_2O_3 was patterned for the ACF bonding pad area by plasma etching using SPR955 as a photoresist mask; the ~2 µm thick resist was spin-coated at 2500 rpm, baked at 105°C for 1 minute, exposed at 340 mJ/cm^2 in the MLA150, and developed in CD26 for 90 seconds. The dry etching process, adapted from [52], was performed in an ICP-RIE tool, Ulvac NE550, with

gas mixtures of BCl_3 (30 sccm) and Cl_2 (10 sccm), at 10 mTorr, with RF power at 1000 W and bias power at 75 W (etch rate ≈ 1500 Å/min) as shown in Figure 5-9(a).

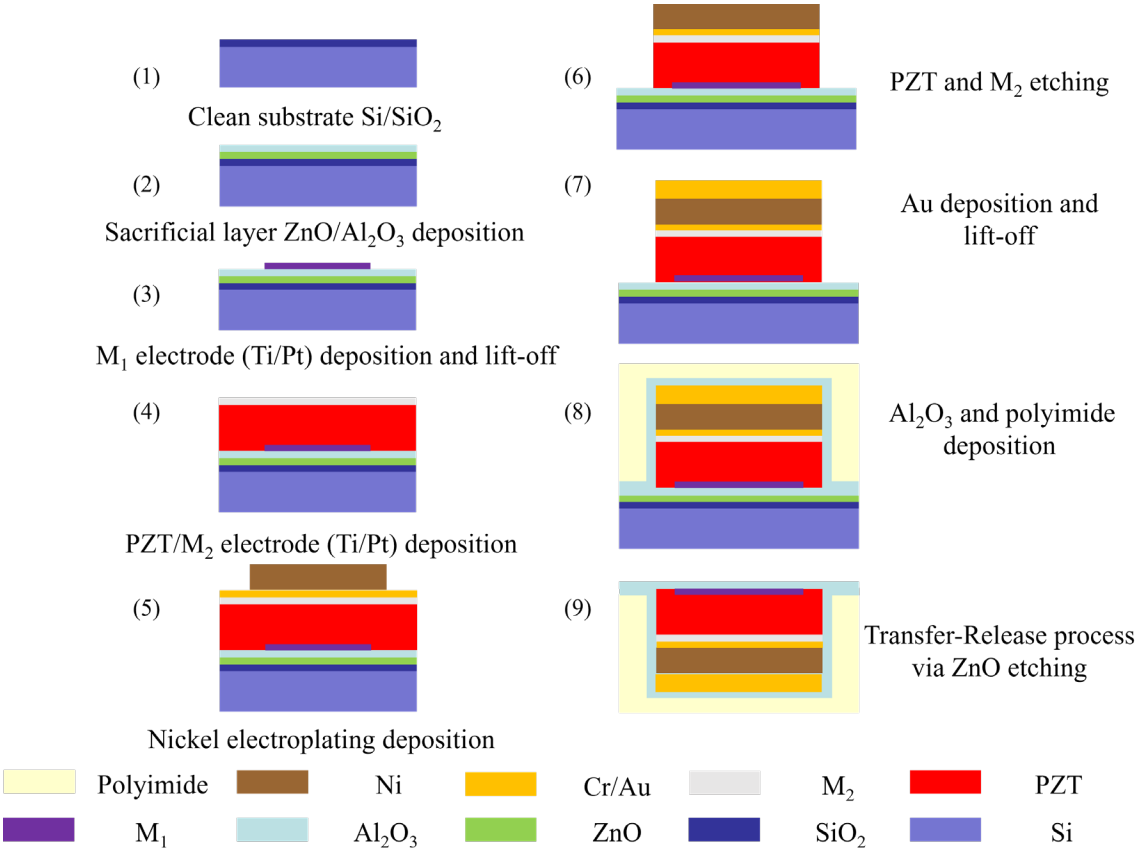

Figure 5-8: Device fabrication schematic of the fully flexible PMUT phased array.

Then, the M_1 electrode (30 nm Ti / 150 nm Pt), as shown in Figure 5-9(b), was deposited using DC magnetron sputtering (CMS-18 Kurt J. Lesker) at room temperature. The Pt was patterned by the lift-off method with LOR5A and SPR3012. For this purpose, LOR5A was spin-coated at 4000 rpm for 45 seconds, then baked at 180°C for 3 minutes. This was followed by spinning SPR3012 at 4000 rpm for 45 seconds and baking at 95°C for 1 minute. The photoresist was exposed at 200 mJ/cm^2 in the MLA150 and developed in CD26 for 75 seconds. The sample was then placed in a sputtering chamber, where 30 nm Ti and 150 nm Pt were deposited by DC sputtering at room temperature with 200 W DC power, 2.0 mTorr, and 360 seconds for Ti, and 200

W, 2.5 mTorr, and 626 seconds for Pt. After deposition, the sample was immersed in a PRS3000 bath at 80°C and cleaned using an oxygen plasma, as previously mentioned in Section 5.2.1.

A blanket film of 1 μm PZT was deposited by the sol-gel method using a commercial 2 mol% Nb-doped $Pb(Zr_{0.52}Ti_{0.48})O_3$ E1 solution with 14% excess Pb with a PbO capping, similar to the process described in Chapter 3. In short, the PZT solution was spin-coated at 2750 rpm for 45 seconds, baked at 100°C for 1 minute and 300°C for 3 minutes, and then heat treated in a rapid thermal annealer (RTA) at 700°C for 1 minute with 2 slpm of O_2 flow to crystallize the layer. This process was repeated until 1 μm thickness was reached. Finally, the PbO solution was spun on at 6000 rpm for 45 seconds, baked at 100°C for 1 minute and 300°C for 2 minutes, and then annealed in the RTA at 700°C for 1 minute with 2 slpm of O_2. The PZT was capped with a blanket film of 3 nm Ti / 100 nm Pt M_2 electrode via DC magnetron sputtering, using similar conditions to the bottom electrode but with adjusted deposition times: 36 seconds for Ti and 417 seconds for Pt.

To pattern the PZT and top electrode, a Ni layer was deposited using electroplating over a 3 nm Cr / 100 nm Au intermediate layer, as described in Section 5.2.2. The effective current for pulse electroplating was set to 4 mA/cm^2, and with a deposition rate of 80 nm per minute, the Ni layer reached a thickness of 2.4 μm, as shown in Figure 5-9(d). The PZT, M_2, and Cr/Au layers were then etched in the Ulvac NE550 system using a similar method to Section 5.2.2. The etched device is shown in Figure 5-9(e). Electrical connection lines to the ACF bonding pad were achieved by depositing 3 nm Cr / 500 nm Au via DC sputtering and patterning using the lift-off method with LOR10B and SPR3012. The photoresist lift-off patterning was done using the same method as for the evaporated Ni hard mask with LOR10B and SPR3012. For metal lines deposition, Cr/Au, the DC sputtering parameters were 200 W power. The chamber pressure was 5 mTorr, and the substrate was unheated for both Cr and Au. The device with the Cr/Au layer is shown in Figure 5-9(f). The post-release process concluded with a blanket deposition of 100 nm of PEALD Al_2O_3, using a

method similar to the Al_2O_3 diffusion barrier layer mentioned earlier. The Al_2O_3 layer served as a protective layer during the polyimide curing process, as indicated [14].

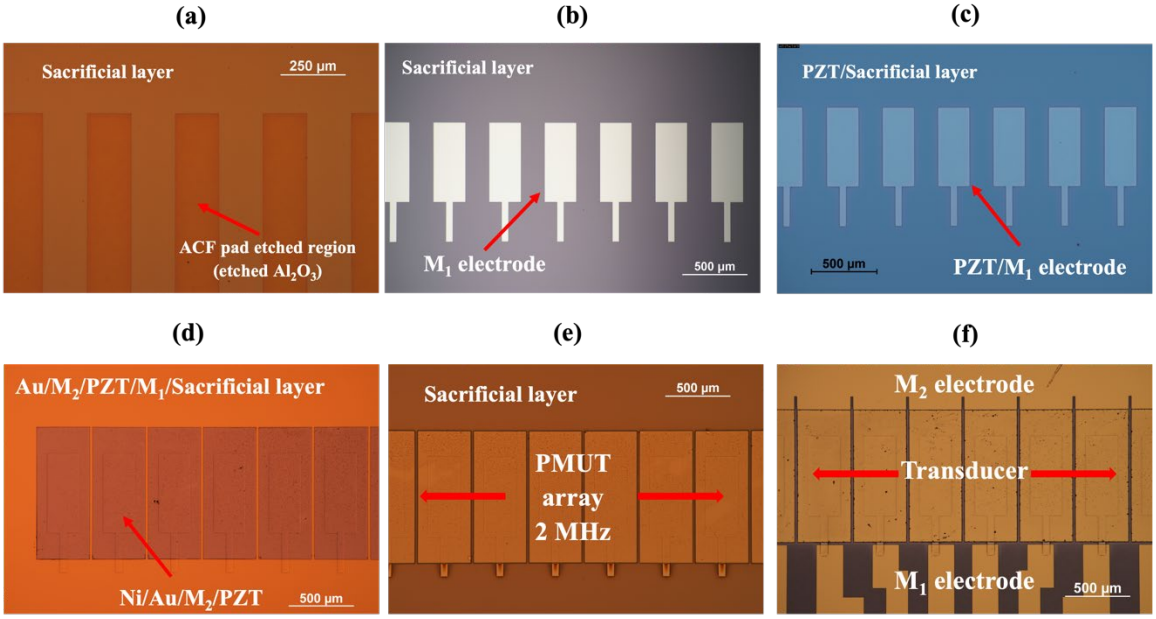

Figure 5-9: Optical microscope images illustrating fabrication stages of flexible PMUT devices: (a) Trenches etched for ACF bonding showcasing the sacrificial Al_2O_3 layer; (b) Patterned M_1 electrode revealing electrode placement; (c) Blanket PZT sol-gel deposited uniformly over the M_1 electrode; (d) Patterned Ni hard mask used for etching, showing the defined areas for PZT structuring; (e) Etched PZT bars with the residual Ni layer post-plasma etching; (f) Completed PZT array stack with deposited and patterned Au metal lines, illustrating the final assembly for the 2 MHz PMUT array.

The dielectric permittivity as a function of frequency was measured using a Hewlett Packard 4284A LCR meter with 30 mV_{AC}, across the three types of phased arrays before the release process. As shown in Figure 5-10(a)-(c), the variations across the 32 elements with the permittivity (loss) at 1 kHz were 1270 ± 15.6 (2.0 ± 0.003%), 1232 ± 6.4 (2.1 ± 0.007), and 1270 ± 15.6 (2.1 ± 0.007) for the 2.5, 5, and 10 MHz arrays, respectively. As shown in Figure 5-10(d), the polarization-electric field loops show a remanent polarization (P_r) and coercive field (E_c) of (23.4, -15.9) µC/cm^2 and (44.8, -58.9) kV/cm for the 2 MHz array, (23.4, -16.2) µC/cm^2 and (50.8, -55.8) kV/cm for the 5 MHz array, and (24.2, -17.4) µC/cm^2 and (48.1, -57.8) kV/cm for the 10 MHz array.

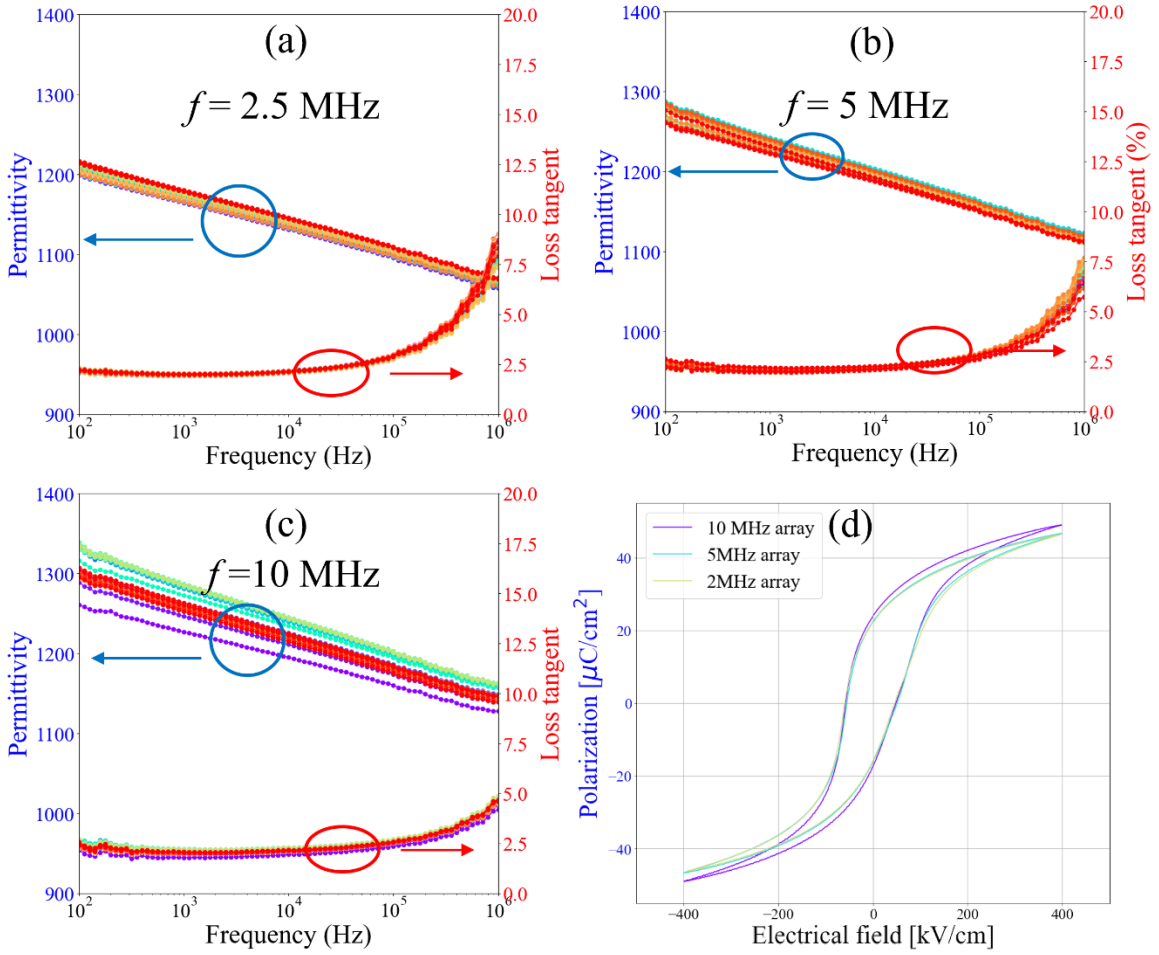

Figure 5-10: (a) – (c) Dielectric permittivity as a function of frequency and (d) polarization electric field measurements for each type of array.

The transfer and release process begins with polyimide deposition, etching, and release processes, originally developed by T. Liu [14] and modified by Victoria Vasquez, a PhD student at the School of Electrical Engineering and Computer Science at Pennsylvania State University, for this work. The polyimide source, MicroSystems PI-2611, was deposited using the spin coating method (spinning at 1500 rpm for 45 seconds) and cured at 100°C for 5 minutes (ramp rate of 3°C per minute), 250°C for 5 minutes (ramp rate of 1.3°C per minute), and 350°C (ramp rate of 1.2°C per minute). The sample was then etched to separate each array for individual release using Al_2O_3 as a hard mask. The Al_2O_3 was plasma etched using the same process outlined earlier in this section.

Afterward, the polyimide was plasma etched with an O_2 (80 sccm) and CF_4 (20 sccm) gas mixture. The pressure was regulated at 100 mTorr, with a bias voltage of 200 V and RF power of 130 W. This process resulted in a polyimide etch rate of 360 Å per minute. Each array was then separated using a dicing saw along the polyimide-etched lines as guides. The ZnO wet etching was achieved by soaking each sample in a 10 vol.% acetic acid solution bath at a bath temperature of 45°C. Experiments were conducted with the ZnO release process to explore the lateral etch rate and device structure after release. The process took 34 hours to fully release the 16 × 13 mm PMUT array's die from the silicon substrate, with an estimated lateral etch rate of 248 μm per hour. Unfortunately, the control sample encountered significant cracks in the PZT as well as peeling of the M_2 electrode after the release process. Due to these complications, releasing the actual devices was halted at the post-release stage. The challenges encountered during this experiment phase will be further discussed in the subsequent section.

5.3 Current Device Fabrication Challenges

5.3.1 Pre-Release Processing

During the early stages of device fabrication, a thicker ZnO layer (200–250 nm) was used to increase the lateral etch rate for the release process, compared to the 150 nm ZnO layer used in Liu's work [15]. However, as shown in Figure 5-11(a), the PZT began to flake off during deposition. This issue was consistently observed across three samples, where the PZT delaminated at different spin-coating layers. EDS analysis was performed to identify the root cause. As seen in Figures 5-11(b)–(e), SEM images of the area near the PZT peeling are shown along with the Al, Pb, and Zn maps. These results indicate that the interface failure occurred between the ZnO and Al_2O_3 layers. The possible reasons for this failure are suggested to be: i) excessive carbon residues reducing the

adhesion strength of the ZnO-Al_2O_3 interface [52], [53], and ii) excessive residual stress from the 200 nm thick ZnO [54]-[60]. High carbon content in thick ZnO film would lead to poor adhesion at the Al_2O_3 interface when exposed to high temperatures during PZT pyrolysis and crystallization. As noted in the device fabrication section, this pre-release problem was alleviated by reducing the ZnO thickness to 150 nm.

Another critical problem was the compatibility of the process between Au wet etching and the electroplated Ni layer. A 500 nm thick Au was used for the array of metal lines to lower the electrical resistivity and hence minimize the circuit's RC time constant. A common method for patterning Au is wet etching with commercial Transene Au Etchant Type TFA, which contains iodine, potassium iodide, and water. Figure 5-11(f) demonstrated the electroplated nickel being attacked by Au etchant [61]. During Au etching, the Ni layer, covered by SPR3012 photoresist, was damaged by the etchant from the nickel sidewalls and through photoresist pinholes, forming small circular patterns along the Ni bar edges. This issue was resolved by switching from wet etching to lift-off using LOR10B/SPR3012. The re-entrant profile thickness suits the 500 nm Au metal lines.

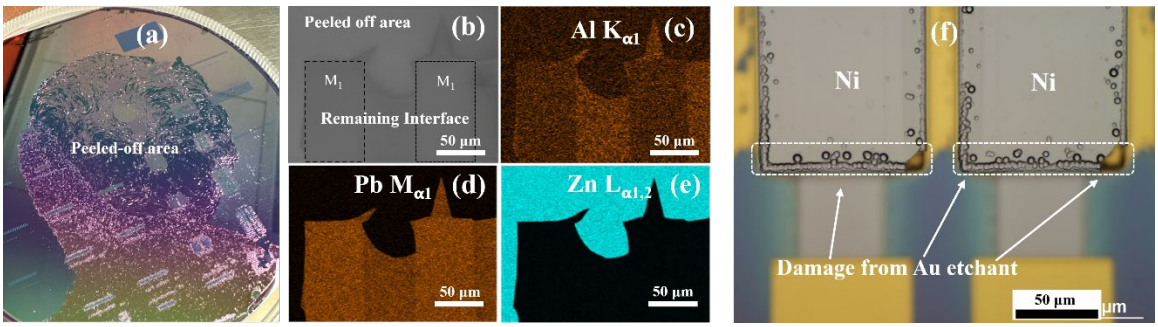

Figure 5-11: Post-release problems: (a) PZT flaking off during PZT deposition, (b) – (e) the EDS results from the flaked off area confirmed that the failed interface was ZnO – Al_2O_3, (f) the bubbles from polyimide deposition appear along the peeled edges, and (g) damage of the electroplated Ni bar during the Au wet etching process.

5.3.2 Post-Release Processing

A sample was fabricated for a release experiment where the device was diced into an individual array and then immersed into the acetic bath with parameters similar to the actual release process: 10% acetic acid, bath temperature of 45°C bath with constant agitation from a stir bar. The test sample had a similar structure to the actual device, except that it had only 1.5 μm of electroplated Ni as the stiff support layer.

After the release process, the array exhibited apparent curling, as depicted in Figure 5-12(b), primarily due to the compressive stress induced by 500 nm thick Au M2 metal lines covering most of the released structure. However, the active area did not show as much bending, potentially because it contained stiffer components such as PZT and Pt. The optical image in Figure 5-12(c) revealed significant damage to the PMUT stack post-release, including prominent cracks along the edges of the PZT bars and widespread peeling of the M_1 electrode. These cracks were primarily located along the edges of the PZT bars not covered by the M_1 electrode. A series of characterization methods was subsequently employed to address these issues.

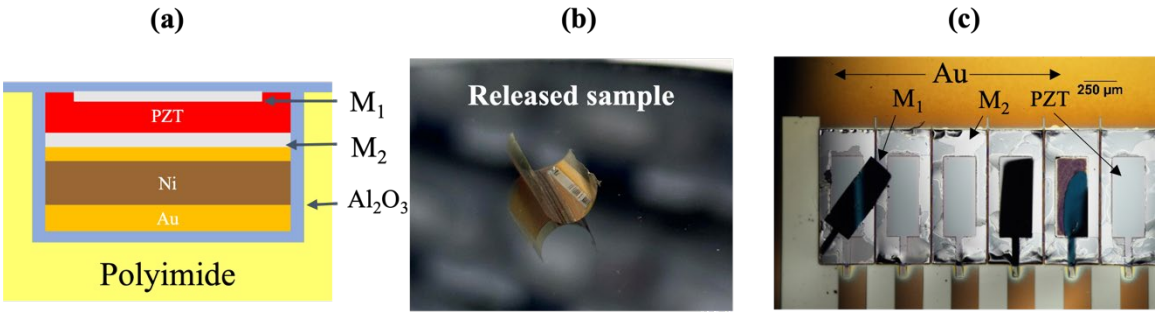

Figure 5-12: Post-release problems observed from a control sample: (a) Schematic of the test sample, (b) images of the PMUT array after the release process, and (c) optical images showing cracks in the PZT bar and peeling of the M_1 electrode.

The optical microscope image in Figure 5-13(a) illustrates the area of interest for SEM and EDS analysis. In Figure 5-13(b), an area where the M_1 electrode peeled off is shown; it is clear that

the PZT layer is damaged at the triple points, where a high concentration of PbO would be expected. This suggests that the following events occurred in this region:

i) the M_1 electrode was under significant tensile stress, which led to its detachment once the stress exceeded the adhesion strength between the PZT and the M_1 electrode,

ii) exposed PZT was etched by the 10% acetic acid solution as it was soaked for several hours during the release process at 40ºC.

In contrast, Figure 5-13(c) displays a region where the PZT was covered by ZnO and Al_2O_3 during the etch step. Furthermore, the EDS spectra from this region show strong peaks of Al and Zn, indicating that Al_2O_3 and ZnO survived the release process. This image implies that the PZT is protected by the ZnO and Al_2O_3 layers.

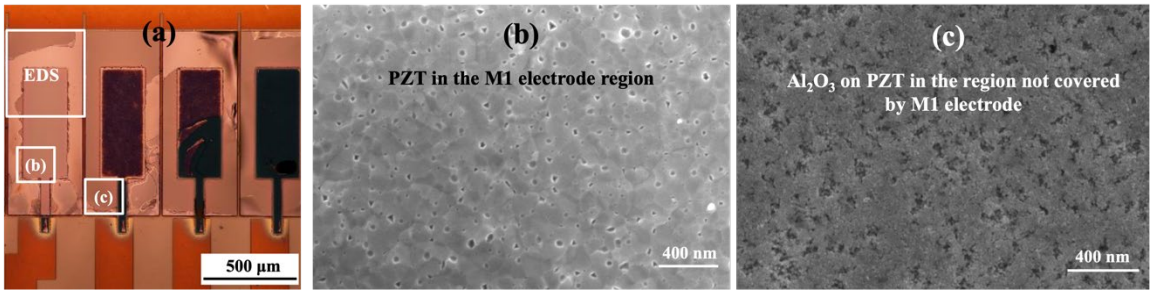

Figure 5-13: (a) Microscope images of a device with cracked PZT and a peeled M_1 layer, (b) the corresponding SEM from the PZT area underneath the peeled M_1 layer, and (c) SEM image of the area with PZT covered by ZnO and Al_2O_3.

To test the hypothesis, EDS analysis from the area highlighted in Figure 5-13(a) is presented in Figure 5-14. The electron image showing the area of interest and the emission spectra are illustrated in Figures 5-14(a) and (b). The selected intensity maps for Pt, Al, Zn, Pb, Ti, and O are displayed in Figures 5-14(c) through (h), respectively. These maps reveal that the area previously occupied by the M1 electrode shows an exposed PZT surface, whereas areas devoid of PZT correspond to the M2 electrode. Notably, Zn and Al signals were detected across most regions except in areas where the M1 electrode had detached.

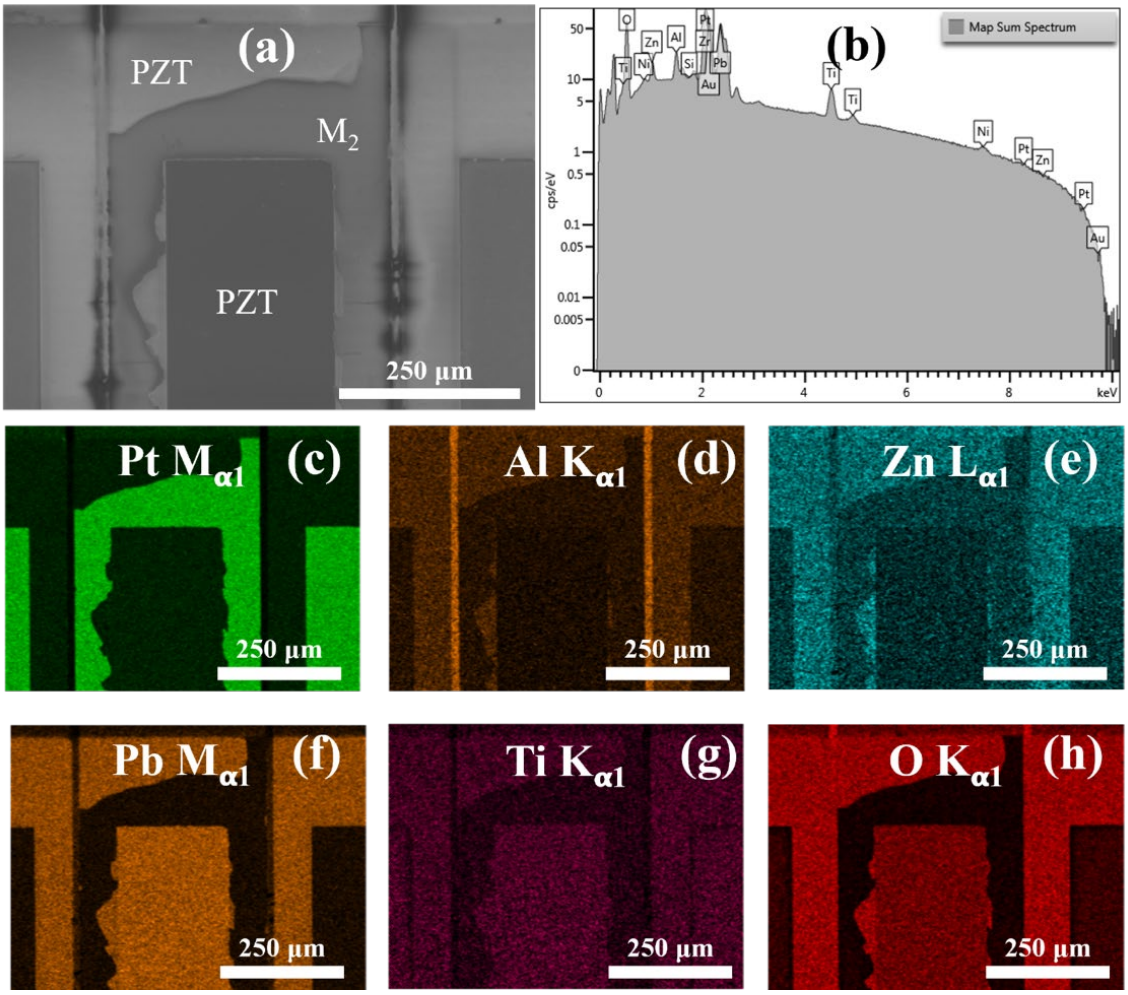

Figure 5-14: SEM-EDS results from the crack region: (a) the electron image of the investigated site, (b) the emission spectra, and the intensity map of (c) – Pt $M_{\alpha1}$, (d) – Al $K_{\alpha1}$, (e) – Zn $L_{\alpha1}$, (f) – Pb $M_{\alpha1}$, (g) – Ti $K_{\alpha1}$, and (h) – O $K_{\alpha1}$.

Subsequently, optical profilometry (Zygo Nexview 3D optical surface profiler) was utilized to understand the height profile of the PMUT element and the cracked region. Imaging was conducted with M_1 at the top of the structure. Figure 5-15(a) represents the PZT region without cracks and with M_1 still intact, and Figure 5-15(b) shows the cracked PZT region with M_1 peeled off. The height profile was obtained for each case. Figure 5-15(a) represents the undamaged area, showing curvature in both in-plane directions. The concave curvature suggests the PZT device was under comparatively higher tensile stress than the thick Ni and Au layers. Figure 5-15(b) illustrates

a height profile of the region shown in Figure 5-14(a), where the PZT is cracked near the M_1 edge, with part of the PZT layer detached, revealing the M_2 electrode. The outer step height remains at approximately 1 µm, suggesting that the Al_2O_3 and ZnO layers, as confirmed by EDS results, did not peel off during the process, thereby protecting the underlying PZT layer during the release process. The central well in the height profile, with a step height of approximately 250 nm, corresponds to the area where M_1 peeled off, which also removed the Al_2O_3 and ZnO layers. This leads to a modest amount (~20 nm) of etching of the PZT, as shown in Figure 5-13(b).

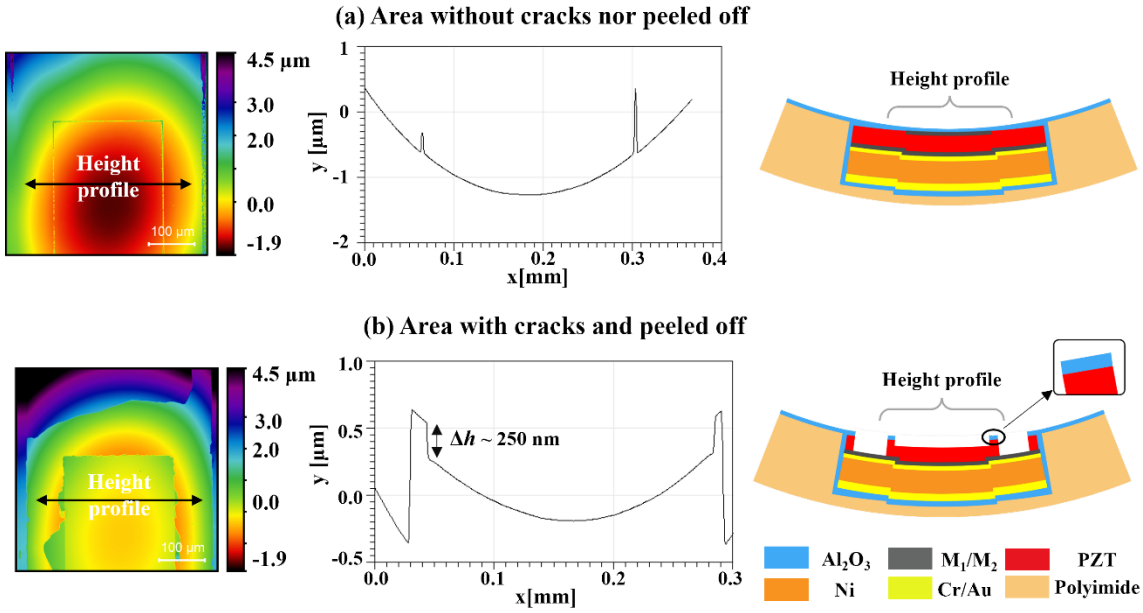

Figure 5-15: Optical profilometry results for two scenarios: (a) an undamaged area and (b) a damaged area depicted in Figure 5-14(a). The three parts of each section include a: (i) a color-coded height map showing the surface profile across the element, (ii) the height profile along the line drawn in the height map, and (iii) a schematic representation of the multilayer structure in each scenario.

It is important to note that a test structure without the Ni layer was examined using an identical release process; it revealed no cracks along the PZT edges or M_1 delamination. This, alongside EDS results that identified surface locations where cracks and delamination occurred, and optical profilometry data revealing local curvature in the device region, suggests that these

failure events likely stemmed from stress concentrations induced by M_2 electrode, Cr/Au, and electroplated Ni. The Ni will be denoted as the "underlying metal layer" for further discussion.

Figure 5-16 summarizes the current challenges in fabricating flexible phased arrays on polyimide substrates. As the device structure was initially deposited and patterned on a rigid substrate, the residual stress was determined based on the processing parameters utilized. For example, PZT thin films prepared by the sol-gel method are reported to be under tensile stress (~100 MPa) [62]-[64], and Pt electrodes initially exhibit compressive stress ranging from -100 to -300 MPa, which can transform into tensile stress of around 500 - 1000 MPa following annealing [65]. This residual stress was later relaxed after being released from the constrained silicon substrate to a flexible polyimide substrate, causing the bending illustrated in Figure 5-16(b). Such residual stresses are critical in the process development of micromachined devices, as they can result in significant mechanical failures, including delamination and cracking [55]-[60] For example, Coleman *et al*. investigated the effect of stresses on PZT thin films prepared on Ni foil via by applying the stress via the radius of curvature (ROC) method where the compressive strains above -0.3% induce delamination between the layers, while the tensile strains larger than 0.5% cause cracks in PZT thin films [64].

Based on the observations and characterization discussed in this section, the flaws in the device design can be attributed to two primary factors: i) excessive residual stress from the underlying metal, and ii) the partial coverage of the M1 electrode, with the PZT area covering only 60%. These design flaws likely cause significant stress concentration, contributing to the failure events depicted in Figure 5-16. The current hypotheses regarding these events are:

1. The comparatively large tensile stress from the Ni layer causes stress concentrations at the edges of the M_1 electrode in the PZT layer, leading to cracks in the brittle PZT layer. A possible scenario is that cracks initiate from the edges of the M_1 electrode when the device is still partially released, and M_1 has not yet delaminated.

2. The delamination of the M_1 layer occurs after the device is fully released due to the tensile stress exerted by the underlying layer. The partial coverage of the M_1 electrode, emphasized by the large tensile stress, exceeds the adhesion strength between the M_1 and PZT, causing the M_1 layer to delaminate from the PZT interface [66]. Additionally, this also was supported by direct observation during the optical microscope session where the curled device (Figure 5-12(b)) was flattened for the experiment, and the left-most M_1 electrode (Figure 5-12(c)) was delaminated from the PZT region on performing the flattening.

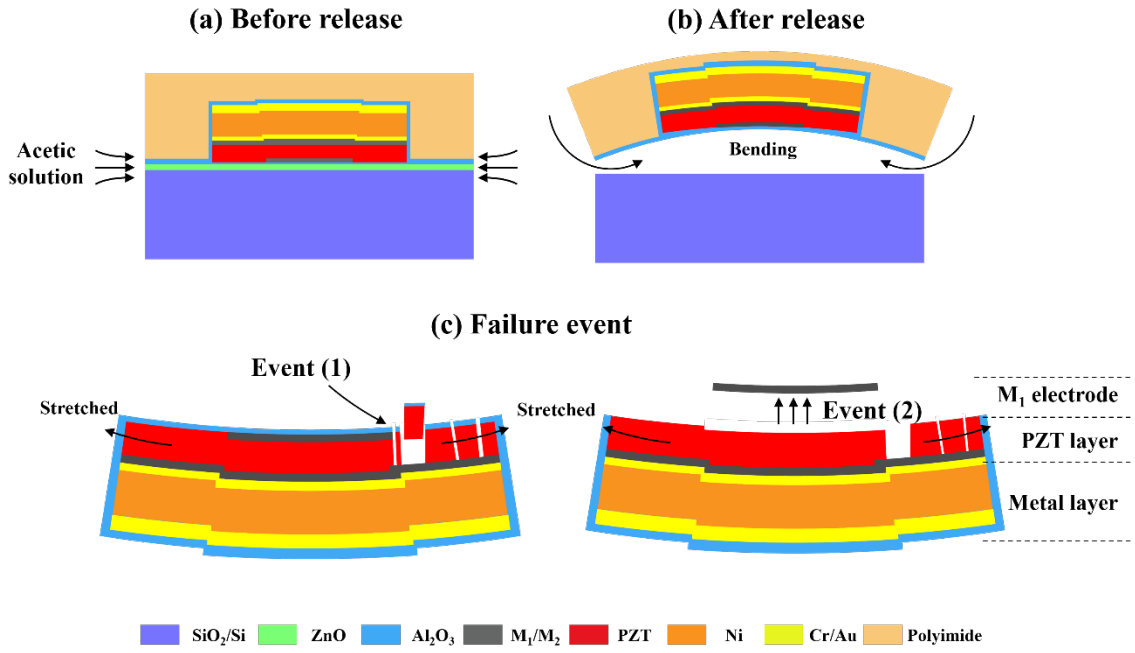

Figure 5-16: The schematic of the current design and the observed challenges: (a) Device before release, constrained to the silicon substrate. (b) Device bending upon release. (c) Event (1) shows stress concentration at the edges of the M_1 electrode, initiating cracks in the PZT region outside the electrode coverage area. This is followed by Event (2), where tensile stress from the underlying layer exceeds the interface strength of M_1, causing M_1 to delaminate from the PZT.

To address this issue, it is recommended that the root cause be mitigated by reducing the stress level in electroplated nickel. The process parameters for electroplating nickel, such as bath

temperature, current density, and pH level, strongly influence the prepared film's residual stress [67]. By optimizing these parameters, it is possible to reduce the residual stress. Alternatively, an additional stress-balancing layer can be introduced. SiO_2 deposited by RF magnetron sputtering is a promising candidate since its intrinsic stress can be fine-tuned by adjusting the process parameters. Furthermore, it can be patterned to form local stress-balancing layers at the transducer sites. Nathan Bishop, a graduate student at the STM research group at Pennsylvania State University, has optimized the process parameters for compressive SiO_2, as shown in Table 5-2. In addition, the M1 electrode can also be redesigned to cover 100% of the PZT bar; this should eliminate the stress concentration point leading to the cracks in PZT observed in the off-M_1 area.

Table 5-2: Process parameter for compressive SiO_2 by RF magnetron sputter by Nathan Bishop.

RF power [W]	RF Substrate bias [W]	O_2 to Ar ratio	Process pressure [mTorr]	Temperature	Expected deposition rate
200 W	25 W	10	5	Room temperature	0.69 Å/second

5.4 Conclusions

This chapter explored the design and fabrication of a flexible PMUT on polyimide substrates. The focus was optimizing the resonance frequency and achieving the desired interelement pitch for phased array operations suitable for neurostimulation applications. Key developments included using electroplated nickel as a hard mask and structural support, ensuring precision in the patterning process while maintaining the flexibility of the device. A stiff support layer could significantly influence the vibrational mode, transitioning from width extension to a flexural mode compatible with the $\lambda/2$ pitch necessary for effective beamforming and steering.

However, significant challenges were encountered in pre- and post-release structures, such as failed ZnO/Al_2O_3 interfaces, poor etching compatibility, stress-induced delamination, and

electrode peeling. Critically, all released samples were damaged during the release process, highlighting the need for further optimization to achieve the desired PMUT structure, especially to mitigate the residual stress and improve the overall mechanical robustness of the device. In principle, flexible PMUT arrays could offer high acoustic output and precise beam steering, which are crucial for applications like neuromodulation. This chapter highlighted the critical factors influencing the device fabrication of flexible ultrasound transducers and paved the way for further innovations in the field of flexible piezoMEMS technology.

Bibliography

[1] M. Kobayashi, C. K. Jen, and D. Lévesque, “Flexible Ultrasonic Transducers,” *IEEE Trans. Ultrason. Ferroelectr. Freq. Control*, vol. 53, no. 8, pp. 1478–1486, 2006.

[2] R. S. Frankle and D. N. Rose, "Flexible Ultrasonic Array System for Inspecting Thick Composite Structures," in *Proc. SPIE Nondestructive Evaluation of Aging Maritime Applications*, vol. 2459, pp. 51–59, 1995.

[3] H. Huang, R. S. Wu, M. Lin, and S. Xu, “Emerging Wearable Ultrasound Technology,” *IEEE Trans. Ultrason. Ferroelectr. Freq. Control*, 2023.

[4] P. Song, M. Andre, P. Chitnis, S. Xu, T. Croy, K. Wear, and S. Sikdar, “Clinical, Safety and Engineering Perspectives on Wearable Ultrasound Technology: A Review,” *IEEE Trans. Ultrason. Ferroelectr. Freq. Control*, 2023.

[5] M. Lin, Z. Zhang, X. Gao, Y. Bian, R. S. Wu, G. Park, Z. Lou, Z. Zhang, X. Xu, X. Chen, A. Kang, X. Yang, W. Yue, L. Yin, C. Wang, B. Qi, S. Zhou, H. Hu, H. Huang, M. Li, Y. Gu, J. Mu, A. Yang, A. Yaghi, Y. Chen, Y. Lei, C. Chengchangfeng, R. Wang, J. Wang, S. Xiang, E. B. Kistler, N. Vasconcelos, S. Xu, “A Fully Integrated Wearable Ultrasound System to Monitor Deep Tissues in Moving Subjects,” *Nat. Biotechnol.*, vol. 42, no. 3, pp. 448–457, 2023.

[6] M. D. Losego, L. H. Jimison, J. F. Ihlefeld, and J. P. Maria, “Ferroelectric Response from Lead Zirconate Titanate Thin Films Prepared Directly on Low-Resistivity Copper Substrates,” *Appl. Phys. Lett.*, vol. 86, no. 17, pp. 1–3, 2005.

[7] J. R. Cheng, W. Zhu, N. Li, and L. E. Cross, “Electrical Properties of Sol-Gel Derived $Pb(Zr_{0.52}Ti_{0.48})O_3$ Thin Films on a $PbTiO_3$-Coated Stainless Steel Substrate,” *Appl. Phys. Lett.*, vol. 81, no. 25, pp. 4805–4807, 2002.

[8] A. I. Kingon and S. Srinivasan, “Lead Zirconate Titanate Thin Films Directly on Copper Electrodes for Ferroelectric, Dielectric and Piezoelectric Applications,” *Nat. Mater.*, vol. 4, no. 3, pp. 233–237, 2005.

[9] H. G. Yeo and S. Trolier-McKinstry, “{001} Oriented Piezoelectric Films Prepared by Chemical Solution Deposition on Ni Foils,” *J. Appl. Phys.*, vol. 116, no. 1, p. 14105, 2014.

[10] S. Sadeghpour, B. Lips, M. Kraft, and R. Puers, “Bendable Piezoelectric Micromachined Ultrasound Transducer (PMUT) Arrays Based on Silicon-On-Insulator (SOI) Technology,” *J. Microelectromech. Syst.*, vol. 29, no. 3, pp. 378–386, 2020.

[11] Y. H. Do, W. Sukjung, M. G. Kang, C. Y. Kang, and S. Yoon, “Preparation on Transparent Flexible Piezoelectric Energy Harvester based on PZT Films by Laser Lift-Off Process,” *Sens. Actuators A Phys.*, vol. 200, pp. 51–55, 2013.

[12] Y. Jeong, J. Genoe, P. Gijsenbergh, J. Segers, P. L. Heremans, and D. Cheyns, “Fully Flexible PMUT Based on Polymer Materials and Stress Compensation by Adaptive Frequency Driving,” *J. Microelectromech. Syst.*, vol. 30, no. 1, pp. 137–143, 2021.

[13] S. Sun, M. Zhang, C. Gao, B. Liu, and W. Pang, "Flexible Piezoelectric Micromachined Ultrasonic Transducers Towards New Applications," *2018 IEEE International Ultrasonics Symposium (IUS)*, Kobe, Japan, 2018, pp. 1-4.

[14] T. Liu, M. Wallace, S. Trolier-McKinstry, and T. N. Jackson, “High-Temperature Crystallized Thin-Film PZT on Thin Polyimide Substrates,” *J. Appl. Phys.*, vol. 122, no. 16, p. 164103, 2017.

[15] T. Liu, A. Dangi, J. N. Kim, S.-R. Kothapalli, K. Choi, S. Trolier-McKinstry, and T. Jackson, “Flexible Thin-Film PZT Ultrasonic Transducers on Polyimide Substrates,” *Sensors*, vol. 21, no. 3, p. 1014, 2021.

[16] J. N. Kim, T. Liu, T. N. Jackson, K. Choi, S. Trolier-McKinstry, R. L. Tutwiler, and J. A. Todd, “10 MHz Thin-Film PZT-Based Flexible PMUT Array: Finite Element Design and Characterization,” *Sensors*, vol. 20, no. 15, p. 4335, 2020.

[17] F. Griggio, S. Jesse, A. Kumar, O. Ovchinnikov, H. Kim, T. N. Jackson, D. Damjanovic, S. V. Kalinin, and S. Trolier-McKinstry, “Substrate Clamping Effects on Irreversible Domain Wall Dynamics in Lead Zirconate Titanate Thin Films,” *Phys. Rev. Lett.*, vol. 108, no. 15, p. 157604, 2012.

[18] M. Wallace, R. L. Johnson-Wilke, G. Esteves, C. M. Fancher, R. H. T. Wilke, J. L. Jones, and S. Trolier-McKinstry, “In Situ Measurement of Increased Ferroelectric/Ferroelastic Domain Wall Motion in Declamped Tetragonal Lead Zirconate Titanate Thin Films,” *J. Appl. Phys.*, vol. 117, no. 5, p. 54103, 2015.

[19] D. N. Stephens, “CMOS Chip for Invasive Ultrasound Imaging,” *IEEE J. Solid-State Circuits*, vol. 29, no. 11, pp. 1381–1387, 1994.

[20] N. G. Pandian, A. Weintraub, S. L. Schwartz, R. Kumar, B. S. Kusay, S. E. Katz, M. Aronovitz, J. Udleson, M. A. Konstam, D. N. Salem, and A. Kreis, “Intravascular and Intracardiac Ultrasound Imaging: Current Research and Future Directions,” *Echocardiography*, vol. 7, no. 4, pp. 377–387, 1990.

[21] F. L. Degertekin, R. O. Guldiken, and M. Karaman, “Annular-Ring CMUT Arrays for Forward-Looking IVUS: Transducer Characterization and Imaging,” *IEEE Trans. Ultrason. Ferroelectr. Freq. Control*, vol. 53, no. 2, pp. 474–482, 2006.

[22] X. Zhuang, D. S. Lin, Ö. Oralkan, and B. T. Khuri-Yakub, “Fabrication of Flexible Transducer Arrays with Through-Wafer Electrical Interconnects based on Trench Refilling with PDMS,” *J. Microelectromech. Syst.*, vol. 17, no. 2, pp. 446–452, 2008.

[23] J. Schulze-Clewing, M. J. Eberle, and D. N. Stephens, “Miniaturized Circular Array [for Intravascular Ultrasound],” *2000 IEEE Ultrasonics Symposium. Proceedings. An*

International Symposium (Cat. No.00CH37121), San Juan, PR, USA, 2000, pp. 1253-1254 vol.2.

[24] J. H. Lee, I. J. Cho, K. Ko, E. S. Yoon, H. H. Park, and T. S. Kim, "Flexible Piezoelectric Micromachined Ultrasonic Transducer (pMUT) for Application in Brain Stimulation," *Microsyst. Technol.*, vol. 23, no. 7, pp. 2321–2328, 2017.

[25] V. Pashaei, P. Dehghanzadeh, G. Enwia, M. Bayat, S. J. A. Majerus, and S. Mandal, "Flexible Body-Conformal Ultrasound Patches for Image-Guided Neuromodulation," *IEEE Trans. Biomed. Circuits. Syst.*, vol. 14, no. 2, pp. 305–318, 2020.

[26] A. Javid, S. Ilham, and M. Kiani, "A Review of Ultrasound Neuromodulation Technologies," IEEE Trans. Biomed. Circuits Syst., vol. 17, no. 5, pp. 1084–1096, 2023.

[27] S. C. Wooh and Y. Shi, "Optimum Beam Steering of Linear Phased Arrays," *Wave Motion*, vol. 29, no. 3, pp. 245–265, 1999.

[28] A. W. Leissa, *Vibration of Plates*, vol. 160. Scientific and Technical Information Division, National Aeronautics and Space Administration, 1969.

[29] G. B. Warburton, "The Vibration of Rectangular Plates," *Proceedings of the Institution of Mechanical Engineers*, vol. 168, no. 1, pp. 371–384, 1954.

[30] G. Perçin, "Plate Equations for Piezoelectrically Actuated Flexural Mode Ultrasound Transducers," *IEEE Trans. Ultrason. Ferroelectr. Freq. Control*, vol. 50, no. 1, pp. 81–88, 2003.

[31] A. Javid, S. Ilham, and M. Kiani, "A Review of Ultrasound Neuromodulation Technologies," *IEEE Trans. Biomed. Circuits Syst.*, vol. 17, no. 5, pp. 1084–1096, 2023.

[32] K. K. Shung and M. Zippuro, "Ultrasonic Transducers and Arrays," *IEEE Engineering in Medicine and Biology Magazine*, vol. 15, no. 6, pp. 20–30, 1996.

[33] O. T. Von Ramm and S. W. Smith, "Beam Steering with Linear Arrays," *IEEE Trans. Biomed. Eng.*, vol. BME-30, no. 8, pp. 438–452, 1983.

[34] S. J. Ilham, Z. Kashani, and M. Kiani, “Design and Optimization of Ultrasound Phased Arrays for Large-Scale Ultrasound Neuromodulation,” *IEEE Trans. Biomed. Circuits. Syst.*, vol. 15, no. 6, pp. 1454–1466, 2021.

[35] F. Purkl, A. Daus, T. S. English, J. Provine, A. Feyh, G. Urban, and T. W. Kenny, “Measurement of Young’s Modulus and Residual Stress of Atomic Layer Deposited Al_2O_3 and Pt Thin Films,” *J. Micromec. Microeng.*, vol. 27, no. 8, p. 085008, 2017.

[36] V. Rontu, A. Nolvi, A. Hokkanen, E. Haeggström, I. Kassamakov, and S. Franssila, “Elastic and Fracture Properties of Free-Standing Amorphous ALD Al_2O_3 Thin Films Measured with Bulge Test,” *Mater. Res. Express*, vol. 5, no. 4, p. 046411, 2018.

[37] T. Tsuchiya, M. Hirata, and N. Chiba, “Young’s Modulus, Fracture Strain, and Tensile Strength of Sputtered Titanium Thin Films,” *Thin Solid Films*, vol. 484, no. 1–2, pp. 245–250, 2005.

[38] R. C. Chang, F. Y. Chen, C. T. Chuang, and Y. C. Tung, “Residual Stresses of Sputtering Titanium Thin Films at Various Substrate Temperatures,” *J. Nanosci. Nanotechnol.*, vol. 10, no. 7, pp. 4562–4567, 2010.

[39] F. Casset, A. Devos, S. Sadtler, A. Le Louarn, P. Emery, G. Le Rhun, P. Ancey, S. Fanget, and E. Defaÿ, “Young Modulus and Poisson Ratio of PZT Thin Film by Picosecond Ultrasonics,” *IEEE International Ultrasonics Symposium, IUS*, pp. 2180–2183, 2012.

[40] H. Wu, L. Wu, Q. Sun, W. Fei, and S. Du, “Mechanical Properties of Sol–Gel Derived Lead Zirconate Titanate Thin Films by Nanoindentation,” *Appl Surf Sci*, vol. 254, no. 17, pp. 5492–5496, 2008.

[41] H. Lille and J. Koo, “Determination of the Modulus of Elasticity, Poisson’s Ratio and the Coefficient of Thermal Expansion of Electrochemically Metallized Nickel Coatings,” *Materials Science*, vol. 11, no. 4, pp. 356–359, 2005.

[42] S. J. Lee, S. W. Han, S. M. Hyun, H. J. Lee, J. H. Kim, and Y. I. Kim, “Measurement of Young’s Modulus and Poisson’s Ratio for Thin Au Films using a Visual Image Tracing System,” *Current Applied Physics*, vol. 9, no. 1, pp. S75–S78, 2009

[43] D. Faurie, P. O. Renault, E. Le Bourhis, P. Villain, P. Goudeau, and F. Badawi, “Measurement of Thin Film Elastic Constants by X-ray Diffraction,” *Thin Solid Films*, vol. 469–470, no. SPEC. ISS., pp. 201–205, 2004.

[44] D. C. Baek, T. S. Park, and S. B. Lee, “Measurement of Mechanical Properties of Electroplated Nickel Thin Film,” *Key Eng Mater*, vol. 261–263, no. I, pp. 417–422, 2004.

[45] C. L. Bauer and R. J. Farris, “Determination of Poisson’s Ratio for Polyimide Films,” *Polym. Eng. Sci.*, vol. 29, no. 16, pp. 1107–1110, 1989.

[46] X. N. Jiang, J. R. Yuan, A. Cheng, G. Lavallee, P. Rehrig, K. Snook, S. Kwon, W. Hackenberger, J. Catchmark, J. McIntosh, and X. Geng, “Micromachined PMN-PT Single Crystal for Advanced Transducers,” in *Solid-state sensors, actuators and microsystems workshop, South Carolina, June*, 2006, pp. 4–8.

[47] A. Welsh, “Damage-Free Patterning of Ferroelectric Lead Zirconate Titanate Thin Films for Microelectromechanical Systems via Contact Printing,” PhD Thesis, Department of Materials Science and Engineering, Pennsylvania State University, University Park, USA, 2016.

[48] P. Werbaneth, Z. Hasan, P. Rajora, and M. Rousey-Seidel, "The Reactive Ion Etching of Au on GaAs Substrates in a High Density Plasma Etch Reactor," *The International Conference on Compound Semiconductor Manufacturing Technology*, St. Louis, 1999.

[49] C. Cheng, “Piezoelectric Micromachined Ultrasound Transducers using Lead Zirconate Titanate Films,” PhD Thesis, Department of Materials Science and Engineering, Pennsylvania State University, University Park, USA, 2021.

[50] S. H. K. Park, C. S. Hwang, H. S. Kwack, J. H. Lee, and H. Y. Chu, “Characteristics of ZnO Thin Films by Means of Plasma-Enhanced Atomic Layer Deposition,” *Electrochemical and Solid-State Letters*, vol. 9, no. 10, p. G299, 2006

[51] D. A. Mourey, D. A. Zhao, J. Sun, and T. N. Jackson, “Fast PEALD ZnO Thin-Film Transistor Circuits,” *IEEE Trans Electron Devices*, vol. 57, no. 2, pp. 530–534, Feb. 2010.

[52] X.-Y. Xue, D. P. Kim, G. H. Kim, J. C. Woo, D. S. Um, and C. I. Kim, "The Etching Properties of Al_2O_3 Thin Films in BCl_3/Cl_2/Ar Plasma," *Ferroelectrics*, vol. 384, no. 1, pp. 39-46, 2009

[53] Ames, D. P., and S. J. Chelli, "Surface Contamination Effects on Film Adhesion on Metals and Organic Polymers," *Surf. Coat. Technol.*, vol. 187, no. 2-3, pp. 199-207, 2004.

[54] D. P. Ames and S. J. Chelli, "Surface Contamination Effects on Film Adhesion on Metals and Organic Polymers," *Surf. Coat. Technol.*, vol. 187, no. 2-3, pp. 199-207, 2004.

[55] M. Ohring, “*The Materials Science of Thin Films,*” New York, NY, USA: Academic Press, 1992.

[56] M. D. Thouless and H. M. Jensen, "The Effect of Residual Stresses on Adhesion Measurements," *J. Adhes. Sci. Technol.*, vol. 8, no. 6, pp. 579-586, 1994.

[57] E. C. Onyiriuka, L. D. Kinney, and N. J. Binkowski, "Adhesion and Delamination of Tantalum and Chromium Films on Glass," *J. Adhes. Sci. Technol.*, vol. 11, no. 7, pp. 929-940, 1997.

[58] R. H. Dauskardt, M. Lane, Q. Ma, and N. Krishna, “Adhesion and Debonding of Multi-Layer Thin Film Structures,” *Eng. Fract. Mech.*, vol. 61, no. 1, pp. 141–162, 1998.

[59] A. Moridi, H. Ruan, L. C. Zhang, and M. Liu, “Residual Stresses in Thin Film Systems: Effects of Lattice Mismatch, Thermal Mismatch and Interface Dislocations,” *Int. J. Solids Struct.*, vol. 50, no. 22–23, pp. 3562–3569, 2013.

[60] M. D. Thouless and H. M. Jensen, "The Effect of Residual Stresses on Adhesion Measurements," *J. Adhes. Sci. Technol.*, vol. 8, no. 6, pp. 579-586, 1994.

[61] “Transene etchant compatibility chart. | Transene,” *Transene* |, Feb. 26, 2014. https://transene.com/etch-compatibility/ (accessed Jun. 03, 2024).

[62] R. J. Ong, D. A. Payne, and N. R. Sottos, "Processing Effects for Integrated PZT: Residual Stress, Thickness, and Dielectric Properties," *J. Am. Ceram. Soc.*, vol. 88, pp. 2839-2847, 2005.

[63] T. A. Berfield, R. J. Ong, D. A. Payne, and N. R. Sottos, "Residual Stress Effects on Piezoelectric Response of Sol-Gel Derived Lead Zirconate Titanate Thin Films," *J. Appl. Phys.*, vol. 101, no. 2, p. 024102, 2007.

[64] K. Coleman, J. Walker, T. Beechem, and S. Trolier-McKinstry, "Effect of Stresses on the Dielectric and Piezoelectric Properties of $Pb(Zr_{0.52}Ti_{0.48})O_3$ Thin Films," *J. Appl. Phys.*, vol. 126, no. 3, p. 034101, 2019.

[65] L. Zhang, M. Ichiki, and R. Maeda, "Residual Stresses in Pt Bottom Electrodes for Sol-Gel Derived Lead Zirconate Titanate Thin Films," *J. Eur. Ceram. Soc.*, vol. 24, no. 6, pp. 1673-1676, 2004.

[66] H.-H. Yu, M. Y. He, and J. W. Hutchinson, "Edge Effects in Thin Film Delamination," Acta Mater., vol. 49, no. 1, pp. 93-107, 2001.

[67] J. K. Luo, M. Pritschow, A. J. Flewitt, S. M. Spearing, N. A. Fleck, and W. I. Milne, “Effects of Process Conditions on Properties of Electroplated Ni Thin Films for Microsystem Applications,” *J. Electrochem. Soc*., vol. 153, no. 10, p. D155, 2006.

Chapter 6

Conclusions and Future Work

6.1 Conclusions

This thesis explores the piezoelectric response of released PZT thin films and their implementation in micromachined ultrasound transducers (PMUT) for neurostimulation applications.

Using double beam laser interferometry, the improvement in the piezoelectric response of a 1 μm thick, 2 mol% Nb-doped $Pb(Zr_{0.48}Ti_{0.52})O_3$ thin film was investigated in partially released and clamped structures. The released structure was fabricated using a two-step backside etching process with ZnO as a DRIE stop layer and later as a sacrificial layer. ZnO was pre-patterned into a circular shape before the PZT stack deposition and patterning and was wet etched through the silicon backside vias. The the large signal effective longitudinal piezoelectric coefficient ($d^*_{33,f}$) of the clamped PZT film was 126 ± 13 pm/V. In comparison, partially released PZT samples with 50% and 75% released area ratios showed a threefold improvement over the clamped sample, with $d^*_{33,f}$ values of 410 ± 6 pm/V and 420 ± 8 pm/V, respectively. Validation using single-beam laser interferometry confirmed that the deflection amplitude was within the correctable range of DBLI. The observed enhancement is attributed to:

i) Changes in stress levels in the released structure,

ii) Removal of mechanical constraints from substrate clamping,

iii) Enhanced domain wall movement.

This finding demonstrates that substrate declamping can bring the film's piezoelectric response closer to that of bulk ceramics of the same composition. It marks the first quantitative measurement of $d^*_{33,f}$ for unclamped piezoelectric thin films.

The released structure was used to fabricate a PMUT phased array for neurostimulation applications. The phased array design was optimized using k-Wave simulation to operate at a focal distance (F) of 20 mm and a steering range (θ_s) of -60° to 60°. Using the classical theory of plates for a rectangular bar with clamped edges, the PZT bar with 8.3 × 0.78 mm dimensions was designed with three active piezoelectric areas defined by the trench dimensions calculated to be ~8000 × 130 μm. The 32-element PZT bar was arranged as a linear phased array for focusing and steering. The elements were driven by unipolar square pulses as a function of frequency, with a maximum acoustic pressure at 1.4 MHz. At the optimum frequency, in-water beamforming targeting at F = 20 and 30 mm from the transducer achieved a maximum peak-to-peak acoustic pressure of 0.44 MPa at a 14.6 V unipolar square pulse, corresponding to a I_{SPPA} of 1.29 W/cm². This work represents the first optimization and fabrication of thin film PMUT for ultrasound neuromodulation applications.

Further steps toward neuromodulation explored the potential of fully flexible ultrasound transducer phased arrays for implantable ultrasound stimulation. A 2 mol% Nb-doped $Pb(Zr_{0.52}Ti_{0.48})O_3$ thin film was selected as the active piezoelectric layer, combined with a transfer and release method to achieve a flexible PZT PMUT on a polyimide substrate. The key design feature in this PMUT is the introduction of a stiff metal support layer to couple the bending mode to the width extension mode of the PZT bar, to lower the resonant frequency and accommodate the interelement pitch for beamforming needed for neurostimulation applications. The device dimensions and fabrication process flow involved using a blanket ZnO thin film as the sacrificial layer and 8 μm polyimide as the flexible substrate. An electroplated Ni hard mask was used to pattern a 1 μm PZT thin film and left on top as a metal contact and stiff elastic layer. The release

process involved wet etching of ZnO using an acetic acid solution at 45ºC. However, the transferred device exhibited cracks along the edges of the PZT rectangular bars, and several M_1 electrodes peeled off. The cracks were confirmed to be in the PZT layer, propagating along the edges where the M1 electrode did not cover the PZT. This suggests that the asymmetric structure from electrode coverage creates stress concentration regions, initiating cracks due to high residual stress in the stack. The residual stress from Ni might also contribute to the M_1 electrode delamination, as the stress level could exceed the adhesion strength of M_1. Proposed solutions to address this problem include:

i) introducing a compressive layer, such as SiO_2, to counterbalance the stress levels in the structure,

ii) adjusting the 60% electrode coverage of M_1 to 100% to reduce stress concentration problems.

Overall, this thesis highlights improvements in the piezoelectric response and the feasibility of PMUT technology for neurostimulation applications, providing a foundation for further development in flexible and implantable ultrasound devices.

6.2 Future Work

- **Improve the released piezoMEMS structure for quantitative measurement of piezoelectric coefficient.**

To extend the sample sets for the piezoelectric measurements, the samples shown in Figure 6-1 were prepared in a manner that was similar to those in Chapter 3, with the top electrode designed to be smaller than the DRIE hole to reduce the bending from the area where the top electrode overlapped with the silicon substrate.

Figure 6-1(a) shows that 150 nm of ZnO was deposited using PEALD and patterned into a circular shape with diameters of 400, 600, 800, 1000, 1200, and 1400 µm on top of the clean silicon substrate. Then, 10 nm of ZnO and 200 nm of Al_2O_3 were subsequently deposited as an insulator layer and diffusion barrier. The bottom electrode layer consisting of 30 nm of Ti and 100 nm of Pt was deposited using DC magnetron sputtering and patterned via the lift-off method, as demonstrated in Figure 6-1(b). Then, PZT deposition and patterning were performed using the sol-gel method and ICP-RIE, as described in Chapter 3, into a circular shape as shown in Figure 6-1(c). The backside etching was done via DRIE using the Bosch process with the substrate temperature regulated at 3ºC. A backside-etched sample with a ZnO diameter (400 µm) smaller than the DRIE vias (800 µm) is shown in Figure 6-1(d). The device schematic, Figure 6-1(e), illustrates the diameter for each layer where the top electrode, PZT, and DRIE vias diameters are fixed, and ZnO diameters are varied to extend the release area. With careful wet etching of the ZnO sacrificial layer, this set of devices should provide insight into the released effect on the piezoelectric coefficient through DBLI measurement.

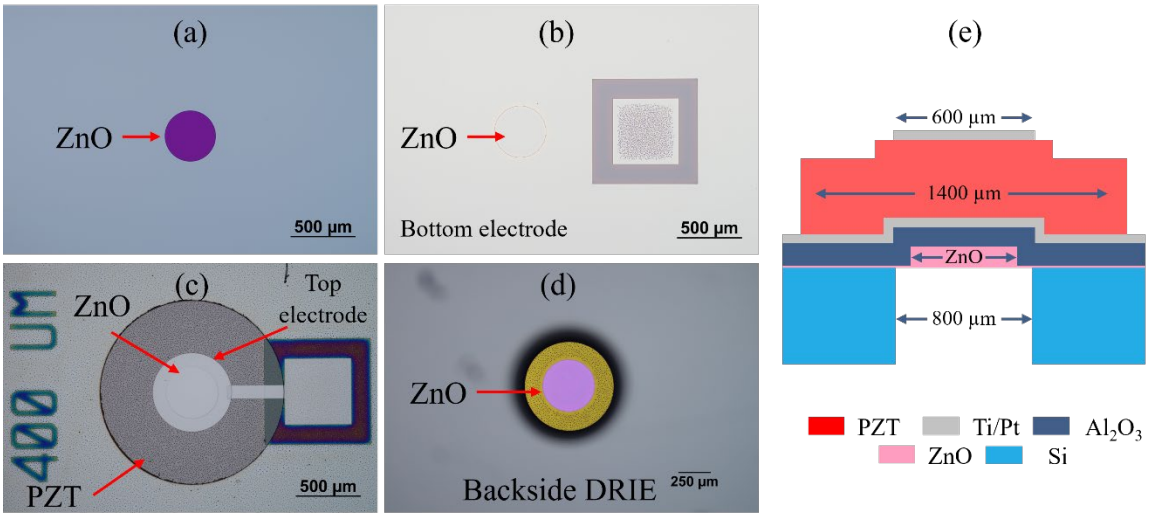

Figure 6-1: Devices fabrication flow showing (a) patterned ZnO sacrificial layer, (b) bottom electrode, (c) circular-shaped PZT and top electrode, (d) DRIE vias, and (e) the device schematic.

The current device exhibits several flaws that limit the released area to 50% and 75%, including:

1) the hinge at the edges of the released structure, which can introduce complex bending after release,
2) a thick top electrode and a continuous bottom electrode that can induce some mechanical clamping of the piezoelectric layer [1], [2],
3) a top electrode overlapping with the substrate, which could introduce an undesirable bending motion (addressed above) [3],
4) a zero-field diaphragm bending which can slow the etching of ZnO by limiting mass transfer through a smaller released gap,
5) a thick Al_2O_3 underneath the released PZT structure can induce an unbalanced stress in the released structure.

Thus, a redesigned structure is proposed to address these issues, as Figure 6-2 illustrates. The fabrication process begins with the deposition and patterning of 150 nm ZnO using PEALD and wet etching to define the released area. This is followed by a blanket deposition of 150 nm SiO_2 via RF magnetron sputtering.

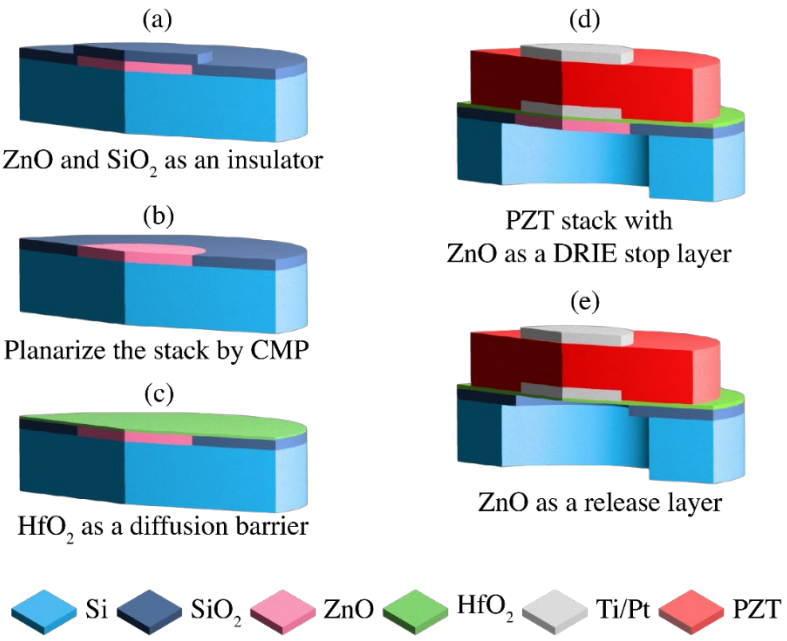

Figure 6-2: The fabrication flow for released piezoMEMS for double beam laser interferometry with ZnO as a release definition layer.

The SiO_2 layer could then planarized using chemical mechanical polishing [4], [5]. Subsequently, a thin layer of approximately 50–80 nm HfO_2 could be deposited to serve as an additional diffusion barrier and insulation layer between the PZT and the silicon substrate, complementing the thin ZnO and SiO_2 layers. The bottom electrode, consisting of 30 nm Ti and 100 nm Pt, would be deposited by DC sputtering and patterned into a circular shape using lift-off method with the diameter designed to be smaller than the through silicon vias. A 1 μm thick, 2 mol% Nb-doped $Pb(Zr_{0.48}Ti_{0.52})O_3$ layer would then be deposited by the sol-gel method and patterned by ICP-RIE, as previously detailed in this thesis. A circular top electrode, comprising a thinner Pt, such as 50 nm in thickness with a diameter matching the bottom electrode, would be deposited and patterned similarly. Following the top electrode deposition, the sample would be annealed at 500°C in an RTA for 15 minutes, which would minimize the clamping effect from the electrode.

The backside process should follow the procedures outlined in Chapter 3. Protek B3 should be applied to protect the front-side of the wafer. Subsequently, HfO_2 and SiO_2 on the substrate backside should be etched using buffered oxide etchant (BOE), and a lithography process with AZ4620 could be used for of the through-silicon vias. Bulk silicon backside etching will continue until the vias reach the ZnO. This process will be monitored using optical profilometry and optical microscopy.

Finally, the ZnO should be wet etched to release the structure. It is interesting to note that one challenge for the wet etching of ZnO is the diaphragm bending at zero-field; this might be fixed by a removable compressive layer to stress balance the film during the wet etching of ZnO. This layer could be a combination of 500 nm electroplated Ni with a 100 nm Au seed layer. Following the ZnO etching, Ni and Au can be removed by wet etching using Transene Nickel and Au etchant.

With these adjustments to the design, the device is expected to exhibit reduced mechanical clamping, specifically from thinner top electrodes and patterned bottom electrodes, and minimize bending motion, as the active part does not cover the substrate area. The planarized membrane with a thinner insulator layer should allow for a symmetrically released membrane. Additionally, a surface metrology technique such as optical profilometry to reveal overall diaphragm deflection motion, together with the DBLI technique to reveal the corresponding piezoelectric response, will further enhance the analysis. Ultimately, this will enable the precise quantification of the longitudinal piezoelectric coefficient with a larger release area as well as expand the $d^*_{33,f}$ database, facilitating piezoMEMS simulations, to include other important piezoelectric materials such as ZnO, AlN, and AlScN.

- **Improve the released process with non-buffer ZnO wet etching.**

Lateral etching through backside etching vias presents significant challenges due to issues with mass transport and local pH variations. An acetic buffered solution was explored to reduce the etch rate and maintain consistency throughout the process, the original process development was done for the purpose of high precision patterning of ZnO thin film transistors [6], [7]. However, this method may not be suitable for etching larger features such as the ZnO release area as the etch rate is slow. Therefore, exploring new types of etchants for ZnO could facilitate the release process, especially when using HfO_2 and SiO_2 as diffusion barriers and insulators [8]-[10]. The goal would be to achieve enhanced selectivity.

Wet etching of ZnO has been extensively investigated using various concentrations of acid solutions such as hydrochloric acid (HCl), nitric acid (HNO_3), sulfuric acid (H_2SO_4), and phosphoric acid (H_3PO_4) [11]-[13]. These acid solutions offer high etch rates (< 100 nm/minute), with the etch selectivity being controllable by varying concentration and pH levels. With HfO_2 and SiO_2 as the barrier layer, higher concentrations can be explored to achieve a faster release process.

Ferric chloride ($FeCl_3$) also exhibits a fast wet etch rate for ZnO; however, the resulting insoluble reaction by-product ($Fe(OH)_3$) must be addressed, particularly in processes where lateral etching is required [13], [14] Ammonium chloride (NH_4Cl) presents an interesting alternative for lateral etch rates. As Lee *et al*. demonstrated, by adding NH_4OH to the solution, the lateral etch rate increased by ten times due to the controlled undercut facilitated by the NH_3 by-product [6].

By investigating these alternative etchants, it may be possible to enhance the selectivity and rate of the etching process, thereby improving the overall quality and precision of ZnO thin film patterning for various applications.

- **Vertical grain size contribution to piezoelectric response study**

As the released structure and wet etching process are optimized, the released structure can be applied to explore more piezoelectric response in piezoelectric thin films. Grain size is a known factor that constrains the piezoelectric response in thin films. However, with the released structure exhibiting improved piezoelectric response close to bulk ceramics, it is intriguing to revisit this concept, especially from the perspective of columnar grain size. In bulk ceramics, Randall *et al.* studied the relation between the volumetric grain size and the piezoelectric response in PZT bulk ceramics, showing that the piezoelectric coefficient (d_{33}) is drastically reduced below 0.8 μm grain size, as shown in Figure 6-3 [15]. Notably, that the lateral grain size in thin films is generally in the sub-micron range, and the vertical grain size is governed by the film thickness, as shown in Figure 6-3(c). Since the piezoelectric response in bulk ceramics improves with increasing grain size, it is hypothesized that the piezoelectric response in thin films will also be enhanced as a function of columnar grain size. Therefore, by measuring $d_{33,f}^{*}$ using the proposed device schematic, we can measure film thickness in released thin films, gaining insights into the contribution of columnar grain size to the piezoelectric coefficient.

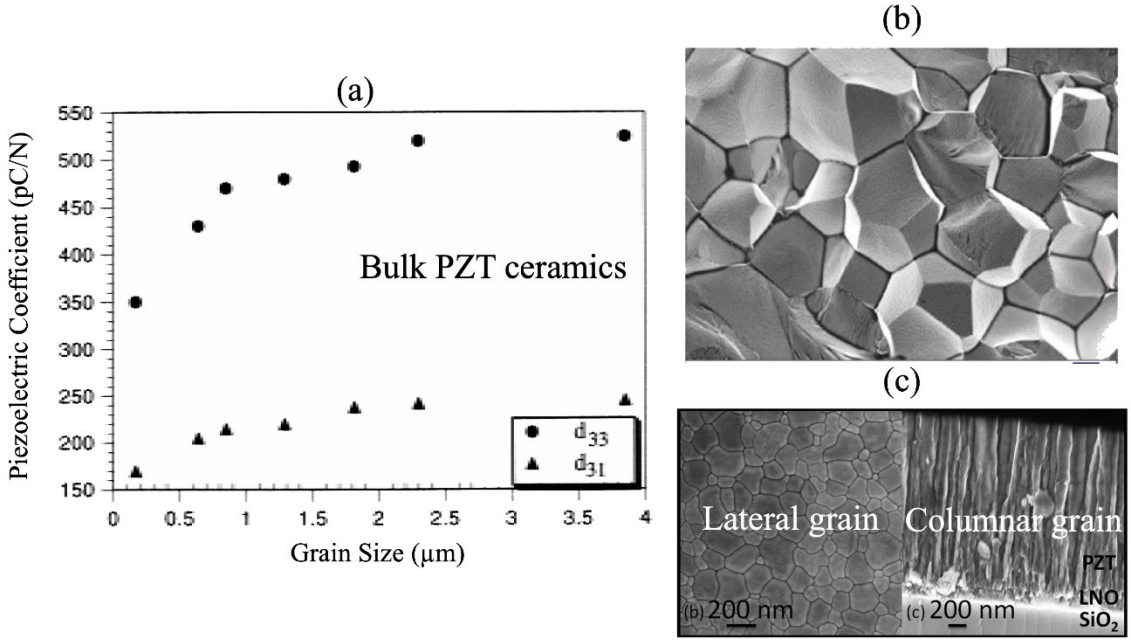

Figure 6-3: (a) The relation between grain size and piezoelectric coefficient in bulk ceramics [15], (b) the grain structure in bulk ceramics [16], and (c) lateral and through thickness grain sizes of columnar thin films [17].

To investigate this limitation in columnar grain size, the released structure proposed earlier can be employed to prepare the released piezoelectric structure with three different thicknesses: 0.5 μm, 1.5 μm, and 2.5 μm, as illustrated in Figure 6-3. By optimizing the lateral grain size for each sample, these thickness variations can help distinguish the effects of columnar grain size on the piezoelectric response in released thin films and compare with the piezoelectric response limited under 1 μm grain size observed in bulk ceramics.

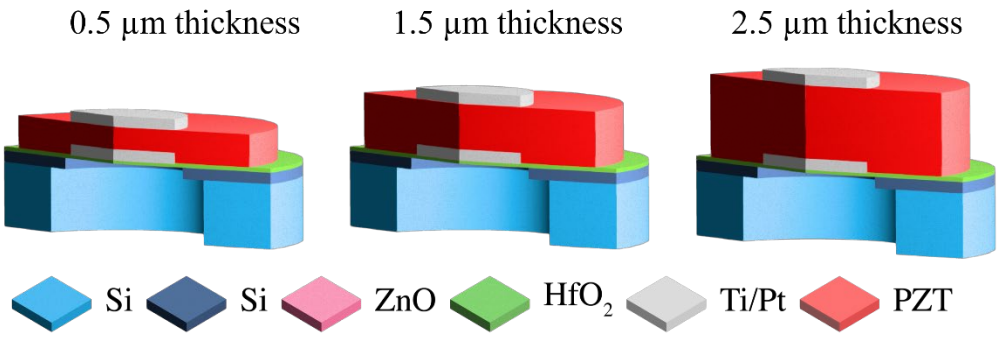

Figure 6-4: The device schematics of released structure with different thicknesses.

- **Multilayer PMUT using PZT/AlN structure**

To enhance the performance of PMUTs for transceiver applications, a multilayer structure combining PZT and AlN is proposed. PZT-based PMUTs excel in transmit performance but often exhibit comparatively poor receive sensitivity. This reduced sensitivity is attributed to a small voltage coefficient, which is inversely proportional to the large dielectric permittivity for PZT (ε_r ~ 1200) as shown in Table 1-1. Specifically, PZT thin films have a voltage coefficient ($h_{31,f}$) approximately ten times lower than that of AlN ($h_{31,f}$ ~ 0.01) for PZT compared to ($h_{31,f}$ ~ 0.1 for AlN). By incorporating a multilayer structure with both PZT and AlN, it is anticipated that the PMUT performance can be improved by using PZT for transmit and AlN for receive, leveraging the complementary properties of the two materials. A multilayer PMUT fabrication could be prepared using the transfer method similar to Chapter 5 [18],[19].

In the interest of maximizing the piezoelectric response, {001} oriented PZT and AlN thin film stack should be investigated. The {001} oriented PZT film could be achieved for the first layer using a {111} oriented Pt bottom electrode, as demonstrated in Chapter 4. To grow (001) AlN on top of the PZT layer, it is essential to find a suitable substrate metal to serve as both a common electrode and template for the AlN. Pt has been reported to induce (001) AlN due to a small lattice mismatch between the (002) plane of AlN and the (111) of FCC Pt. Therefore, (111) Pt deposited

on a {001} oriented PZT layer could serve as a common electrode and seed layer for (002) AlN [20].

This section presents preliminary work on the optimization of *c*-axis oriented AlN for a multilayer transducer PMUT, following prior reports of AlN sputtering [20]-[26]. The AlN deposition was optimized using a pulsed DC reactive magnetron sputter system, Kurt J. Lesker CMS18 system, and the target-to-substrate distance was fixed at 5.5 inches. The substrate temperature dependence on was studied for temperatures ranging from 250 °C, 350°C, and 450°C. Other deposition parameters remained fixed: the chamber pressure was 3.3 mTorr, and the reactive gas ratio was 1:1 Ar:N_2. The power supply was operated at 300 W. Film crystallinity was studied via XRD, as shown in Figure 6-5(a). Films deposited at 250 °C did not show a (002) peak, implying that the film was amorphous. However, the diffraction peak intensity (002) increased as the substrate temperature increased; the sample prepared at 450°C had the highest intensity as high thermal energy-assisted crystallization and improved the surface diffusion of atoms during deposition. Thus, a 450°C deposition temperature was selected for further investigation.

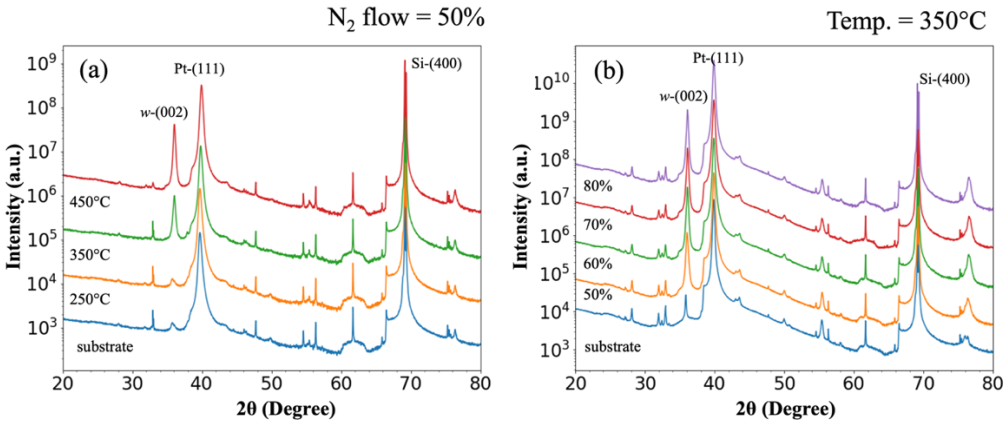

Figure 6-5: XRD patterns for AlN deposition via pulsed DC deposition; effects of a) substrate temperature and b) the N_2: Ar ratio. The wurtzite AlN, *w*-(002) and *w* -(004), (111) Pt, and (004) Si peaks are labeled, while the other peaks are attributed to the substrate, as shown in the bottom line of each graph.

The second parameter to be studied was the gas mixture. Ar, an inert gas, and N_2, a reactive gas, were involved in the deposition. N_2 improved film crystallinity while Ar maintained the sputter rate. Due to heavier Ar atomic mass, higher kinetic energy during a collision with the Al target produced a higher sputter rate [20], [25][27]. N_2 varied from 50% to 80% when the deposition temperature was 450°C, the chamber pressure was 3.3 mTorr, and the power was 300 W. A higher N_2 percentage was expected to improve film crystallinity and lower the concentration of N vacancies. Figure 6-5(b) shows a strong (002) wurtzite structure AlN in the XRD patterns for all deposition conditions.

The electrical and piezoelectric properties of the thin film were characterized. Figure 6-6(a) shows the dielectric permittivity and loss tangent measured at 10 kHz with 100 mV_{AC} excitation. The dielectric permittivity and loss tangent show a decreasing trend as the N_2 content in the case phase increases. The measured loss tangent was mostly below 1%, except for the sample deposited at 50% N_2 showing ~ 1%. This increase in loss tangent might result from a higher defect content associated with a relatively low N_2 content and energetic bombardment [28][31]. The films' transverse piezoelectric coefficient ($e_{31,f}$) was measured and converted to the voltage coefficient $h_{31,f}$ as shown in Figure 6-6(b) and (c), with the corresponding deposition rate. It was apparent that the film prepared at 60% N_2 had a relatively high $h_{31,f}$ (-0.09 ± 0.015 C/m^2), which is in good agreement with the reported value in the literature (~ -0.1 C/m^2) [32]-[34]. The AlN prepared with 60% N_2 to Ar could be used to fabricate a multilayer transducer in the future. However, a significant process for optimizing the deposition condition to achieve a good quality c-axis-oriented AlN on top of PZT is still needed.

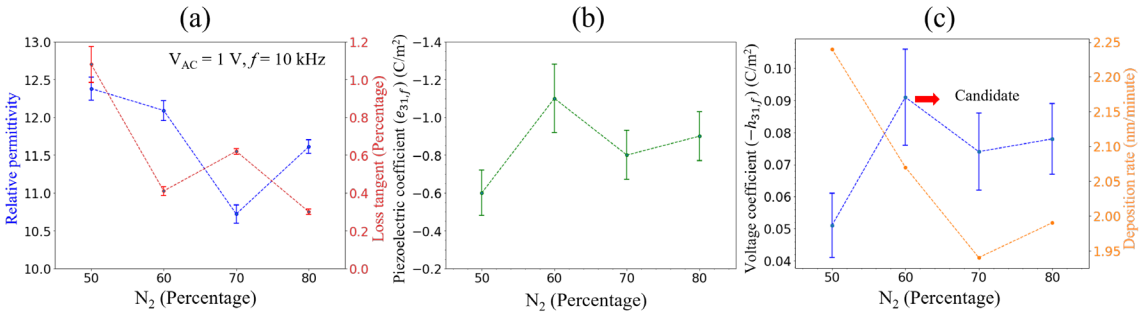

Figure 6-6: The properties of prepared AlN thin films: (a) The relative permittivity, (b) transverse piezoelectric coefficient ($e_{31,f}$), (c) the voltage coefficient ($h_{31,f}$) with deposition as a function of N_2 content.

To illustrate an approach to a multilayer PMUT, a PZT/AlN bar design is proposed, as depicted in Figure 6-7, which outlines the multilayer transducer design and process flow. This process follows the transfer and release method using ZnO, as detailed in Chapter 5. Most deposition and patterning steps can be adapted from the processes developed in Chapter 5.

The fabrication process begins with the deposition of ZnO as a sacrificial layer and Al_2O_3 as a diffusion barrier and insulator onto the silicon substrate. The first, Ti/Pt, electrode (M_1) is deposited and patterned via sputter deposition and lift-off. Next, the PZT layer is deposited via sol-gel method and patterned using plasma etching, with width and length dimensions similar to the M1 electrode for 100% electrode coverage structure. This is followed by the deposition of the common electrode denoted as M_2 electrode, M_2, Ti/Pt, which is also deposited and patterned using sputter deposition and lift-off technique.

Subsequently, AlN is deposited on top of the stack via pulsed DC sputtering as discussed earlier. A Ni hard mask was utilized; the hard mask was deposited by an evaporator and pattern via lift-off similar to Section 5.2.2 in Chapter 5. To pattern AlN, the process developed by the Nanofabrication Staff at Pennsylvania State University was adapted for this work. Inductively coupled plasma reactive ion etching (ICP-RIE system), Ulvac NE550, was used to pattern the film with the process parameter be: a gas mixture of 30 sccm of BCl_3 and 5 sccm of Cl_2, 175 W bias power, and 1200 W ICP power, maintaining an etching pressure of 4 mTorr with the etch rate of

20 A/s. The deposition of the third electrode, Cr/Au, (M_3) will be deposited by sputter deposition and patterned using a lift-off process. Then, the Al_2O_3 protective layer should be deposited, using ALD, before the deposition and polyimide. Following this, the deposition of the polyimide layer can be done by the spin coating method.

After fabrication, the transmit and receive sensitivity should be tested with a calibrated hydrophone to characterize transducer performance and examine the generated acoustic pressure and voltage. Then, pitch and catch experiments could be performed to reveal the imaging capability.

The presence of bending motion in unclamped films and the lateral extension on polymeric should be investigated directly. The vibration characteristic of this multilayer piezoelectric structure could be studied via a high-frequency laser Doppler vibrometer (LDV). This could provide a better understanding of the resonant frequency for PMUTs for a free plate boundary on a flexible substrate.

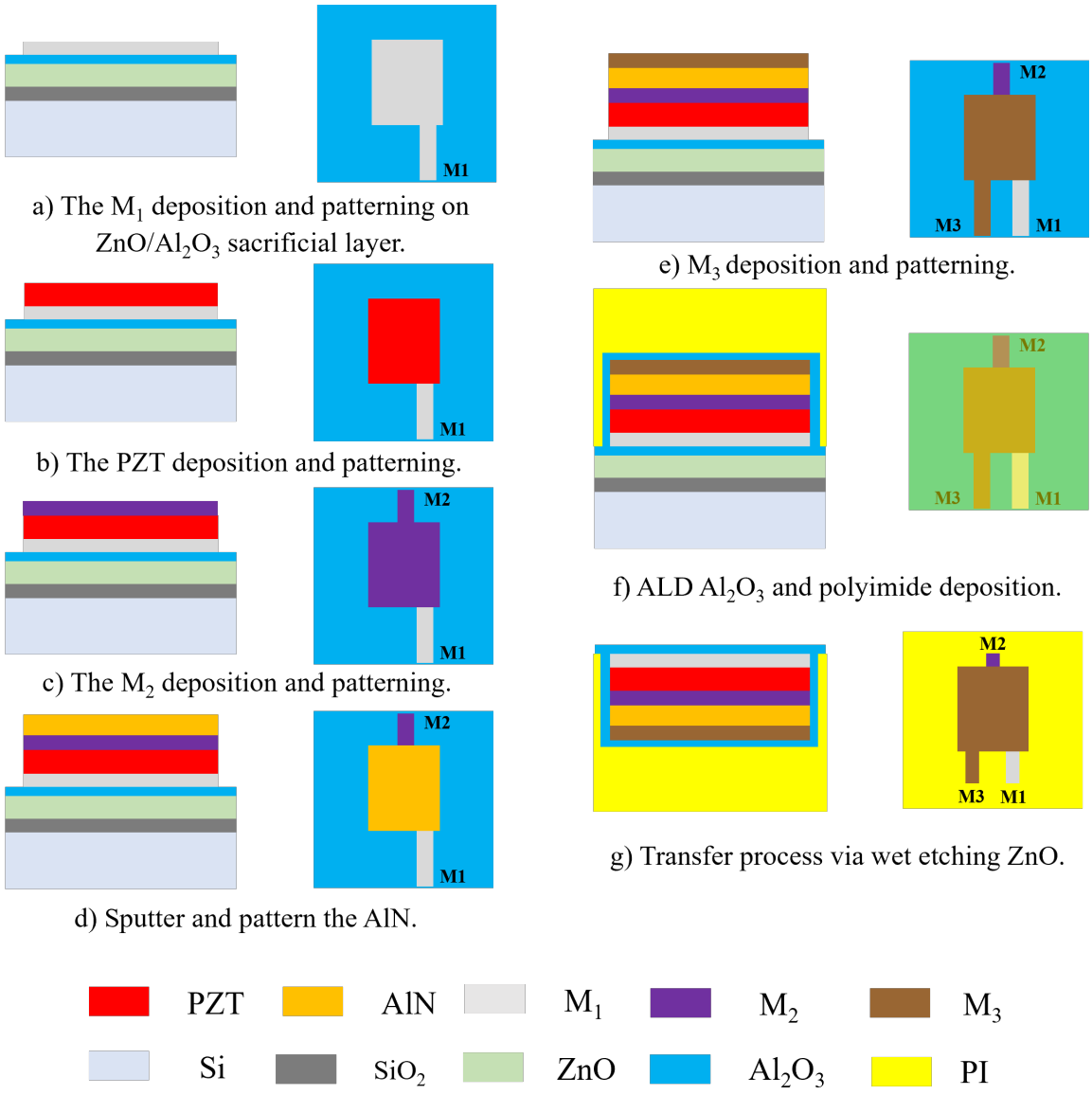

Figure 6-7: Process flow for co-fabrication of AlN/PZT transducers on a polyimide substrate via a transfer process: a) M_1 deposition and patterning on a ZnO/Al_2O_3 sacrificial/protection layer on a Si substrate, b)-c) PZT and M_1 deposition and patterning, d)-e) AlN and M_3 electrode deposition and patterning, f) Al_2O_3 and polyimide deposition, and g) transfer process via wet etching of the ZnO sacrificial layer.

- **Alternative transfer and release method.**

The transfer and release method has been widely used to fabricate free-standing piezoelectric and ferroelectric devices. Various sacrificial layers, such as BaO, $Sr_3Al_2O_6$,

SiO_2, Si, and carbon paste, have been utilized to create different device configurations through wet etching, dry etching, or annealing to remove the sacrificial layer [35][40]. To expedite and simplify the current release method using ZnO wet etching, a transfer and release process employing vapor phase etching of silicon in XeF_2, similar to surface micromachined silicon, is combined with the transfer and release process.

As illustrated in Figure 6-8, the process begins with the preparation of a stack of PZT thin-film capacitors on a SiO_2/Si substrate, as discussed throughout the dissertation. Next, the desired released substrate, such as a polymeric or electroplated metal substrate, is deposited. The release process starts with the deposition and patterning of a hard mask, such as SiO_2, which serves as an etching mask for patterning the released substrate (in the case of a polymer) and later for etching the silicon substrate via XeF_2 etching [41][43]. Then, the isotropic silicon etching with XeF_2 is utilized to remove the underlying silicon substrate to release and transfer the active devices from a rigid silicon substrate to the desired released substrate.

Alternative released substrates can also be explored to facilitate device handling after release and optimize the post-release substrate curling. For example, a thick polyimide layer can be deposited on top of the active element to offer minimal mechanical clamping due to its low Young's modulus. It will also serve as an insulator layer. Following this, a rigid layer, such as electroplated metals and its seed layer, can be deposited to serve as a stress balance layer as well as a stiff supporting layer for the released device.

In conclusion, this proposed fabrication process should facilitate the release process by switching the release mechanism to vapor phase etching of silicon and offer the

flexibility to optimize device rigidity without introducing mechanical constraints from the rigid substrate.

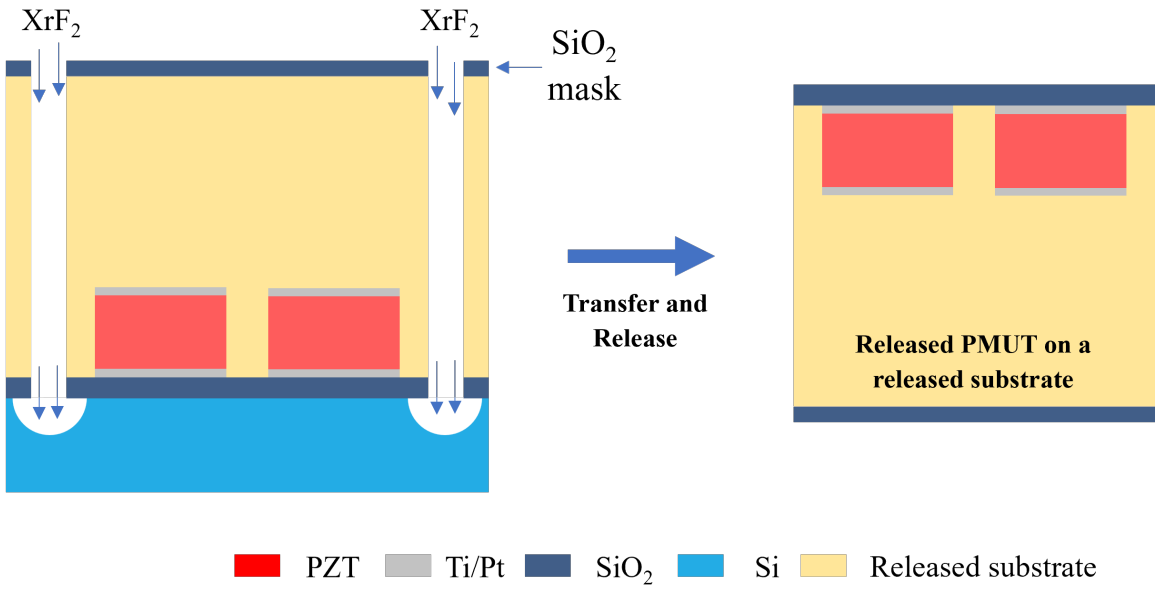

Figure 6-8: The schematic illustrates the transfer and release of a PZT thin film device from a silicon substrate to the desired substrate via silicon surface micromachining using XeF_2.

Bibliography

[1] S. V. Kalinin, B. J. Rodriguez, S.-H. Kim, S.-K. Hong, A. Gruverman, and E. A. Eliseev, "Imaging Mechanism of Piezoresponse Force Microscopy in Capacitor Structures," *Applied Physics Letters*, vol. 92, no. 15, 2008.

[2] L. Wang, Y. Dai, L. Yang, J. Xu, L. Zou, B. Tian, and D. Huang, "Effect of Top Electrode Thickness on the Piezoresponse of Polycrystalline Ferroelectric Capacitors," *J. Phys. D: Appl. Phys.*, vol. 45, no. 50, p. 505302, 2012

[3] S. Sivaramakrishnan, P. Mardilovich, A. Mason, A. Roelofs, T. Schmitz-Kempen, and S. Tiedke, "Electrode Size Dependence of Piezoelectric Response of Lead Zirconate Titanate Thin Films Measured by Double Beam Laser Interferometry," *Appl. Phys. Lett.*, vol. 103, no. 13, p. 132904, 2013.

[4] J. A. Levert, F. M. Mess, R. F. Salant, S. Danyluk, and A. R. Baker, "Mechanisms of Chemical-Mechanical Polishing of SiO_2 Dielectric on Integrated Circuits," *Tribol. Trans.*, vol. 41, no. 4, pp. 593–599, 1998.

[5] J. Hernandez, P. Wrschka, Y. Hsu, T.-S. Kuan, G.S. Oehrlein, H.J. Sun, D.A. Hansen, J. King, and M.A. Fury, "Chemical Mechanical Polishing of Al and SiO_2 Thin Films: The Role of Consumables," *J. Electrochem. Soc.*, vol. 146, no. 12, pp. 4647–4653, 1999.

[6] S. Lee, T. N. Walter, S. Noh, S. E. Mohney, and T. N. Jackson, "Precision wet etching of ZnO using buffer solutions," *J. Microelectromech. Syst.*, vol. 29, no. 6, pp. 1504-1509, 2020.

[7] S. Lee, T. N. Walter, S. E. Mohney, and T. N. Jackson, "High-Temperature-Capable ALD-Based Inorganic Lift-Off Process," *Mater. Sci. Semicond. Process.*, vol. 130, p. 105809, 2021.

[8] V. Lowalekar and S. Raghavan, "Etching of Zirconium Oxide, Hafnium Oxide, and Hafnium Silicates in Dilute Hydrofluoric Acid Solutions," *J. Mater. Res.*, vol. 19, no. 4, pp. 1149–1156, 2004.

[9] D. Seo, J. S. Bae, E. Oh, S. Kim, and S. Lim, "Selective Wet Etching of Si_3N_4/SiO_2 in Phosphoric Acid with the Addition of Fluoride and Silicic Compounds," *Microelectron. Eng.*, vol. 118, pp. 66–71, 2014.

[10] P. A. M. Van Der Heide, M. J. Baan Hofman, and H. J. Ronde, "Etching of Thin SiO_2 Layers Using Wet HF Gas," *J. Vac. Sci. Technol. A*, vol. 7, no. 3, pp. 1719–1723, May 1989.

[11] N. Ohashi, K. Takahashi, S. Hishita, I. Sakaguchi, H. Funakubo, and H. Haneda, "Fabrication of ZnO Microstructures by Anisotropic Wet-Chemical Etching," *J. Electrochem. Soc.*, vol. 154, no. 2, p. D82, 2007.

[12] J. Zhu, N. W. Emanetoglu, Y. Chen, B. V. Yakshinskiy, and Y. Lu, "Wet-Chemical Etching of (1120) ZnO Films," *J. Electron. Mater.*, vol. 33, no. 6, pp. 556–559, 2004.

[13] D. G. Yoo, S.-H. Nam, M.H. Kim, S.H. Jeong, H.-G. Jee, H.J. Lee, N.-E. Lee, B.Y. Hong, Y.J. Kim, D. Jung, and J.-H. Boo, "Fabrication of the ZnO Thin Films Using Wet-Chemical Etching Processes on Application for Organic Light Emitting Diode (OLED) Devices," *Surf. Coat. Technol.*, vol. 202, no. 22–23, pp. 5476–5479, 2008.

[14] H. Zheng, X. L. Du, Q. Luo, J. F. Jia, C. Z. Gu, and Q. K. Xue, "Wet Chemical Etching of ZnO Film Using Aqueous Acidic Salt," *Thin Solid Films*, vol. 515, no. 7–8, pp. 3967–3970, 2007.

[15] C. A. Randall, N. Kim, J. P. Kucera, W. Cao, and T. R. Shrout, "Intrinsic and Extrinsic Size Effects in Fine-Grained Morphotropic-Phase-Boundary Lead Zirconate Titanate Ceramics," *J. Am. Ceram. Soc.*, vol. 81, no. 3, pp. 677–688, 1998.

[16] R. Pramanik, M. K. Sahukar, Y. Mohan, B. Praveenkumar, S. R. Sangawar, and A. Arockiarajan, "Effect of Grain Size on Piezoelectric, Ferroelectric and Dielectric Properties of PMN-PT Ceramics," *Ceram. Int.*, vol. 45, no. 5, pp. 5731–5742, 2019.

[17] M. Wallace, R. L. Johnson-Wilke, G. Esteves, C. M. Fancher, R. H. T. Wilke, J. L. Jones, and S. Trolier-McKinstry, "In Situ Measurement of Increased Ferroelectric/Ferroelastic Domain Wall Motion in Declamped Tetragonal Lead Zirconate Titanate Thin Films," *J. Appl. Phys.*, vol. 117, no. 5, p. 54103, 2015.

[18] T. Liu, M. Wallace, S. Trolier-McKinstry, and T. N. Jackson, "High-Temperature Crystallized Thin-Film PZT on Thin Polyimide Substrates," *J. Appl. Phys.*, vol. 122, no. 16, p. 164103, 2017.

[19] T. Liu, A. Dangi, J. Nyeon Kim, S.-R. Kothapalli, K. Choi, S. Trolier-McKinstry, and T. Jackson, "Flexible Thin-Film PZT Ultrasonic Transducers on Polyimide Substrates," *Sensors*, vol. 21, no. 3, p. 1014, 2021.

[20] P. Muralt, "AlN Thin Film Processing and Basic Properties," in *Piezoelectric MEMS Resonators*, H. Bhugra and G. Piazza, Eds. Cham: Springer, 2017, pp 3-37.

[21] K. Jagannadham, A.K. Sharma, Q. Wei, R. Kalyanraman, and J. Narayan, "Structural Characteristics of AlN Films Deposited by Pulsed Laser Deposition and Reactive Magnetron Sputtering: A Comparative Study," *J. Vac. Sci. Technol. A: Vac. Surf. Films*, vol. 16, no. 5, pp. 2804-2815, 1998.

[22] G. F. Iriarte, F. Engelmark, and I. V. Katardjiev, "Reactive Sputter Deposition of Highly Oriented AlN Films at Room Temperature," *J. Mater. Res.*, vol. 17, no. 6, pp. 1469-1475, 2002.

[23] J. S. Cherng and D. S. Chang, "Effects of Pulse Parameters on the Pulsed-DC Reactive Sputtering of AlN Thin Films," *Vacuum*, vol. 84, no. 5, pp. 653-656, 2009.

[24] H. Takeuchi, M. Ohtsuka, and H. Fukuyama, "Effect of Sputtering Power on Surface Characteristics and Crystal Quality of AlN Films Deposited by Pulsed DC Reactive Sputtering," *phys. status solidi (b)*, vol. 252, no. 5, pp. 1163-1171, 2015.

[25] A. Ababneh, U. Schmid, J. Hernando, J. L. Sánchez-Rojas, and H. Seidel, "The Influence of Sputter Deposition Parameters on Piezoelectric and Mechanical Properties of AlN Thin Films," *Mater. Sci. Eng. B*, vol. 172, no. 3, pp. 253-258, 2010.

[26] L. Vergara, M. Clement, E. Iborra, A. Sanz-Hervás, J. García López, Y. Morilla, J. Sangrador, and M. A. Respaldiza, "Influence of oxygen and argon on the crystal quality and piezoelectric response of AlN sputtered thin films," *Diamond Relat. Mater.*, vol. 13, no. 4-8, pp. 839-842, 2004.

[27] M. I. Abd Samad, M. M. Noor, N. Nayan, A. S. A. Bakar, M. Mansor, A. W. M. Zuhdi, A. A. Hamzah, and R. Latif, "Effects of Argon/Nitrogen Sputtering Gas on the Microstructural, Crystallographic and Piezoelectric Properties of AlN Thin Films," *Scr. Mater.*, vol. 226, p. 115228, 2023.

[28] H. Cheng, Y. Sun, J. X. Zhang, Y. B. Zhang, S. Yuan, and P. Hing, "AlN Films Deposited Under Various Nitrogen Concentrations by RF Reactive Sputtering," *J. Cryst. Growth*, vol. 254, no. 1-2, pp. 46-54, 2003.

[29] S.-H. Lee, K. H. Yoon, D.-S. Cheong, and J.-K. Lee, "Relationship Between Residual Stress and Structural Properties of AlN Films Deposited by RF Reactive Sputtering," *Thin Solid Films*, vol. 435, no. 1-2, pp. 193-198, 2003.

[30] Z. X. Bi, Y. D. Zheng, R. Zhang, S. L. Gu, X. Q. Xiu, L. L. Zhou, B. Shen, D. J. Chen, and Y. Shi, "Dielectric Properties of AlN Film on Si Substrate," *J. Mater. Sci. Mater. Electron.*, vol. 15, pp. 317–320, 2004.

[31] H. Y. Liu, G. S. Tang, F. Zeng, and F. Pan, "Influence of Sputtering Parameters on Structures and Residual Stress of AlN Films Deposited by DC Reactive Magnetron Sputtering at Room Temperature," *J. Cryst. Growth*, vol. 363, pp. 80-85, 2013.

[32] M. A. Dubois and P. Muralt, “Measurement of the Effective Transverse Piezoelectric Coefficient $e_{31,f}$ of AlN and Pb(Zr_x, Ti_{1-x})O_3 Thin Films,” *Sens. Actuators A Phys.*, vol. 77, no. 2, pp. 106–112, Oct. 1999.

[33] M. A. Dubois and P. Muralt, “Properties of Aluminum Nitride Thin Films for Piezoelectric Transducers and Microwave Filter Applications,” *Appl. Phys. Lett.*, vol. 74, no. 20, pp. 3032–3034, 1999.

[34] M.-A. Dubois, P. Muralt, D. V. Taylor, and S. Hiboux, "Which PZT Thin Films for Piezoelectric Microactuator Applications?," *Integr. Ferroelectr.*, vol. 22, no. 1-4, pp. 535–543, 1998.

[35] R. Takahashi and M. Lippmaa, "Sacrificial Water-Soluble BaO Layer for Fabricating Free-Standing Piezoelectric Membranes," *ACS Appl. Mater. Interfaces*, vol. 12, no. 22, pp. 25042–25049, 2020.

[36] P. Salles, I. Caño, R. Guzman, C. Dore, A. Mihi, W. Zhou, and M. Coll, "Facile Chemical Route to Prepare Water Soluble Epitaxial Sr3Al2O6 Sacrificial Layers for Free-Standing Oxides," *Adv. Mater. Interfaces*, vol. 8, no. 5, p. 2001643, 2021.

[37] S. Sun, M. Zhang, C. Gao, B. Liu, and W. Pang, "Flexible Piezoelectric Micromachined Ultrasonic Transducers Towards New Applications," *2018 IEEE International Ultrasonics Symposium (IUS)*, Kobe, Japan, 2018, pp. 1-4.

[38] F. Griggio, S. Jesse, A. Kumar, O. Ovchinnikov, H. Kim, T. N. Jackson, D. Damjanovic, S. V. Kalinin, and S. Trolier-McKinstry, “Substrate Clamping Effects on Irreversible Domain

Wall Dynamics in Lead Zirconate Titanate Thin Films," *Phys. Rev. Lett.*, vol. 108, no. 15, p. 157604, 2012.

[39] Y. Lu, A. Heidari, S. Shelton, A. Guedes, and D. A. Horsley, "High Frequency Piezoelectric Micromachined Ultrasonic Transducer Array for Intravascular Ultrasound Imaging," *2014 IEEE 27th International Conference on Micro Electro Mechanical Systems (MEMS)*, San Francisco, CA, USA, 2014, pp. 745-748.

[40] S.-L. Kok, N. M. White, and N. R. Harris, "Fabrication and characterization of free-standing thick-film piezoelectric cantilevers for energy harvesting," *Meas. Sci. Technol.*, vol. 20, no. 12, p. 124010, 2009.

[41] N. H. Tea, V. Milanovic, C. A. Zincke, J. S. Suehle, M. Gaitan, M. E. Zaghloul, and J. Geist, "Hybrid postprocessing etching for CMOS-compatible MEMS," *J. Microelectromech. Syst.*, vol. 6, no. 4, pp. 363-372, 1997.

[42] T. Zhu, P. Argyrakis, E. Mastropaolo, K. K. Lee, and R. Cheung, "Dry etch release processes for micromachining applications," J. Vac. Sci. Technol. B, Microelectron. Nanometer Struct. Process. Meas. Phenom., vol. 25, no. 6, pp. 2553-2557, 2007.

[43] F. Griggio, "Local Piezoelectric Behavior in PZT-Based Thin Films for Ultrasound Transducers," PhD Thesis, Department of Materials Science and Engineering, Pennsylvania State University, University Park, USA, 2011.

VITA

Pannawit Tipsawat

Pannawit Tipsawat was born in Bangkok, Thailand, and grew up in Nakhon Ratchasima in the Northeast region of Thailand. He completed his high school education at Ratchasima Witthayalai, an all-boys school. Prior to starting his doctoral degree at Pennsylvania State University, he earned a Bachelor of Science in Physics with first-class honors in 2016, followed by a Master of Science in Physics in 2019 from Suranaree University of Technology, Nakhon Ratchasima, Thailand. It was here that he discovered his interest in materials science research, initially working on the synthesis of Fe_3O_4 nanoparticles as an undergraduate student and continuing his research on small polaron hopping in the doped CeO_2 system at the National Institute of Materials Science (NIMS), Tsukuba, Japan, during his master's degree as a visiting scholar. He joined the Department of Materials Science and Engineering at Pennsylvania State University in 2019 as part of the STM research group under the supervision of Dr. Susan Trolier-McKinstry, focusing on the fabrication and characterization of piezoelectric materials and devices.